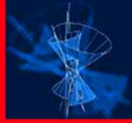


Paulo Bártolo  
Bopaya Bidanda  
*Editors*



# Bio-Materials and Prototyping Applications in Medicine

 Springer

# Bio-Materials and Prototyping Applications in Medicine

Paulo Bártolo · Bopaya Bidanda  
Editors

# Bio-Materials and Prototyping Applications in Medicine

 Springer

*Editors*

Paulo Bártolo  
Polytechnic Institute of Leiria  
School of Technology and Management  
Department of Mechanical Engineering  
Leiria, Portugal 2411-901

Bopaya Bidanda  
University of Pittsburgh  
Department of Industrial Engineering  
Pittsburgh, Pennsylvania 15261

ISBN: 978-0-387-47682-7

e-ISBN: 978-0-387-47683-4

Library of Congress Control Number: 2007932883

© 2008 Springer Science+Business Media, LLC

All rights reserved. This work may not be translated or copied in whole or in part without the written permission of the publisher (Springer Science+Business Media, LLC, 233 Spring Street, New York, NY 10013, USA), except for brief excerpts in connection with reviews or scholarly analysis. Use in connection with any form of information storage and retrieval, electronic adaptation, computer software, or by similar or dissimilar methodology now known or hereafter developed is forbidden. The use in this publication of trade names, trademarks, service marks, and similar terms, even if they are not identified as such, is not to be taken as an expression of opinion as to whether or not they are subject to proprietary rights.

Printed on acid-free paper

9 8 7 6 5 4 3 2 1

springer.com

*This book is dedicated to our parents  
Maria Alice and Francisco Bártolo  
and  
Neena and Monapa Bidanda  
and our families  
Helena and Pedro  
Louella, Maya and Rahul  
for their constant support and cheeriness  
throughout this project!*

# Contents

<b>1 Metallic and Ceramic Biomaterials: Current and Future Developments</b> .....	1
Salil Desai, Bopaya Bidanda and Paulo Bártolo	
<b>2 Polymers, Composites and Nano Biomaterials: Current and Future Developments</b> .....	15
Salil Desai and M. Ravi Shankar	
<b>3 Polyurethane Based Materials with Applications in Medical Devices</b> .....	27
Fred J. Davis and Geoffrey R. Mitchell	
<b>4 Rapid Prototyping of Hydrogels to Guide Tissue Formation</b> .....	49
Jordan S. Miller and Jennifer L. West	
<b>5 Engineered Scaffold Architecture Influences Soft Tissue Regeneration</b> .....	67
Darice Y. Wong, Elly E. Liao, J. C. Leveque, Hunter Brumblay, Chia-Ying Lin, Frank LaMarca, Paul H. Krebsbach and Scott J. Hollister	
<b>6 Customised Implants for Bone Replacement and Growth</b> .....	79
Liang Hao and Russell Harris	
<b>7 Direct Digital Manufacturing of Complex Dental Prostheses</b> .....	109
B. Vandenbroucke and J. -P. Kruth	
<b>8 Digital Design and Fabrication in Dentistry</b> .....	125
Ming C. Leu, Parthiban Delli and Mary P. Walker	

**9 The Development of an Artificial Finger Joint** . . . . . 157  
I. Gibson, S. P. Chow, K. W. Lam, W. W. Lu, A. H. W. Ngan,  
W. Y. Yip and K. Y. Chiu

**10 Computer-aided Development of Mega Endo-Prostheses** . . . . . 191  
B. Ravi and Manish Agarwal

**Index** . . . . . 209

# Contributors

## **Manish Agarwal**

Tata Memorial Hospital,  
Dr. E. Borges Road,  
Parel, Mumbai 400012,  
Maharashtra, India.

## **Paulo Bártolo**

Polytechnic Institute of Leiria,  
School of Technology and  
Management, Department of  
Mechanical Engineering, Leiria,  
Portugal 2411-901.

## **Bopaya Bidanda**

University of Pittsburgh,  
Department of Industrial  
Engineering, Pittsburgh,  
PA 15261, USA.

## **Hunter Brumblay**

Spine Research Laboratory,  
Departments of Neurosurgery  
& Biomedical Engineering,  
The University of Michigan,  
Ann Arbor, MI 48109, USA.

## **K.Y. Chiu**

Department of Orthopaedics  
and Traumatology, The University  
of Hong Kong, Queen Mary Hospital,  
Pokfulam, Hong Kong.

## **S.P. Chow**

Department of Orthopaedics and  
Traumatology, The University  
of Hong Kong, Queen Mary Hospital,  
Pokfulam, Hong Kong.

## **Fred J. Davis**

School of Chemistry,  
The University of Reading,  
Whiteknights, Reading,  
RG6 6AD, UK.

## **Parthiban Delli**

Department of Mechanical  
and Aerospace Engineering,  
University of Missouri-Rolla, Rolla,  
MO 65409, USA.

## **Salil Desai**

Department of Industrial and Systems  
Engineering, North Carolina A & T  
State University, Greensboro,  
NC 27411, USA.

## **I. Gibson**

Department of Mechanical  
Engineering, National University  
of Singapore, Singapore.

## **Liang Hao**

School of Engineering,  
Computer Science and Mathematics,  
University of Exeter, EX4 4QF, UK.



**Russell Harris**

Wolfson School of Mechanical and Manufacturing Engineering, Loughborough University, LE11 3TU, UK.

**Scott J. Hollister**

Scaffold Tissue Engineering Group, Department of Biomedical Engineering; Spine Research Laboratory, Departments of Neurosurgery and Biomedical Engineering; Departments of Surgery and Mechanical Engineering, The University of Michigan, Ann Arbor, MI, USA.

**Paul H. Krebsbach**

Department of Biologic and Materials Sciences, School of Dentistry, The University of Michigan, Ann Arbor, MI, USA.

**J.-P. Kruth**

Division PMA, Department of Mechanical Engineering, Katholieke Universiteit Leuven, Celestijnenlaan 300b, 3001 Heverlee, Belgium.

**K.W. Lam**

Department of Orthopaedics and Traumatology, The University of Hong Kong, Queen Mary Hospital, Pokfulam, Hong Kong.

**Frank LaMarca**

Spine Research Laboratory, Departments of Neurosurgery and Biomedical Engineering, The University of Michigan, Ann Arbor, MI, USA.

**Ming C. Leu**

Department of Mechanical and Aerospace Engineering, University of Missouri-Rolla, Rolla, MO 65409, USA.

**J.C. Leveque**

Spine Research Laboratory, Departments of Neurosurgery and Biomedical Engineering, The University of Michigan, Ann Arbor, MI, USA.

**Elly E. Liao**

Scaffold Tissue Engineering Group, Department of Biomedical Engineering, The University of Michigan, Ann Arbor, MI, USA.

**Chia-Ying Lin**

Spine Research Laboratory, Departments of Neurosurgery and Biomedical Engineering, The University of Michigan, Ann Arbor, MI, USA.

**W.W. Lu**

Department of Orthopaedics and Traumatology, The University of Hong Kong.

**Jordan S. Miller**

Rice University, Department of Bioengineering MS-142, W100E George R. Brown Hall, 6100 Main Street, Houston, TX 77005, USA.

**Geoffrey R. Mitchell**

Department of Physics and Polymer Science Centre, University of Reading Whiteknights, Reading RG6 6AF, UK.

**A.H.W. Ngan**

Department of Mechanical Engineering, The University of Hong Kong, Pok Fu Lam Road, Hong Kong.

**B. Ravi**

Indian Institute of Technology, Bombay, Department of Mechanical Engineering, Powai, Mumbai 400076, Maharashtra, India.

**M. Ravi Shankar**

Department of Industrial Engineering, University of Pittsburgh, 1034 Benedum Hall, 3700 O'Hara Street, Pittsburgh, PA 15261, USA.

**B. Vandenbroucke**

Division PMA, Department of Mechanical Engineering, Katholieke Universiteit Leuven, Celestijnenlaan 300b, 3001 Heverlee, Belgium.

**Mary P. Walker**

Departments of Restorative Dentistry and Oral Biology, University of Missouri-Kansas City School of Dentistry, Kansas City, MO 64108, USA.

**Jennifer L. West**

Rice University, Department of Bioengineering MS-142, W100E George R. Brown Hall, 6100 Main Street, Houston, TX 77005, USA.

**Darice Y. Wong**

Scaffold Tissue Engineering Group, Department of Biomedical Engineering, The University of Michigan, Ann Arbor, MI, USA.

**W.Y. Yip**

Department of Orthopaedics and Traumatology, The University of Hong Kong, Queen Mary Hospital, Pokfulam, Hong Kong.

# Chapter 1

## Metallic and Ceramic Biomaterials: Current and Future Developments

Salil Desai, Bopaya Bidanda and Paulo Bártolo

**Abstract** This chapter discusses the different types of biomaterials used for medical applications. Metallic, ceramic and nanomaterial based biomaterials are classified and described based on their physical and biocompatibility properties. Various applications of these biomaterials are discussed. State-of-the-art in biomaterial research is also introduced.

### 1.1 Preface

Materials that interface with biological entities and are used to create prosthesis, medical devices and replace natural body tissue are broadly called as biomaterials. An expert definition of biomaterial is [1, 2] (Williams, 1987; Ratner et al., 2004):

A biomaterial is a nonviable material used in a medical device, intended to interact with biological systems

Though the initial definition of biomaterial was restricted to medical devices, biomaterials in the present times encompass both synthetic and natural materials that promote human health. A distinctive difference between a biomaterial over other materials is its benign coexistence with a biological system with which it interfaces. This phenomenon is called as biocompatibility and is defined as [1] (Williams, 1987):

Biocompatibility is the ability of a material to perform with an appropriate host response in a specific application

The biocompatibility of materials is of considerable interest because implants and tissue interfacing devices can corrode in an in vivo environment [3]. The

---

Salil Desai  
Department of Industrial and Systems Engineering North Carolina A&T State University,  
Greensboro, North Carolina, USA, 27411  
sdesai@ncat.edu

corrosion of the implant can lead to loss of load bearing strength and consequent degradation into toxic products within the tissue.

Biomaterials applications span from prostheses (e.g. hip implants and artificial heart valves), tissue regeneration, medical devices, to drug delivery. A biomaterial is specifically chosen based on its compatibility with the host tissue and structural integrity over its designed life. In order to identify each material type based on their properties and application intent, it is important that they be systematically classified. Biomaterials can be broadly categorized under the four categories namely:

- Metals
- Ceramics
- Polymers
- Composites

## **1.2 Metals**

This class of material is known for their high stiffness, ductility, wear resistance, thermal and electrical conductivity. Metals and their alloys are commonly used in implants, medical device manufacture and related accessories. Due to their mechanical reliability, metallic biomaterials are difficult to be replaced by ceramic and polymer substitutes [4]. One of advantages of using metals as biomaterials is their availability and relative ease of processing from raw ore to finished products. The material properties of metals have been studied in the context of biocompatibility, surface interaction and structural integrity [3, 5, 6, 7, 8]. Moreover, customized properties including flexibility, high strength and abrasion resistance can be developed by alloying constituent elements of different metals. Metallic biomaterials are classified as inert because they illicit minimal tissue response. Given their higher fatigue strength and chemical resistance to corrosion they are used in load bearing applications. This section describes the different types of metals and their alloys that are commonly used.

### ***1.2.1 Titanium***

#### **1.2.1.1 Description**

Titanium has one of the highest strength-to-weight ratio and corrosion resistance of metals [9, 10]. It has a lustrous metallic-white color and exhibits high hardness. In its pure form titanium is ductile [11] and is often alloyed with other elements for enhanced toughness. Titanium is extracted from rutile ( $\text{TiO}_2$ ) a mineral deposit and is processed in multiple steps [12, 13] to obtain the finished material. Due to its non-corrosive properties titanium has excellent

biocompatibility. The material passivates itself in vivo by the formation of an adhesive oxide layer [14, 15]. Titanium also displays a unique property of osseointegration where it connects both structurally and functionally with the underlying bone [16]. It is commonly used in total joint replacements [17], dental implants [18], internal and external fixators, artificial heart valves, spinal fusion and medical devices. However, due to the high processing cost titanium is expensive.

### 1.2.1.2 Applications

Due to its high strength, low weight and non-corrosive properties, titanium and its alloys are used in a wide range of medical applications. Titanium is a major material used in the skeletal system for joint replacement such as hip ball and sockets and in internal fixators such as plates and screws. A titanium implant has high fracture toughness and enhanced fatigue properties over competing metals. These load bearing implants can stay in place for 15–20 years thereby, improving the quality of human life. Figure 1.1 shows the acetabular shell (socket portion) and the femoral stem. The socket is made of metal shell with a medical grade plastic liner which acts like a bearing. The femoral stem is made of metal such as titanium alloy.

Figure 1.2 shows one of the femoral stems being cemented to the bone using an epoxy. In the other design the femoral stem has fine mesh of holes on the surface that promotes tissue growth and subsequent attachment of the prosthesis to the bone.

Titanium is also used for bone-fracture fixation in spinal fusion devices, pins, bone-plates and screws. Due to its non-magnetic properties it does not pose any threat to patients with implants during magnetic resonance imaging and exposure to electronic equipment. Titanium is also used for wide range of surgical instruments. It does not corrode or lose surface properties with repeated sterilization and its light weight reduces surgeon fatigue during repetitive operations. Titanium is used in craniofacial and maxillofacial treatments to replace facial features of patients.

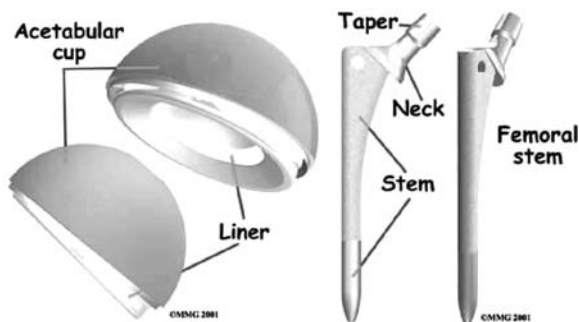
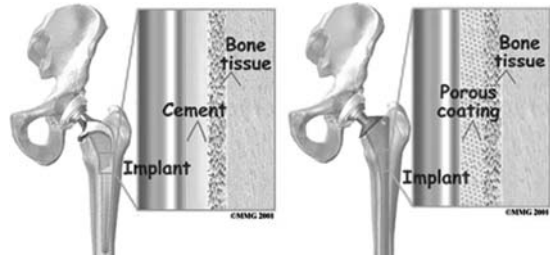


**Fig. 1.1** Acetabular shell (socket-left) and femoral stem (right) implants (Courtesy: Depuy Orthopedics, Inc. [19])

**Fig. 1.2** Cemented (*left*) and uncemented (*right*) designs of femoral stem implants (Courtesy: DePuy Orthopaedics, Inc. [19])



Another prominent application of titanium alloy is in dental implants for tooth fixation. After the osseointegration of the implant with the bone an abutment is inserted into the implant. The abutment provides a seat for the crown which replaces the natural tooth. Tooth replacement using titanium implants is more effective than the use of traditional root canal and bridge constructs.

## 1.2.2 Stainless Steel

### 1.2.2.1 Description

Stainless steel is a versatile class of material that has high strength and resistance to oxidation. Typically, stainless steels have a minimum of 12% chromium content that forms a thin oxide film which resists oxidation. The addition of nickel and molybdenum further enhances the corrosion and pitting resistance. As compared to titanium it is easy to machine and thus commonly used for surgical instruments, bone screws, stents and other medical equipment. Of the numerous grades of stainless steels the 300 series is used in medical applications. Typical medical grades include the 304 and the 316L. It can be also electropolished for aesthetic appeal. Because of its high strength and chemical inertness to bodily fluids, blood and enzymes it is FDA approved as a biomaterial. Moreover, it can be processed using multiple methods including forming, welding, bending and machining. Medical grade stainless is available in various stock forms making it is easy to fabricate the material into its final form. However, it is heavier than titanium which can lead to heavier implants and fatigue during repeated handling of surgical tools. Based on their microstructure and the resulting properties steels are broadly classified as austenitic, martensitic and ferritic.

### 1.2.2.2 Applications

Commercial-grade stainless steel is used to manufacture operating room accessories, dental and surgical instruments which involve superficial contact of the

device with the human tissue. Austenitic steels are used for implant fabrication, hypodermic needles, sterilizers, work tables and autoclave compartments where moderate strength, formability and corrosion resistance is desired [20]. This class of stainless steel is nonmagnetic, can be cold hardened and possesses higher corrosion resistance than other types. 316L is the most common stainless steels used in medical industry. The “L” within the 316L designation stands for low carbon steel. As compared to the 0.08% carbon content in regular 304 or 316 steel, the 316L contains 0.03% carbon. The lower carbon content reduces carbide precipitation thereby minimizing in vivo corrosion. Higher percentages of nickel (~12%) are added to stabilize the austenitic phase of steel. Other alloying elements include chromium, molybdenum, manganese, silicon, sulfur, phosphorous and nitrogen. Type 316L austenitic steels can be heat treated for wide range of mechanical properties. Because they corrode under highly stressed and oxygen-depleted [21] environments they are generally used for temporary implant devices. BioDur<sup>®</sup> 108 is a nickel-free austenitic stainless steel alloy with high nitrogen content [22]. It has higher tensile and fatigue strength as compared to nickel-containing alloys such as 316L. It is a non-magnetic alloy that can be fabricated by forging or machining. Due to its high strength and corrosion resistance it is used in bone plates, spinal fixation, screws, hip and knee components and medical devices.

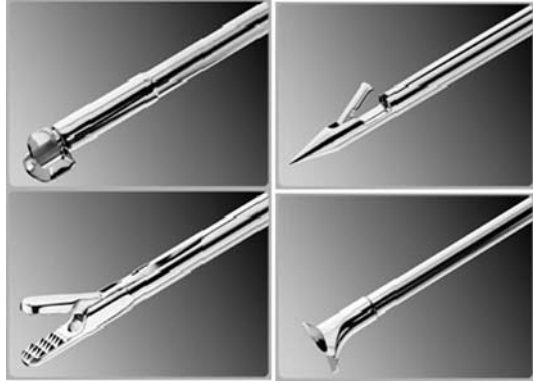
Figure 1.3 (*left*) shows a stainless screw and washer for soft tissue fixation to the bone. Figure 1.3 (*right*) shows a low-profile, wide staple based fixation system that provides better load distribution. The unique staple design enhances uninterrupted vascular flow to the underlying tissue [23].

Martensitic stainless steels contain iron, chromium and carbon alloys with other additives including niobium, silicon, tungsten and vanadium. The properties (hardness, toughness) of these stainless steels can be altered based on heat treatment conditions. These types of steels possess lower corrosion resistance over austenitic steels. They are used for dental and surgical instruments such as chisels, scalpels, pliers, forceps, etc. Figure 1.4 shows instruments made from surgical grade stainless steel.

**Fig. 1.3** Stainless steel screw and washer (*left*) for soft tissue fixation, staple fixation system to attach tissue to bone (*right*) (Courtesy: ConMed Linvatec Corporation [23])



**Fig. 1.4** Surgical grade stainless steel rotary punch (*top-left*), suture tram (*top-right*), linear alligator grasper (*bottom-left*), rotary scissors (*bottom-right*). (Courtesy: ConMed Linvatec Corporation [24])



## 1.2.3 Shape Memory Alloys

### 1.2.3.1 Description

Shape memory alloys (SMA) are materials that retain their original shape after severe deformations when subjected to heat above their transformation temperature. NiTiNOL which stands for Ni-Nickel, Ti-Titanium, NOL-Naval Ordnance Laboratory is a popular shape memory alloy discovered by Buehler et al. at the US Naval Ordnance Laboratory in 1960s [25]. Shape memory alloys have two distinct crystallographic phases namely; austenite and martensite. The martensitic phase is a low temperature stable phase with the absence of stress. The austenite phase is stable at high temperature and displays a stronger body-center cubic structure [26]. SMA are capable of large amounts of bending and torsional deformation and high strain rates (6–8%) in the martensitic phase [27]. Once deformations are induced in the material in the martensitic phase, it is heated at the phase transformation temperature. The alloy undergoes a crystalline reversible solid state phase change from martensite to austenite. The above phenomenon is known as one-way shape memory effect. Another unique property of shape memory alloy is pseudo-elasticity wherein the two-way phase transformation occurs at a constant temperature  $A_F$ .  $A_F$  is defined as the temperature where the austenitic phase is finished forming. A shape memory alloy fully composed of austenite phase is mechanically deformed at constant temperature  $A_F$ . The loading transforms the material into a martensitic phase. When the load is released, reverse transformation (martensitic to austenitic) occurs bringing the material back to its original shape. The properties of shape memory alloys are significantly affected by composition, processing methods and other factors. Nitinol alloys are processed using various powder metallurgy techniques [28]. Nitinol implants are used as hard tissue implants in orthopedics and dentistry because of its porous structure, good mechanical



properties, biocompatibility and shape memory effect [29, 30]. One of promising processes for manufacturing hard tissue TiNi alloy implants is HIPing [31]. HIPing stands for Hot Isostatic Pressing wherein different material powders are consolidated using heat and high pressure simultaneously. Using the HIPing process it is possible to attain implant properties such as controlled porosity and elastic modulus nearer to the natural bone. Figure 1.5 shows SEM micrographs of HIPped samples under different heating temperatures and time durations made from elemental powders of Ti (50%) and Ni (50%) composition [32].

### 1.2.3.2 Applications

Shape memory alloys (SMA) possess excellent corrosion resistance, wear and mechanical properties with good biocompatibility. NiTi based shape memory alloys are used as biomaterials for in vivo applications including implants and minimally invasive surgeries [34, 35]. This is because NiTi alloys maintain their functional ability without degrading when in contact with living tissue [36]. One of the prominent applications of nitinol alloy is in self-expanding cardiovascular stents. Stents are used in angioplasty procedures to open blocked and

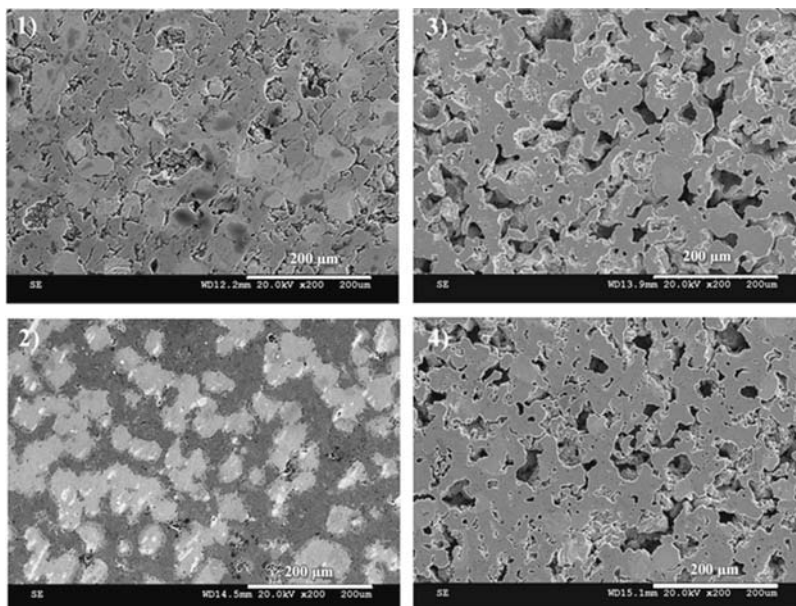
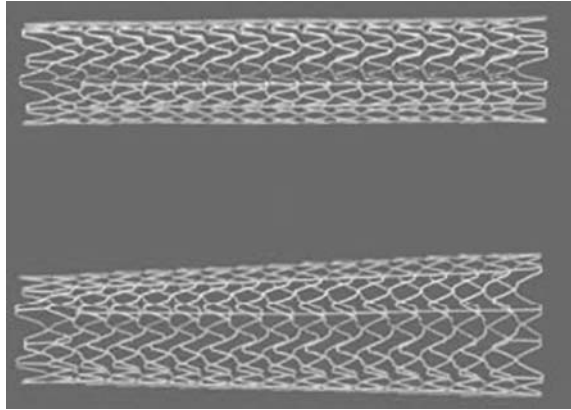


**Fig. 1.5** Micrographs show the porous structures of the HIPed specimens. 1) and 2) are for the specimens HIPed at 900°C for 1h, 3) and 4) are for those HIPed at 980°C for 4h. Specimens 1) and 3) had wax binder in powder preparation and 2) and 4) had PDDA binder. (Courtesy: Zhigang Xu: Center for Advanced materials and Smart Structures – NC A&T SU [33])

**Fig. 1.6** RX ACCULINK Carotid self-expanding nitinol stents manufactured in straight (*top*) and tapered (*bottom*) configurations (Images courtesy of Abbott Vascular. (c) 2007 Abbott Laboratories. All Rights Reserved [38])



weakened blood vessels such as the coronary, iliac, carotid, aorta and femoral arteries [37]. Stent is a cylindrical scaffold made of shape memory material. Initially, a stent is introduced inside the blood vessel in its pre-compressed martensitic state using a catheter. After reaching the body temperature, the stent expands to open the blood vessel and increase blood flow. Figure 1.6 shows straight and tapered configurations of nitinol stents manufactured by Abbott Vascular Laboratories.

Shape memory alloys are commercially available as alloy combinations of different compositions including copper, zinc, aluminum, cadmium, indium, iron, magnesium, gold and silver. Copper based shape memory alloys are used in external biomedical applications which do not need biocompatibility [39]. Applications that exploit the superelasticity and shape changing properties of shape memory alloys include eyeglass frames, rehabilitation devices, guide wires for introduction of therapeutic and diagnosis devices [40] and snare wires used for removing tonsils and polyps [41, 42]. Other applications of shape memory alloy include vena cava filters that trap blood clots and prevent their flow to other body parts [43, 44]. The device consists of a straight wire that is inserted into the vena-cava with a cooled catheter. On reaching body temperature the wire reverts to an umbrella shaped filter to trap small blood clots.

SMA are also used for orthodontic archwires to apply a consistent force for correcting misaligned teeth [45, 46]. The dental application utilizes the superelasticity property of shape memory alloys without the need to periodically retighten wires as in conventional stainless steel material.

### ***1.2.4 Noble Metals***

Noble metals show a marked reluctance to combine with other elements to form compounds. As such they have excellent resistant to corrosion or oxidation and

good candidate for biomaterials. Noble metals such as gold, silver and platinum are used when there is a need for functionality other than the basic mechanical performance. Typically, they are used in devices requiring specific electrical or mechanical properties.

#### **1.2.4.1 Gold**

Gold is an inert metal that has high resistance to bacterial colonization. Gold and its compounds have been historically used in oriental cultures for the treatment of ailments. It has been one of the first materials to be used as an implantable material (dental tooth implant). Due to its high malleability it is used in restorative dentistry for crowns and permanent bridges. Gold possesses excellent electrical conductivity and biocompatibility and is used in wires for pacemakers and other medical devices.

#### **1.2.4.2 Platinum**

Platinum possesses excellent corrosion resistance, biocompatibility, and stable electrical properties. It is used for manufacture of electrodes in devices such as cardiac pacemakers and electrodes in cochlear (cavity within the inner ear) replacement for the hearing impaired. A typical pacemaker uses platinum-iridium electrodes that send electrical pulses to stabilize the rhythm of heart-beat. Miniaturized platinum coils are used in endovascular therapy for the treatment of aneurysms. Using a micro catheter these platinum coils are inserted within an aneurysm. The flexible platinum coils conform to the shape of the aneurysm and obstruct the flow of blood.

#### **1.2.4.3 Silver**

Silver is used in surgical implants and as a sanitizing agent. They are used as studs of earrings to prevent infection of newly pierced ears. Silver compound is used in burn therapy to improve the healing and prevent infection of burns. Wound dressing fibers are plated with silver to provide a germicidal and analgesic enclosure on the wound. Silver is also used in urinary bladder catheters and stethoscope diaphragms.

### **1.3 Ceramics**

Ceramic comes from a Greek word 'keramikos' which stands for burnt materials. Ceramic biomaterials are inorganic and nonmetallic elements predominantly formed by ionic bonding. They are produced under high

temperature heat treatment process called firing. The use of ceramics as biomaterials has allowed for tailored surfaces that exhibit minimal reaction with host tissues in addition to providing high-bearing properties [47]. Based on their excellent biocompatibility they are used as implants within bones, joints and teeth. They are used as coatings in conjunction with metallic core structures for prosthesis. Herein the ceramic provides the hardness and wear resistance while the metallic core provides toughness and high strength for load bearing applications [48]. Ceramic structures can be designed with varying porosity for bonding with the natural bone.

### ***1.3.1 Hydroxyapatite (HA)***

#### **1.3.1.1 Description**

Hydroxyapatite (HA) is calcium phosphate based ceramic with high hardness. HA ceramic structures can be developed with a unique bone like porous structure and is widely used for creating scaffolds in tissue engineering. It can be used for long-term bone replacement due to its slow-decaying properties. Synthetic Hydroxyapatite ( $\text{Ca}_{10}(\text{PO}_4)_6(\text{OH})_2$ ) is an inorganic biomaterial with chemical characteristics similar to hard tissues such as the bone and teeth. Hydroxyapatite ceramics are bioactive, such that they promote hard tissue ingrowth and osseointegration when implanted within the human body [49]. The porous structure of this material can be tailored to suit the interfacial surfaces of the implant. However they lack mechanical strength for load bearing applications as standalone structural members.

#### **1.3.1.2 Applications**

The porosity of the hydroxyapatite structure can be controlled similar to the human bone. Thus it is ideal to be used in implants for artificial tooth, hip and knee replacements. Typically most high-bearing implants contain hydroxyapatite coating. The hydroxyapatite coating is applied to the core metallic implant using plasma spray technology. This minimizes the delamination of the hydroxyapatite coating from the metal implant and prolongs the working life of the prosthesis. Figure 1.7 shows the femoral component of the hip implant that has been coated with hydroxyapatite ceramic to promote rapid ingrowth of bone structure. Hydroxyapatite ceramic has also been used in maxillofacial implants as bone filler and as orbital implants within the eye socket.

**Fig. 1.7** Femoral component coated with hydroxyapatite ceramic coating (Courtesy: Biomet Orthopedics [50])



## 1.3.2 Zirconia

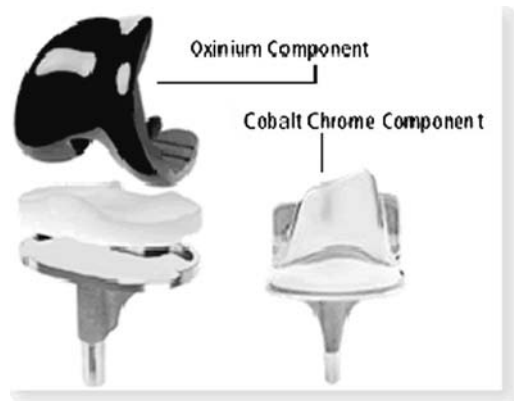
### 1.3.2.1 Description

Zirconia ( $ZrO_2$ ) is a white amorphous powder and dioxide of zirconium. Zirconia is bioinert and thus does not interact with the human body. With an increase in temperature Zirconia changes its monoclinic crystalline state and morphs into tetragonal crystalline and subsequent cubic crystalline. Zirconium Oxide ceramic has several advantages over other ceramic materials, due to its transformation toughening mechanisms, low thermal conductivity, abrasion resistance, desirable biocompatibility, diminished plaque accumulation and excellent light dynamics [51].

### 1.3.2.2 Applications

Partially stabilized zirconia is commonly used in prosthetic devices because it is stronger and has high resistance to wear. The flexural strength and fracture toughness of zirconia is higher as compared to other ceramics which makes it resistant to masticatory forces when used as crowns with exact precision of fit [52, 53]. Also, zirconia implants have shown to accumulate less bacteria in vivo [54] and undergo a lower rate of inflammation-associated processes compared to titanium [55]. Zirconia has also been used in shoulder reconstruction surgery and as a coating over titanium in dental implants. Yttria stabilized zirconium oxide implants include knee

**Fig. 1.8** Zirconium oxide (Oxinium™) knee implant (Courtesy: Smith and Nephew Inc. [56])



joints and spinal implants. Figure 1.8 shows zirconium oxide knee implant component manufactured by Smith & Nephew Inc.

## References

1. Williams DF. Definitions in biomaterials. *Proceedings of a consensus conference of the european society for biomaterials*, vol. 4. Chester, England, March 3–5, 1986. New York: Elsevier, 1987.
2. Ratner BD and Bryant SJ. Biomaterials: Where we have been and where we are going, *Annual Reviews of Biomedical Engineering*, 6: 41–75, 2004.
3. Williams DF. Orthopedic implants: Fundamental principles and the significance of biocompatibility. In Williams DF (ed.), *Biocompatibility of Orthopedic Implants*, vol. 1. Boca Raton, Fla: CRC Press, 1982, pp. 1–50.
4. Hanawa T. Evaluation techniques of biomaterials in vitro, *Science and Technology of Advanced Materials*, 3 (2002), 289–295.
5. Ratner BD, Hoffman AS, Schoen FJ, and Lemons JE. *Biomaterials Science: An Introduction to Materials in Medicine*, 2nd edition. San Francisco: Elsevier Academic Press, 2004.
6. Good RJ. Contact angle, wetting, and adhesion: A critical review. In Mittal KL (ed.), *Contact Angle, Wettability and Adhesion*, Netherlands: VSP publishers, 1993.
7. Beeves CJ and Robinson JL. Some observations on the influence of oxygen content on the fatigue behavior of  $\alpha$ -titanium. *J. Less-Common Metals*, 17: 345–352, 1969.
8. Conrad H, Doner M and de Meester B. Critical review: Deformation and fracture. In Jaffee RI, Burte HM (eds.), *Titanium, science and technology*, vol. 2. Warrendale, PA: TMS, 1973.
9. Matthew J. Donachie, Jr. *Titanium: A Technical Guide*. Metals Park, OH: ASM International, 1988, p. 11. ISBN 0871703092.
10. Titanium. *Columbia Encyclopedia* (6th edition). New York: Columbia University Press, 2000–2006. ISBN 0787650153.
11. Titanium. *Encyclopædia Britannica*, 2006.
12. Matthew J. Donachie, Jr. *Titanium: A Technical Guide*. Metals Park, OH: ASM International, 1988, Chapter 4. ISBN 0871703092.

13. Chen, GZ, Fray, DJ, and Farthing, TW. Direct electrochemical reduction of titanium dioxide to titanium in molten calcium chloride. *Nature* 407: 361–64, 2000. DOI:10.1038/35030069. *Abstract*
14. Breme HJ, Biehl V, and Helsen JA. Metals and implants. In Helsen JA, Breme HJ (eds.), *Metals as Biomaterials*. Chichester: Wiley, 1998, pp. 37–72.
15. Park JB. Metallic biomaterials. In Bronzino JD (ed.), *The biomedical engineering handbook*. Boca Raton: CRC Press; 1995, pp. 537–51.
16. Davies JE, Lowenberg B, and Shiga A. The bone–titanium interface in vitro. *J Biomed Mater Res*, 24: 1289–306, 1990.
17. Hallab NJ, Jacobs JJ, and Katz JL. Orthopedic applications. In Ratner BD, Hoffman AS, Schoen FJ, and Lemons JE (eds.), *Biomaterials science—an introduction to materials in medicine*. San Diego: Elsevier Academic Press, 2004, pp. 526–55.
18. Cranin AN, Lemons JE. Dental implantation. In Ratner BD, Hoffman AS, Schoen FJ, and Lemons JE (eds.), *Biomaterials science—an introduction to materials in medicine*. San Diego: Elsevier Academic Press, 2004, pp. 555–72.
19. DePuy Orthopaedics Inc. [http://www.jointreplacement.com/xq/ASP.default/pg.content/content\\_id.84/mn.local/joint\\_id.5/joint\\_nm.Hip/local\\_id.4/qx/default.htm](http://www.jointreplacement.com/xq/ASP.default/pg.content/content_id.84/mn.local/joint_id.5/joint_nm.Hip/local_id.4/qx/default.htm)
20. Tony N, Report on Stainless Steel – A Family of Medical Device Materials, *Business Briefing: Medical Device Manufacturing & Technology*, 2002.
21. Serhan H, Slivka M, Albert T, and Kwak S. Is galvanic corrosion between titanium alloy and stainless steel spinal implants a clinical concern? *The Spine Journal*, 4 (4): 379–387, 2004.
22. Carpenter Technology Corp, <http://cartech.ides.com/datasheet.aspx?&I=101&E=6>
23. ConMed Linvatec Corporation, <http://www.conmed.com/products-knee-fixation.php>
24. ConMed Linvatec Corporation, <http://www.conmed.com/products-maninst-concept.php>
25. Buehler WJ, Gilfrich JV, and Wiley RC. Effect of characteristic temperatures of thermoelastic martensitic properties of alloys near composition TiNi. *J. Appl. Phys.*, 34: 1475–1476, 1963.
26. Machado LG and Savi MA. Medical applications of shape memory alloys, *Brazilian Journal of Medical and Biological Research* 36: 683–691, 2003.
27. Hodgson DE, Wu MH, and Biermann RJ. *Shape Memory Alloys, Metals Handbook*. Vol. 2. ASM International, Ohio, 897–902, 1990.
28. Kyogoku H and Komatsu S. *J. Japan Society of Powder and Powder Metallurgy*, 46(10): 1103, 1999.
29. Saito S, Wachi T, and Hanada S. *Mater. Sci. Eng.*, A161: 91, 1992.
30. Itin VI, Gjunter VE, Shabalovskaya SA, Sachdeva RLC. *Mater. Charact.* 32: 179, 1994.
31. Hey JC and Jardine AP. *Mat. Res. Soc. Symp. Proc.* 360: 483, 1995.
32. Zhigang Xu, Waters CK, Rajaram G, Sankar J. Preparation of Porous Nitinol Material by Hot-Isostatic Pressing, *Proceedings of Advances in Materials Processing for Challenging Environments*, ASME International Mechanical Engineering Congress & Exposition, November 5–11, 2005, Orlando, Florida.
33. Zhigang Xu, Center for Advanced Materials and Smart Structures, North Carolina A & T State University, 2005.
34. Stockel D. Nitinol medical devices and implants, *Min Invas Ther & Allied Technol*, 9: 81–8, 2000.
35. Pelton AR, Stöckel D, and Duerig TW. Medical uses of nitinol. *Materials Science Forum*, 327–328: 63–70, 2000.
36. Mantovani D. Shape memory alloys: Properties and biomedical applications. *Journal of the Minerals, Metals and Materials Society*, 52: 36–44, 2000.
37. Duerig TM, Pelton A, and Stöckel D. An overview of nitinol medical applications. *Materials Science and Engineering A*, 273–275: 149–160, 1999.
38. RX Acculink Carotid Stent System, Abbot Vascular Images courtesy of Abbott Vascular. (c) 2007 Abbott Laboratories. All Rights Reserved. <http://www.abbotvascular.com/>

39. Gil FJ and Planell JA, Shape memory alloys for medical applications, *Proc Instn Mech Engrs*, 212, Part H, 473–488, 1998.
40. Stice J. The use of superelasticity in guidewires and arthroscopic instrumentation. In TW Duering, KN Melton, D Stöckel and CM Wayman (eds.) *Shape Memory in Engineering Aspects of Shape Memory Alloys*, London: Butterworth-Heinemann, 1990, pp. 483–486.
41. James DW. High damping for engineering applications, *Mater. Sci. Engng*, 1969, 4, 322.
42. Sekiguci Y. *Medical Applications in Shape Memory Alloys*, ed. H Funakubo, London: Gordon and Breach Science Publishers, 1984, pp. 10–23.
43. Zhang XF. A study of shape memory alloy for medicine. In Shape Memory Alloy 86, Proceedings of the International Symposium on *Shape Memory Alloys*, China. New York: Academic Publishers, 1986, pp. 24–28.
44. Simon M, Kaplow R, Salzman E. and Freiman DA, Vena cava filter using thermal shape memory alloy. *Radiology*, 125: 89–90, 1977.
45. Andreasen GF. A clinical trial of alignment of teeth using a 0.019 inch thermal nitinol wire with a transition temperature range between 31 °C and 45 °C. *Am. J. Orthod.*, 78: 528–536, 1980.
46. Miura F, Mogi M, Ohura Y. and Karibe M. The superelastic japanese NiTi alloy wire for use in orthodontics. *Am. J. Orthod. Dent. Orthop.*, 94(2): 89–96, 1988.
47. Jose' Domingos Santos, *Ceramics in Medicine, Business Briefing: Medical Device Manufacturing and Technology*, 2002, pp. 1–2.
48. Vlasov AS and Karabanova TA. Ceramics and Medicine (Review), *Glass and Ceramics*, 50(9–10), September, 1994.
49. Rodriguez-Lorenzo LM, Vallet-Regi M, Ferreira JMF, Ginebra MP, Aparicio C, and Planell JA, Hydroxyapatite ceramic bodies with tailored mechanical properties for different applications, *Journal of Biomedical Materials Research*, 60(1): 159–166.
50. Biomet®; Hip Hydroxyapatite Joint Replacement Prostheses, Biomet Orthopedics, Inc. <http://www.biomet.com/hcp/prodpage.cfm?s=0901&p=090F>
51. Garvie RC, Hannink RH, and Pascoe RT. Ceramic steel. *Nature*, 258 (5537): 703–704, 1975
52. Yildirim M, Fischer H, Marx R, and Edelhoff D, In vivo fracture resistance of implant-supported all-ceramic restorations, *J. Prosthet Dent*, 90(4): 325–31, 2003.
53. Kessler-Liechti G, and Mericske-Stern R. Rehabilitation of an abraded occlusion with Procera-ZrO<sub>2</sub> all-ceramic crowns. A case report. *Schweiz Monatsschr Zahnmed*, 116:156–167, 2006.
54. Rimondini L, Cerroni L, Carrassi A, and Torricelli P. Bacterial colonization of zirconia ceramic surfaces: an in vitro and in vivo study. *Int J Oral Maxillofac Implants*, 17(6):793–8, 2002.
55. Degidi M, Artese L, Scarano A, Perrotti V, Gehrke P, and Piattelli A. Inflammatory infiltrate, microvessel density, nitric oxide synthase expression, vascular endothelial growth factor expression, and proliferative activity in peri-implant soft tissues around titanium and zirconium oxide healing caps. *J Periodontol*. 77(1): 73–80, January, 2006.
56. Smith & Nephew Inc., Oxinium™ knee implant [http://www.voteoxinium.com/1100\\_oxmaterial.html](http://www.voteoxinium.com/1100_oxmaterial.html)



# Chapter 2

## Polymers, Composites and Nano Biomaterials: Current and Future Developments

Salil Desai and M. Ravi Shankar

### 2.1 Introduction

Polymers are long-chains molecules that are formed by connecting large numbers of repeating units (monomers) by covalent bonds. Polymers form the largest category of diverse biomaterials. Based on their source of origin, they can be categorized as synthetic (e.g. polyethylene) or natural type (e.g. collagen). Synthetic polymers can be further sub-divided into biodegradable and nondegradable types. In the degradable type, the polymer is broken down in vivo due to hydrolytic and enzymatic [1] degradation. The resultant nontoxic compounds include lactic and glycolic acid, respectively. One of the key issues while considering polymers for bio applications is their biocompatibility with the host tissue and their degradation characteristics over extended periods of time. Biopolymer applications range from drug release carriers, implants, tissue regeneration scaffolds to sutures.

### 2.2 Synthetic Polymers

Synthetic polymers range from polytetrafluoroethylene (PTFE), silicon rubber, poly(methyl methacrylate) (PMMA), copoly(lactic-glycolic acid) (PLGA), polyethylene (PE), to polyurethanes. This section details specific applications of synthetic biopolymers.

#### 2.2.1 Polytetrafluoroethylene (PTFE)

Commonly known as Teflon<sup>®</sup>, polytetrafluoroethylene (PTFE) is a synthetic polymer with extremely low coefficient of friction. It exhibits hydrophobicity,

---

Salil Desai

Department of Industrial and Systems Engineering North Carolina A&T State University,  
Greensboro, North Carolina, USA, 27411  
sdesai@ncat.edu

non-reactive behavior and has high elasticity. This makes Teflon<sup>®</sup>, a prime candidate for the implanting of an artificial tendon or ligament in the musculoskeletal system. Its commercial woven form (ePTFE) it is called as GORE-TEX<sup>®</sup>. It is also used to make catheters and in facial reconstructive surgery. Figure 2.1 shows the GORE VIABAHN<sup>®</sup> endoprosthesis stent-graft. Endoprosthesis is a flexible metallic tubular shaped device which is lined with plastic (ePTFE). This device is released within a blocked femoral artery to improve blood flow.

Vascular grafts and sutures as shown in Fig. 2.2 are made from GORE-TEX<sup>®</sup> and are non-reactive and resist the spread of infection. These grafts can be designed in a wide range of configurations including straight, tapered and bifurcated. GORE-TEX<sup>®</sup> suture is microporous and manufactured from expanded polytetrafluoroethylene (ePTFE). It also offers minimal biological tissue response with cellular ingrowth.

### 2.2.1.1 Hydrogels

Hydrogel is a colloidal gel in which water is the medium of dispersion and is formed by the cross-linking network of hydrophilic polymer chains [4]. Hydrogel can either be formed by chemical or physical bonds. Hydrogels containing more than 95% of water of the total weight (or volume) of the hydrogel are called superabsorbent. Hydrogels can maintain their shape due to the isotropic swelling. Some of the important properties of hydrogels for biomedical applications include their in situ formability, responsive swelling, biodegradability, and natural tissue-like properties. Hydrogels can be cross-linked using radiation and heat. They can also be degraded by mechanism of hydrolysis and enzymatic action. They exhibit responsive swelling behavior due to changes in temperature, PH potential. The structure of hydrogels can be compared with collagen and elastin which form the natural tissue. Typical

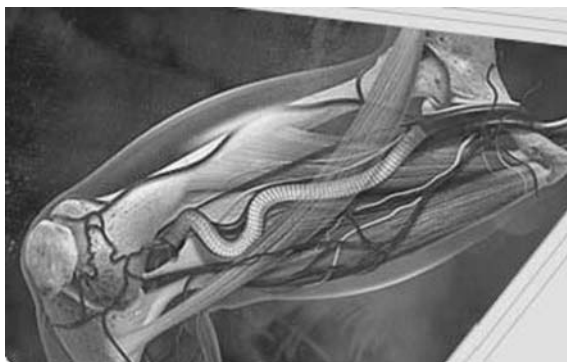
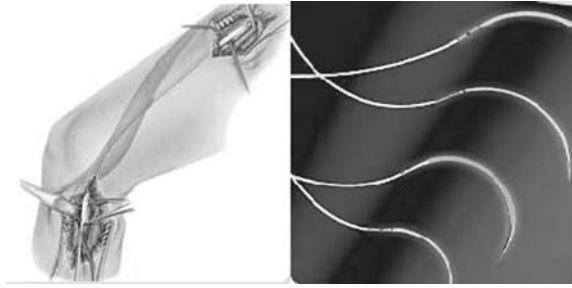


**Fig. 2.1** GORE VIABAHN<sup>®</sup> endoprosthesis stent-graft (©Courtesy: W. L. Gore & Associates, Inc. [2])

**Fig. 2.2** Vascular Grafts  
*(left)* GORE-TEX<sup>®</sup> Sutures  
*(right)* (©Courtesy: W. L. Gore & Associates, Inc. [3])



applications include controlled drug release [5], tissue regeneration scaffolds [6], cell and DNA encapsulation [7], contact lenses [8], wound healing dressings [9] and biosensors [10]. Hydrogels are formulated from variety of materials including silicon, cellulose derivatives, poly (vinyl alcohol), poly (ethylene glycol), calcium alginate and the most widely used poly (hydroxyethyl methacrylate) PHEMA.

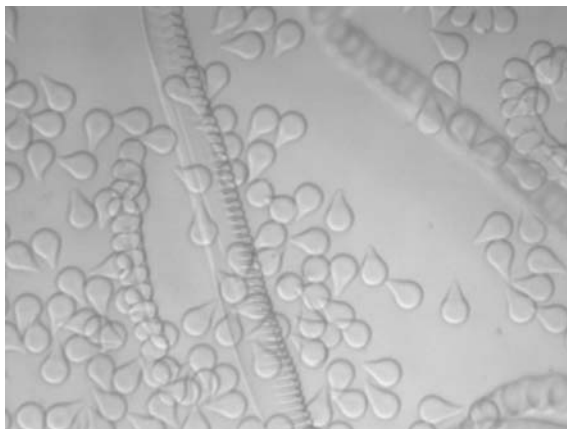
Silicon hydrogel contact lenses offer superior benefits of oxygen replenishment to the cornea over traditional hydrogel soft contact lenses. Due to their high oxygen permeability, these lenses can be worn for extended periods of time over conventional hydrogel lenses. In addition these lenses maintain hydration levels for eye comfort and have reduced occurrence of eye-infections.

Figure 2.3 [11] shows microcapsules and scaffolds of calcium alginate hydrogels manufactured using specialized jetting techniques in aqueous media. Alginate is an extract of the seaweed which is used to obtain a dry, powdered sodium alginate. The sodium alginate solution is used as a precursor material to form calcium alginate microcapsules. These microcapsules have a tight control on the size distribution and can be used as drug delivery carriers. They can also be used to encapsulate cells, DNA and biofluids. A promising application of these hydrogels is in the field of regenerative tissue engineering. Orientation specific tissue scaffolds can be fabricated using the calcium alginate biopolymer system with different polymer loadings.

### 2.2.2 Polymers for Dental Restorative Applications

A particularly wide-spread application of non-biodegradable polymer systems is replacements for amalgam in dental restorations such as dental fillings. The utilization of polymer systems in dental restorations is typically determined by a) Mechanical durability b) bio-compatibility c) ease of application and d) aesthetic properties. The characteristics and performance of such dental restorative materials have been formalized via standards established by the

**Fig. 2.3** Calcium alginate biopolymer microcapsules and tissue scaffolds in aqueous media (Courtesy: Desai et al., Invention Disclosure, NC A&T SU [11])



International Standards Organization and the American Dental Association [12–15].

Traditionally, methacrylate based photopolymerizable resins have been utilized since their introduction by R. F. Bowen [16,17]. Typically bis-Phenol A-glycidyl methacrylate (Bis-GMA) in combination with different fractions of Triethylene glycol dimethacrylate (TEGDMA) are photo-polymerized with visible light in the presence of suitable photo-initiators to create dental fillings. Such polymer based fillings possess two significant advantages in comparison to traditional amalgams. Firstly, they eliminate entirely the utilization of toxic heavy metals such as mercury in a biomedical application. Secondly, the optical characteristics of polymer systems enhance their aesthetic characteristics and these restorations essentially blend in with the surrounding dental structure. In comparison the amalgams are characterized by a typically metallic luster and thus, they do not compare well with the polymer systems. However, currently prevalent polymer-based dental restorations suffer significant shortcomings that have stimulated considerable amount of research. Polymeric systems are mechanically weaker and concomitantly much less durable than say, the traditional amalgams. In fact, it was determined that resin based restorations typically lasted  $\sim 7.8$  years in comparison to  $\sim 12.8$  years for amalgam based fillings [16].

The poor durability of the polymer systems can be traced to their intrinsically poor yield and fracture strengths, a typical characteristic of several methacrylate-based polymers. Another debilitating aspect of these polymer systems is the shrinkage that accompanies the polymerization process. Such shrinkage would inevitably lead to the formation of gaps between the restoration and the surrounding dental structure. This leads to microleakage and the deposition and entrapment of fluids, food debris and microorganisms in the gap between the filling and the tooth. In turn, this can further engender tooth decay and overall failure of the restoration. Several developments recently have focused

on overcoming these two limitations of dental restorative polymers by developing a) Reinforced polymers for improved strength and b) Low-shrinkage polymer systems for reduced microleakage.

### 2.2.2.1 Reinforced Polymers for Improved Strength

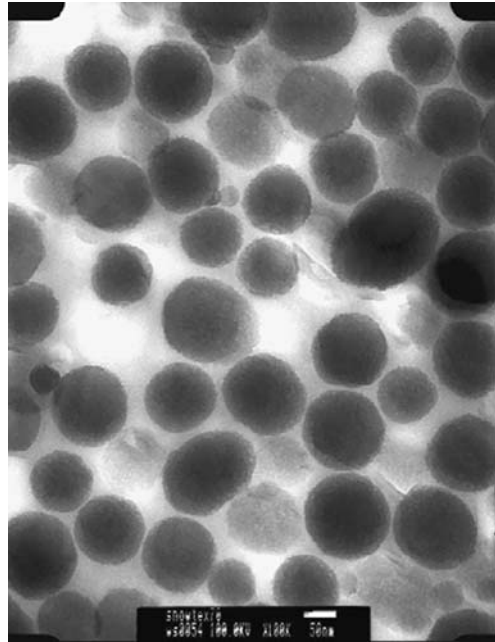
The mechanical strength of polymers can be improved by reinforcing the polymer matrix via the addition of micrometer scale filler materials (e.g. zirconia, alumina, silica) [19, 20]. These micro-filled composite materials are stronger than the bulk un-reinforced polymers as a result of the high-strength reinforcement phase accommodating the applied loads. This improvement in mechanical performance is much more significant when the particles are chemically treated in order to functionalize them to ensure excellent bonding between the hard reinforcement and the polymer matrix [20]. The more effective this functionalization, the greater is the improvement in the composite strength. This is because better bonding improves the effectiveness of load transfer between the surrounding matrix and the high-strength reinforcement.

In the case of these reinforced composite however, it was noted that the improvement in mechanical characteristics do not monotonically increase as a function of increasing fraction of the filler material [19]. In fact it was demonstrated that there exists an optimal fraction beyond which mechanical performance such as fatigue life in fact declines in these polymer systems.

More recently, the advances in nanotechnology have led to the development of nano-filled polymers for achieving a step change in the mechanical performance of composite materials for dental restorations. The premise of these developments is that the unprecedented opportunities enabled by the novel mechanical phenomena operative at the nanometer length-scale can be exploited in suitably designed polymer matrices to create high-performance nanostructured systems. Figure 2.4 illustrates a nanostructured composite material reinforced by nano-scale silica particles.

Such nano-composites are commercially available under brand names such as Ceram X (Dentsply/Caulk, USA), Grandio (Voco, Germany), Tetric EvoCeram (Vivadent, Liechtenstein) and Filtek Supreme (3M ESPE, USA). It should however be noted that exploiting the mechanical consequences of nanostructured dental composites still requires the rigorous development of protocols for ensuring effective bonding between the matrix and the nano-particles as well as the generation of a fine dispersion of nano-particles throughout the matrix. This is because lack of insufficient bonding between the matrix and the nano-particle reinforcement and concomitantly, inefficient load transfer usually results in insignificant improvement of mechanical properties over conventional materials. Instead of the high-strength, high-elastic modulus nano-particle reinforcement accommodating the applied stresses, the poorly-bonded nano-composite would behave as if it were nano-porous. This would then result in little or no improvement over the non-reinforced bulk composite

**Fig. 2.4** Nanostructured dental composite reinforced by nano-scale silica particles for superior mechanical performance (Courtesy: Elsevier [19])



material [20–22]. Furthermore, the nano-scale reinforcements are best exploited when they are uniformly dispersed in the softer matrix and there is negligible clumping or aggregation of the nano-particulates [21, 22]. Lack of aggregation is particularly important since, extended ensembles of the nano-particles would essentially behave as if they were micrometer-scale hard phases and offer little improvement over conventional polymer composites with micrometer sized reinforcements [23].

#### **2.2.2.2 Low-Shrinkage Polymer Systems for Reduced Microleakage**

In a parallel development, to overcome the other debilitating limitation of polymeric dental restorative materials, low-shrinkage resins have been envisaged. In comparison to the methacrylate-based systems, these low-shrinkage materials are typically characterized by ring-opening polymerization reactions that involve an increase in the excluded free volume and concomitantly much smaller shrinkage. Epoxy-polyol blends that can be cured with light in the visible part of the spectrum by utilizing photo-initiators such as camphorquinone are particularly interesting for dental restorative applications. In fact, it has been suggested that such systems may offer an unprecedented combination of properties that are best suited for dental restorative applications, i.e. higher mechanical strength, rapid curing with visible light as well as significantly attenuated polymerization shrinkage [24, 25]. The polymerization shrinkage

in these systems was found to be further decreased by the addition of spiro-orthocarbonates [26].

The development of nanostructured composites in combination with the design of polymer matrices that demonstrate zero or net positive volume change during polymerization are expected to lead to the development of novel high-performance dental restorative systems by overcoming all the current limitations of prevalent methacrylate-based, micro-filled polymer materials.

### ***2.2.3 Polymeric Biomaterials for Structural Applications***

Recently, significant interest has emerged in the development of polymer-based biomaterials for the fabrication of mechanically robust implants for utilization in orthopedic surgery. Traditionally, metallic alloys have been used in orthopedic implants to utilize their high elastic modulus and materials strength in a typically load bearing applications. However, introduction of metallic systems can entail numerous effects on the overall physiology. Typically, pure metals are not sufficiently strong to be directly utilized as load bearing biomaterials. To improve their material strength, metal alloys are utilized. For example, pure unalloyed iron does not possess sufficient material strength or the durability for utilization in biomedical implants. However, when alloyed to create stainless steel, pure iron is transformed into a much more suitable metallic system. However, stainless steel that contains chromium that can be gradually released into the body thus entailing potential allergic and toxic reactions.

Furthermore, the elastic modulus of say cortical bones ranges from 10 to 20 GPa [27]. In comparison, the modulus of typical metallic alloys is in the range of 100–200 GPa. When materials with dramatically different properties are in intimate contact and subjected to stresses, stress concentrations that are associated with the strain mismatch can occur. Consider for example a Ti plate with a modulus of  $\sim 100$  GPa that has undergone effective osseointegration with a bone that is characterized by a modulus of  $\sim 10$  GPa. When this “composite” system of the implant and the bone is deformed by a remote stress, the majority of the load would be accommodated by the stiffer Ti implant. This is particularly true if effective osseointegration has occurred and concomitantly there is no interfacial slip between the implant and the bone.

In accordance with the Wolff’s law of stress induced bone remodeling, if a majority of the applied loads is accommodated by the implant, then over time the surrounding native bone structure may reconfigure over time and lose bone mass [28]. Furthermore, usually the implant is smaller than the surrounding bone and at the edges the mismatch in mechanical properties can in fact lead to strong stress concentrations. This scenario is very analogous to that observed during typical indentation scenarios when a flat punch deforms a substrate [29]. Cumulatively, these two effects can lead to secondary fractures as well as anomalous reconfiguration of the bone structure as a result of the highly

heterogeneous stress state that is directly related to the mismatch in the mechanical properties between the implant and the native bone structure [30].

Utilization of polymer systems offers a versatile system wherein to enable the manufacture of implants with mechanical properties that match that of the bone. Furthermore, it is known that the native bone itself is characterized by anisotropic mechanical stiffness. For example, the cortical bone in the longitudinal direction is characterized by a stiff of 17 GPa and  $\sim$ 13 GPa in the transverse direction. Most conventional polymers however do not possess the intrinsic stiffness that matches that of the native bone. However, the primary advantage of the polymers is the control that can be exercised via controlled dispersion of second phases.

Consider the case of fiber reinforced polymers wherein the fibers are aligned in a certain direction. Figure 2.5 illustrates carbon fiber reinforced epoxy plates that have been utilized in epiphyseal fractures [31]. In such devices carbon fibers of exceptional intrinsic tensile stiffness can be utilized wherein mechanical properties can be tailored by controlling the orientation of the high-modulus reinforcing phase. Carbon fibers can ensure a much greater improvement in the modulus in a direction that is parallel to their predominant direction of alignment while they may not be as effective in the transverse direction. Therefore, it is then possible to tailor via appropriate processing schemes to match the anisotropic elastic properties of the bone by controlling the dispersion and the orientation of the fibers in the composite.

Much like the case of the metallic implants, polymer composite systems are also required to ensure sufficient biocompatibility. While the aforementioned carbon fiber reinforced composites are expected to possess significant biocompatibility, in practice however, biocompatibility has been affected due to the substantial release of carbon particles into the surrounding tissues [32]. Alternatively, it has been suggested that “bioglass” may be an effective reinforcement material that overcomes the limitations of the carbon fibers because they may remain bioactive even when in contact with the surrounding tissues unlike the carbon fibers [33].



**Fig. 2.5** Carbon fiber reinforced epoxy plates for epiphyseal fractures (Courtesy: Elsevier and Orthodynamics, UK [31])



Significant challenges remain in the design and manufacture of suitable biocomposites for orthopedic and restorative applications to ensure durability, biocompatibility all the while accomplishing the desired therapeutic effect.

## 2.3 Nanomaterials

Materials that display structural configuration and morphology at the nanometer scale (less than 100 nm) are called as nanomaterials. These include different types of materials namely; bulk materials with nanocrystalline grain sizes, 1D nanomaterials such as thin films, 2D nanomaterials including nanowires or nanotubes and 3D nanomaterials such as quantum dots and particulates with overall dimensions in the nanometer ranges. Nanomaterials possess unique properties over conventional materials that can be exploited for various medical applications. These include enhanced reactivity, strength, magnetic, electrical and optical characteristics due to size and surface effects [34–38]. Based on the material type it is possible to alter the melting point, transparency, color and solubility of nanoparticles by varying their particle size. Nanomaterials have potential biomedical applications that include biomarking, cancer treatment, gene therapy, biosensors, orthopedic and device implants and targeted drug delivery. Magnetic nanoparticles are being investigated for targeting chemotherapy drugs using external magnetic field.

### 2.3.1 Carbon Nanotubes (CNTs)

#### 2.3.1.1 Description

Carbon nanotubes are cylindrical tubes of carbon with very high aspect ratios. The lengths of the carbon nanotubes are extremely large as compared to its diameter. These tubes are allotropes of carbon called fullerenes. Carbon nanotubes can either have closed or open end configurations. Depending on their structural configuration which includes the diameter, length and spiral twist they possess a wide range of structural, electronic and thermal characteristics. Carbon nanotubes are produced in two forms namely; single wall and multiwall nanotubes. Some of prominent characteristics of CNTs include high strength, good electrical and thermal conductivity and functional properties [39–43].

#### 2.3.1.2 Applications

Carbon nanotubes are being currently researched for a variety of medical applications. These include imaging, drug delivery and bio-sensing for detecting disease related proteins and chemical toxins. Carbon nanotubes can be used as

structural reinforcement for tissue scaffolds. Their enhanced electrical conductivity can be exploited for directional cell growth. The different applications of carbon nanotubes in tissue engineering include cellular sensing, cell tracking and labeling and improving tissue matrices [44]. One of the promising approaches to disease detection is the study of novel electrochemical impedance properties of carbon nanotube (CNT) tower electrode. In this method CNT arrays are synthesized on a multilayered silicon ( $\text{Fe}/\text{Al}_2\text{O}_3/\text{SiO}_2/\text{Si}$ ) substrate using thermal chemical vapor deposition. By controlling the process parameters high density and purity CNT arrays are grown which are suitable for biosensor development. Further these CNT towers are peeled off from the silicon substrate and casted in epoxy composite. After casting, the bottom section of the CNT tower is polished and connected to a copper wire for conductive leads. The top section of the CNT arrays is polished to expose the nanotube electrodes. These open electrodes are further functionalized by carboxylic acid groups so that they can act as receptors for other molecules. Anti-mouse IgG is covalently immobilized on the nanotube array. Finally electrochemical impedance spectroscopy (EIS) is used to characterize the binding of mouse IgG to its specific antibody that has been immobilized on the nanotube electrode surface. Figure 2.6 shows the electrochemical impedance spectra for different activation conditions.

In recent years engineered nanomaterials with specific chemical and physical properties are being manufactured. Given their potential use in biomedical applications it is important to understand their toxicological effects on the human body [45]. The exposure of engineered nanomaterials during the entire lifecycle of products takes a variety of routes into the body. Some of the studied exposure routes include inhalation, dermal and oral [46, 47]. Studies have indicated oxidative stress-related inflammatory reactions due to deposition of nanoparticles within the respiratory tract after inhalation [48]. Also,

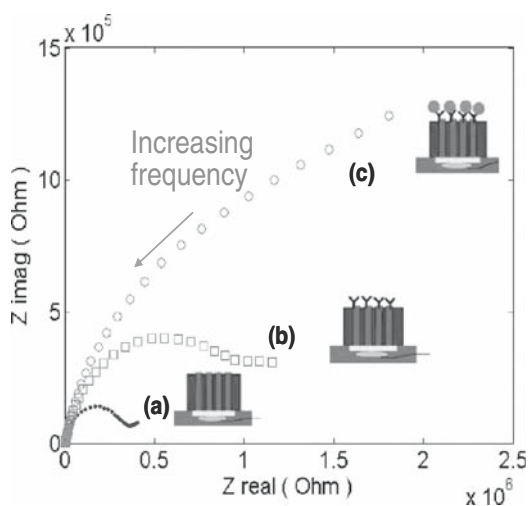


**Fig. 2.6** Electrochemical impedance spectra for carbon nanotube array electrode: (a) activated nanotube array; (b) immobilized with donkey anti-mouse IgG; and (c) bond to mouse IgG; at 0.2 V over a frequency range between 0.1 Hz and 300 KHz

the uptake of nanoparticles within the brain and gastrointestinal tract has been reported [49, 50]. However, only a limited number of materials have been studied and further research on combinatorial nanomaterial systems needs to be explored.

## References

1. Yaacobi Y, Sideman S, and Lotan N. A mechanistic model for the enzymic degradation of synthetic biopolymers, *Life Support Syst.*, 3(4): 313–326, Oct–Dec 1985.
2. W. L. Gore & Associates, <http://www.goremedical.com/viabahnfsa/index>
3. W. L. Gore & Associates Inc., <http://www.goremedical.com/vg/index>; <http://www.goremedical.com/suture/index>
4. Wichterle O and Lim D. Hydrophilic gels for biological use, *Nature*, 185: 117–118, 1960.
5. He H, Cao X, and Lee LJ. Design of a novel hydrogel-based intelligent system for controlled drug release, *J Control Release*, 95(3): 391–402, 2004 March 24.
6. Nguyen KT and West JL. Photopolymerizable hydrogels for tissue engineering applications. *Biomaterials*23: 4307–4314, 2002.
7. An Y. and Hubbell JA. Intraarterial protein delivery via intimately-adherent bilayer hydrogels. *J Control Release*64: 205–215, 2000.
8. Larsen, United States Patent – 4,495,313, Preparation of hydrogel for soft contact lens with water displaceable boric acid ester, Jan 1985.
9. Hubbell JA. Hydrogel systems for barriers and local drug delivery in the control of wound healing. *Journal of Controlled Release* 39: 305–313, 1996.
10. Gardner PJ and Fountain AW III (eds.). Chemical and Biological Sensing VII. *Proceedings of the SPIE*, vol. 6218, pp. 62180K, 2006.
11. Desai S, Moore A, and Sankar. Invention Disclosure: Method for Producing Uniform Sized Bio-polymer Microbeads Using Specialized Inkjet Printing, NC A & T SU: EN 0046 0307, Nov 2006.
12. International Standards Organization. Dental materials—water-based cements Part 1—powder/liquid acid–base cement, 2001; ISO 9917-1.
13. International Standards Organization. Dentistry—resin-based filling, restorative and luting materials, 2000; ISO 4049.
14. International Standards Organization. Dental water-based cements Part 2—light activated cements, 1998; ISO 9917-2.
15. <http://www.ada.org/prof/resources/positions/standards/denmat.asp>
16. Van Nieuwenhuysen JP, D’Hoore W, Carvalho J, and Qvist V. *Journal of Dentistry*, 31(6): 395–405, 2003.
17. Htang A, Ohsawa M, and Matsumoto H. *Dental Materials*, 11(1): 7, 1995.
18. Yap UJ, Wang X, Wu X, and Chung SM. *Biomaterials*, 25: 2179, 2004.
19. Chen M, Chen C, Hsu S, Sun S, and Su W. *Dental Materials*, 22(2): 138–145, 2006.
20. Ajayan PM and Schadler LS. *Advanced Materials*, 12(10): 750, 2000.
21. Breuer O and Sundararaj U. *Polymer Composites*, 25(6): 630, 2004.
22. Schadler LS, Giannaris SC and Ajayan PM. *Applied Physics Letters*, 73(26): 3842, 1998.
23. Ou Y, Yang F, and Yu ZZ. *Journal of Polymer Science Part B: Polymer Physics*, 36(5): 789, 1998.
24. Oraleg AB, Victorin L, and Larsson A. Photopolymerizable composition, Patent WO 95/30402, 1995.
25. Kaisaki D, Mitra S, Schultz WJ, and Devoe RJ. Visible light curable epoxy system with enhanced depth of cure. Patent WO 96/13528, 1–49, 1996.
26. Chappelow CC, Pinzino CS, Jeang L, Harris CD, Holder AJ, and Eick JD. *Journal of Applied Polymer Science*, 76: 1715, 2000.

27. Black J. and Hastings GW. *Handbook of Biomaterial properties*, Chapman and Hall, London, UK, 1998.
28. Hayes WC and Snyder B. Mechanical Properties of Bone, *The joint ASME-ASCE Applied Mechanics, Fluid Engineering and Bioengineering Conference, AMD*, vol. 45, Boulder, Colorado, 1981.
29. Johnson KL. *Contact Mechanics*, Cambridge University Press, Cambridge, 1985.
30. Huiskes R. *Acta Orthopædica Scandinavica*, 64(6): 699, 1993.
31. Evans SL and Gregson PJ. *Biomaterials*, 19: 1329, 1998.
32. Claes L, Burri C, Neugebauer R, and Gruber U. Experimental investigations of hip prostheses with carbon fiber reinforced carbon shafts and ceramic heads, *Ceramics in Surgery*, Amsterdam, Elsevier, 1983.
33. Marcolongo M, Ducheyne P, Schepers E, and Garino J. The halo effect: surface reactions of a bioactive glass fiber/ polymeric composite in vitro and in vivo, 5th Biomaterial Congress, Toronto, 1996.
34. Qin XY, Kim JG, and Lee JS. Synthesis and magnetic properties of nanostructured g-Ni-Fe alloys, *Nanostruct Mater*, 11(2): 259–270, 1999.
35. Ferrari M. Cancer nanotechnology: opportunities and challenges. *Nat Rev Cancer*, 5(3): 161–171, 2005.
36. Vasir JK, Reddy MK, and Labhasetwar VD. Nanosystems in drug targeting: opportunities and challenges. *Curr Nanosci*, 1(1): 47–64, 2005.
37. Webster TJ, Siegel RW, and Bizios R. Osteoblast adhesion on nanophase ceramics. *Biomaterials*, 20(13): 1221–1227, 1999.
38. Iijima S. Helical microtubules of graphitic carbon. *Nature*, 354: 56–58, 1991.
39. Lu JP. Elastic properties of carbon nanotubes and nanoropes, *Phys Rev Lett*, 79: 1297–1300, 1997.
40. Treacy MMJ, Ebbesen TW, and Gibson JM. Exceptionally high Young's modulus observed for individual carbon nanotubes. *Nature*, 381: 678–680, 1996.
41. Kociak M, Kasumov AY, Gueron S, Reulet B, Khodos II, Gorbatov YB, et al. Superconductivity in ropes of single-walled carbon nanotubes. *Phys Rev Lett*, 86: 2416–2419, 2001.
42. Song SN, Wang XK, Chang RPH, and Ketterson JB. Electronic properties of graphite nanotubes from galvanomagnetic effects. *Phys Rev Lett*, 72: 697–700, 1994.
43. Gwinn MR and Vallyathan V. Nanoparticles: Health Effects—Pros and Cons, *Environ Health Perspect*, 114(12): 1818–1825, 2006 December.
44. Harrison BS and Atala A. Carbon Nanotube Applications in Tissue Engineering, *Biomaterials* 28: 344–353, 2007.
45. Borm PJA, Robbins D, Haubold S, Kuhlbusch T, Fissan H, Donaldson K, Schins R, Stone V, Kreyling W, Lademann J, Krutmann J, Warheit D, and Oberdorster E. The potential risks of nanomaterials: a review carried out for ECETOC, *Part Fibre Toxicol.*, 11: 3, 2006.
46. Oberdörster G, Oberdörster E, and Oberdörster J. Nanotoxicology: An emerging discipline evolving from studies of ultrafine particles, *Environ Health Perspect.*, 113(7): 823–839, 2005 July.
47. Donaldson K, Stone V, Clouter A, Renwick L, and MacNee W. Ultrafine particles. *Occup Environ Med.*, 58: 211–216, 119, 2001.
48. Oberdorster G, Finkelstein JN, Johnston C, Gelein R, Cox C, Baggs R et al. Acute pulmonary effects of ultrafine particles in rats and mice, *Res Rep Health Eff Inst.*, 96: 5–74, 2000.
49. Jani PU, McCarthy DE, and Florence AT. Titanium dioxide (rutile) particles uptake from the rat GI tract and translocation to systemic organs after oral administration. *J Pharm.*, 105: 157–168, 1994.
50. Bockmann J, Lahl H, Eckert T, and Unterhalt B. Titanium blood levels of dialysis patients compared to healthy volunteers, *Pharmazie.*, 55: 468, 2000.

# Chapter 3

## Polyurethane Based Materials with Applications in Medical Devices

Fred J. Davis and Geoffrey R. Mitchell

### 3.1 Introduction

Polyurethane materials have a huge role in everyday materials, for example, as foams they are used in car and household furnishings; the polymer is used in the construction industry, in the manufacture of footwear, and for coatings and adhesives, as well as in textiles. The demand for polyurethane materials is high (Biesman, 2002). Thus in a number of everyday guises and in specialist devices, polyurethanes play a vital role in medicine and are involved at all scales, from the construction materials used to build the wards through to bedding, surgical instruments, medical implants and ultimately microscale encapsulation devices. In this article, however, we shall focus largely on those structural devices which come into contact with the patient, for which the property of biocompatibility must be added to the other properties required such as flexibility, strength, and of course processibility. This places substantial additional demands on a material and a restricted range of synthetic organic polymers have been used in a wide variety of medical applications. Of these many materials, polyurethanes have attracted particular interest; firstly because the diisocyanate and diol monomers can be altered to provide materials with widely differing properties, such as melting or softening point and mechanical strength; secondly, other modifications such as the introduction of diamines to provide thermoplastic elastomers, or the combined use of multifunctional diols and foaming agents to produce rigid or flexible foams allow for the production of materials with the widest possible range of morphologies. In addition to the widely tunable physical properties, it has been found that these materials can also be made to be substantially biocompatible, but where required can be made to biodegrade. Thus almost uniquely polyurethanes have the potential to be used both for permanent medical implants and to be used in systems where degradation is required such as scaffolds for tissue regeneration.

---

Fred J. Davis

Polymer Science Centre, Departments of Chemistry and Physics, University of Reading,  
Whiteknights, Reading, RG6 6AD, UK  
f.j.davis@reading.ac.uk

Despite the huge potential of polyurethane based materials, the story is not one of unqualified success; some of the early devices, particularly catheter leads were found to degrade over time and the use of polyurethane foams in breast implants led to a health scare over the presence of carcinogenic amines, though the received wisdom now is that the risk involved was at the most slight. That being said scientists and engineers have continued to investigate the potential of these materials both to understand likely problems with their *in vivo* use (and consequently how to overcome them), and to expand the potential of these materials. The effort involved is vast. In this contribution we shall look at some selected applications of polyurethanes, and show how these applications rely on the morphology of the polymer and thus its underlying chemical composition.

### 3.2 Medical Applications of Polyurethane

Polyurethanes have a wide variety of uses, but in terms of mass of material used, polyurethane represents only a small fraction of the synthetic polymer use in medical applications (Lamba et al., 1998); in fact it would seem that PVC is the most common medical polymer, largely due to its use in disposable devices, such as blood tubing and blood storage bags. Other major materials commonly used include polystyrene, polyethylene, and polypropylene. This however, underplays the importance of the polyurethanes; where complex mechanical and biocompatibility problems occur polyurethane is often the material of choice. Polyurethane has been used for example as a coating for cardiac pacemaker leads, as a coating for breast implants, in vascular devices, such as intra aortic balloons, and for gastric balloons. It is also often used for catheters and other general purpose tubing. However, in this respect, it should be noted that often the material requirements are rather stringent, particularly in terms of surface quality as shown in Fig. 3.1. Inflatable polyurethane implants can be used to aid sufferers of erectile dysfunction. The polymer is also used for wound dressings, such as Tegaderm<sup>TM</sup> (manufactured by 3M), and for tissue adhesives (Gogolewski, 1989). It should also be noted that the ubiquitous nature of this material in clothing means that it is used in peripheral applications such as surgical drapes. Polyurethane is also used as an alternative to latex, to make disposable gloves and condoms (though strictly this is not a medical application; Bhattacharya et al., 1996).

Since polyurethane is generally more expensive than many bulk polymers, such as those mentioned in the previous paragraph, an obvious question is why use it? It is this question that this article is intended to address. In some cases the answer is simple. In the case of disposable gloves and condoms, this material provides an alternative to latex; latex allergy has become an increasing problem, to the extent that latex gloves, particularly the close fitting kind are being increasingly phased out of use. The use in foam dressings stems from the ability to produce hydrophilic foams which have an enhanced ability to soak up and

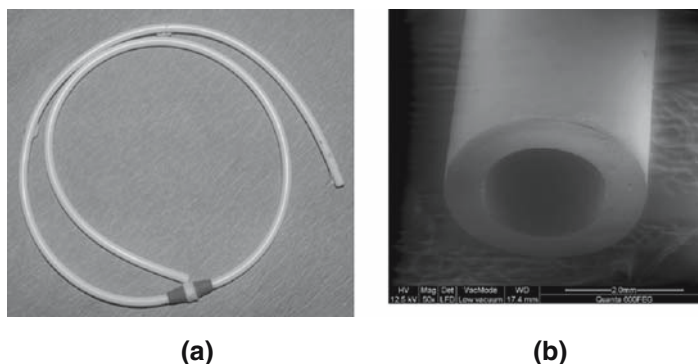


**Fig. 3.1** (a) A polyurethane based catheter with an outside diameter of  $\sim 4\text{mm}$ ; (b) Scanning electron microscope image taken of a cross-section of the polyurethane-based catheter in Fig. 1(a) showing the high quality of both surface finish and dimensional regularity which can be achieved

retain water by capillary action. The sophistication of such systems can be further increased by the use of silver containing additives, incorporated to reduce infection (Percival et al., 2005). The choice of wound dressing type may have substantial advantages in terms of patient response, and polyurethane dressings may be particularly useful in this regard, for example in the treatment of the particularly difficult healing problems presented by burns (Akita et al., 2006; Martineau and Shek, 2006).

Polyurethane in its elastomeric form is extremely common in clothing; Lycra<sup>®</sup> (a thermoplastic elastomer) is added in small amounts to a wide range of both natural fibres such as wool and cotton, and synthetic fibres such as polyester and nylon; surgical apparel is no different in this regard. Among many advantages, probably the most notable is the improved shape retention.

Biological systems are complex and often this complexity makes the choice of material difficult. For example, polyurethane catheters soften considerably on insertion into the body, largely because they are to some extent hydrophilic. This has the substantial advantage of reducing both patient discomfort, and possible trauma. In other circumstances, the use of polyurethane may be problematic, for example there is evidence to suggest that polyurethane catheters may not always be appropriate as totally implantable venous access devices in children owing to difficulties in their removal (Wilson et al., 2006). The use in other applications is often for far more complex reasons, may not always be totally satisfactory, but polyurethanes offer the best available solution.

In terms of implantable devices examples of commercially available materials include Elastane<sup>™</sup> a polyetherurethane, and a similar material, Pellethane<sup>®</sup>, although this is not now recommended for use in long-term

implants. A combination of polyurethane and silicone currently known as Cardiothane is used for example, in intraaortic balloons. Historically, a material known as biomer<sup>TM</sup> based on the segmented polyurethane Lycra<sup>®</sup> has been used in a range of applications, but more recently this product has been withdrawn, although an alternative material known as BioSpan<sup>®</sup> is available.

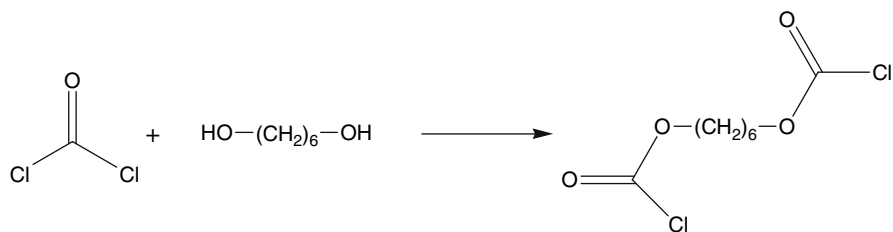
### 3.3 Polyurethane Chemistry

Polyurethane was invented in 1937 by the German company Bayer, prompted at least in part as an alternative to Nylon, which was effectively protected by patents. It came into general use in the 1950's where it was either used in an expanded form (as polyurethane foam) for mattresses and bedding etc., or used to produce speciality fibres such as Lycra and Spandex (*vide supra*).

The chemistry underlying all polyurethane synthetic pathways is the reactivity of the isocyanate group. This functionality imparts sufficient high reactivity to the appropriate monomers to polymerise in an acceptable time-scale, whilst remaining sufficiently kinetically inert towards reactions such as nucleophilic attack to allow its use without requiring special handling (Burkus and Eckert, 1958). The two most common routes to polyurethanes are the reaction between a diamine and a bischloroformate<sup>1</sup> or, more usually, the reaction between an isocyanate and an alcohol as shown in Fig 3.2. The alcohol may be a simple diol, as in the example in Fig. 3.2 or it may be an oligomeric hydroxyl-terminated polyester or polyether. The reaction can be catalyzed by a wide range of catalysts, most commonly tertiary amines and certain tin compounds. Although there are a range of kinetic profiles for the reaction and certain monomers react more rapidly than others (e.g. aliphatic diols react more rapidly than phenols) in general the reactions occur on a timescale that allows the synthesis and processing to occur in a single shot in a process known as reaction injection molding.

---

<sup>1</sup> Though not commonly performed on an industrial scale, bischloroformates are accessible through the reaction of alcohols with phosgene as in the following example.





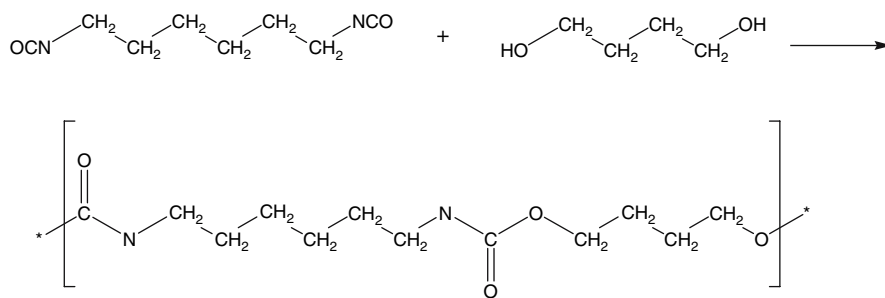


**Fig. 3.2** The reaction between a linear diol and a hexamethylene diisocyanate yields a simple linear polymer with some similarities to Nylon

Isocyanates can be formed in a number of ways in the laboratory; possibly the most well known examples being through rearrangements such as the Curtius and Hoffmann Rearrangements (Harwood, 1992). Industrially however, the major route to such materials is via the reaction of an amide with an isocyanate, Common monomers are shown in Fig. 3.3; these include tolylene diisocyanate (TDI, [1]) prepared via the nitration and subsequent reduction of toluene (either found as the pure 2,4-isomer, or as a mixture of the 2,4 and 2,6 diisocyanate); and methylene-4,4'-diphenyldiisocyanate (MDI [2]) which is produced from the reaction of aniline with formaldehyde (Saunders, 1973). Aliphatic isocyanides include 1,6-hexamethylene-diisocyanate (HDI, [3]), 3-Isocyanatomethyl-3,5,5-trimethyl-cyclohexylisocyanate commonly known as isophorone Diisocyanate (IPDI, [4]) and the hydrogenated form of MDI known as 4,4'-Dicyclohexylmethane-diisocyanate (or H<sub>12</sub>-MDI, [5]). Such monomers when combined with the array of available diols offer considerable scope for tailoring properties, for example the aromatic systems impart rigidity to the polymer.

There are concerns that, during *in vivo* use of polyurethanes based on some of the isocyanides shown in Fig. 3.3, degradation will occur to form amides, particularly aromatic amides, which may be toxic and/or carcinogenic. This there is considerable interest in the use of monomers such as lysine diisocyanate ethyl ester [6], amongst others, since the likely degradation product is lysine, which of course is present naturally. The use of such alternatives however may involve substantial adjustments to the chemistry, as we shall see later.

Though a polyurethane fibre based on 1,4-butanediol was considered for commercial production as a material in the early 1940's, the fibres produced are generally felt to be inferior for commercial reasons to the Nylons<sup>2</sup> and their use is restricted to mouldings for small mechanical components such as

<sup>2</sup> Polyurethanes are more expensive, generally have a lower melting point, are difficult to dye, and have a rather rough surface texture.

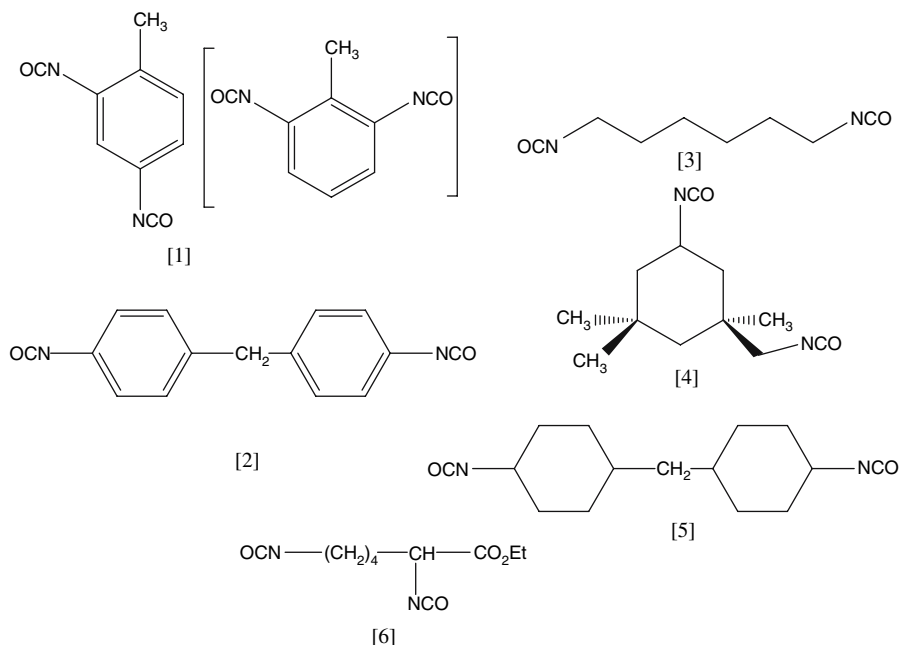


**Fig. 3.3** [1]–[6] show the chemical structures of some typical isocyanates used in polyurethane production

bearings or gears. However, polyurethanes have found a multitude of other uses, amongst these coatings as in, for example, paints and of course polyurethane foams are important commercial materials.<sup>3</sup> These and other applications tend to use hydroxyl-terminated polymers in particular polyesters and polyethers rather than simple glycols. In fact most commercial foams are based on polyethers (Saunders, 1973). Polyurethanes based on biologically compatible monomers such as polycaprolactone [7] have attracted considerable interest (Guan et al., 2005; Ping et al., 2005) for biomedical applications. In terms of fibre production, the success of polyurethanes lies in the ability to form elastomeric fibres. Polyurethane elastomers are effectively block copolymers; containing alternating “hard” and “soft” segments, a well-known example of this is Spandex, which is manufactured by Du Pont. If the two segments are incompatible then there is the possibility of microphase separation; thus the hard segment in effect acts as

<sup>3</sup> A full description of the production of polyurethane foams is outside the scope of this work. However, the procedure involves the formation of cross-linked polymer (by using a trifunctional monomer) whilst simultaneously generating gas; this gas may be CO<sub>2</sub> generated from the reaction of excess diisocyanate with water, or formed by the use of a blowing agent, a process which may in the past have had unfortunate environmental consequences.

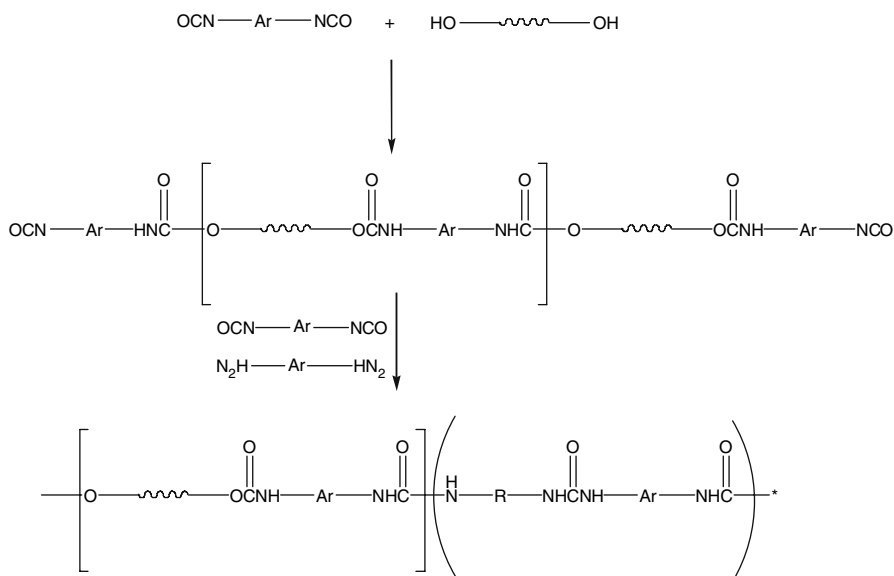
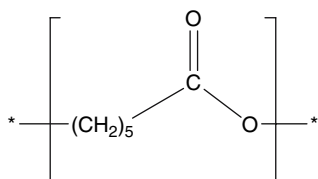


**Fig. 3.4** The synthesis of a polyurethane elastomer using a diamine chain extender (Stevens, 1990)

a cross-linker leading to a thermoplastic elastomers. The synthetic route to this type of material involves the reaction of a hydroxyl-terminated polyether or polyester with an excess of diisocyanate to form a high molecular weight diisocyanate. This macromonomer is then reacted with a so-called chain extender, which can be a diol, an amine or a hydrazine, to form a high molecular weight system. The soft section is the polyurethane based on the diol while the hard section is actually a polyurea. This process is described in Fig. 3.4.



[7]

Polyurethane is a term which can be used to describe many different materials derived in part from isocyanates. It is essential in any discussion to identify the key components. By adapting the fraction and distribution of these components many different materials can be produced.

### 3.4 Physical Properties of Polyurethanes

The physical properties of the polymer of course determine ways in which it can be applied in the biomedical environment and it is the ability to tailor the material properties that encompass the versatility. The required properties of a polymer include flexibility, high elongation, and high mechanical strength. Biodegradability is also a factor; this will be discussed in the next section. The structure property relationships of polyurethane systems, while complex have been extensively studied and are well understood. This allows considerable scope for tailoring the polymer to the needs of the system (Lamba et al., 1998). In the following discussion we shall focus on the behaviour of elastomeric materials as it is these, which dominate the market in terms of medical devices.

The principal feature of polyurethane elastomers is the phase segmentation of the hard and soft segments (Król, 2007). Strictly the polymer shown in Fig. 3.3 is a block copolymer of a polyether urethane and a polyurea, as shown in Fig. 3.5. As with other block copolymers it is the possibility of micro phase segregation, which makes these materials particularly interesting. In this case the polyurea segment constitutes a hard block, as it is normally glassy or semi-crystalline at room temperature, while the polyether urethane is soft. If this is not the case then the materials cannot behave as an elastomer. With polyesters, there is more possibility of interaction between the two components and the properties are less favourable, in addition the flexibility is reduced by the higher levels of interactions between the neighbour polyester chains (Król, 2007; Liaw, 1997). Aside from the elastomeric properties, the development of phase separation can be probed by electron microscopy. For example Fig. 3.6 shows an SEM picture of a

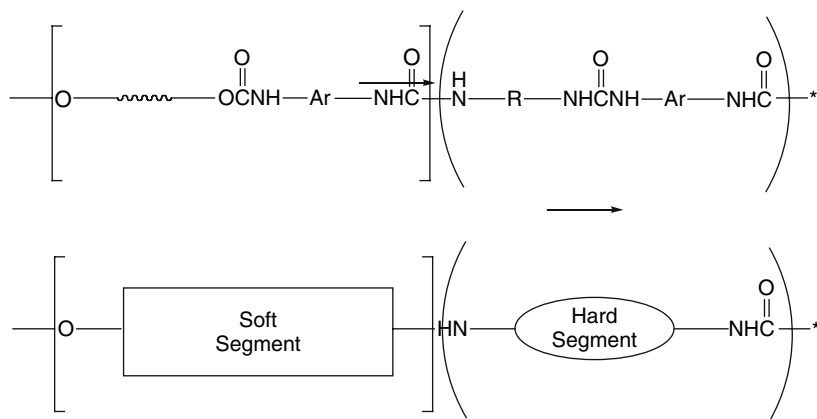
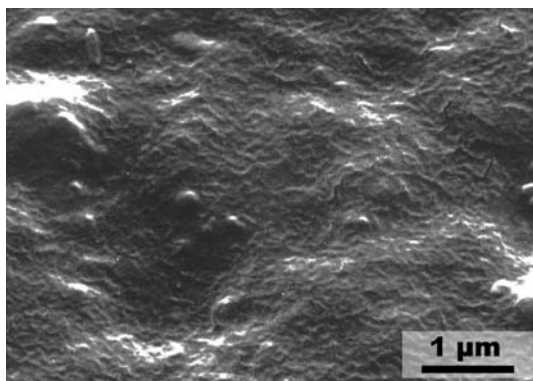


Fig. 3.5 Segmented behaviour of a thermoplastic polyurethane elastomer

**Fig. 3.6** SEM image (at high resolution) of a polyetherurethanes sample showing fine structure on a scale consistent with hard block segregation (Photo courtesy of Mr RH Olley)



poly(etherurethane) the fine structure at a scale less than 100 nm has been related to the segregation of the hard segment and the soft segment (Prisacariua et al., 2003). In fact SEM is not the most appropriate technique for studying morphology on this scale; ideally transmission electron microscopy should be used, but to do this effectively suitable etchants would need to be used which is not always a straight forward process (Prisacariua et al., 2003).

Whilst this is composite system, the mechanical properties depend very much on the nature of the hard segment. This is exemplified by the data in Fig. 3.7. The figure shows respectively the tensile strength (a), elongation (b), and hardness (c) of a series of polyurethane based elastomers based on MDI, polyethylene glycol and with butane diol as the chain extender (Yoon et al., 2000). As is clear from the plots shown all these mechanical properties can be closely related to the proportion of hard segment.

The chemical structure of the hard segment also makes a substantial contribution to the properties; thus for a series of related polymers, containing the same proportion of hard segment show greatly differing mechanical strength, as shown in Fig. 3.8 (Lee and Tsai, 2000) (this is for a series of polyether based urethanes once again with a butane diol extender). Here it would seem that the stronger materials are based on MDI and HMDI, this has been related to the more linear nature of these two monomers and the effect of a mixing the 2,4 and 2,6 TDI monomers is consistent with this. It is important to note that the influence of the soft segment is also crucial to the mechanical properties; for example the elasticity is almost entirely dependent on this component. If this is glassy or crystalline at room temperature the materials could not be elastomers. Fig. 3.8(b) shows there is no correlation between changing the hard segment and elongation; indeed most of the samples shown, give similar elongations, consistent with the materials using the same poly(tetramethyleneoxide) as the soft segment. However, this aside the dominance of the hard segment in

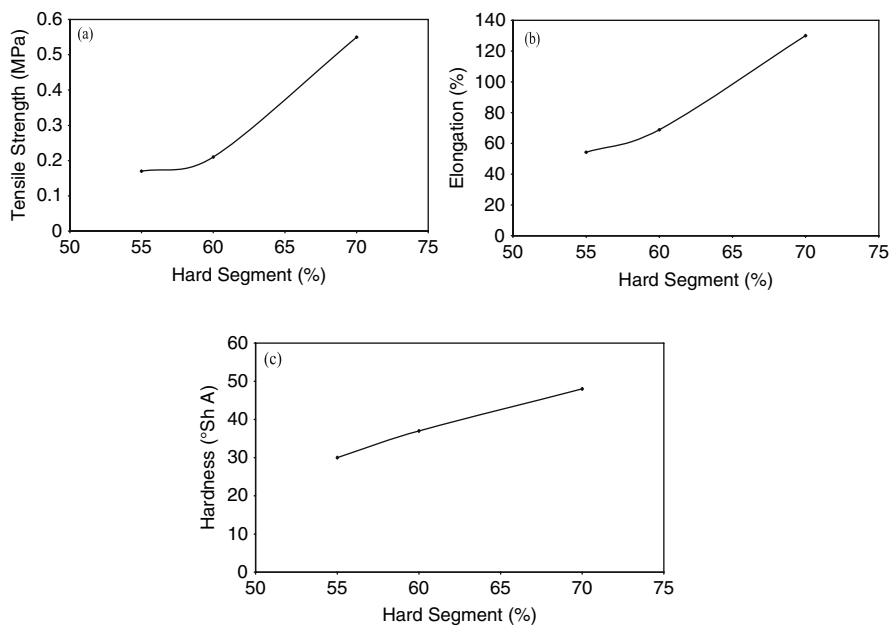


**Fig. 3.7** The mechanical properties of a series of polyurethane elastomers based on MDI, polyethylene glycol, and a butane diol chain extender (a) tensile strength; (b) elongation (c) hardness all plotted as a function of the proportion of hard segment

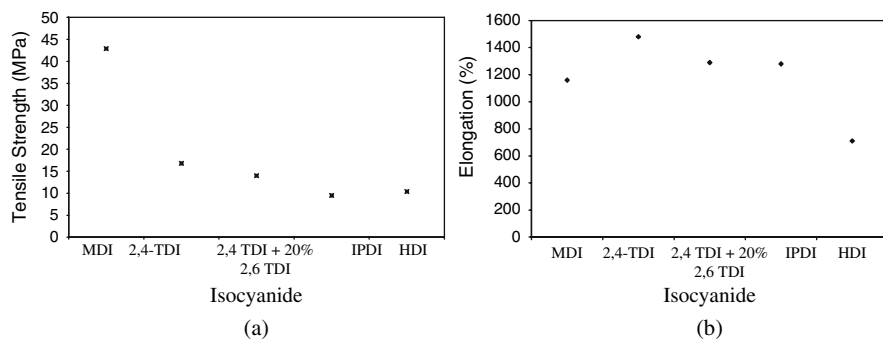


**Fig. 3.8** (a) Tensile strength for a range of comparable polyurethanes with different hard segments; (b) elongation for the same samples

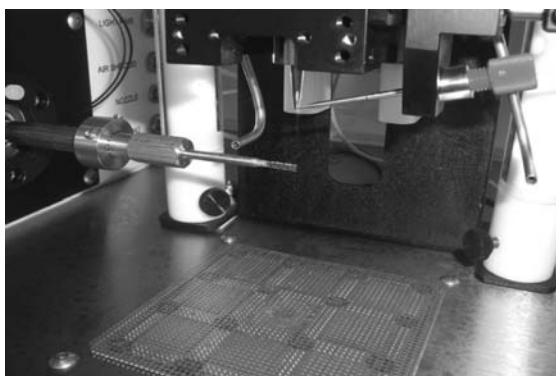
determining the mechanical strength of the materials has important consequences in biomedical applications; as we shall see below, biodegradation of the polymers are largely related to the structure of the soft segment, and thus this can be changed without substantially sacrificing the mechanical properties.

### 3.5 Processing of Polyurethanes

The unique chemistry and material properties of polyurethanes of course are vital in the applications, but crucial to the application of devices is the processing. In this case this is not just a matter of producing materials of a particular shape although this is often a complex challenge, but as we shall discuss below, the finishing particularly the surface finishing is vital and it even small defects in the surface morphology can decrease the *in vivo* lifetime of a device. Thus the processing route is an important consideration in determining the effectiveness of a device (Taylor et al., 2005). In some cases surface coating is done as a separate process. This is particularly so when the surface coating is a solvent bound polymer system containing a pharmaceutical material such as heparin for slow release. For example, metal devices such as stents are often coated with polymeric materials to improve their biocompatibility (Lee et al., 2007). The coating must be carefully controlled and highly specialised equipment is required, such as the apparatus shown in Fig. 3.9.

Polyurethanes offer many challenges and many opportunities in relation to polymer processing; there are a number of potential routes to materials. This section is not intended to list all the options available, but rather to highlight one or two examples of how processing methods facilitate medical applications of polyurethanes. The very favourable kinetic time scale of polyurethane formation makes the production of highly cross-linked materials in the desired shape relatively simple by virtue of a process known as reaction injection moulding (Mills, 1993). This may be used to make preformed automotive parts and some foams for example, Rapid prototyping is of course an important area in terms of producing polyurethane castings (Cormier and Taylor, 2001). In fact, much of the science behind processing is wrapped up in proprietary knowledge, and dissemination is limited for sound commercial reasons, however, surface uniformity does appear to be a constant requirement in medical implants and solution casting of polyurethane in various guises is often particularly suitable in this regard. Thus, a three leaflet heart valve made from

**Fig. 3.9** A Sono-Tek Micro-Mist MediCoat Stent Coating System in operation. This apparatus is designed to surface coat stents with a range of polymeric materials, particularly where slow release is required. (Photo courtesy of BioInteractions Ltd, University of Reading, Science and Technology Centre, Reading)



polyurethane has been produced by casting estane 58201(a polyether based elastomer) from dimethylacetamide. It is claimed that better results are obtained by using a concentrated polyurethane solution, rather than repeated dipping into dilute solutions (Mackay et al., 1996).

Obviously commercial environments face different requirements, particularly if low cost, higher volume materials (as opposed to the often customised polymer-coated stents described above). Dip moulding is on the face of it, a simple route to processing materials. The mould is a metal or glass mandrel which is carefully dipped into a solution of the polymer. The mandrel is then withdrawn and the polymer allowed to cure. A disadvantage of this process in terms of polyurethanes is that the use of an organic solvent such as tetrahydrofuran or dimethylacetamide is required. In addition processing conditions have to be carefully controlled to avoid the formation of bubbles or other defects (Shah, 2001). Even with apparently straight forward technology, manufacturers face significant challenges, thus for example, dip coating can be used to cast a range of low pressure balloons constructed from polyurethane; however, if large neck to body ratios are required this process is not appropriate. To form the balloons shown in Fig. 3.10, a thermoforming film was required using a welding process, which produces a smooth outer finish and leaves the seam on the inside of the balloon (Shah, 2002).

Electrospinning involves the production of fibres under conditions of a high electric field. In a typical experiment a solution of polyurethane in dimethyl formamide, contained in a syringe, is ejected in a thin stream whilst subjected to an electric field of tens of kilovolts (Demir et al., 2002), passing a solution of a polymer from a syringe through an electric field. Electrospinning is a route to

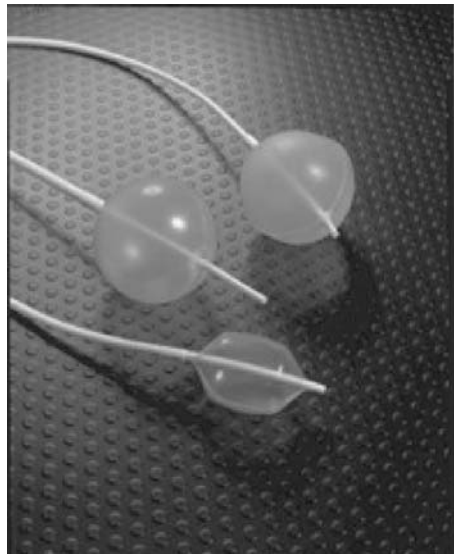


**Fig. 3.10** Low Pressure balloons designed for medical applications manufactured using a thermoformable polyurethane film. Photo courtesy of Polyzen, Inc. ([www.polyzen.com](http://www.polyzen.com))



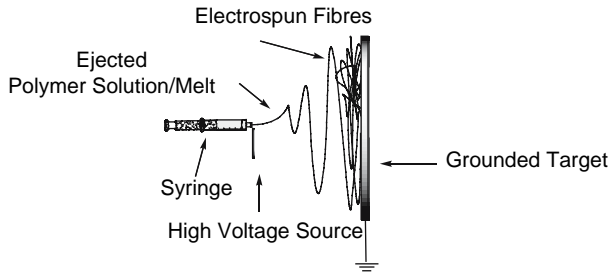


**Fig. 3.11** The basic design of an electrospinning system

obtaining fibres in diameter ranges inaccessible through conventional spinning technology material in the range of less than 3 nm to over 1  $\mu\text{m}$ , although melt blowing can approach the upper limit since fibres of 500 nm have been generated (Ellison et al., 2007). Electrospun fibres have attracted considerable interest in areas where a supporting structure is required to promote tissue regeneration (Courtney et al., 2006) most often in the mechanically differing requirements of bone and skin (Chong et al., 2007). As might be expected the processing conditions influence the mechanical properties; for example it has been shown that by electrospinning onto a rotating mandrel, rather than the flat surface shown in Fig. 3.11, materials with highly anisotropic mechanical properties can be produced. The mechanical properties of these closely resembling those of the native pulmonary heart valve leaflet (Courtney et al., 2006). Even if the mechanical properties can be matched, it may be difficult incorporating the electrospun fibre into the tissue scaffold and a more sophisticated arrangement involves electro spraying the biological material on to the fibres as they are formed (Stankus et al., 2006; Stankus et al., 2007).

## 3.6 Polyurethanes in Biological Environments

### 3.6.1 *Advantages of Polyurethane*

The use of polyurethane in medical devices, particularly those devices which are implanted in vivo and therefore have a constant contact with the biological entity, is prompted by their relatively good haemocompatibility in particular they are thought to have a low thrombogenicity<sup>4</sup> and the excellent mechanical properties of the materials; coupled with the versatile chemistry described

<sup>4</sup> Thrombogenicity refers to the tendency of a material in contact with blood to form a clot, clearly for implants which are required to allow the passage of blood this is a major factor in determining the lifetime of the implant.

above has led to polyurethanes rapidly becoming the materials of choice for uses where the polymer has to be implanted into the body; thus uses such as heart valves, dialysis membranes, breast implants, aortic grafts, and bone adhesives have been prepared from polyurethane based systems. The implantation of any polymer into the body is a complex business and there are a range of factors to be considered (Puskas and Chen, 2004), toxicity and stability are of course major ones, others include the effect of sterilization on the material, and whether it react with any medications. In addition, to this the mechanical properties must match the requirements of the biological application; and the material must have complete long-term stability for permanent implants, or degrade at the precise rate required for degradable systems. The demands are extremely challenging and numerous approaches have been adopted to meet these demands. Space allows us to mention only a few of these in the following section but it is hoped that this gives a flavour of some of the work being undertaken.

### ***3.6.2 Biocompatibility***

Degradation of long-term implants is of course a major problem, however, probably the most difficult problem relating to the use of these materials, and in fact all polymers, *in vivo* is that they are prone to interaction with the biological entity. Thus encapsulation by various biological components is a common problem, this may present as tissue growth, or it may present as calcification; for example urethral stents commonly become encrusted with materials such as calcium phosphate (Singh et al., 2001). Calcification is also a problem for heart valves and other blood contacting uses (Vyavahare et al., 1997), though here the development of blood clots is likely to be particularly problematic.

Crucial to the use of polyurethane in blood contacting applications is the prevention of blood clot formation, which of course could have fatal consequences. Even though, this material is considered to have good blood compatibility, the development of even small blood clots can have serious medical consequences. Thus many attempts have been made to improve the haemocompatibility of polyurethanes, and in particular a commercially available poly(urethane-urea) based on MDI and ethylene diamine or 4,4'-diaminodiphenylmethane, with a poly(tetramethylene oxide) flexible segment, known as Biomer (see below), has been used for the fabrication of devices such as artificial hearts and vascular grafts. It would appear that the effectiveness is somewhat influenced by the way the material is processed (Jagur-Grodzinski 1999; Orang et al., 1996), though this generally involves repetitive solvent casting, depositing a series of layers; and various surface treatments have also been effective in this regard. However, the anti-thrombogenic properties have been particularly enhanced by a range of chemical modifications to the surface. This can be done in a number of ways, but of particular interest is the addition of heparin

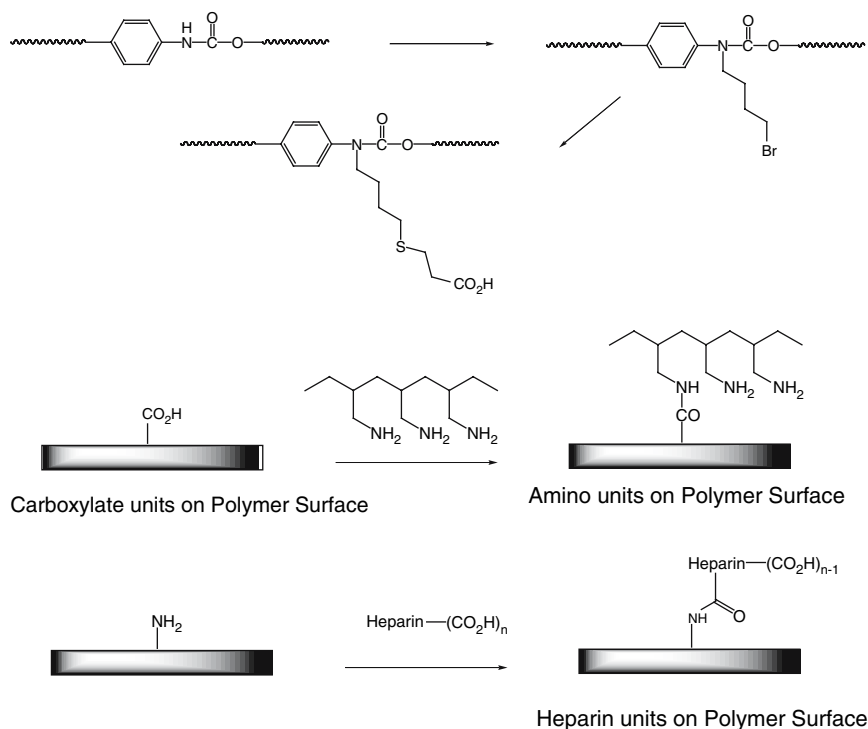


**Fig. 3.12** Covalent attachment of Heparin onto the surface of a polyurethane elastomer

to the system either using non-covalent interactions or by covalent attachment using a chemically modified polymer (Goddard and Hotchkiss, 2007) as shown in Fig. 3.12. Here a functionalized polyurethane is aminated and subsequently reacted with heparin (Alferiev et al., 2006). There is considerable interest in this area, and it seems likely that a combination of high-quality processing and a range of surface treatments, offer a real solution to the problems associated with long term implantation of polyurethane materials in blood contacting environments. This will of course subsequently offer a range of additional options (particular interest is shown in polymer replacements for heart components for example) for medical practitioners.

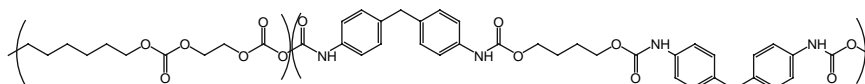
### 3.6.3 Biodegradation

In the 1980s, it became clear that there were problems with the use of polyurethane, most famously the foamed polyurethane used as the outer casing for breast implants. This material was particularly chosen because it reduced the problem of “capsular contracture”, a common complication in breast augmentation surgery where tissue forming around the implant

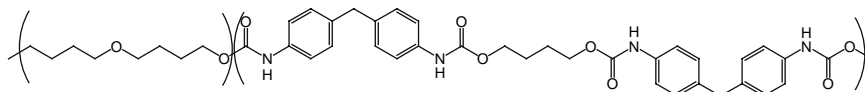
contracts and causes the implant to appear hardened (Handel and Gutierrez, 2006). It was found that on removal of the implants substantial amounts of the polyurethane material was missing (Slade 1982) this led to concerns that the degradation of the polyurethane in these materials could release substantial amounts of toluene diisocyanate, a potential carcinogen. Though there was found to be evidence of the presence of this material in women with polyurethane-coated implants, the levels were small and the risks felt to be remote (Sepai et al., 1995), this particular approach is no longer used in the US and Europe at least. There would appear to be no evidence of any long-term health problems as a result of the use of these devices.

From a mechanistic point of view the degradation of catheter leads used for pacemaker leads was a more informative problem (Santerre et al., 2005) and was particularly studied by Stokes (1993). On the basis of this work and others, it is apparent that there are a number of processes that can contribute to the in vivo degradation of polyurethane systems, these include hydrolysis of the polymer; in particular the ester linkages in ester urethane based systems are susceptible, in the case of the degradation of catheter leads the polyether urethane system degrades via an oxidative process, and that this was catalysed by metal ions present in the pacemaker leads. Thus in the most general terms it would appear that polyether urethanes degrade by oxidation and polyester urethanes by hydrolysis.

There are many approaches to this problem but a chemical approach has been to utilise variations on the ester or ether flexible component. For example, the polycarbonate systems [8] [bionate™ 80A, which has a MDI hard segment chain extended with butane diol and a poly(1,6-hexyl 1,2-ethylcarbonate) soft segment] has been shown to be less labile towards oxidation than the polyether urethanes [9] [Elasthane™, with the same type of hard segment, but a poly(tetramethylene oxide) soft segment] (Seifalian et al., 2003).



[8]



[9]

Unfortunately, while more stable, there is evidence that polycarbonate systems also degrade. It has been suggested that the mechanism is also oxidative and involves the in vivo formation of reactive oxygen radicals (Christenson,

Anderson and Hiltner, 2004). The biological system represents a hostile environment to the polymer thus poly ether systems are oxidised it would seem by reactive oxygen species generated from adherent macrophages and foreign body giant cells (Christenson, Wiggins et al., 2004). The reactive oxygen radicals then react at the carbon adjacent to the oxygen creating a site for cross-linking or subsequent chain scission (Handel and Gutierrez, 2006). In this case the ether oxygen provides additional stability to the unpaired electron by virtue of its lone pairs [Fig. 3.13(a)]. It has been suggested that the (albeit a smaller amount of) degradation by polycarbonate occurs in the same way through reaction at the carbon adjacent to the oxygen [Fig. 3.13(b)]; however, it should be noted that the proximity of the  $\pi$ -bonded carbonyl may reduce this stability,<sup>5</sup> and this particular hydrogen is not particularly reactive (Qureshi et al., 1995). It has further been suggested, that the degradation then proceeds via further reaction with hydroxyl radicals followed by fragmentation of the hemiacetal produced. Of course in the presence of oxygen an alternative pathway would be the addition of oxygen followed by hydrogen atom abstraction and subsequent decomposition of the hydroperoxide produced, (as in the autoxidation on storage of low molecular weight ethers, which is a well known explosion hazard); but the end result is largely the same. The important point here is that oxidation is the problem and may be countered with appropriate antioxidants; however, the problem of degradation by hydrolytic enzymes must also be considered (Labow et al., 2005; Tang et al., 2001) although there is some evidence to suggest that this is less of a problem than oxidation (Christenson et al., 2006), the complexities of biological systems suggests that the relative

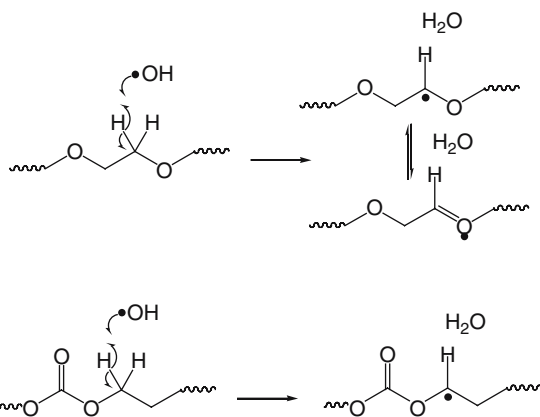
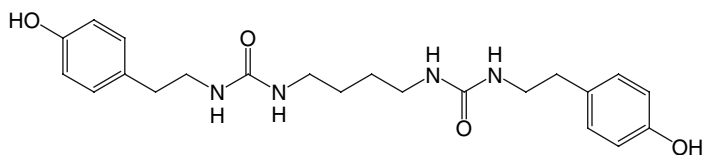


**Fig. 3.13** The reaction of hydroxyl radicals with (a) polyether units to form a stabilised radical and (b) with the carbonate

<sup>5</sup> The possibility of electron overlap between the oxygen lone pair and the  $\pi$ -electron system of the carbonyl group effectively reduces the availability of the lone pair electrons for interaction with the radical centre.

importance of the two components are likely to vary from material to material and from application to application.

Such is the versatility of the polyurethane approach that there are a number of applications which rely on an entirely the opposite principle; namely the ability of certain polyurethanes to decompose in situ. Applications include the use of polyurethanes for tissue and bone scaffolds and for drug delivery systems. The principal is a simple one namely that the biological tissue once grown back is the most appropriate system and the scaffold provides a temporary structures which allows regeneration. The scaffold may be impregnated with material, such as fibroblast growth factor (bFGF), which is slowly released from the polymer and will assist in tissue development (Guan et al., 2007). One particular concern however with the use of the aromatic systems is any in vivo degradation will result in the generation of harmful amines (Zhang et al., 2000). Thus in general, but particularly for applications where biodegradation might be needed, considerable interest has been shown in the use of lysine diisocyanate (or strictly lysine diisocyanate ethyl ester) and butyl diisocyanate. The likely degradation products of these are lysine and diaminobutane (also known as putrescine) which are commonly found in biological systems and might be expected to be of relatively low toxicity; indeed studies show this to be the case (Guan et al., 2004). The problem the of course being that these aliphatic systems do not exhibit the same properties as the aromatic systems in particular the hard segment may be less rigid. A way around this is to use other aromatic groups such as tyrosine in the chain extender to provide additional rigidity without the potential toxicity and the system outlined in [10] has been prepared (Guelcher et al., 2005).



[10]

It is early days in terms of the application of these biodegradable scaffolds, but it is clear that with there are range of materials possible. In particular by varying the nature of the polyester component the rate of degradation can be controlled, and suitable (non toxic) hard segment chemistry can be used to match the mechanical properties to the application required. Processing methodologies such as electrospinning offer substantial control of fibre dimensions, and short of growing biological replacements in vitro, this approach offers probably one of the best options for tissue regeneration.

### 3.7 Conclusions

The term polyurethane represents a wide range of polymeric materials available for use in the biomedical field. There are particular features of this material which offer substantial advantages over competitors such as polyethylene, polypropylene, and nylon. The main one of these is the composite nature of polyurethane systems, which allows materials to take on a range of different material properties, not the least of which is the ability to form elastomers. Polyurethanes, depending on their chemical compositions offer the potential for use both as permanent implants and as biodegradable temporary scaffolds, in circumstances where regeneration is required. More obvious immediate and current applications which involve short-term temporary exposure to the biological environment, offer less of a challenge and many systems are currently in use. The use of polyurethane as permanent implants has a controversial history, not least because degradation of these materials can lead to potentially toxic diamines, but a changes in the design and chemistry of the materials offer a real chance to overcome these problems in addition new biocompatible monomers have been developed allowing these materials to be used in situations where they are expected to biodegrade. This has opened up new opportunities for the use of this material as scaffolds in the very different medical environments of skin and of bone.

### References

- Akita S, Akino K, Imaizumi T, Tanaka K, Anraku K, Yano H, Hirano A (2006) A polyurethane dressing is beneficial for split-thickness skin-graft donor wound healing. *Burns* 32:447–451
- Alferiev IS, Connolly JM, Stachelek SJ, Ottey A, Rauova L, Levy RJ (2006) Surface heparinization of polyurethane via bromoalkylation of hard segment nitrogens. *Biomacromolecules* 7:317–322
- Bhattacharya P, Wild D, Rosenburg MJ, Waugh MS, Solomon HM, Lyszkowski ADL (1996) The male polyurethane condom: a review of current knowledge. *Contraception* 53(3):141–146
- Biesman G (2002) The global polyurethane market. In: Randell D, Lee S (eds) *The polyurethanes book*, Wiley, UK, pp 9–22
- Burkus J, Eckert CF (1958) The Kinetics of the Triethylamine-catalyzed Reaction of Diisocyanates with 1-Butanol in Toluene, *J Amer Chem Soc* 80:5948–5950
- Cormier D, Taylor J (2001) A process for solvent welded rapid prototype tooling. *Robotics and Computer Integrated Manufacturing* 17:151–157
- Chong EJ, Phann TT, Lim IJ, Zhang YZ, Bay BH, Ramakrishn S, Lim CT (2007) Evaluation of electrospun PCL/gelatin nanofibrous scaffold for wound healing and layered dermal reconstitution. *Acta Biomaterialia* 3:321–330
- Christenson EM, Anderson JM, Hiltner A (2004) Oxidative Biodegradation of Poly(carbonate urethane) and Poly(ether urethane): In Vivo and In Vitro Correlations. *J Biomed Mater Res* 70A:245–255

- Christenson EM, Wiggins MJ, Dadsetan M, Anderson JM, Hiltner A (2004) Poly(carbonate urethane) and Poly(ether urethane) Biodegradation: In Vivo Studies. *J Biomed Mater Res* 69A:407–416
- Christenson EM, Patel S, Anderson JM, Hiltner A (2006) Enzymatic degradation of poly(ether urethane) and poly(carbonate urethane) by cholesterol esterase. *Biomaterials* 27:3920–3926
- Courtney T, Sacks MS, Stankus J, Guan J, Wagner WR (2006) Design and analysis of tissue engineering scaffolds that mimic soft tissue mechanical anisotropy. *Biomaterials* 27:3631–3638
- Demir MM, Yilgor I, Yilgor E, Erman B (2002) Electrospinning of Polyurethane Fibres. *Polymer* 43:3303–3309
- Ellison CJ, Phatak A, Giles DW, Macosko CW, Bates FS (2007) Melt blown nanofibers: fiber diameter distributions and onset of fiber breakup. *Polymer* 48(11):3306–3316
- Goddard JM, Hotchkiss JH (2007) Polymer surface modification for the attachment of bioactive compounds. *Prog Polym Sci* 32:698–725
- Gogolewski S (1989) Selected topics in biomedical polyurethanes – a review, *Colloid Polym Sci* 267:757–785
- Guan J, Fujimoto KL, Michael S, Sacks MS, Wagner WR (2005) Preparation and characterization of highly porous, biodegradable polyurethane scaffolds for soft tissue applications. *Biomaterials*, 26:3961–3971
- Guan J, Sacks MS, Beckman EJ, Wagner WR (2004) Biodegradable poly(ether ester urethane)urea elastomers based on poly(ether ester) triblock copolymers and putrescine: synthesis, characterization and cytocompatibility. *Biomaterials* 25:85–96
- Guan J, Stankus JJ, Wagner WR (2007) Biodegradable elastomeric scaffolds with basic fibroblast growth factor release. *J Controlled Release* 120:70–78
- Guelcher SA, Gallagher KM, Didier JE, Klindedinst DB, Doctor JS, Goldstein AS, Wilkes GL, Beckman EJ, Hollinger JO (2005) Synthesis of biocompatible segmented polyurethanes from aliphatic diisocyanates and diurea diol chain extenders. *Acta Biomaterialia* 1:471–484
- Handel N, Gutierrez J (2006) Long-term safety and efficacy of polyurethane foam-covered breast implants. *Aesthetic Surgery J* 26:265–274
- Harwood LM, (1992) Polar rearrangements. Oxford University Press, Oxford UK, pp 49–52
- Jagur-Grodzinski J (1999) Biomedical application of functional polymers. *Reactive & Functional Polymers* 39:99–138
- Król P (2007) Synthesis methods, chemical structures and phase structures of linear polyurethanes. Properties and applications of linear polyurethanes in polyurethane elastomers, copolymers and ionomers. *Progress in Mater Sci*, 52:915–1015
- Lamba NMK, Woodhouse KA, Cooper SL (1998) Polyurethanes in biomedical applications. CRC Press, Boca Raton
- Labow RS, Sa D, Matheson LA, Dinnes DLM, Santerre JP (2005) The human macrophage response during differentiation and biodegradation on polycarbonate-based polyurethanes: Dependence on hard segment chemistry. *Biomaterials* 26:7357–7366
- Lee DK, Tsai HB (2000) Properties of segmented polyurethanes derived from different diisocyanates. *J Appl Polym Sci* 75:167–174
- Lee Y-K, Park JH, Moon HT, Lee DY, Yun JH, Byun Y (2007) The short-term effects on restenosis and thrombosis of echinomycin-eluting stents top-coated with a hydrophobic heparin-containing polymer. *Biomaterials* 28:1523–1530
- Liauw DJ (1997) The relative physical and thermal properties of polyurethane elastomers: effect of chain extender based on dihydroxynaphthalene and its derivatives. *Angew Makromol Chem* 245:89–104
- Mackay TG, Wheatley DJ, Bernacca, GM, Fisher AC, Hindlet, CS (1996) New polyurethane heart valve prosthesis: design, manufacture and evaluation, *Biomaterials* 17:1857–1863



- Martineau L, and Shek PN (2006), Evaluation of a bi-layer wound dressing for burn care II. In vitro and in vivo bactericidal properties, *Burns*, 32, 172–179
- Mills NJ (1993) *Plastics, Microstructure and engineering applications* (2nd ed). Edward Arnold, Sevenoaks UK, pp 123–125
- Orang F, Plummer CJ, Kausch HH (1996) Effect of processing conditions and in vitro ageing on the physical properties of biomer. *Biomaterials* 17:485–490
- Percival SL, Bowler PG, Russell D (2005) Bacterial resistance to silver in wound care. *J Hospital Infection* 60:1–7
- Ping P, Wang W, Chen X, Jing X (2005) Poly(E-caprolactone) polyurethane and its shape-memory property. *Biomacromolecules*, 6:587–592
- Prisacariva C, Olley RH, Caraculacu AA, Bassett DC, Martin C (2003) The effect of hard segment ordering in copolyurethane elastomers obtained by using simultaneously two types of diisocyanates. *Polymer* 44:5407–5421.
- Puskas JE, Chen Y (2004) Biomedical applications of commercial polymers and novel polyisobutylene-based thermoplastic elastomers for soft tissue replacement. *Biomacromolecules* 5(4):1142–1154
- Qureshi, A, Solomon DH, Kelly DP, (1995) Investigations into the free radical polymerizations of allyl carbonates-I. The reaction of t-butoxyl radical. *Eur Polym J* 31(9):809–818
- Santerre JP, Woodhouse K, Laroche G, Labow RS (2005) Understanding the biodegradation of polyurethanes: From classical implants to tissue engineering materials. *Biomaterials* 26:7457–7470
- Saunders KJ (1973) *Organic polymer chemistry*. Chapman and Hall, London, pp 318–345
- Seifaliana, AM, Salacinski HJ, Tiwari A, Edwards A, Bowald S, Hamilton G, (2003) In vivo biostability of a poly(carbonate-urea)urethane graft. *Biomaterials* 24:2549–2557
- Sepai O, Henschler D, Czech S, Eckert P, Sabbioni G (1995) Exposure to toluenediamines from polyurethane-covered breast implants. *Toxicology Letters* 77:371–378
- Shah TM (2001) Dip moulding of polyurethane and silicone for latex-free nonallegenic products. *Medical and Diagnostics Industry*, pp 75–81
- Shah TM (2002) Polyurethane thin-film welding for medical device applications. *Medical and Diagnostics Industry*, pp 62–68
- Singh, I, Gupta NP, Hemal AK, Aron M, Seth A, Dogra PN (2001) Severely encrusted polyurethane ureteral stents: management and analysis of potential risk factors. *Urology* 58:526–531
- Slade, CL, Peterson HD (1982) Disappearance of the polyurethane cover of the ashley natural y prosthesis: *Plastic And Reconstructive Surgery* 70(3):379–382
- Stankus JJ, Guan J, Fujimoto K, Wagner WR (2006) Microintegrating smooth muscle cells into a biodegradable, elastomeric fiber matrix. *Biomaterials* 27:735–744
- Stankus JJ, Soletti L, Fujimoto K, Hong Y, Vorp DA, Wagner WR (2007) Fabrication of cell microintegrated blood vessel constructs through electrohydrodynamic atomization. *Biomaterials* 28:2738–2746
- Stevens, MP (1990) *Polymer Chemistry, an introduction*. Oxford University Press, New York, pp 440–446
- Stokes K (1993) *Biodegradation, Cardiovascular Pathology, Vol 2(1), Chapter 10*, pp 111–119
- Taylor JE, Laity PR, Freeburn S, Wong SS, Norris K, Khunkamchoo P, Cable M, Andrews G, Johnson AF, Cameron RE (2005) Effect of processing route and acetone pre-treatment on the biostability of pelletehane materials used in medical device applications. *Biomaterials* 26:6467–6476
- Tang Y, Labow RS, Santerre JP (2001) Enzyme-induced biodegradation of polycarbonate-polyurethanes: Dependence on hard-segment chemistry. *J Biomed Mater Res*, 57:597–611
- Vyavahare NR, Chen W, Joshi RR, Lee C-H, Hirsch D, Levy J, Schoen FJ, Levy RJ (1997) Current Progress in anticalcification for bioprosthetic and polymer heart valves. *Cardiovascular Pathology* 6:219–229

- Wilson GJP, Van Noesel MM, Hop WCJ, Van de Ven C (2006) The catheter is stuck: complications experienced during removal of a totally implantable venous access device. A single-center study in 200 children. *J Pediatric Surgery* 41:1694–1698
- Yoon KH, Yoon ST, Park OO (2000) Damping properties and transmission loss of polyurethane. I. Effect of soft and hard segment compositions, *J Appl Polym Sci* 75:604–611
- Zhang JY, Beckmann EJ, Piesco NP, Agarwal, S (2000) A new peptide-based urethane polymer: synthesis, biodegradation, and potential to support cell growth in vitro. *Biomaterials* 1247–1258

# Chapter 4

## Rapid Prototyping of Hydrogels to Guide Tissue Formation

Jordan S. Miller and Jennifer L. West

### 4.1 Hydrogels

Hydrogels are crosslinked, polymer-based networks that are very hydrophilic, causing them to be highly swollen with water. Hydrogels can be formed by physically or covalently crosslinking a liquid prepolymer solution into a solid hydrogel. A variety of material compositions can be used to make hydrogels, including agarose [1], alginate [2, 3], hyaluronic acid [4, 5], chitosan [6], poly-hydroxyethylmethacrylate (pHEMA) [7–9], dextran [10], polyvinyl alcohol [11], acrylamide derivatives [12, 13], polyethylene glycol (PEG) [14–16], and even peptide amphiphiles [17, 18]. Examples of polymer structures that can form hydrogels are shown in Fig. 4.1. Note that these polymers are highly hydrophilic and also provide the opportunity for crosslinking.

Hydrogels are an exciting class of materials for applications in tissue engineering, regenerative medicine and drug delivery due to their excellent biocompatibility, hydrophilicity and the ease with which their mechanical properties can be tuned to match those of soft tissues. They have been utilized over the past several decades for a broad range of medical applications including contact lenses [19]; implant coatings [20–22]; tissue coatings and wound dressings [23–26]; cell transplantation [27]; microfluidic valves, actuators, and sensors [28–33]; and drug delivery [34–37]. More recently, it has been demonstrated that hydrogels can be molecularly designed to exhibit many of the biological characteristics required to guide cell interactions for applications in tissue engineering.

One particular system of hydrogels, based on polyethylene glycol (PEG) and its derivatives, has proven extremely versatile for tissue engineering applications [27, 38, 39].

PEG has a long history of use in many medical devices and pharmaceutical formulations and exhibits high hydrophilicity, high biocompatibility, and little

---

Jennifer L. West

Rice University, Department of Bioengineering, 6100 Main St., MS-142, Houston, Texas 77005, Rice University, USA  
jwest@rice.edu

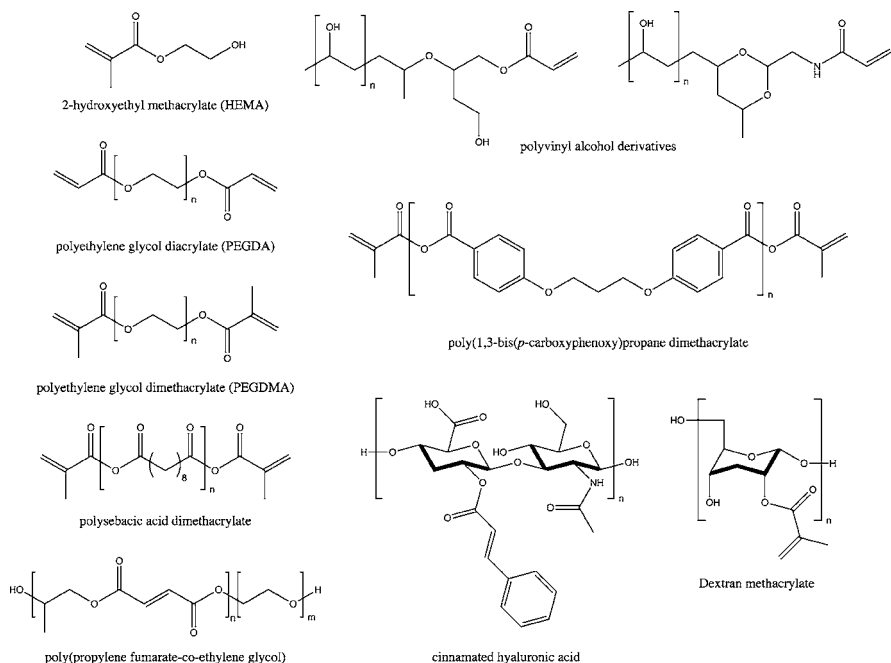


**Fig. 4.1** Examples of polymers that can be used to form hydrogels. Note that these polymers are highly hydrophilic and also have sites that can allow crosslinking

to no immunogenicity [40]. PEG hydrogels can be formed by first modifying individual PEG chains with two or more crosslinkable moieties such as acrylate groups (Fig. 4.2). Acrylates are susceptible to free radical polymerization, allowing crosslinking of the polymer solution to form a solid hydrogel. These

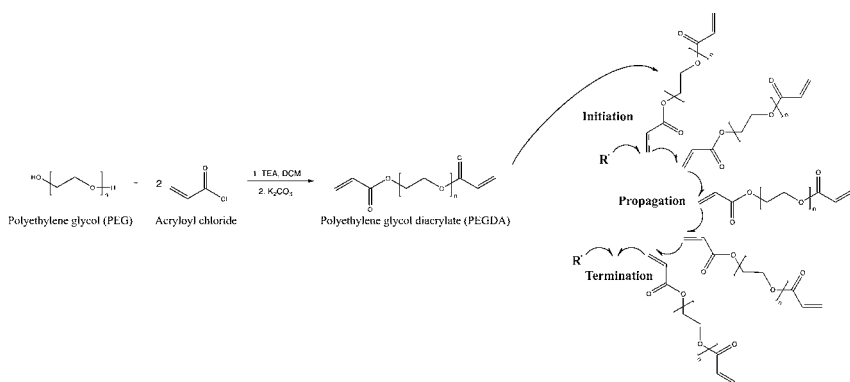


**Fig. 4.2** PEG can be modified with acrylate groups at the termini by reaction with acryloyl chloride, providing double bonds that can undergo addition polymerization to form cross-linked hydrogels

materials can be crosslinked in direct contact with cells and tissues. This has allowed their application as barriers to prevent post-operative adhesion formation [15, 41], non-thrombogenic coatings on arteries following angioplasty [42, 43], tissue sealants [44, 45], and immunoprotective coatings for transplanted cells [27]. Cells can also be encapsulated within these hydrogels for tissue engineering applications [46–48].

## 4.2 Photopolymerization

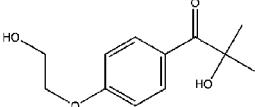
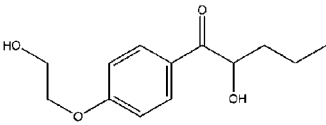
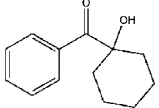
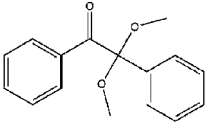
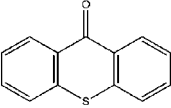
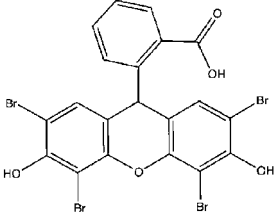
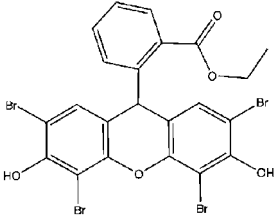
By utilizing photoinitiators, light-sensitive compounds that can generate free radicals, polymerization can be spatially and temporally controlled by exposure to UV or visible light [27, 49, 50]. This degree of control over the polymerization process can enable a variety of patterning and rapid prototyping technologies. Photopolymerization processes have been employed widely in dentistry and in fields such as electronic materials, optical materials, membranes and surface modification. Over the past 15 years, these techniques have been widely adapted for biomedical hydrogel applications as well.

The photoinitiators typically used for hydrogel formation, as well as the photopolymerization process itself, exhibit low cytotoxicity making it possible to polymerize a cell suspension and thus encapsulate viable cells within hydrogels [15, 27]. Cells that have been viably encapsulated within hydrogels include fibroblasts [39, 51], hepatocytes [52, 53], chondrocytes [54, 55], smooth muscle cells [56, 50, 57], osteochondrocytes and their progenitors [58–60], adipocytes [61], and neuronal cells [62]. Transduced cells have also been encapsulated in photopolymerized hydrogels to serve as a long lasting source of protein drugs [48]. Numerous photoinitiators are available, each with different characteristics of water solubility, biocompatibility, and means of decomposition. Examples of photoinitiators are given in Table 4.1.

## 4.3 Design of Bioactive Hydrogels

Most hydrogel materials are highly resistant to cell adhesion due to their low levels of protein adsorption [40, 71]. This provides excellent biocompatibility for many of the applications, but can limit their use in tissue engineering and regenerative medicine. However, it is possible to modify biologically inert hydrogels with peptides, proteins or polysaccharides to mediate specific biological interactions. This can provide an exceptional degree of control over cell-material interactions to guide and control tissue formation processes. For example, modification of hydrogels with cell adhesive peptides derived from extracellular matrix proteins can render the materials cell adhesive, and if appropriate peptides are chosen, even cell selective. The peptide RGD is found in many extracellular matrix proteins and can bind to integrin receptors on many cell types to

**Table 4.1** Selection of biocompatible photoinitiators that can be used for hydrogel photo-polymerization

Trade Name	Structure (Chemical Name)	Abs. Max. (nm)	Ref(s)
Irgacure-2959	 (2-hydroxy-1-[4-(hydroxyethoxy)phenyl]-2-methyl-1-propanone)	< 313	5, 47, 55
Darocur-2959	 (2-hydroxy-1-[4-(hydroxyethoxy)phenyl]-1-pentanone)	< 313	63
Irgacure-184	 (1-hydroxycyclohexane acetophenone)	326	47, 63
Irgacure-651	 (2,2-dimethoxy-2-phenylacetophenone)	335	47, 49, 50, 56, 63-65
THX	 (thioxanthone)	378	47, 63
Eosin Y	 (2',4',5',7'-tetrabromofluorescein)	514	66-70
Ethyl Eosin	 (2',4',5',7'-tetrabromo eosin ethyl ester)	532	

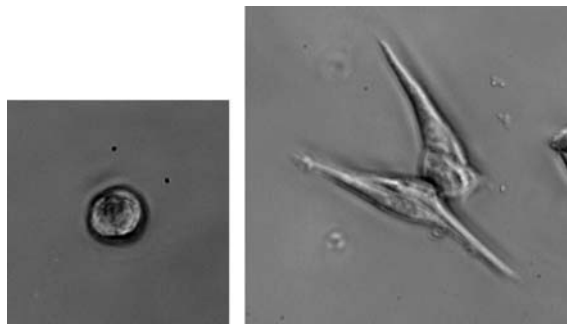


**Fig. 4.3** PEG-based hydrogels are intrinsically cell non-adhesive since they do not support protein adsorption (left). However, cell adhesion can be achieved by covalently immobilizing cell adhesive peptides to the hydrogel materials. In this case, the ubiquitous adhesion peptide RGD was grafted into hydrogels formed from PEG diacrylate. Cells seeded onto these materials attached and spread (right)

mediate adhesion [72]. As shown in Fig. 4.3, when PEG hydrogels are modified with the RGD peptide, they support robust cell adhesion and spreading [49, 73]. Depending on the receptor(s) to which a specific peptide can bind, it is sometimes possible to mediate adhesion of only targeted cell types. For example, the peptides REDV and YIGSR have been shown to be selective for endothelial cells [74, 75], IKVAV for neurons [76], and VAPG for smooth muscle cells [50, 64]. In addition to peptides, larger proteins, such as growth factors, may also be covalently immobilized within hydrogel networks [65, 77]. This can provide additional “instruction” to cells growing within the hydrogel to control processes such as proliferation, migration and differentiation.

#### 4.4 Templating Techniques to Form Porous Hydrogels

Methods to create highly controlled microporous hydrogels have also recently been investigated [78–81]. This technique relies on sphere-templating — or more generally, colloidal-crystal templating — in which a monodisperse spherical porogen is assembled into a packed bed as shown in Fig. 4.4. The hydrogel precursor solution is then infused into the voids between the packed porogen. Crosslinking the hydrogel into a solid skeleton followed by removal of the porogen generates microporous hydrogels with well-defined spherical, interconnected voids that can allow passage of cells through the material. Void space is controlled by the size and shape of the porogen, while the size of interconnected pores can be controlled by sintering the porogen prior to introducing the polymer solution [82]. Sphere-templated hydrogels made of pHEMA [79, 80], PEG [81], or polyacrylamide [78] have been demonstrated using spherical porogens made from polymethylmethacrylate (PMMA) [79–81], or polystyrene [78].

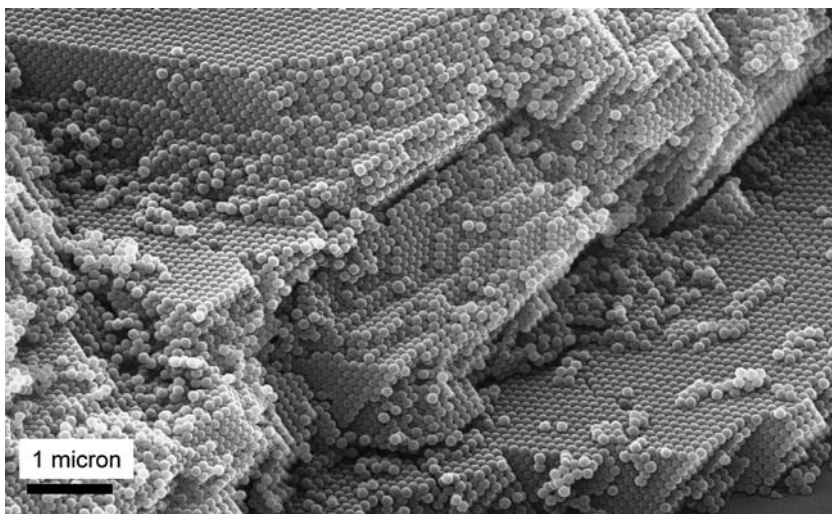


**Fig. 4.4** Dense packing of porogen particles creates a template structure that can be infused with a hydrogel precursor. Following crosslinking, the porogen can be dissolved to generate a hydrogel structure with highly controlled and regular pore structures. Photo courtesy of Vicki Colvin

## 4.5 Photolithographic Patterning of Hydrogels

The union of hydrogel photopolymerization chemistry with photolithographic techniques from the microprocessor industry has enabled the rapid prototyping of hydrogel structures that are uniform in the z-direction but vary in structure or composition in the x- and y-directions. In one method, a cell suspension is mixed with a hydrogel precursor solution and applied to a flat substrate [28, 83, 84]. Illumination of the solution through a mask permits crosslinking only in defined regions. The opaque regions of this photomask block light and inhibit photopolymerization in these shadowed regions while the transparent regions allow light to pass through and initiate hydrogel crosslinking. Simply rinsing the substrate with water removes the uncrosslinked regions, revealing free-standing hydrogel posts containing living cells (Fig. 4.5). It is important to note that although free radical polymerization is a fast chemical process, it is efficiently quenched by atmospheric oxygen and other free radicals. This quenching is believed to prevent the polymerization from extending far into the light-shielded regions on the typical timescales of hydrogel formation, thus providing high contrast at feature edges [85]. An inverse approach involves creating free-standing walls of PEG that form individual wells for the isolation of cells and cell populations. Microwells can be created directly with photolithography using various masking techniques [86, 87]. Research in this area is ongoing to create addressable templates for high throughput screening.



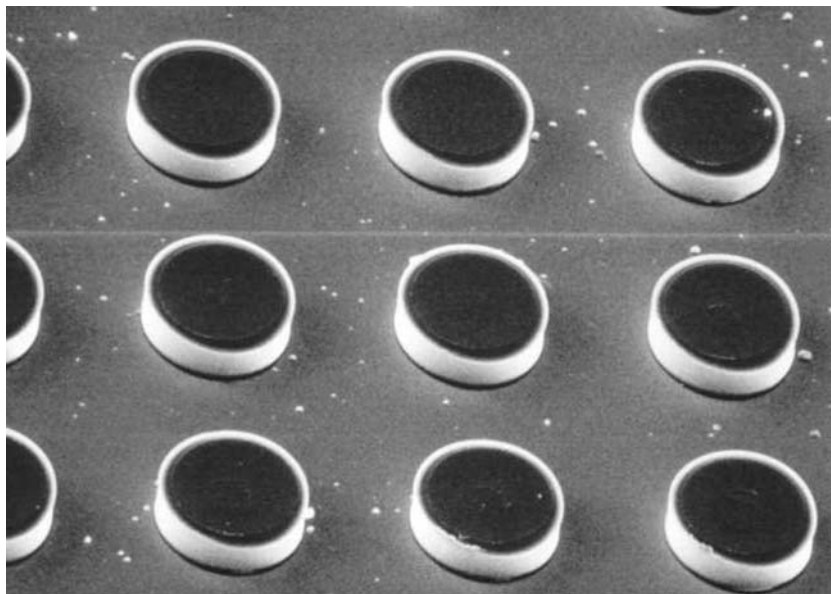
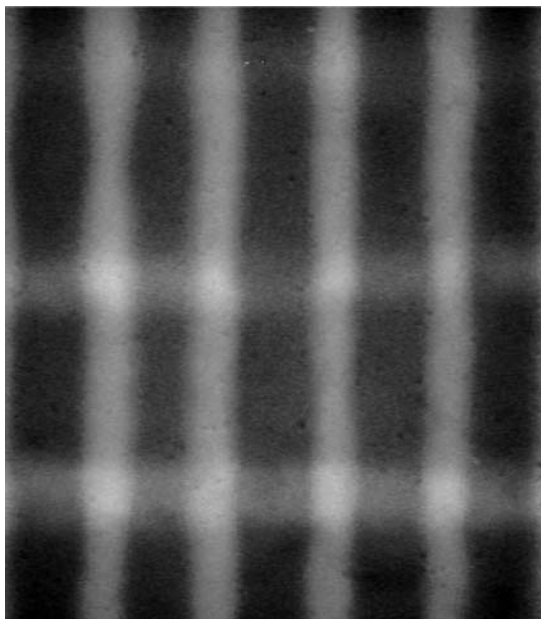


**Fig. 4.5** These hydrogel posts were formed using a photolithographic technique. Mixing cells with the precursor solution could allow creation of cell-based microarrays. Photo reprinted by permission from [83]

Photolithography can also be utilized to create two-dimensional patterns of bioactive factors on the surface of hydrogels. This technique utilizes incomplete polymerization of a base hydrogel, leaving free acrylate groups available for further modification. When acrylated bioactive factors are applied to the surface of the hydrogel and illuminated through a photomask, the factors are covalently immobilized to the surface of the hydrogel, as shown in Fig. 4.6 [88]. Iterative replication of this process enables the attachment of multiple factors to the surface of the hydrogel with much lower expense and complication than if the factors were dissolved in the original prepolymer solution. Lower expense is achieved because the bioactive factors need only be applied to the surface of the hydrogel rather than the bulk polymer solution. Additionally, a key advantage of using a hydrogel for the immobilization of ligands is that unpatterned regions remain highly bioinert while the entire hydrogel is both flexible and compliant.

Rather than utilizing photomasks, liquid crystal display (LCD) projection photolithography utilizes a commercially available LCD projector to cast an image from a computer directly onto the polymer solution to create photocrosslinked hydrogel structures [89–92]. This technique typically has a feature resolution of 50  $\mu\text{m}$  and sometimes suffers exposure artifacts from the embedded wires used to control each pixel in the LCD [89]. Nevertheless, LCD projectors are inexpensive and can serve as an excellent starting point for exploring the parameters needed for the photolithography of hydrogels.

**Fig. 4.6** Photolithography was used to control immobilization of fluorescently tagged cell adhesion peptides on PEG diacrylate hydrogels. Multiple peptides can be immobilized to a single hydrogel via sequential processing (vertical stripes are regions with immobilized RGDS, horizontal stripes contain REDV). Cells can only adhere to regions modified with peptides. Photo reprinted by permission from [88]



## 4.6 Laser Scanning Lithography

An intriguing approach for patterning thick hydrogels has involved the use of laser scanning lithography to modify a photosensitive agarose derivative [1]. A confined laser caused photochemical modification of the engineered hydrogel to reveal free sulfhydryl groups within the x,y patterned regions extending through the z-thickness of the material. The sulfhydryl groups were then reacted with derivatized RGD peptides to create columns of RGD peptide within the hydrogel. These patterned RGD-containing channels were able to confine the extension of primary rat dorsal root ganglia cells to the patterned regions of the scaffold. The main limitations of this technology are the requirement for patterning uniformly in the z direction and the low resolution ( $\sim 200 \mu\text{m}$ ) provided by use of a confined laser.

Higher resolution patterning of two-dimensional hydrogel structures can be achieved with focused laser beams, for example using a confocal microscope [93]. Confocal microscopes have been optimized over the past several decades for cell imaging. These microscopes illuminate the sample with a laser focused to a diffraction limited spot size that is then raster scanned across the sample surface. Computer control of the scanning lasers and the laser shutter enables two-dimensional hydrogel patterning without the need for a physical photomask. Although raster scanning is slower than wide-field illumination through a photomask, the tradeoff is increased precision of the patterned region, typically on the order of one micron [93]. Patterning of cell adhesive peptides on hydrogels using confocal laser scanning lithography is shown in Fig. 4.7.

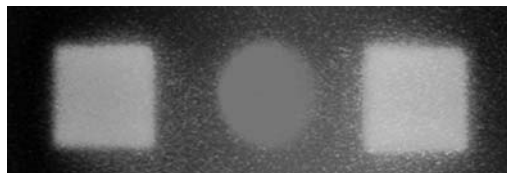


**Fig. 4.7** Confocal laser scanning lithography can be used for patterned immobilization of cell adhesion peptides on hydrogels with micron scale resolution. The cell-adhesive peptide RGDS was immobilized in squares, while the REDV peptide was immobilized in a circle. Photo reprinted by permission from [93]

## 4.7 Three-Dimensional Rapid Prototyping of Hydrogels

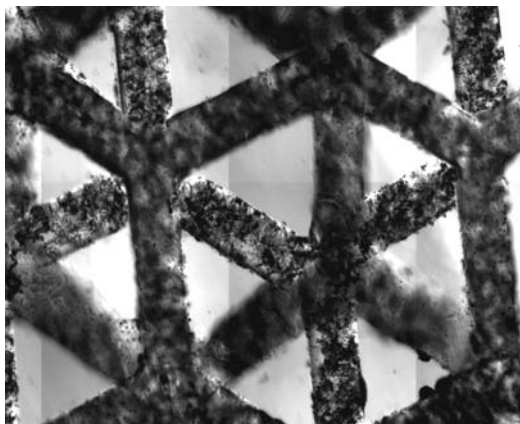
While two-dimensional patterning of hydrogels continues to be widely investigated and has proven useful for numerous and elegant *in vitro* studies, the most promising and versatile methods for constructing mimics of native tissue are those techniques which enable the creation of true three-dimensional constructs. Additionally, although PEG hydrogels exhibit excellent permeability to water, oxygen, and nutrients compared to many other biocompatible materials, the passive permeability of these hydrogels is typically in the range of hundreds of microns to a few millimeters [5, 28, 53, 54, 84, 94]. Therefore, hydrogels thicker than a few hundred microns should be made porous or—even better—made with active vascular networks to nourish entrapped or invading cells. Additionally, engineering complex tissue structures can require three dimensional control over the organization of multiple cell types, and this may be possible through controlled immobilization of cell adhesive and bioactive factors.

### 4.7.1 *Single Photon Excitation*

The simplest method to create three-dimensional constructs is iterative or layer-by-layer extension of the techniques discussed above for two-dimensional patterning (Fig. 4.8). Bhatia and co-workers utilized multiple applications of a photomask to polymerize overlapping PEG hydrogel microstructures [85]. In this study, up to three hydrogel layers were overlaid with a resolution of hundreds of microns. More recent extension of this work has resulted in much larger structures with improved resolution. Additionally, these structures were open and interconnected, which enabled cellular maintenance by convective flow of tissue culture media [53].

Laser-based layer-by-layer polymerization has typically involved custom-built laser-scanning systems with a programmable stage. Roy and co-workers have created extended microwell scaffolds hundreds of microns tall for the study of stem cell differentiation [92, 95]. Even more recently, Wicker and co-workers have used a similar process to create hydrogel structures tens of

**Fig. 4.8** An iterative photolithographic approach allowed layer-by-layer construction of a hydrogel with a defined pore architecture. Photo reprinted by permission from [53]



millimeters tall. Multi-lumen PEG hydrogel conduits and hydrogel constructs with extended channel architecture have also been demonstrated [96].

#### ***4.7.2 Multiphoton Excitation***

In the construction of a three-dimensional scaffold to support and guide tissue formation, one would ideally like a fast and easy method that can achieve subcellular resolution of patterned features. It is well known that cells sense and respond to their surroundings on the scale of one micron or less [75], so to gain excellent cellular control one would like to construct the cellular microenvironment with a resolution on the order of one micron. The methods mentioned above for three-dimensional polymerization suffer from resolution problems that will hamper the ability to precisely control this microenvironment. To achieve three-dimensional subcellular resolution in material constructs, photopolymerization directed by multiphoton lasers have recently proven extremely useful [38, 97–102].

A multiphoton laser system attached to a commercially available confocal microscope can be used for the rapid prototyping of hydrogels for tissue engineering applications. Multiphoton lasers operate according to quantum mechanical principles first theorized in the 1930s by Göppert-Mayer [103]. In the simplest case, two-photon excitation, two photons of a given wavelength can excite the electrons of a target molecule with effects equivalent to a single photon at half the wavelength. In a practical example, two photons of red light can induce fluorescence of a fluorophore which is typically excited only by green light. This so-called two-photon effect varies with the square of the laser intensity, or the number of photons passing through a unit area per unit time [102]. For the two-photon effect to occur, two photons need to be absorbed by the same molecule nearly simultaneously ( $\sim 10^{-16}$  s). It was found that an extremely high photon flux, from MW/cm<sup>2</sup> to GW/cm<sup>2</sup>, was needed to achieve

this multiphoton effect on a scale large enough to be observed. Light intensities in this range would obliterate biologic samples, so pulsed Ti:Sapphire lasers are employed. These lasers are able to achieve  $\text{MW}/\text{cm}^2$  to  $\text{GW}/\text{cm}^2$ , but bypass these huge energy requirements by generating this photon flux only over very short time scales ( $10^{-13}$  s) with average power output of only 1 W.

Many groups have leveraged the two-photon effect with confocal microscopes for high resolution fluorescence imaging and deeper tissue penetration, as first reported by Webb and coworkers [98]. Confocal microscopes focus a laser beam to a diffraction limited size, so the laser intensity at the focal point is exponentially higher than that outside the focal plane. By optimizing the power output of these pulsed lasers, the two-photon effect has been successfully confined to within the focal point [98, 104]. These same principles used for three-dimensional fluorescence excitation can also be applied to photopolymerization. To photopolymerize three-dimensional structures, the hydrogel precursors are polymerized only at the focal point of the two-photon laser. Computer control of the laser shutter, the focal point position, and the sample stage enable buildup of complex hydrogel structures, such as the porous structure shown in Fig. 4.9. The three-dimensional resolution inherent in two-photon lasers obviates the need for layer-by-layer substrate deposition making structure formation much more efficient and precise. A complementary method is to start with a bulk PEG hydrogel that has been incompletely polymerized. The hydrogel can be permeated with peptide-modified PEG-acrylate precursors, and the two-photon laser is raster-scanned inside the hydrogel in three-dimensions. Following polymerization, residual precursors are allowed to diffuse out of the hydrogel to reveal a heterogeneously distributed peptide. Initial work in this area has demonstrated the ability create complicated three-dimensional patterns of bioactivity within a largely unmodified PEG hydrogel [38].

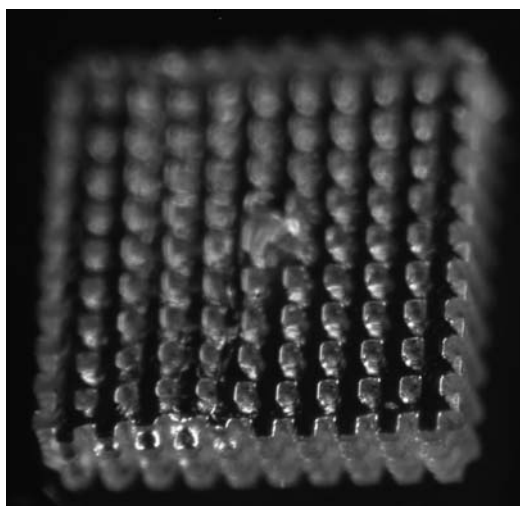


**Fig. 4.9** Two photon laser scanning lithography allows free form patterning in three dimensions. Complex pore structures can be generated using this technology

## 4.8 Summary

The high biocompatibility of hydrogels, their tunable biochemical and mechanical properties, and the myriad methods available for patterning their structure in both two and three dimensions make hydrogels an excellent family of materials for investigating fundamental mechanisms of cell biology and engineering the cellular microenvironment. Ultimately, the vascularization of hydrogels through three-dimensional rapid prototyping and three-dimensional biochemical patterning at subcellular resolution will enable the investigation of small tissue mimics and continue progress toward true synthetic tissues and organs for human transplantation.

## References

1. Luo Y, Shoichet MS. A photolabile hydrogel for guided three-dimensional cell growth and migration. *Nat Mater* 2004;3(4):249–53.
2. Augst AD, Kong HJ, Mooney DJ. Alginate hydrogels as biomaterials. *Macromol Biosci* 2006;6(8):623–33.
3. Drury JL, Boontheekul T, Boontheeku T, Mooney DJ. Cellular cross-linking of peptide modified hydrogels. *J Biomech Eng* 2005;127(2):220–28.
4. Matsuda T, Moghaddam MJ, Miwa H, Sakurai K, Iida F. Photoinduced prevention of tissue adhesion. *ASAIO J* 1992;38(3):M154–7.
5. Bryant SJ, Anseth KS. The effects of scaffold thickness on tissue engineered cartilage in photocrosslinked poly(ethylene oxide) hydrogels. *Biomaterials* 2001;22(6):619–26.
6. Ishihara M, Obara K, Nakamura S, Fujita M, Masuoka K, et al. Chitosan hydrogel as a drug delivery carrier to control angiogenesis. *J Artif Organs* 2006;9(1):8–16.
7. Willcox MD, Harmis N, Cowell, Williams T, Holden. Bacterial interactions with contact lenses; effects of lens material, lens wear and microbial physiology. *Biomaterials* 2001;22(24):3235–47.
8. Flynn L, Dalton PD, Shoichet MS. Fiber templating of poly(2-hydroxyethyl methacrylate) for neural tissue engineering. *Biomaterials* 2003;24(23):4265–72.
9. Ratner BD, Hoffman AS, Whiffen JD. The thrombogenicity of radiation grafted polymers as measured by the vena cava ring test. *J Bioeng* 1978;2(3–4):313–23.
10. Cadée JA, de Groot CJ, Jiskoot W, den Otter W, Hennink WE. Release of recombinant human interleukin-2 from dextran-based hydrogels. *J Control Release* 2002;78(1–3):1–13.
11. Schmedlen RH, Masters KS, West JL. Photocrosslinkable poly(vinyl alcohol) hydrogels that can be modified with cell adhesion peptides for use in tissue engineering. *Biomaterials* 2002;23(22):4325–32.
12. Hynd MR, Frampton JP, Dowell-Mesfin N, Turner JN, Shain W. Directed cell growth on protein-functionalized hydrogel surfaces. *J Neurosci Methods* 2007;162(1–2):255–63.
13. Saraydin D, Karadağ E, Oztop HN, Güven O. Adsorption of bovine serum albumin onto acrylamide-maleic acid hydrogels. *Biomaterials* 1994;15(11):917–20.
14. Nicodemus GD, Villanueva I, Bryant SJ. Mechanical stimulation of TMJ condylar chondrocytes encapsulated in PEG hydrogels. *J Biomed Mater Res A* 2007;
15. Hill-West JL, Chowdhury SM, Sawhney AS, Pathak CP, Dunn RC, Hubbell JA. Prevention of postoperative adhesions in the rat by in situ photopolymerization of bioresorbable hydrogel barriers. *Obstet Gynecol* 1994;83(1):59–64.

16. Sawhney AS, Pathak CP, van Rensburg JJ, Dunn RC, Hubbell JA. Optimization of photopolymerized bioerodible hydrogel properties for adhesion prevention. *J Biomed Mater Res* 1994;28(7):831–38.
17. Hartgerink JD, Beniash E, Stupp SI. Peptide-amphiphile nanofibers: a versatile scaffold for the preparation of self-assembling materials. *Proc Natl Acad Sci U S A* 2002;99(8):5133–38.
18. Hartgerink JD, Beniash E, Stupp SI. Self-assembly and mineralization of peptide-amphiphile nanofibers. *Science* 2001;294(5547):1684–88.
19. Goda T, Ishihara K. Soft contact lens biomaterials from bioinspired phospholipid polymers. *Expert Rev Med Devices* 2006;3(2):167–74.
20. Harris LG, Patterson LM, Bacon C, Gwynn I, Richards RG. Assessment of the cytocompatibility of different coated titanium surfaces to fibroblasts and osteoblasts. *J Biomed Mater Res A* 2005;73(1):12–20.
21. Prokop A, Kozlov E, Nun Non S, Dikov MM, Sephel GC, et al. Towards retrievable vascularized bioartificial pancreas: induction and long-lasting stability of polymeric mesh implant vascularized with the help of acidic and basic fibroblast growth factors and hydrogel coating. *Diabetes Technol Ther* 2001;3(2):245–61.
22. Spargo BJ, Rudolph AS, Rollwagen FM. Recruitment of tissue resident cells to hydrogel composites: in vivo response to implant materials. *Biomaterials* 1994;15(10):853–58.
23. Eaglstein WH. Experiences with biosynthetic dressings. *J Am Acad Dermatol* 1985;12(2 Pt 2):434–40.
24. Leaper DJ, Brennan SS, Simpson RA, Foster ME. Experimental infection and hydrogel dressings. *J Hosp Infect* 1984;5 Suppl A:69–73.
25. Geronemus RG, Robins P. The effect of two new dressings on epidermal wound healing. *J Dermatol Surg Oncol* 1982;8(10):850–52.
26. West JL, Chowdhury SM, Sawhney AS, Pathak CP, Dunn RC, Hubbell JA. Efficacy of adhesion barriers. Resorbable hydrogel, oxidized regenerated cellulose and hyaluronic acid. *J Reprod Med* 1996;41(3):149–54.
27. Pathak CP, Sawhney AS, Hubbell JA. Rapid photopolymerization of immunoprotective gels in contact with cells and tissue. *J Am Chem Soc* 1992;114:8311–2.
28. Koh WG, Itle LJ, Pishko MV. Molding of hydrogel microstructures to create multiphenotype cell microarrays. *Anal Chem* 2003;75(21):5783–89.
29. Sheppard NFJr, Lesho MJ, McNally P, Francomacaro AS. Microfabricated conductimetric pH sensor *Sensors and Actuators B: Chemical* 1995;28(2):95–102.
30. Russell RJ, Pishko MV, Gefrides CC, McShane MJ, Coté GL. A fluorescence-based glucose biosensor using concanavalin A and dextran encapsulated in a poly(ethylene glycol) hydrogel. *Anal Chem* 1999;71(15):3126–32.
31. Sudhölter EJR, van der Wal PD, Skowronska-Ptasinska M, van den Berg A, Bergveld P, Reinhoudt DN. Modification of ISFETs by covalent anchoring of poly(hydroxyethyl methacrylate) hydrogel. Introduction of a thermodynamically defined semiconductor-sensing membrane interface *Analytica Chimica Acta* 1990;230:59–65.
32. Kim DH, Kim P, Song I, Cha JM, Lee SH, et al. Guided three-dimensional growth of functional cardiomyocytes on polyethylene glycol nanostructures. *Langmuir* 2006;22(12):5419–26.
33. Sershen SR, Mensing GA, Ng M, Halas NJ, Beebe DJ, West JL. Independent optical control of microfluidic valves formed from optomechanically responsive nanocomposite hydrogels. *Advanced Materials* 2005;17(11):1366–68.
34. Eddington DT, Beebe DJ. Flow control with hydrogels. *Adv Drug Deliv Rev* 2004;56(2):199–210.
35. Peppas NA, Bures P, Leobandung W, Ichikawa H. Hydrogels in pharmaceutical formulations. *Eur J Pharm Biopharm* 2000;50(1):27–46.
36. Peppas NA, Wood KM, Blanchette JO. Hydrogels for oral delivery of therapeutic proteins. *Expert Opin Biol Ther* 2004;4(6):881–87.

37. Serra L, Doménech J, Peppas NA. Drug transport mechanisms and release kinetics from molecularly designed poly(acrylic acid-g-ethylene glycol) hydrogels. *Biomaterials* 2006;27(31):5440–51.
38. Hahn MS, Miller JS, West JL. Three-dimensional biochemical and biomechanical patterning of hydrogels for guiding cell behavior. *Adv Mater* 2006;18(20):2679–84.
39. Lutolf MP, Lauer-Fields JL, Schmoekel HG, Metters AT, Weber FE, et al. Synthetic matrix metalloproteinase-sensitive hydrogels for the conduction of tissue regeneration: engineering cell-invasion characteristics. *Proc Natl Acad Sci U S A* 2003;100(9):5413–18.
40. Gombotz WR, Wang GH, Horbett TA, Hoffman AS. Protein adsorption to poly(ethylene oxide) surfaces. *J Biomed Mater Res* 1991;25(12):1547–62.
41. Sakarya A, Ilkgül O, Aydede H, Erhan Y, İçöz G, et al. Effect of polyethylene glycol 4000 on adhesion formation following thyroid surgery in rats. *Indian J Med Res* 2002;115:255–59.
42. Consigny PM, Barry JJ, Vitali NJ. Local delivery of an antiproliferative drug with use of hydrogel-coated angioplasty balloons. *J Vasc Interv Radiol* 1994;5(4):553–60.
43. Park S, Bearinger JP, Lautenschlager EP, Castner DG, Healy KE. Surface modification of poly(ethylene terephthalate) angioplasty balloons with a hydrophilic poly(acrylamide-co-ethylene glycol) interpenetrating polymer network coating. *J Biomed Mater Res* 2000;53(5):568–76.
44. Torchiana DF. Polyethylene glycol based synthetic sealants: potential uses in cardiac surgery. *J Card Surg* 2003;18(6):504–6.
45. Hu BH, Messersmith PB. Enzymatically cross-linked hydrogels and their adhesive strength to biosurfaces. *Orthod Craniofac Res* 2005;8(3):145–49.
46. Elisseeff J, McIntosh W, Anseth K, Riley S, Ragan P, Langer R. Photoencapsulation of chondrocytes in poly(ethylene oxide)-based semi-interpenetrating networks. *J Biomed Mater Res* 2000;51(2):164–71.
47. Bryant SJ, Nuttelman CR, Anseth KS. Cytocompatibility of UV and visible light photo-initiating systems on cultured NIH/3T3 fibroblasts in vitro. *J Biomater Sci Polym Ed* 2000;11(5):439–57.
48. Bikram M, Fouletier-Dilling C, Hipp JA, Gannon F, Davis AR, et al. Endochondral Bone Formation from Hydrogel Carriers Loaded with BMP2-transduced Cells. *Ann Biomed Eng* 2007;35(5):796–07.
49. Gobin AS, West JL. Cell migration through defined, synthetic ECM analogs. *FASEB J* 2002;16(7):751–53.
50. Mann BK, West JL. Cell adhesion peptides alter smooth muscle cell adhesion, proliferation, migration, and matrix protein synthesis on modified surfaces and in polymer scaffolds. *J Biomed Mater Res* 2002;60(1):86–93.
51. Lutolf MP, Hubbell JA. Synthetic biomaterials as instructive extracellular microenvironments for morphogenesis in tissue engineering. *Nat Biotechnol* 2005;23(1):47–55.
52. Itle LJ, Koh WG, Pishko MV. Hepatocyte Viability and Protein Expression within Hydrogel Microstructures. *Biotechnol Prog* 2005;21(3):926–32.
53. Tsang VL, Chen AA, Cho LM, Jadin KD, Sah RL, et al. Fabrication of 3D hepatic tissues by additive photopatterning of cellular hydrogels. *FASEB J* 2006;21(3):790–801.
54. Bryant SJ, Bender RJ, Durand KL, Anseth KS. Encapsulating chondrocytes in degrading PEG hydrogels with high modulus: engineering gel structural changes to facilitate cartilaginous tissue production. *Biotechnol Bioeng* 2004;86(7):747–55.
55. Cooper JA, Li WJ, Bailey LO, Hudson SD, Lin-Gibson S, et al. Encapsulated chondrocyte response in a pulsatile flow bioreactor. *Acta Biomater* 2007;3(1):13–21.
56. Mann BK, Gobin AS, Tsai AT, Schmedlen RH, West JL. Smooth muscle cell growth in photopolymerized hydrogels with cell adhesive and proteolytically degradable domains: synthetic ECM analogs for tissue engineering. *Biomaterials* 2001;22(22):3045–51.



57. Peyton SR, Raub CB, Keschrums VP, Putnam AJ. The use of poly(ethylene glycol) hydrogels to investigate the impact of ECM chemistry and mechanics on smooth muscle cells. *Biomaterials* 2006;27(28):4881–93.
58. Elisseeff J, Puleo C, Yang F, Sharma B. Advances in skeletal tissue engineering with hydrogels. *Orthod Craniofac Res* 2005;8(3):150–61.
59. Sharma B, Williams CG, Khan M, Manson P, Elisseeff JH. In vivo chondrogenesis of mesenchymal stem cells in a photopolymerized hydrogel. *Plast Reconstr Surg* 2007;119(1):112–20.
60. Yang F, Williams CG, Wang DA, Lee H, Manson PN, Elisseeff J. The effect of incorporating RGD adhesive peptide in polyethylene glycol diacrylate hydrogel on osteogenesis of bone marrow stromal cells. *Biomaterials* 2005;26(30):5991–98.
61. Patel PN, Gobin AS, West JL, Patrick CW. Poly(ethylene glycol) hydrogel system supports preadipocyte viability, adhesion, and proliferation. *Tissue Eng* 2005;11(9–10):1498–505.
62. Mahoney MJ, Anseth KS. Three-dimensional growth and function of neural tissue in degradable polyethylene glycol hydrogels. *Biomaterials* 2006;27(10):2265–74.
63. Lai YC, Quinn ET. The effects of initiator and diluent on the photopolymerization of 2-hydroxyethyl methacrylate and on properties of hydrogels obtained. In: Scranton AB, Bowman CN, Peiffer RW, editors. *Photopolymerization: fundamentals and applications* Washington, DC: American Chemical Society, 1997; pp. 35, 50.
64. Gobin AS, West JL. Val-ala-pro-gly, an elastin-derived non-integrin ligand: smooth muscle cell adhesion and specificity. *J Biomed Mater Res A* 2003;67(1):255–9.
65. Mann BK, Schmedlen RH, West JL. Tethered-TGF-beta increases extracellular matrix production of vascular smooth muscle cells. *Biomaterials* 2001;22(5):439–44.
66. Sawhney AS, Pathak CP, Hubbell JA. Interfacial photopolymerization of poly(ethylene glycol)-based hydrogels upon alginate-poly(l-lysine) microcapsules for enhanced biocompatibility. *Biomaterials* 1993;14(13):1008–16.
67. Cruise GM, Hegre OD, Scharp DS, Hubbell JA. A sensitivity study of the key parameters in the interfacial photopolymerization of poly(ethylene glycol) diacrylate upon porcine islets. *Biotechnol Bioeng* 1998;57(6):655–65.
68. An Y, Hubbell JA. Intraarterial protein delivery via intimately-adherent bilayer hydrogels. *J Control Release* 2000;64(1–3):205–15.
69. Kizilel S, Pérez-Luna VH, Teymour F. Photopolymerization of poly(ethylene glycol) diacrylate on eosin-functionalized surfaces. *Langmuir* 2004;20(20):8652–58.
70. Kizilel S, Sawardecker E, Teymour F, Pérez-Luna VH. Sequential formation of covalently bonded hydrogel multilayers through surface initiated photopolymerization. *Biomaterials* 2006;27(8):1209–15.
71. Horbett TA. Protein adsorption on biomaterials. *Adv Chem Ser* 1982;199:233–44.
72. Pierschbacher MD, Ruoslahti E. Cell attachment activity of fibronectin can be duplicated by small synthetic fragments of the molecule. *Nature* 1984;309(5963):30–3.
73. Ruoslahti E, Pierschbacher MD. Arg-Gly-Asp: a versatile cell recognition signal. *Cell* 1986;44(4):517–8.
74. Hubbell JA, Massia SP, Desai NP, Drumheller PD. Endothelial cell-selective materials for tissue engineering in the vascular graft via a new receptor. *Biotechnology (NY)* 1991;9(6):568–72.
75. Massia SP, Hubbell JA. An RGD spacing of 440 nm is sufficient for integrin alpha V beta 3-mediated fibroblast spreading and 140 nm for focal contact and stress fiber formation. *J Cell Biol* 1991;114(5):1089–100.
76. Tashiro K, Sephel GC, Weeks B, Sasaki M, Martin GR, et al. A synthetic peptide containing the IKVAV sequence from the A chain of laminin mediates cell attachment, migration, and neurite outgrowth. *J Biol Chem* 1989;264(27):16174–82.
77. DeLong SA, Moon JJ, West JL. Covalently immobilized gradients of bFGF on hydrogel scaffolds for directed cell migration. *Biomaterials* 2005;26(16):3227–34.

78. Lee J, Shanbhag S, Kotov NA. Inverted colloidal crystals as three-dimensional micro-environments for cellular co-cultures *J MATER CHEM* 2006;16(35):3558–64.
79. Liu Y, Wang S, Krouse J, Kotov NA, Eghtedari M, et al. Rapid aqueous photopolymerization route to polymer and polymer-composite hydrogel 3D inverted colloidal crystal scaffolds. *J Biomed Mater Res A* 2007;
80. Marshall AJ, Ratner BD. Quantitative characterization of sphere-templated porous biomaterials *AIChE J* 2005;51(4):1221–32.
81. Stachowiak AN, Bershteyn A, Tzatzalos E, Irvine DJ. Bioactive hydrogels with an ordered cellular structure combine interconnected macroporosity and robust mechanical properties *ADV MATER* 2005;17(4):399–+.
82. Ma PX, Choi JW. Biodegradable polymer scaffolds with well-defined interconnected spherical pore network. *Tissue Eng* 2001;7(1):23–33.
83. Revzin A, Russell RJ, Yadavalli VK, Koh WG, Deister C, et al. Fabrication of poly(ethylene glycol) hydrogel microstructures using photolithography. *Langmuir* 2001;17(18):5440–47.
84. Koh WG, Revzin A, Pishko MV. Poly(ethylene glycol) hydrogel microstructures encapsulating living cells. *Langmuir* 2002;18(7):2459–62.
85. Liu VA, Bhatia SN. Three-dimensional photopatterning of hydrogels containing living cells. *Biomedical Microdevices* 2002;4(4):257–66.
86. Chin VI, Taupin P, Sanga S, Scheel J, Gage FH, Bhatia SN. Microfabricated platform for studying stem cell fates. *Biotechnol Bioeng* 2004;88(3):399–415.
87. Yu T, Ober CK. Methods for the topographical patterning and patterned surface modification of hydrogels based on hydroxyethyl methacrylate. *Biomacromolecules* 2003;4(5):1126–31.
88. Hahn MS, Taite LJ, Moon JJ, Rowland MC, Ruffino KA, West JL. Photolithographic patterning of polyethylene glycol hydrogels. *Biomaterials* 2005;27(12):2519–24.
89. Itoga K, Yamato M, Kobayashi J, Kikuchi A, Okano T. Cell micropatterning using photopolymerization with a liquid crystal device commercial projector. *Biomaterials* 2004;25(11):2047–53.
90. Itoga K, Yamato M, Kobayashi J, Kikuchi A, Okano T. Micropatterned surfaces prepared using a liquid crystal projector-modified photopolymerization device and microfluidics. *J Biomed Mater Res A* 2004;69(3):391–97.
91. Itoga K, Kobayashi J, Yamato M, Kikuchi A, Okano T. Maskless liquid-crystal-display projection photolithography for improved design flexibility of cellular micropatterns. *Biomaterials* 2006;27(15):3005–9.
92. Lu Y, Mapili G, Suhali G, Chen S, Roy K. A digital micro-mirror device-based system for the microfabrication of complex, spatially patterned tissue engineering scaffolds. *J Biomed Mater Res A* 2006;77(2):396–05.
93. Hahn MS, Miller JS, West JL. Laser scanning lithography for surface micropatterning on hydrogels. *Advanced Materials* 2005;17(24):2939–42.
94. Nuttelman CR, Tripodi MC, Anseth KS. Synthetic hydrogel niches that promote hMSC viability. *Matrix Biol* 2005;24(3):208–18.
95. Mapili G, Lu Y, Chen S, Roy K. Laser-layered microfabrication of spatially patterned functionalized tissue-engineering scaffolds. *J Biomed Mater Res B Appl Biomater* 2005;75(2):414–24.
96. Arcaute K, Mann BK, Wicker RB. Stereolithography of three-dimensional bioactive poly(ethylene glycol) constructs with encapsulated cells. *Ann Biomed Eng* 2006;34(9):1429–41.
97. Cumpston BH, Ananthavel SP, Barlow S, Dyer DL, Ehrlich JE, et al. Two-photon polymerization initiators for three-dimensional optical data storage and microfabrication. *Nature* 1999;398:51–4.
98. Denk W, Strickler JH, Webb WW. Two-photon laser scanning fluorescence microscopy. *Science* 1990;248(4951):73–6.

99. Helmchen F, Denk W. New developments in multiphoton microscopy. *Curr Opin Neurobiol* 2002;12(5):593–601.
100. Helmchen F, Denk W. Deep tissue two-photon microscopy. *Nat Methods* 2005;2(12):932–40.
101. Olson CE, Previte MJ, Fourkas JT. Efficient and robust multiphoton data storage in molecular glasses and highly crosslinked polymers. *Nat Mater* 2002;1(4):225–28.
102. Zipfel WR, Williams RM, Webb WW. Nonlinear magic: multiphoton microscopy in the biosciences. *Nat Biotechnol* 2003;21(11):1369–77.
103. Göppert-Mayer M. Über elementarakte mit zwei quantensprüngen. *Annalen der Physik* 1931;401(3):273–94.
104. Xu C, Zipfel W, Shear JB, Williams RM, Webb WW. Multiphoton fluorescence excitation: new spectral windows for biological nonlinear microscopy. *Proc Natl Acad Sci U S A* 1996;93(20):10763–68.

# Chapter 5

## Engineered Scaffold Architecture Influences Soft Tissue Regeneration

Darice Y. Wong, Elly E. Liao, J. C. Leveque, Hunter Brumblay, Chia-Ying Lin, Frank LaMarca, Paul H. Krebsbach and Scott J. Hollister

### 5.1 Introduction

Tissue engineering scaffolds must define shape for anatomic tissue regeneration, provide temporary mechanical support, and enhance tissue regeneration through delivery of biologics and a suitable mass transport environment. Scaffold material and 3D porous architecture design will determine how well the scaffold can fulfill these requirements. Optimizing scaffold design will require experiments that specifically test how variations in scaffold material and architecture affect mechanical properties, mass transport properties and tissue regeneration. These issues have been studied intensively for bone formation during the past decade (see for example, Karageorgiou et al., 2005; Otsuki et al., 2006; Li et al., 2007). These studies have concluded that well connected pore structures favor bone regeneration independent of pore size. However, this conclusion could only be confirmed with the capability to design and fabricate scaffolds with reproducible and rigorously controlled pore architectures.

By comparison, there is much less research regarding how scaffold material and architecture design affect soft tissue regeneration. Soft tissue regeneration represents a much larger array of tissue engineering applications including cartilage, fibrocartilaginous tissues, cardiovascular tissues, neural tissues, ligaments, tendons, and skeletal muscle. Whereas for bone, one may define “osteconductive” materials (LeGeros, 2002) that favor bone regeneration, it does not appear that comparable “chondroconductive” or “neuroconductive” definitions exist. Furthermore, while one could argue that the necessity for high pore connectivity for bone regeneration is intuitive based on bone being a highly metabolically active tissue, soft tissues have a wide array of metabolic activity ranging from cartilage (low) to CNS (medium) to skeletal muscle (high).

---

Scott J. Hollister

Scaffold Tissue Engineering Group, Department of Biomedical Engineering; Spine Research Laboratory, Departments of Neurosurgery and Biomedical Engineering; Departments of Surgery and Mechanical Engineering, The University of Michigan, Ann Arbor, MI, USA  
scottho@umich.edu

**Table 5.1** Tangent moduli of selected soft tissues at 1% and 10% strain fit to model  $S = A(e^{B\varepsilon}-1)$ . Tangent moduli range over 4 orders of magnitude

Tissue	Tangent modulus at 1% strain (MPa) = $ABe^{B\varepsilon}$	Tangent modulus at 10% strain (MPa) = $ABe^{B\varepsilon}$	Reference for data fit
Articular Cartilage	0.4–11.0	0.444–17.3	Mow, Ratcliffe (1997)
Intervertebral Disc – Fibrocartilage	0.26–0.94	0.41–2.74	Klisch, Lotz (1999)
Spinal Cord	0.76	5.1	Fiford, Bilston (2005)
Skin/ Subcutaneous Tissue	0.0015	0.011	Wu et al. (2007)
Heart Valve	0.06	0.78	Weinberg (2006)

This metabolic activity could be related to tissue permeability, which also ranges from cartilage having a low value at  $2.5e^{-15} \text{ m}^4/\text{Ns}$  (Demartean et al., 2006) to brain tissue at  $7e^{-13} \text{ m}^4/\text{Ns}$  (Linninger et al., 2007) to bone having a high value at  $1e^{-7} \text{ m}^4/\text{Ns}$  (Kohles et al., 2001).

Additionally, soft tissue mechanical properties are extremely varied, with complex nonlinear elastic and viscoelastic behavior. A widely used 1D nonlinear elastic model for soft tissues is  $S = A(e^{B\varepsilon}-1)$ , where  $A, B$  are fit coefficients,  $\varepsilon$  is the large strain tensor and  $S$  is the 1st Piola-Kirchoff stress. The tangent modulus for this model is  $E = AB\varepsilon e^{B\varepsilon}$ . Fitting soft tissue experimental data to this model shows the broad range of soft tissue mechanical properties (Table 5.1).

Given the large tissue engineering literature in soft tissue regeneration, we will focus on cartilage and central nervous system (CNS) tissue applications in this chapter. Specifically, this chapter will present results on designed scaffolds with controlled mass transport and mechanical properties, and how these controlled scaffold architectures influence cartilage and CNS tissue regeneration.

## 5.2 Scaffold Architecture Effects on Cartilage Regeneration

Articular cartilage is an avascular, fluid-solid composite with very low permeability that has little regenerative capacity. The common hypothesis concerning scaffold design is that the scaffold should match native tissue mechanical properties (Hutmacher, 2001; Raghunath et al., 2007) and also mass transport properties.

However, there is controversy over how closely scaffolds should match cartilage mass transport properties, given conflicting data on how oxygen

diffusion and tension affect cartilage regeneration (Malda et al., 2003). For example, developing cartilage has partial oxygen pressures ( $pO_2$ ) as low as 3.2%, and cells from embryonic chick tibia developed into bone under high  $pO_2$  (35%), but developed cartilage under low  $pO_2$  (5%; Malda et al., 2003). On the other hand, cartilage tissue engineering studies have suggested that scaffolds with higher mass transport properties achieved greater cartilage matrix regeneration. Malda et al. compared sponge architectures ( $\sim 125 \mu\text{m}$  pores) with designed 3D Printed architectures (525  $\mu\text{m}$  pores) for cartilage regeneration on poly(ethylene glycol)-terephthalate/poly(butylene terephthalate) (PEGT/PBT). They found significantly more cartilage matrix on the designed architectures, citing their increased pore connectivity and lower tortuosity. Yamane et al. examined pore size effects (100–400  $\mu\text{m}$ ) on cartilage regeneration, finding more cartilage matrix in 400  $\mu\text{m}$  pores.

Although the general hypothesis that scaffolds should match mechanical and mass transport properties has been proposed for nearly 10 years, it has not been systematically tested due to the inability, until recently, to design and fabricate scaffolds with controlled mechanical and mass transport properties. Thus, a first step toward rigorously testing the general scaffold hypothesis is creating scaffolds that have controlled mechanical and mass transport properties. Following this, such scaffolds must be tested in animal models to determine how effective mechanical and mass transport properties, in addition to other scaffold architecture design variables, relate to cartilage regeneration.

Our research group has investigated the use of designed scaffolds made from polypropylene fumarate (PPF), polycaprolactone (PCL), poly(1,8) octane diol citrate (POC), and poly(glycerol-sebacate) (PGS). These biodegradable polymers can be formed into complex 3D porous architectures and offer mechanical properties. By combining image-based design techniques (Hollister et al., 2000, 2002; Hollister, 2005) with polymer fabrication techniques, it is possible to construct scaffolds with controlled mechanical and mass transport properties to test in cartilage regeneration models.

Our scaffold model for cartilage regeneration is to utilize the designed porous polymer to define mechanical and mass transport properties and a pliable hydrogel to serve as a cell carrier. Using this approach, Liao et al. (2006, 2007a, b) tested the effect of hydrogel cell carrier and designed pore shape on cartilage regeneration. In the first study, primary chondrocytes were loaded in collagen I gel and collagen I gel mixed with 1%, 2%, 5%, and 10% Hyaluronic Acid (HyA). The collagen I/5% HyA composite hydrogel cell carrier showed the greatest enhancement of cartilage matrix production (Fig. 5.1).

A second study by Liao et al. (2006) examined the effect of cubic versus ellipsoidal pore shape when delivering chondrocytes or bone marrow stromal cells pulsed in chondrogenic media (DMEM, 10% fetal bovine serum (FBS), 1% penicillin/streptomycin (P/S), 10 ng/mL TGF $\beta_1$ , 0.1 nM dexamethasone, 50  $\mu\text{g/mL}$  2-phospho-L-ascorbic acid, 0.4 mM proline, 5  $\mu\text{g mL}^{-1}$  insulin and 0.1 mM non-essential amino acids) for two weeks. The cubic pore architecture

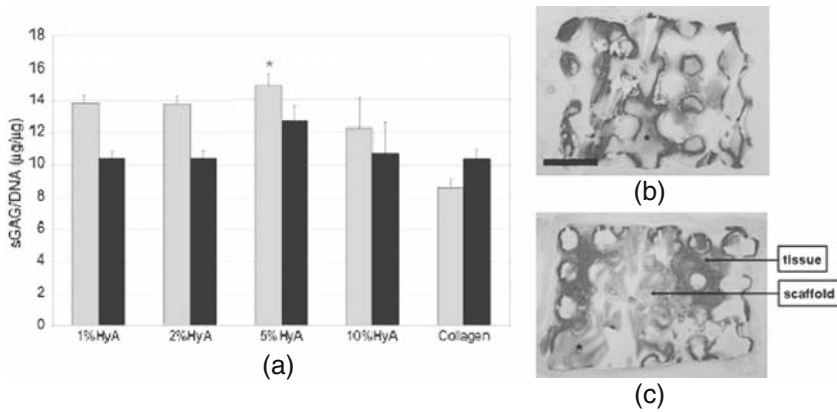


**Fig. 5.1** Effect of collagen I hydrogel with varying hyaluronic acid concentrations on sulfated glycosaminoglycan (sGAG) production. (a) Comparison of collagen I gel alone with collagen I gel having 1%, 2%, 5%, and 10% HyA concentrations demonstrated that 5% HyA concentration was optimal for cartilage matrix formation. (b) Example of cartilage matrix formation in designed PPF scaffold using collagen I hydrogel. (c) Example of cartilage formed in designed PPF scaffold using collagen I/5% HyA composite hydrogel

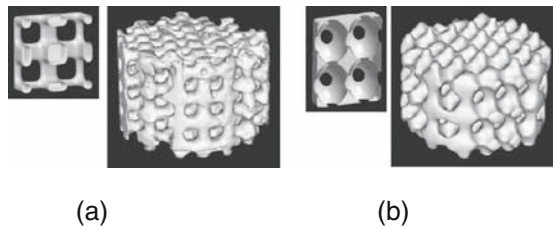


**Fig. 5.2** Designed cubic and ellipsoidal pore scaffolds (a) Section of cubic pore architecture design (left) and micro-CT scan of fabricated scaffold (right). (b) Section of ellipsoidal pore architecture design (left) and micro-CT scan of fabricated scaffold (right)

scaffolds (Fig. 5.2a) were 50% porous with a computed permeability of  $2.16 \times 10^{-7} \text{ m}^4/\text{Ns}$  and a computed normalized diffusivity of 0.44. The ellipsoidal pore scaffolds (Fig. 5.2b) were 52% porous with a computed permeability of  $0.36 \times 10^{-7} \text{ m}^4/\text{Ns}$  and a computed normalized diffusivity of 0.25.

The ellipsoidal pores demonstrated significantly more cartilage matrix regeneration with both bone marrow stromal cells and chondrocytes (Fig. 5.3).

The increased cartilage matrix production by cells in the ellipsoidal pore architecture (Fig. 5.4) was attributed to increased cell condensation demonstrated by rhodamine-conjugated peanut agglutinin (PNA) staining.

These results demonstrate that both cell carrier and scaffold architecture have a significant effect on cartilage tissue regeneration. The increase in cartilage matrix synthesis could be attributed to increased cell aggregation. However, whether this increased aggregation is due to decreased mass transport in

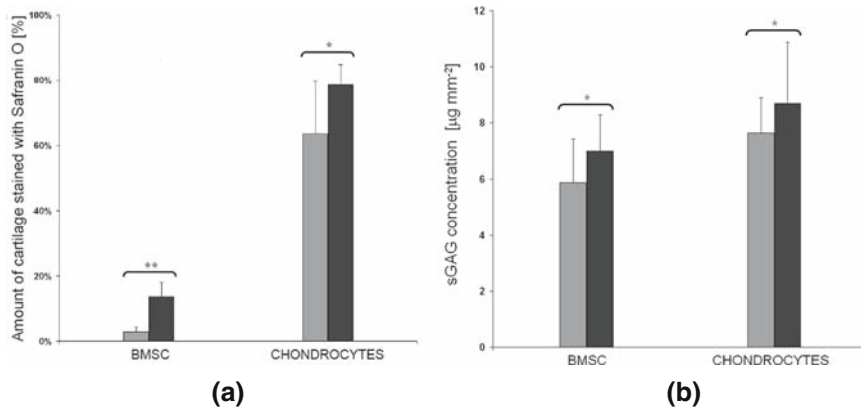
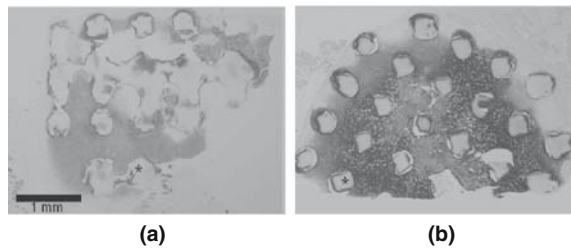


**Fig. 5.3** Effect of cubic versus ellipsoidal pore shape on cartilage matrix synthesis. Ellipsoidal pore scaffolds (dark gray bars) exhibited larger areas of cartilage formation (a) and greater sulfated glycosaminoglycan staining (b) when both bone marrow stromal cells (BMSC) and chondrocytes were delivered. Double asterisks denote  $p < 0.001$  and single asterisk denotes  $p < 0.05$

**Fig. 5.4** Demonstration of cartilage matrix formation in cubic and ellipsoidal pore scaffolds by Safranin O staining. (a) Saf O staining of cartilage matrix in cubic pores. (b) Saf O staining of cartilage matrix in ellipsoidal pore scaffold



terms of permeability or diffusion, or the pore shape itself, cannot be determined solely from these results. Scaffolds in which cubic pore structures have lower diffusivity are compared to ellipsoidal pores with higher diffusivity must be used to test this question. Such tests are possible, however, with the image-based scaffold engineering approach.

### 5.3 Scaffold Architecture Effects on CNS Regeneration

A number of previous studies have suggested that scaffold architecture can influence neural regeneration in the CNS. Most prominently, it has long been recognized that guidance tubes can bridge nerve defects (Nomura et al., 2006). Moore et al. (2006) found that PLGA scaffolds with oriented channels 220  $\mu\text{m}$  in diameter supported axon regeneration in spinal cord defects. Tsai et al. (2004) found that poly(2-hydroxyethyl methacrylate-co methyl methacrylate) (PHEMA-MMA) scaffolds with channels also supported axon regeneration.



However, in the Tsai study, the PHEMA-MMA hydrogel scaffolds with a stiffness of 0.3 MPa collapsed which may have compromised axonal regeneration. Nomura et al. (2006) then reinforced the PHEMA-MMA with coils to improve mechanical stiffness. The reinforced scaffolds did not collapse and also achieved axonal regeneration. However, a significant number of syringomyelia (fluid-filled cavities within the spinal cord tissue) occurred outside the scaffolds. Nomura et al. attributed the presence of syringomyelia to the scaffold blocking the flow of cerebrospinal fluid (CSF) in the subarachnoid space, causing the CSF to be forced through the spinal cord itself. This conclusion agrees with a theory of syringomyelia proposed by Gretz (2006). These studies suggest that scaffold architecture may influence CNS regeneration both through mass transport characteristics that influence CSF flow in addition to cell migration, and mechanical properties where a minimum stiffness is needed to avoid collapse that will inhibit axonal growth.

Wong et al. (2007a, b) studied the effect of scaffold architecture on CNS tissue regeneration in both brain and spinal cord defect models in rats. For brain defects, Wong et al. (2007a) fabricated polycaprolactone (PCL) scaffolds with three different architectures: 1) a porogen leached sponge (**cylinder design**),

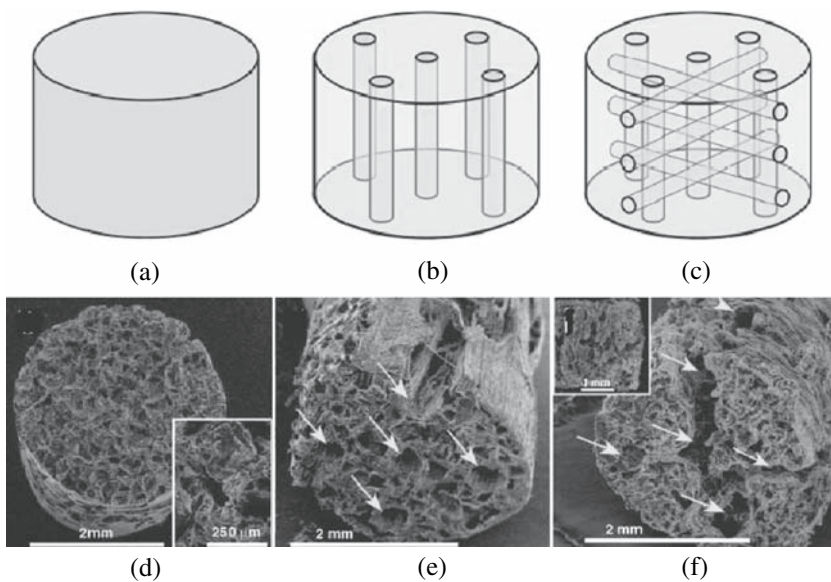


**Fig. 5.5** Designed and fabricated scaffold PCL architectures implanted in brain defects. (a) porogen leached sponge with no designed channels. (b) porogen leached cylindrical sponge with five longitudinal macroscopic channels. (c) porogen leached cylindrical sponge with five longitudinal macroscopic channels and three sets of two transverse macroscopic channels. (d) fabricated PCL porogen leached sponge. (e) fabricated scaffold showing macroscopic channels in addition to longitudinal microscopic grooves. (f) fabricated scaffold with longitudinal and transverse macroscopic channels and transverse circumferential microscopic grooves

2) five longitudinal channels running through a porogen leached sponge (**channel design**) and 3) five longitudinal channels with two connecting transverse channels (**orthogonal design**) at different levels (Fig. 5.5). The longitudinal channels in both the channel and orthogonal design were  $421 \pm 27 \mu\text{m}$  in diameter while the transverse channels in the orthogonal design were  $280 \pm 37 \mu\text{m}$  in diameter. In addition, microgrooves were created in the fabricated scaffold as an artifact from the layered wax manufacturing system. The orientation of the 30–40  $\mu\text{m}$  wide microscopic grooves can be controlled through orientation of the design on the fabrication system build platform.

Animals were sacrificed at 4 and 8 weeks. Results demonstrated significantly higher tissue ingrowth in the scaffold design with both longitudinal and transverse channels than the other two scaffold designs (Fig. 5.6). In addition, astrocyte infiltration as measured by Glial Fibrillary Acidic Protein (GFAP) staining was significantly greater in the orthogonal and cylinder design compared to the channel design (Fig. 5.7).

Wong et al. (2007b) also investigated the effect of designed PCL scaffold architecture on tissue regeneration in a rat spinal cord transection model. In this model, Female Sprague Dawley rats (200–250 g) were anesthetized and spinal cords completely transected at T9 with a 3 mm long transection. Control groups received no implant. Implants were sutured to proximal and distal stumps and then covered with Durapair. Animals were sacrificed at one month and three

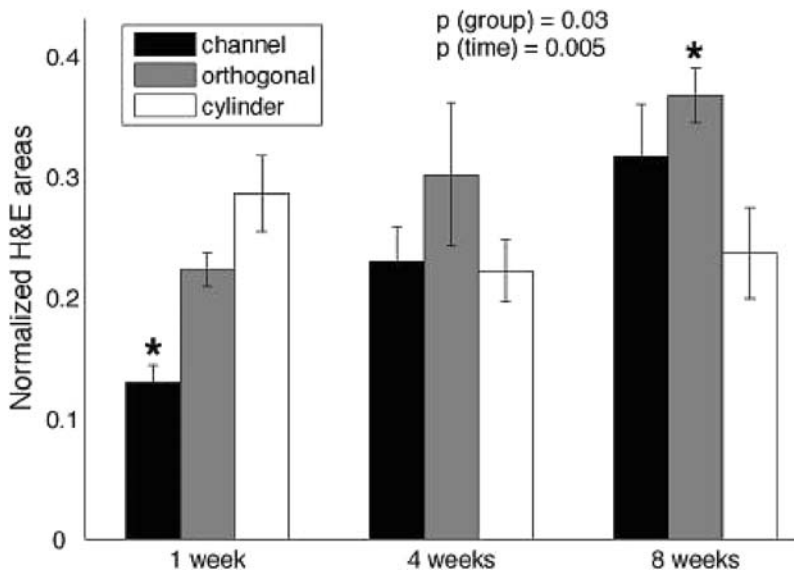


**Fig. 5.6** Effect of scaffold architecture on total tissue ingrowth in rat brain defects. Orthogonal design scaffolds exhibit significantly greater tissue ingrowth at 8 weeks than the other two scaffold designs ( $p = 0.03$ ). The channel design has significantly less tissue ingrowth at 1 week ( $p = 0.03$ )

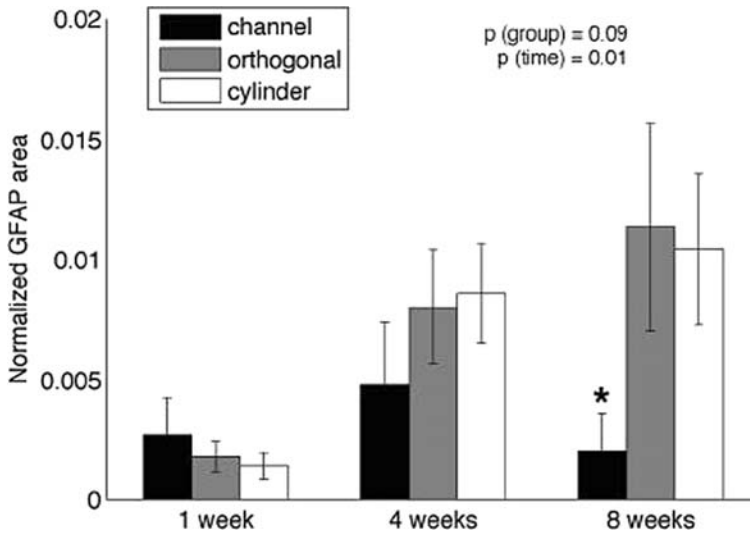


**Fig. 5.7** Effect of scaffold architecture on astrocyte infiltration as measured by GFAP staining. The channel design had significantly less GFAP staining per tissue area than the orthogonal or cylinder scaffold designs at 8 weeks

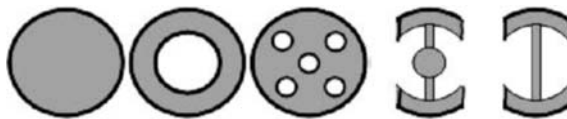


**Fig. 5.8** Axial cross-sections of implant designs from left to right; cylinder, hollow tube, 5-channel, open-path with core, open-path without core

months. Five designs were used; cylinder, hollow tube, 5-channel, open-path with core, and open-path with no core (Fig. 5.8). Within each macro-design, the implants base structure (grey areas in Fig. 5.8) were given a porous structure by salt leaching.

From H&E staining, and gross images, connectivity between the stumps was obtained in all implants to varying degrees. Much of the growth for the cylinder, tube, and channel groups occurred along the outside of these implants and was generally fibrous tissue (Fig. 5.9). Small portions of this exterior growth were labeled with GFAP and neuro-specific transcription factor, Tuj-1, but generally stopped near the implant ends. Tissue grew interiorly and exteriorly along the entire length of both open-path implants and appeared well connected. There was less necrosis and scar tissue at both ends of these implants and Tuj-1 labeled neural tissue from both proximal and distal stumps entered, and surrounded the implants. (Fig. 5.10) From serial sections, distances between proximal and distal stumps were measured using GFAP labeled intact

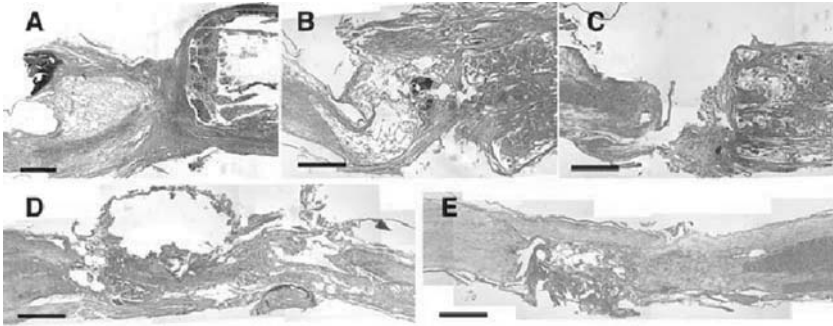


**Fig. 5.9** H&E stained sections of spinal cords after 3 months. (A) Cylinder, (B) tube, (C) channel, (D) open-path without core, (E) open-path with core. Scale bars = 1 mm

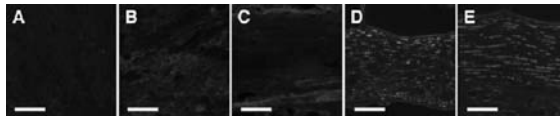


**Fig. 5.10** Axonal labeling with Tuj-1 antibody within defects at three months. (A) Cylinder, (B) tube, (C) channel, (D) open-path without core, (E) open-path with core. Scale bars = 100  $\mu$ m

neural tissue. The defect sizes of the cylinder, tube and channel groups nearly doubled, while the open-path designs remained stable and even decreased from the initial 4mm defect created.

The overall qualitative assessment from serial histology and immunohistochemistry using hematoxylin and eosin (H&E), myelinated fibers shown by Luxol Fast Blue (LFB), and antibodies for astrocytes (GFAP) and axons (Tuj-1) within and around the implants are summarized in Table 5.2.

## 5.4 Summary

Results for both cartilage and CNS tissue engineering clearly demonstrate that scaffold architecture plays a significant role in regeneration of both tissues. The results also demonstrate the need to be able to tailor mass transport properties for specific tissue applications. Initial results suggest that scaffolds with lower diffusion and permeability properties enhance cartilage matrix regeneration. Conversely, scaffolds with higher diffusion and permeability properties seem to enhance neural tissue regeneration in both brain and spinal cord defects. Although more experiments are required, from these results one can begin to build design guidelines for engineering soft tissue scaffolds.

**Table 5.2** Qualitative assessment of scaffold design effects on neural tissue regeneration in spinal cord defect. – indicates not present, + to +++ indicates increasing presence of specified stain in defect region

	Tissue ingrowth (H&E)	Myelinated fibers (LFB)	Astrocyte infiltration (GFAP)	Axonal infiltration (Tuj-1)
Cylinder	–	–	–	–
Tube	+	–	–	+
Channel	+	–	–	+
Open-path without core	++	++	+	++
Open-path with core	++	+++	+	+++

More broadly, regeneration of any tissue requires the capability to engineer systems that incorporate optimal combinations of cells, signaling factors and scaffolds. Just as cells and signaling factors are specific for a given tissue, so must the scaffold architecture and material designs be tailored for a specific tissue application. Image-based scaffold engineering techniques can create scaffolds with the broad range of mechanical and mass transport properties from a variety of biomaterials necessary to determine tissue specific scaffold design guidelines.

**Acknowledgment** Some work presented in this chapter was supported by NIH R01 DE 13608 (SJH), a Musculoskeletal Regenerative Sciences Training Grant T90-DK0710071 (EEL), and a NIH Training Grant: T32 DE-007057-31 (DYW). The authors would also like to thank Dr. Michael Yaszemski for providing PPF material, Dr. Chris Nosrat for help with rat brain surgeries, and Alex Garnepudi for all his assistance with the rat spinal cord study.

## References

- Demartean O, Pillet MS, Inaebrit A, Borens O, Quinn TM (2006) Biomechanical characterization and in vitro mechanical injury of elderly human femoral head cartilage: comparison to adult bovine humeral head cartilage. *Osteoarthritis and Cartilage* 14:589–596.
- Fiford RJ, Bilston LE (2005) The mechanical properties of rat spinal cord in vitro. *J. Biomechanics* 38:1509–1515.
- Greitz D (2006) Unraveling the riddle of syringomyelia. *Neurosurg Rev.* 29:251–264.
- Hollister SJ, Levy RA, Chu TM, Halloran JW, Feinberg SE. (2000) An image-based approach for designing and manufacturing craniofacial scaffolds. *Int J Oral Maxillofac Surg* 29:67–71.
- Hollister SJ, Maddox RD, Taboas JM. (2002) Optimal design and fabrication of scaffolds to mimic tissue properties and satisfy biological constraints. *Biomaterials* 23:4095–4103.
- Hollister SJ. (2005) Porous scaffold design for tissue engineering. *Nat Mater* 4:518–524.
- Karageorgiou V, Kaplan D. (2005) Porosity of 3D biomaterial scaffolds and osteogenesis. *Biomaterials* 26:5474–5491.

8. Klisch SM, Lotz JC (1999) Application of a fiber-reinforced continuum theory to multiple deformations of the annulus fibrosus. *J. Biomechanics* 32:1027–1036.
9. Kohles SS, Roberts JB, Upton ML, Wilson CG, Bonassar LJ, Schlichting AL (2001) Direct perfusion measurements of cancellous bone anisotropic permeability. *J. Biomechanics* 34:1197–1202.
10. LeGeros RZ. (2002) Properties of osteoconductive biomaterials: calcium phosphates. *Clin. Orthop. Rel. Res.* 395:81–98.
11. Li JP, Habibovic P, van den Doel M, Wilson CE, de Wijn JR, van Blitterswijk CA, de Groot K. (2007) Bone ingrowth in titanium implants produced by 3D fiber deposition. *Biomaterials* 28:2810–2820.
12. Liao EE, Yaszemski MJ, Krebsbach PH, Hollister SJ (2006) Chondrocytic differentiation of porcine bone marrow stromal cells in designed poly(propylene fumarate) scaffolds. *6th International Cartilage Repair Society Symposium*. San Diego, CA.
13. Liao E, Yaszemski M, Krebsbach P, Hollister S. (2007) Tissue-engineered cartilage constructs using composite hyaluronic acid/collagen I hydrogels and designed poly(propylene fumarate) scaffolds. *Tissue Eng* 13:537–550.
14. Liao E, Yaszemski M, Krebsbach P, Hollister S. (submitted) Designed ellipsoidal pore architecture of biomaterial scaffolds enhances chondrogenic differentiation of BMSC and increases cartilage matrix synthesis.
15. Linninger AA, Xenos M, Zhu DC, Somayaji MR, Kondapalli S, Penn RD (2007) Cerebrospinal fluid flow in the normal and hydrocephalic human brain. *IEEE Trans. Biomedical Engineering* 54:291–302.
16. Malda J, Martens DE, Tramper J, van Blitterswijk CA, Riesle J (2003) Cartilage tissue engineering: controversy in the effect of oxygen. *Crit. Reviews in Biotechnology* 23:175–194.
17. Malda J, Woodfield TBF, van der Vloodt F, Wilson C, Martens DE, Tramper J, van Blitterswijk CA, Riesle J. (2005) The effect of PEGT/PBT scaffold architecture on the composition of tissue engineered cartilage. *Biomaterials* 26:63–72.
18. Moore MJ, Friedman JA, Lewellyn EB, Mantila SM, Krych AJ, Ameenuddin S, Knight AM, Lu L, Currier BL, Spinner RJ, Marsh RW, Windebank AJ, Yaszemski MJ (2006) Multiple channel scaffolds to promote spinal cord axon regeneration. *Biomaterials* 27:419–429.
19. Mow VC, Ratcliffe A. (1997) Structure and function of articular cartilage and meniscus, in *Basic Orthopaedic Biomechanics*, 2nd Edition, Mow VC, Hayes WC eds., 113–177.
20. Nomura H, Katayama Y, Shoichet MS, Tator CH (2006) Complete spinal cord transection treated by implantation of a reinforced synthetic hydrogel channel results in syringomyelia and caudal migration of the rostral stump. *Neurosurgery*. 59:183–192.
21. Nomura H, Tator CH, Shoichet MS (2006) Bioengineered strategies for spinal cord repair. *J. Neurotrauma*. 23:496–507.
22. Otsuki B, Takemoto M, Fujibayashi S, Neo M, Kokubo T, Nakamura T (2006) Pore throat size and connectivity determine bone and tissue ingrowth into porous implants: three-dimensional micro-CT based structural analyses of porous bioactive titanium implants. *Biomaterials* 27:5892–5900.
23. Raghunath J, Rollo J, Sales KM, Bulter PE, Seifalian AM (2007) Biomaterials and scaffold design: key to tissue-engineering cartilage. *Biotechnol. Appl. Biochem.* 46:73–84.
24. Tsai EC, Dalton PD, Shoichet MS, Tator CH (2004) Synthetic hydrogel guidance channels facilitate regeneration of adult rat brainstem motor axons after complete spinal cord transection. *J. Neurotrauma*. 21:789–804.
25. Weinberg EJ, Kaazempur-Mofra MR. (2006) A large-strain finite element formulation for biological tissues with application to mitral valve leaflet tissue mechanics. *J. Biomechanics* 39:1557–1561.
26. Wong DY, Krebsbach PH, Hollister SJ (2007a) Scaffold Architectures Affect Brain Cortex Regeneration. Abstract, TERMIS NA 2007 Conference and Exposition, Toronto, Canada.

27. Wong DY, Leveque JC, Brumblay H, Krebsbach PH, Hollister SJ, La-Marca F (2007b) Macro-architectures in Spinal Cord Implants Play a Role in Guidance and Regeneration. Abstract, TERMIS NA 2007 Conference and Exposition. Toronto, Canada.
28. Wu JZ, Cutlip RG, Andrew ME, Dong RG (2007) Simultaneous determination of the nonlinear-elastic properties of skin and subcutaneous tissue in unconfined compression tests. *Skin Res. Tech.* 13:34–42.
- 29 Yamane S, Iwasaki N, Kasahara Y, Harada K, Majima T, Monde K, et al. (2007) Effect of pore size on in vitro cartilage formation using chitosan-based hyaluronic acid hybrid polymer fibers. *J Biomed Mater Res A.* 81:586–593.

# Chapter 6

## Customised Implants for Bone Replacement and Growth

Liang Hao and Russell Harris

### 6.1 Introduction

Bone is dynamic, highly vascularised tissue with a unique capacity to heal + and remodel. Its main role is to provide structural support for the body. Furthermore the skeleton also serves as a mineral reservoir, supports muscular contraction resulting in motion, withstands load bearing and protects internal organs [1]. Hence, it is logical to say that major alterations in its structure due to injury or disease can dramatically alter one's body equilibrium and quality of life. There are roughly 1 million cases of skeletal defects a year that require bone-graft procedures to achieve repair. Socioeconomic consequences in treating these patients with bone fractures is a major concern in both the USA and EU, which are likely to increase due to the ageing of their populations.

Bone repair may be treated by grafts taken from either the patient's own existing bone from other sites (autografts) or donor sources (allografts). The use of synthetic substitutes eliminates the need for further surgery for autografts and the risk of infectious disease transmission from allografts. The significant limitations of current treatments have compelled researchers to develop synthetic alternatives for bone reconstruction. In the early 1950s Swedish orthopaedic surgeon Per Ingvar Branemark began studying the healing process of titanium anchoring screws, which proved to be a seminal point for modern dental and orthopaedic implants [2]. Current bone substitutes using metal, ceramic, polymer and composites, though far from ideal, are commonly implanted materials, second only to blood products. Currently, bone tissue engineering is being researched including scaffolds, growth factors and engineering cells which may provide next-generation bone substitutes.

Production of such bone implants and scaffolds requires complex structures that would provide the necessary bone shape and morphology. In general,

---

Liang Hao  
School of Engineering, Computer Science and Mathematics, University of Exeter,  
EX4 4QF, UK  
hao@exeter.ac.uk



current orthopaedic prostheses are modular in nature and, although scalable, adhere to a range of basic generic designs. The surgeon, therefore, must select the best size fit based upon preoperative evaluation of radiographs. Current production methods for these devices, which are made from metal/ceramic/polymers, include casting, compression moulding, sintering, and bar stock milling. These approaches have some inherent restrictions, these include the use of static moulds/tooling which do not allow rapid design changes or one-off patient-specific devices to be produced, or they have geometry restrictions, and high material wastage. One school of thought believes that patient-oriented devices have the potential to enhance the longevity of a device by providing a securer fit, especially in those cases where the devices are not cemented. Closeness of fit aims to aid the distribution and normalization of the stresses incurred in the remaining skeletal system, thereby reducing stress shielding, micromotion, and sinkage. Accurate fits are typically achieved by removing the patient's bone stock to accommodate the prosthesis, thereby destroying valuable viable bone and making any revision surgery more difficult. It would be preferable to produce custom prostheses for individual patients that required little or no healthy bone stock removal to increase the device stability, especially in young patients, and thus increase the options for a successful revision surgery if required [3].

Today reverse engineering (RE) and medical image-based modelling technologies allow the construction of three-dimensional (3D) models of anatomical structures of human body based on information from imaging data such as computerized tomography (CT), magnetic resonance imaging (MRI), and laser (or structured light) scanning [4]. Based on 3D models, advanced mouldless manufacturing techniques, commonly known as solid free-form fabrication (SFF) or rapid prototyping (RP) have been used to build 3D physical models for surgical training, preoperative planning, surgical simulation and more recently applied to fabricate customised implants and scaffolds for individual patients.

This chapter gives a background on bone structure and properties, biomaterials for bone implants and requirements for bone implant and scaffolds. It then introduces state-of-the-art reverse engineering and rapid prototyping techniques to assist in the manufacture of customised bone implants and then focuses on current research on the techniques to fabricate bone implants and scaffolds directly.

## 6.2 Bone Structure and Properties

Bone – a living tissue – is a highly specialised hard form of connective tissue that forms most of the skeleton and is the chief tissue of the body. Bone can provide the support for the body and protection for vital organs. Bone also provides the storage of mineral and a continuous supply of new blood cells [5]. Bone tissue in the adult skeleton is arranged in two architectural forms: trabecular, also called

cancellous or spongy bone, and cortical or compact bone. The proportions of these two architectural forms differ at various locations in the skeleton. Cortical bone is almost solid, being only 10% porous. Trabecular bone presents a higher porosity, 50%–90%, making its modulus and ultimate compressive strength around 20 times lower than that of cortical bone. Trabecular bone is arranged in a sponge-like form, with a honeycomb of branching bars, plates and rods of various sizes called trabeculae. It is commonly found in metaphysis of long bones, surrounded by cortical bone, and in the vertebral bodies.

Bone is a dynamic living tissue that shows marked structural alteration in response to loading changes of stress and to vascular, endocrine, and nutritional influences. The development of a bone analogue material starts with understanding of the mechanical behaviour of the bone. Most of the outstanding properties of bone are related to its matrix constitution. Bone matrix has two components: a mineral part of hydroxyapatite which contributes with 65%–70% of the matrix, and an organic part composed of glycoproteins, proteoglycans, siloproteins and bone proteins that comprises the remaining 25%–30% of the total matrix. Because of this, bone can be considered as a truly composite material.

### 6.3 Materials for Bone Implants

Material scientists have investigated metals, ceramics, polymers and composites as biomaterials. The general criteria for materials selection for bone implant materials are [6]: high biocompatibility; appropriate mechanical properties; economically viable manufacturing and processing methods.

Ideally, a bone implant such as a hip implant should exhibit a comparable response to loading as real bone and also be biocompatible with existing tissue. The compatibility issue involves surface compatibility, mechanical compatibility and also osteocompatibility. Materials are also classified as bioactive (eliciting a favourable biological response), bioinert and biodegradable.

As a class of materials, metals are the most widely used for load-bearing implants. For instance, some of the most common orthopaedic operations involve the implantation of metallic implants. These range from simple wires and screws to fracture fixation plates and total joint prostheses (artificial joints) for hips, knees, shoulders, ankles, and so on. In addition to orthopaedics, metallic implants are used in maxillofacial surgery, cardiovascular surgery, and as dental materials. Although many metals and alloys are used for medical device applications, the most commonly employed metals are stainless steels, commercially pure titanium and titanium alloys, and cobalt-base alloys.

Ceramics have been widely used in the biomedical engineering and bone substitution/regeneration field. Since calcium phosphates are naturally present as apatites in bones, researchers have investigated calcium phosphates

extensively [6, 7]. Typically, the calcium phosphorus atomic ratios range from 1.5 to 1.67. Tricalcium phosphate (TCP) ( $\text{Ca}_3(\text{PO}_4)_2$ ) and HA ( $\text{Ca}_{10}(\text{PO}_4)_6(\text{OH})_2$ ) are the two minerals at the extremes of this range of calcium–phosphorus ratios. Both TCP and HA are biocompatible materials. Calcium phosphate ceramics, especially HA and  $\beta$ -TCP are widely used for hard tissue replacement due to their biocompatibility and osteoconductive properties. However, its poor mechanical properties such as low strength and limited fatigue resistance restrict its applications. Alumina, because of the ability to be polished to a high surface finish and its excellent wear resistance, is often used for wear surfaces in joint replacement prostheses. Zirconia, known as tetragonal zirconia polycrystals (TZP), is the material of choice currently for ball heads.

The use of polymeric materials in bone biomaterials research is extensive due to many useful properties of polymers [6]. For orthopaedic applications, common polymers used are: acrylic, nylon, silicone, polyurethane, ultra high molecular weight polyethylene (UHMWPE), and polypropylene (PP). Highly stable polymeric systems such as Polytetrafluoroethylene (PTFE), UHMWPE or poly(etheretherketone) (PEEK) have been investigated due to their excellent mechanical properties. Polymers prepared from lactic acid and glycolic acid have been used in the biomedical field since the 1960s as sutures due to their highly unstable structure which provides bio-degradability. As biodegradable polymers, besides poly(lactic acid) PLA and poly(glycolic acid)PGA, polycaprolactone (PCL), polyanhydrides (PA), polyorthoesters are also subject of current research. Due to their degradation properties these polymers have extensive application in tissue engineering. The initial high strength of some degradable polymers such as poly-L-lactide (PLLA) has spurred interest in the use of these polymers as composite systems with ceramic fillers. The use of these materials for composites where stiffening agents are used to enhance mechanical properties is the subject of several current studies.

Generally the investigation of composites for bone biomaterials has included three broad areas [6]: 1) Functional gradient materials (FGM) – The main feature of a FGM is the graded variation of compositions that results in two different properties in different locations of the composite. Powder metallurgy methods have been used to make HA/titanium FGM offering the biocompatible HA for tissue interaction and titanium for mechanical properties. 2) Polymer-ceramic composites (with and without fibre reinforcements) – Ceramic polymer composites have superior properties than either ceramics or polymers for use as total hip replacement materials. Typically the polymer components have included polymers that have shown good biocompatibility and are routinely used in surgical applications. 3) Biomimetic composites or composites with biological macromolecules – Bone is a nanocomposite of HA and type I collagen. The HA-polymer composites are typically simple mixtures fabricated to give a combination of properties of biocompatibility and mechanical strength. Methods to mimic biological processes with synthetic and biological macromolecules have been the focus of recent research.

## 6.4 Requirements for Bone Implants

Optimally, bone implants and scaffolds would have to be customized to fit specific requirements of the patient and individualized to fit the geometrical features of the patient's anatomy. The need of customised implants has been partly addressed in total hip arthroplasty and oral-maxillo-facial bone surgery. Some customisation concepts have been integrated in the design and fabrication of hip implants which exactly fit the anatomical shape of the femoral canal. A customised hip implant can be more durable, especially in younger patients, by improving the characteristics of the femoral stem such as stability, load transfer to the proximal part of the femur and restoration of normal geometry of the hip joint. Implants must fit very complex three-dimensional (3D) anatomic defects in oral-maxillo-facial applications that can be much more complicated than those in the appendicular skeleton [8].

In order to perform like natural bone, bone implants should match the mechanical properties of natural bone. The mismatch of the mechanical property could result in "stress shielding" when the mechanical properties of the implant is in excess of the properties of bone. Bone tissue scaffolds must provide initial sufficient mechanical strength and stiffness to oppose contraction forces, and later for the remodelling of tissue. In regenerating load-bearing bone tissues, additional issues relating to the scaffolds' mechanical properties have to be resolved. To allow early mobilization of the treated site, the degradable scaffold should retain sufficient mechanical strength to manage any in vivo stress and physiological loadings imposed on the engineered construct. The scaffolds' degradation must be tuned appropriately such that it retains sufficient structural integrity until the newly grown tissue has replaced the scaffolds supporting function [9, 10].

Implants and scaffolds must possess an open-pore geometry with a highly porous surface and microstructure that allows cell in-growth and reorganization and provides the necessary space for neovascularisation from surrounding tissues in vivo. By manufacturing porous implants through which blood vessels and bone could grow (thus integrating the implant into the body) would remove the risk of implant extrusion which may occur with conventionally manufactured implants. This deliberate and controlled porosity would further mean that even if the initial implant strength and toughness were below that required for long-term use, as occurs with porous pure HA implants, the ingrown bone would increase the strength of the bone-implant composite by a factor of 3 or 4 [11]. The scaffold's porosity and degree of pore interconnectivity directly affect cell in-growth, an accurate cell distribution, the diffusion of physiological nutrients, and the removal of metabolic waste and by-products from cells that have penetrated the scaffold [9].

The biocompatibility of bone implants is imperative; the material must not elicit an unresolved inflammatory response nor demonstrate immunogenicity

or cytotoxicity. In order to encourage the formation of natural bone, bioactivity or osteoinductivity is also desirable for bone substitutes. Osteoinduction is the process by which stem and osteoprogenitor cells are recruited to a bone healing site, and stimulate the osteogenic differentiation pathway. Currently, composites of polymers and ceramics are being developed with the aim of improving bone tissue reaction and regeneration. In addition, efforts have also been invested in developing scaffolds with a drug-delivery capacity. These scaffolds can locally release growth factors or antibiotics and enhance bone ingrowth to treat bone defects and even support wound healing [12].

## 6.5 Bone Modelling and Design

Reverse Engineering (RE) and Rapid Prototyping (RP) technologies have revolutionized the generation of physical models, allowing the engineer to efficiently and accurately produce physical models and customised implants with high levels of geometric intricacy [4]. For 3D models of anatomical structures there are many medical applications including surgical training, preoperative planning, surgical simulation, and diagnosis. With the use of RP technology, complex 3D physical objects of anatomical structure can be fabricated in a variety of materials and sizes. Medical RP has played an important role in diagnosis and treatment, especially in preoperative planning, design and manufacturing of surgical aid tools and implants.

Three-dimensional geometrical data of anatomical structures, which are constructed from RE and medical imaging data are used as the drivers for medical RP and computer aided design/manufacturing (CAD/CAM). Therefore, geometrical modelling is a key process in medical RP, especially in design and manufacturing of implants, surgical aid tools, surgical training models and medical devices. There are four main steps: 1. data acquisition; 2. data registration and processing; 3. geometrical modelling and design; 4. medical application development [4].

In addition to defining the external shape of implants, computer aided design can also apply a biomimetic design approach to introduce multiple biological and biophysical requirements into the internal structure design for bone implants and scaffolds. Biomimetic features can be based upon real anatomical data regenerated from CT/MRI images, or can be created as a unspecific structure. CAD is able to present heterogeneous biological tissue structures and introduce various design intents of internal and external architectures which may dictate or influence porosity, interconnectivity, mechanical properties, vascularisation, and drug/growth factor delivery in the scaffold design.

## 6.6 Rapid Manufacturing of Customised Bone Implants

A custom-made implant of actual dimensions would reduce the time it takes to perform the medical implantation procedure and subsequently lower the risk to the patient. Another advantage of a prefabricated, exact-fitting implant is that it can be used more effectively and applied directly to the damaged site rather than a replacement which is formulated during surgery from a paste or granular material. This advantage is especially beneficial for bone reconstructions involving large voids. Repairing large voids in bone currently presents one of the biggest obstacles in reconstructive surgery.

Layer manufacturing was initially developed for prototype models and has subsequently emerged as a key enabling technology for rapid manufacturing (RM) to produce directly useable products or parts. RP produces parts for prototyping or tooling purposes, while RM pursues the production of objects for direct application. RM facilitates total customisation of products and permits one individual product to be manufactured as easily as millions of products (i.e. mass production). Layer based RM approaches allows extremely complex shapes to be produced and enables the economically viable production of implants that are customised with respect to size and functionality for individual patients. In addition, one of the potential benefits of RM technology in the context of bone implants is the potential to create parts with highly complex internal architectures and compositional variation. At present, a number of layer manufacturing techniques have been exploited for indirect and direct manufacturing of custom bone implants and scaffolds.

### 6.6.1 Laser Based Techniques

#### 6.6.1.1 Laser Engineered Net Shaping (LENS)

Originally conceived at the US Sandia National Laboratories and commercialised by Optomec Inc, the LENS process is depicted in Fig. 6.1. The process uses a CAD driven, high power, laser focused onto a metal substrate to create a molten pool. Metal powder is then injected into the melt pool to increase the material volume. The CAD data is used to move the laser back-and-forth, overlapping line-by-line, until a layer of metal is laid down on the substrate. By repeating this process, layer by layer, the machine then additively produces the part.

LENS aims to directly manufacture metal implants and medical device with highly net shape and fine detailed complex geometries as shown in Fig. 6.1 [13]. The standard medical device materials deposited using the LENS process are titanium alloys, stainless steels, and cobalt alloys. The properties obtained by the LENS process in different alloys are comparable to forged materials, and in several cases exceed them due to the extremely rapid solidification of the

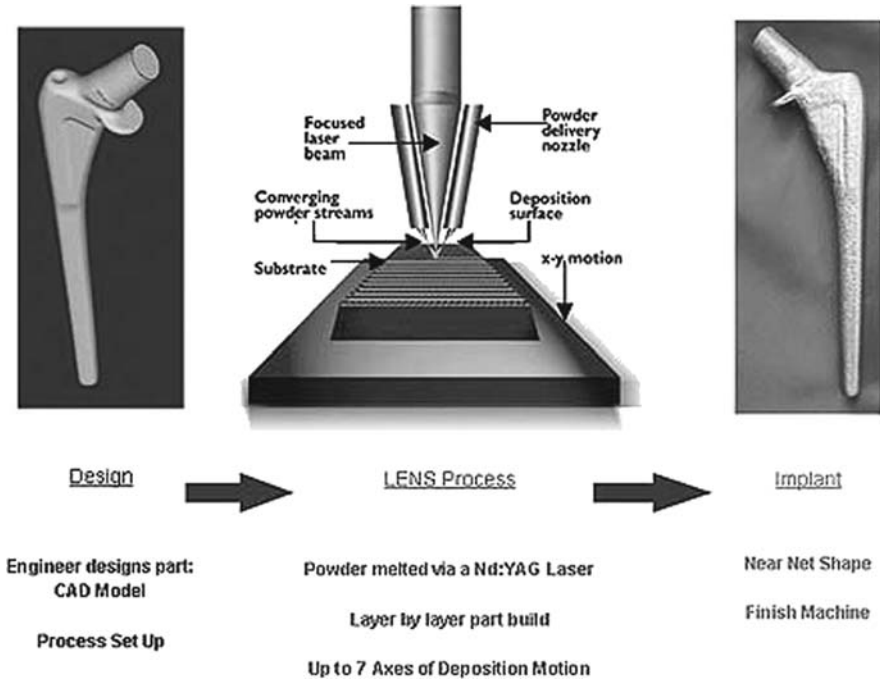
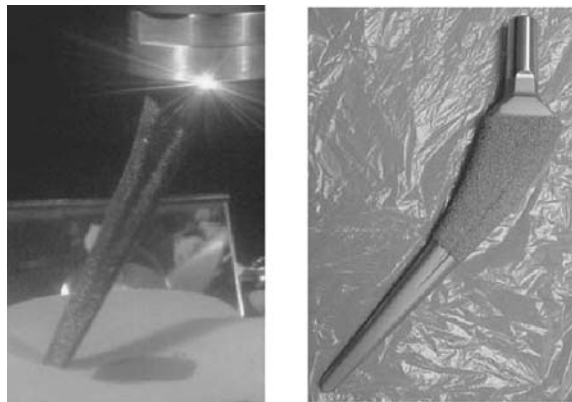


Fig. 6.1 A schematic diagram showing the LENS process [Optomec Inc.]

material and fine microstructures. Recent studies on the fatigue properties of LENS Ti6Al4V have shown fatigue properties comparable to the highest properties obtained from forged parts. Figure 6.2 shows LENS building a hip implant and the final finished component after being post processed in the standard production route. This involves: turning of the taper, drilling of the

Fig. 6.2 LENS building a Ti6Al4V hip implant and the final finished implant after post processing . [Biomet Europe & Powdermatrix.]



inductor hole, finishing/grinding the stem, grit blasting, shot peening, application of porous Ti coating and finally washing and passivating the implant.

Some studies in the US and Europe, indicate that LENS has the potential to reduce the cost of Ti implants compared to forged and machined parts. Hip stems typically cost \$90 when forged in high volume as a standard implant. Custom versions are machined at \$200. Using LENS, a customised part can be produced in volume at an estimated cost of \$60, which may further be reduced with the ongoing increases in LENS deposition rates [14]. In addition, the LENS process is able to easily fabricate FGM which offers the potential for improved implant designs. Current challenges for the LENS process in implant manufacture are the need to get closer to Near Net Shape (to reduce finishing time/cost) and to increase the ability to process highly complex biological shapes.

### 6.6.1.2 Selective Laser Sintering/Selective Laser Melting

Selective Laser Sintering (SLS) is a particular additive manufacturing technique. SLS operates by selectively sintering a powdered material using heat supplied by exposure to a laser. The technique forms an object by fusing sequential 2D layers that formulate the required object. A schematic diagram of the SLS process is shown in Fig. 6.3.

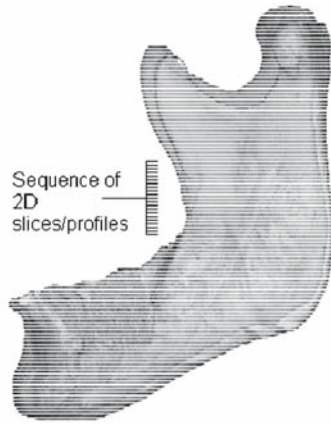
Rimell and Marquis [3] fabricated linear continuous UHMWPE solid bodies for clinical application by using a non-commercial SLS machine without pre-heating, but faced the problems caused by material shrinkage and degradation of UHMWPE under ambient atmospheric processing conditions.

Das et al. [15] investigated the fabrication of biomimetic bone architectures derived from the micro-CT of human proximal femur trabecular bones using SLS Nylon-6. The porous specimens of both cylindrical and cubical periodic geometry with 800  $\mu\text{m}$  channels and 1200  $\mu\text{m}$  pillars were fabricated. The micro-CT scan showed the ingrowth of mineralized bone tissue into the pore channels of the implanted cylinder sample after implantation into a Yucatan minipig mandible for 6 weeks.

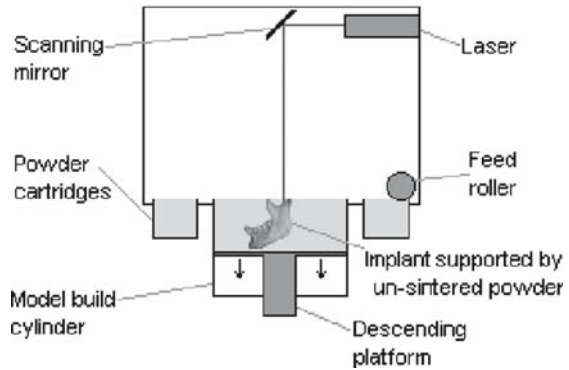
Using SLS, Williams et al. [16] fabricated porous bioresorbable PCL polymer scaffolds which were computationally designed and had the potential application for bone and cartilage repair. The compressive modulus values (52–67 MPa) and strength values (2.0–3.2 MPa) fall within the lower ranges of human trabecular bone. The smallest designed pores fabricated were 1.75 mm in diameter fabricated using a  $\text{CO}_2$  laser with a focus spot of 450  $\mu\text{m}$ . Both  $\mu\text{CT}$  and histological staining reveal the presence of a cortex that enveloped the entire implant scaffolds with an orthogonal interconnected pore design (pore size = 1.5 mm, porosity = 68%) which were seeded with primary human gingival fibroblasts and implanted for 5–8 weeks in immunocompromised mice. Partee [17] optimised the SLS process using systematic factorial design of experiments and achieved the manufacture of test scaffolds with designed



**Fig. 6.3 (a)** ‘Sliced’ 3D model of the required implant example **(b)** selective laser sintering process schematic



**(a)**



**(b)**

porous channels with dimensional accuracy within 3%–8% of design specifications and densities of approximately 94% relative to full density. The process was demonstrated by fabricating PCL scaffolds based on actual minipig and human condyle scaffold designs incorporating complex interior and exterior geometries.

Initial investigations for fabricating bioactive ceramic were conducted by Lee [18] and Vail [19] for calcium phosphate ceramic scaffold implants using an indirect SLS process. Polymethylmethacrylate (PMMA) coated calcium phosphate powders were successfully processed via SLS and subsequent post-processed to produce porous HA structures. Mechanical strength, porosity, and pore size of implants were considered to be consistent with requirements for biological applications. Radiographic and histologic analysis showed that the implants placed into mandibular molars of mongrel canines in vivo exhibited

excellent biocompatibility, intimate apposition to new bone, and evidence of resorption. The drawbacks of this process were additional post-process debinding of polymer binder and the sintering of ceramic, and the use of organic solvents of diluted methanol.

Tan et al. [20] studied the SLS of scaffolds by utilising pure polyetheretherketone (PEEK) powder and physically blended mixtures of PEEK and HA powders. It was found that part bed temperature, laser power and scan speed were the significant parameters influencing the integrity of the test specimens. The scaffolds featured macropores specified through a parametric library [21] with strut lengths of 1.5 mm, theoretical pore size of  $\sim 600 \mu\text{m}$  and porosity greater than 80% were fabricated. The scaffolds were easily cleaned, but there was difficulty in measuring the structural accuracy and mechanical properties of the scaffolds. The immersion of PEEK-HA scaffolds in simulated body fluid (SBF) exhibited the precipitation of bone-like apatite as supported by X-ray Diffraction (XRD) and Scanning electron microscope (SEM) results, indicating the bioactivity of the specimens. Positive cell adhesion and growth was found by the qualitative analysis of the culture of fibroblast cell lines. Chua et al. [22] further developed a powder system of the blend of polyvinyl alcohol (PVA) and HA for SLS obtained via spray-drying and physical blending. The physically blended powders yielded tests that exhibited good micropore interconnectivity and reproducibility. Bioactivity tests of specimens using SBF showed that laser-sintering did not affect the chemical composition of HA in the PVA matrix.

Cruz et al. [23] selected PLLA as binder for the direct manufacturing of hydroxyapatite based bone implants by SLS due to the higher degradation time and low melting temperature of this polymer compared with other lactic acid biodegradable materials. The compression and bending strength and density of the PLLA-HA were within the range of reported strength and modulus for cancellous bone and limited their potential application only in non-loading situations or supported load bearing use. The internal pores, with average size of  $200 \mu\text{m}$  measured by SEM, were found to be positive for tissue ingrowth but negative for the mechanical properties of PLLA-HA parts. Coole et al. [24] evaluated this process for the production of human foot bone structures from MRI medical scan data. The geometrical accuracy of the bones produced was poor and was as high as 9.7%, 12.4% and 16.1% average deviation in *X*, *Y*, *Z* directions respectively from the CAD model due to the area affected by the laser heat around the part during the build and the occurrence of particle agglomeration surrounding the parts due to the effect of the binder action. The application of dimensional offsets to compensate the contraction/expansion of the polymeric parts was necessary to obtain dimensional accuracy which was deemed satisfactory.

To rapid manufacture customised bioactive implants, Hao et al. [25, 26] evaluated and compared the performance of a  $\text{CO}_2$  and Nd:YAG lasers for SLS of a clinical grade HAPEX<sup>TM</sup> (high-density polyethylene (HDPE) reinforced with HA). The material powders were prepared by extruding two material mixtures and then powderising using centrifugal milling. The reinforcement

of HA particles in the polymer powder matrix aimed to avoid the separation of the two components in the sintering process. CO<sub>2</sub> laser presented a better performance than the Nd:YAG laser for the SLS of HAPEX<sup>TM</sup> in terms of operation range, speed, and processing efficiency. At certain parameters, the SLS processing allowed exposure of HA particles on the composites' surface. The inter-particle connectivity and pore size range of the specimens was found to be predominantly determined by the particle size and to a lesser extent also influenced by the process parameters [27]. Cross-sectioned analysis showed that the pores were highly connected within the SLS parts and the width of porous channel depended on the sizes of powder particles (see Fig. 6.4). By varying the particle size and laser processing parameters, the pores inside parts were mainly irregular and in range from 10 to 150 μm. A sintered layer (see Fig. 6.5) was produced which exhibited designed regular pores within a range of approximate 200–500 μm. Pores with such size are required in implants for the nutrient provision and vascularisation which are critical for bone tissue generation. The ability to vary the internal porous structure also allows variation of mechanical properties – more dense sections of material with the bulk strength, interfacing with more porous sections in areas for bone ingrowth.

Goodridge et al. [28, 29] investigated and compared direct and indirect SLS of porous apatite mullite glass ceramics based on the system SiO<sub>2</sub>-Al<sub>2</sub>O<sub>3</sub>-P<sub>2</sub>O<sub>5</sub>-CaO-CaF<sub>2</sub> with the assistance of an acrylic binder. The processing window, and coherence of the indirectly sintered components was considerably greater than those produced by the direct route due to crystallisation only occurring upon post-processing in the indirect samples, therefore allowing an increase in liquid phase sintering. An increase in strength was achieved by infiltrating the parts with a resorbable phosphate glass, but this altered the crystal phases present in the material.

Hayashi et al. [30] investigated the use of a Nd:YAG laser to sinter titanium powder sheet which was formed by mixing titanium powder and organic agents.

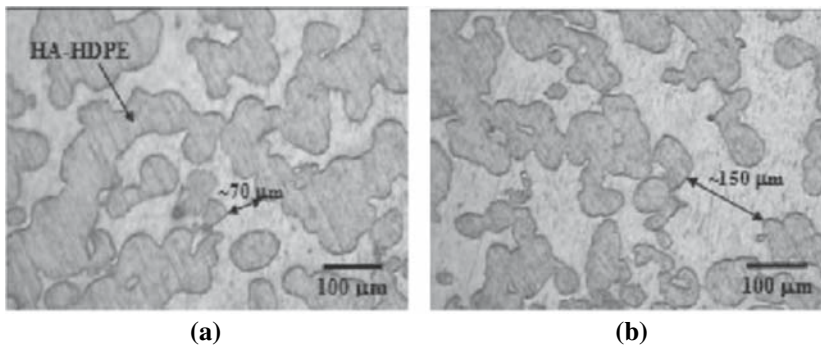


**Fig. 6.4** Typical optical images of the cross-section of the HA-HDPE specimens at scanning speed of 3600 mm s<sup>-1</sup> at 3.6 W laser power and particle size (PS) (a) 0 < PS < 105 μm, (b) 105 μm < PS

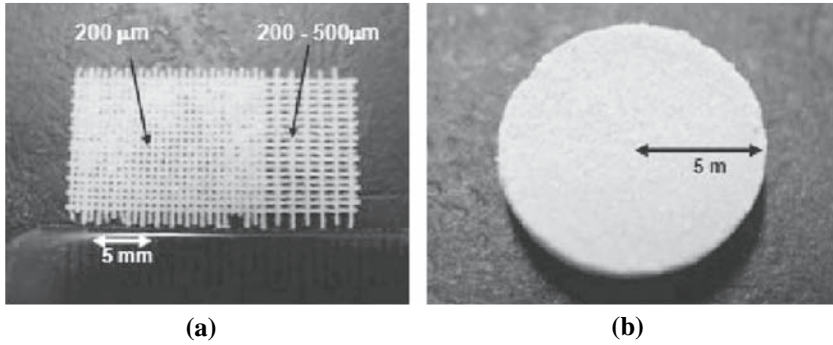


**Fig. 6.5** (a) A scanned layer of HA-HDPE with specified pore size (b) a circle sample for cell culture test

Operating parameters, such as laser power and scanning paths were examined to suppress distortion, increase strength and adjust pore sizes of the sintered part. Pores varied from 200 to 300  $\mu\text{m}$  were distributed over the sintered matrix. To improve osseointegration, Hunt et al. [31] investigated the production of Co-Cr implants with controlled surface topography by indirect SLS methods. Two different designed surface morphologies, described as Stipple (St) and Pyramid (Py) were produced by SLS of polymer (Dura-Form nylon) coated Cobalt Chromium powders with the polymer being later removed by post-process heat treatment. The results from in vivo implantation in skeletally mature male New Zealand white rabbits indicated that SLS fabricated Co-Cr alloy implant with a shaped surface and plasma HA coating enhanced osteogenesis and tissue implant cohesion.

Selective laser melting (SLM) [32] is used to fully melt powder materials, mainly metals. SLM equipment (MCP Realizer) utilises a very precise laser beam of 30  $\mu\text{m}$  diameter which builds in Z axis steps of 50  $\mu\text{m}$  metal parts in high complexity. The laser beam melts the powder and achieves 100% dense steel at 5  $\text{cm}^3/\text{h}$  building speed. SLM generates components as dense metals and the mechanical properties of finished components are like to those of the elementary powder metal materials used. Requiring no post-processing, they are completely dense and homogenous without pores or voids. SLM was used to produce biological structures as shown in Fig. 6.6. The cortical lower jaw geometry was fabricated in full metal; the structures of the spongiosa and the mandibular canal were produced as cavities. Supporting structures were partly inserted as an example of the spongiosa structure. The teeth were modelled including the roots and could be illustrated in the model within the mandibular canal. The spinal column model was developed to have a cage with a viewing window and supporting structures for the vertebral body was produced. Both the solid extension and the cage with the supporting structure were included in detail. The third model, the tubular bone at the femur, contained viewing windows, screw connections and support structure.

**Fig. 6.6** A stainless steel parts of a lower jaw, lumbar vertebra, a middle segment of the tubular femoral bone produced by selective laser melting



SLM, referred to as direct laser form (DLF) by Hollander et al. [33], was developed to manufacture hard tissue implants on the basis of titanium and its alloys. Porous Ti6Al4V structures modelled according to a regular offset array of parallel cylindrical pores were manufactured with nominal pore diameters of 500, 700 and 1000  $\mu\text{m}$  which reduced by approximately 300  $\mu\text{m}$ . Human osteoblast cells were found to spread and proliferate on Ti6Al4V specimens fabricated by SLM over a culture time of 14 days. On porous specimens, osteoblasts grew along the rims of the pores and formed circle-shaped structures. The tensile and yield strengths of dense specimens directly fabricated by SLM ranged beyond 1000 MPa, and breaking elongation was  $6.5\% \pm 0.6\%$ . After an additional post annealing treatment, the tensile and yield strength were reduced by approximately 8%, but still satisfy the ASTM specification for the use of this alloy as a medical material. Rotating bending tests revealed that the fatigue profile of post annealed Ti6Al4V was comparable to cast/hot isostatic pressed alloy.

### 6.6.2 Electron Based Techniques

Developments in metals processing are being made at Arcam AB, Sweden, in which fully dense parts are built from metal powder. The technology is based on electron beam melting (EBM), and the parts are built by melting the metal in a layer-by-layer manner. Advantages of using an electron beam as the energy source, as opposed to laser processing, include very small spot sizes ( $\sim 100 \mu\text{m}$ ); very high beam-material coupling efficiencies, high scanning speeds (up to  $\sim 1000 \text{ m/s}$ ); and allowing beam deflection without the use of moving mirrors. The material is processed in a vacuum, which increases material quality. The use of extremely low processing pressures minimizes the adverse effects of impurities such as oxides and nitrides and allows for processing of reactive materials such as titanium. A schematic of the Arcam system is shown in Fig. 6.7.

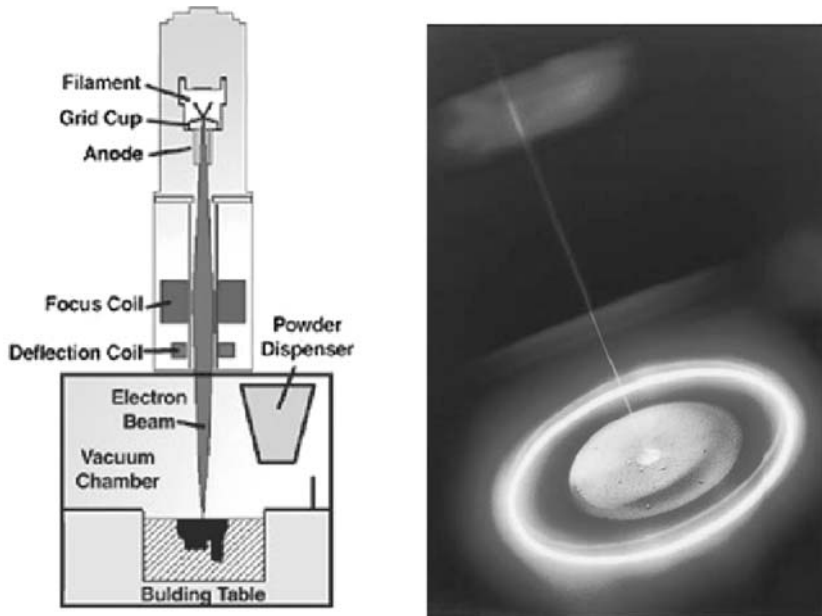


**Fig. 6.7** Schematic of the Arcam electron beam melting (EBM) system. The electron beam is generated in an EB gun, and the beam is deflected to the top of the powder layer by two magnetic fields. The first acts as a magnetic lens and focuses the beam to the desired diameter. The second deflects the focused beam to the desired location [www.arcam.com]

The maximum build size of the Arcam EBM system measures  $200 \times 200 \times 160$  mm, with a reported accuracy of  $\pm 0.3$  mm]. The EBM process is able to use standard biocompatible materials, such as Ti6Al4V ELI, Ti Grade 2 and Cobalt-Chrome and lends itself particularly well to metal implant manufacturing. The process has been verified for tool steel, low alloy steel, alloyed titanium, and nickel alloys. Mechanical properties of samples fabricated of the Ti6Al4V are 30–35 HRC hardness, 930 MPa/135 ksi tensile strength ( $R_m$ ), 880 MPa/125 ksi yield strength ( $R_{p0.2}$ ). Examples of custom implant are shown in Fig. 6.8. Disadvantages of electron beam technology are: the need for a vacuum, the production of gamma rays and the requirement for conductive materials.

### 6.6.3 Extrusion Based Techniques

#### 6.6.3.1 Fused Deposition Modelling (FDM)

FDM employs the concept of melt extrusion to deposit a parallel series of continuous material beads that form a layer. In FDM, filament material stock (generally thermoplastics) is softened and extruded through a heated nozzle and

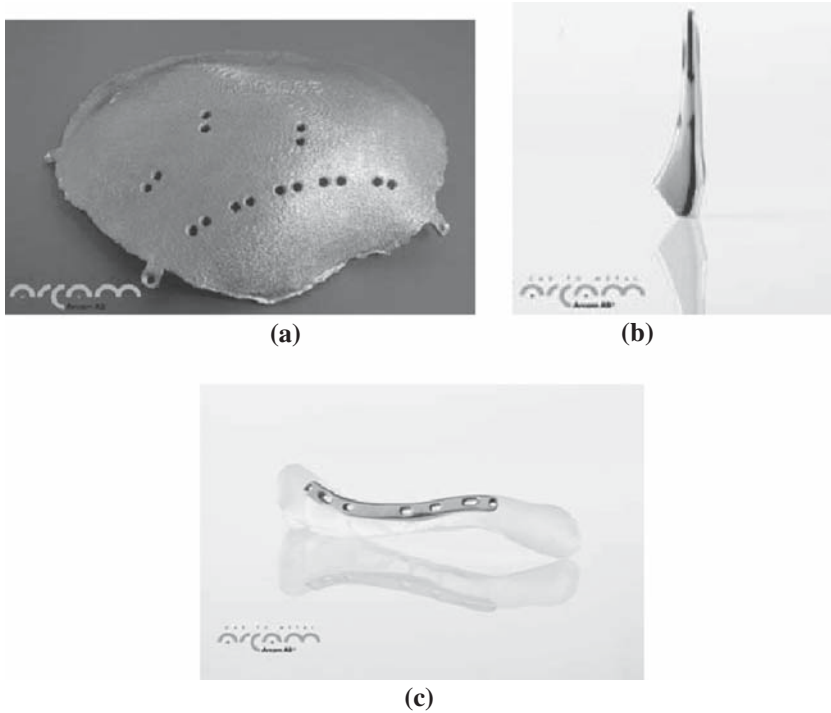


**Fig. 6.8** (a) customised skull plate implant (material: Ti6Al4V, 4 hours) (b) hip stem implant (material: Ti6Al4V, build time: 20 pieces in 24 hours) (c) customised bone plate

deposited in such a pattern to form a layer. By changing the direction of material deposition for consecutively deposited layers and the spacing between the material roads, scaffolds with highly uniform internal honeycomb-like structures, controllable pore morphology and complete pore interconnectivity may be obtained. In order to fabricate scaffold designs with overhanging features, removable supporting structures are deposited alongside the scaffold to support such features.

An interdisciplinary group in Singapore has studied and patented the parameters for processing PCL and several composites (PCL/HA, PCL/TCP etc.) by FDM [34, 10]. These first generation scaffolds (PCL) have been studied for several years with, and without, cells in a clinical setting ([www.osteopore-intl.com](http://www.osteopore-intl.com)). The second generation scaffolds for bone engineering using FDM were made of polymer and CaP composites because they confer favourable mechanical and biochemical properties, including strength via the ceramic phase, and toughness and plasticity via the polymer phase, with favourable degradation and resorption kinetics and graded mechanical stiffness. Other advantages include improvements to cell seeding and the enhanced incorporation and immobilization of growth factors. Endres et al. [35] and Rai et al. [36]

have tested these PCL/CaP composite scaffolds for bone engineering and reported encouraging results. Shao et al. [37] have evaluated the feasibility and potential of a hybrid scaffold system for large and high-load-bearing osteochondral defect repair. The implants were made of medical-grade PCL (mPCL) for the bone component whereas fibrin glue was used for the cartilage element using FDM. Both matrices were seeded with allogenic bone marrow-derived mesenchymal cells (BMSC) and implanted in the defect (4 mm diameter $\times$ 5 mm depth) on medial femoral condyle of adult New Zealand White rabbits. Mature trabecular bone regularly formed in the mPCL scaffold at both 3 and 6 months post-operation. Micro-Computed Tomography showed progression of mineralization from the host–tissue interface towards the inner region of the grafts. After 3 months, the specimens showed good cartilage repair. In vivo viability of the transplanted cells was demonstrated for the duration of 5 weeks. The results demonstrated that mPCL scaffolds provided a potential matrix for osteochondral bone regeneration and that fibrin glue does not possess the physical properties to allow for cartilage regeneration in a large and high-load-bearing defect site.

Drawbacks of the FDM techniques include the need for input material of a specific diametric size and material properties to feed through the extrusion nozzle. Any changes in the properties of the material require efforts to recalibrate and optimise the feeding parameters. As a result, FDM has a narrow processing window. The resolution of FDM is relatively low, at 250  $\mu\text{m}$ . In FDM, a limited range of materials can be used, with almost complete exclusion of natural polymers, as the material used must be made into filaments and melted into a semi-liquid phase before extrusion. The operating temperature of the system is too high to incorporate biomolecules into the scaffold. Moreover, the material deposited solidifies into dense filaments, blocking the formation of microporosity [38].

### **6.6.3.2 Precision Extruding Deposition (PED) and Precise Extrusion Manufacturing**

The precision extruding deposition (PED) system was developed at Drexel University to fabricate PCL scaffolds with a pore size of 250  $\mu\text{m}$  [39]. The major difference between PED and conventional FDM is that the scaffold material can be directly deposited without preparation of a filament. Pellet-formed PCL is liquefied by two temperature controlled heating bands and is then extruded by pressure created by a precision turning screw.

Xiong et al. [40] have developed precise extrusion manufacturing (PEM) to fabricate bone tissue scaffolds. In the PEM process, the thermoplastic material feeds into a heated extrusion sprayer capable of moving in *X-Y* directions. The sprayer extrudes a fine filament of the material onto a working platform capable of moving in the *Z* direction. So the material is extruded and deposited layer by layer in areas defined by the CAD model to build a 3D object. PEM



was used to fabricate poly(l-lactic acid) (PLLA) scaffolds with controllable porous architectures from 200 to 500  $\mu\text{m}$ . With the aim of preserving bioactivities of scaffold materials, a new process of low-temperature deposition manufacturing (LDM) [41] was developed to fabricate PLLA/tricalcium phosphate (TCP). Instead of melting solid materials by heating, PLLA grains, TCP powders and dioxane were mixed for use as a slurry. The material slurry was fed into a screw pump nozzle and deposited in low temperature environment ( $<0^\circ\text{C}$ ). The frozen scaffolds were then freeze-dried to remove the solvent. The scaffolds had macro-pores of approximately 400  $\mu\text{m}$  and micro-pores of approximately 5  $\mu\text{m}$ , with a porosity of 89.6%. The mechanical properties of the manufactured scaffolds are close to those of human spongy bone and much lower than those of human compact bone. The scaffolds loaded with bovine bone morphogenic protein (bBMP) were used to repair 20 mm segmental defects in canine radiuses in implantation experiments using mature beagle dogs. The results showed that bone and bone marrow like tissue were regenerated and the scaffold degraded after 24 weeks with no trace of aseptic inflammation found in the histological section image. The LMD was further developed for use in a multi-nozzle deposition system (MDM) [42]. It achieved the deposition of PLLA/TCP materials with different composition by bi-nozzle deposition and spraying BMP particles into the scaffold during its forming process by tri-nozzle deposition. Support structures could be built using water, which is nontoxic and easy to remove.

### 6.6.3.3 Bio-Plotter

The Bio-Plotter, developed by Landers et al. [43] at the Freiburg Materials Research Centre is a 3D dispensing technique that uses a pressure-controlled dispenser movable in each direction. 3D objects can be fabricated layer by layer with each layer composed of single parallel strands. By setting a certain distance between the stands, porous structures can be built. The key feature of this method is the 3D dispensing of liquids and pastes into a liquid medium with matched density. Initially, this technique was used to fabricate hydrogel soft tissue scaffolds [44]. Carvalho et al. [45] reported the use of this technique to fabricate hydroxyapatite with polyvinyl alcohol. The scaffolds were freeze-dried and sintered in an oven. Li et al. [46] used this technique to fabricate porous titanium scaffolds for orthopaedic implants and bone tissue applications. A Ti6Al4V slurry prepared from the mixture of Ti6Al4V powder and an aqueous solution of methylcellulose and stearic acid was deposited by a 3D dispensing unit consisting of a syringe and nozzle at room temperature. The scaffold samples were first dried at room temperature and then sintered in a high vacuum furnace. The result showed that Ti6Al4V slurry was successful for building 3D scaffolds and the scaffolds were not only nontoxic but also favourable for cell attachment, proliferation and

differentiation. The drawbacks of this process are the lower limit of the nozzle size, anisotropy of the deposited structure and some pore occlusion at boundaries.

#### ***6.6.4 Printing Based Techniques – 3D Printing***

3D printing (3DP) technology was developed at MIT [47] and operates by selective deposition of a binder onto a powder bed. It is one of the most investigated SFF techniques in tissue engineering and drug-delivery applications [10].

Sherwood [48] used the TheriForm 3D printing process to fabricate osteochondral scaffolds with material composition, porosity, and macroarchitecture varying throughout the scaffold structure. The upper, cartilage region was 90% porous and composed of PLGA/PLA, with macroscopic staggered channels to facilitate homogenous cell seeding. The lower, cloverleaf-shaped bone portion was 55% porous and consisted of a PLGA/TCP composite, designed to maximize bone ingrowth while maintaining critical mechanical properties. The transition region between these two sections contained a gradient of materials and porosity to prevent delamination. The tensile strength of the bone region was similar in magnitude to fresh cancellous human bone.

Dutta et al. [49] investigated the performance of Theriform 3D printing fabricated degradable composite (PLGA/ $\beta$ -TCP) bone repair products and hydroxyapatite bone repair scaffolds in a rabbit calvaial defect model at an 8-week time point. Scaffolds with engineered macroscopic channels had higher percentages of new bone compared to scaffolds with engineering channels for composite and hydroxyapatite scaffolds. The porous HA scaffolds with channels had a significantly higher percentage of new bone area compared with composite scaffolds of PLGA/ $\beta$ -TCP composites. Seitz et al. [50] used modified HA powders for the fabrication of 3D printed scaffolds and then consolidated the green bodies at 1250°C in a high temperature furnace in ambient air. The polymeric binder pyrolysed during sintering. Prototypes of scaffolds had internal channels with a dimensions as low as 450  $\mu\text{m}$  and wall structure with a thickness down to 330  $\mu\text{m}$ . The mechanical strength of dense test parts was up to 22 MPa. An advantage of 3DP is that it can be performed in an ambient environment. However, if the part is designed to be porous, one drawback of a powder-supported and powder-filled structure is the difficulty in removing internal unbound powder. The resolution of the 3D printer is also limited by the nozzle size and the degree of control allowed over the positional controller that defines print head movement. In addition, the particle size of the powder governs the layer thickness (usually 80–250  $\mu\text{m}$ ) [10].

### **6.6.5 Stereolithography (SLA)**

Chu et al. [51] investigated the direct and indirect SLA of ceramics. Using UV-curable suspensions of powders in acrylates in a conventional SLA machine, HA prototypes for bone tissue scaffolds were directly built from image based design files, featuring an interior architecture of void passages. However, direct ceramic SLA was limited in building refractive index ceramics and achieving features finer than 600  $\mu\text{m}$ . The indirect SLA method comprised a lost-mold technique with negative molds made with Stereolithography and a highly loaded curable HA suspension as the ceramic carrier [52]. HA suspensions were cast into the epoxy molds and cured into solids at 85°C. The molds and acrylate binders were removed by pyrolysis, followed by HA green body sintering. With this method, implants with six different channel designs were built successfully and the designed channels were reproduced in the HA implants. The channels created in the HA implants were between 366 and 968  $\mu\text{m}$  in diameter with standard deviations of 50  $\mu\text{m}$  or less. The compressive strength and compressive modulus measured for HA implants with orthogonal channels at 40% porosity were  $30 \pm 8$  MPa and  $1.4 \pm 0.4$  GPa, comparable to coralline porous HA [53]. Cylindrical HA implants with two architecture designs, orthogonal and radial channels, were implanted in the mandibles of four Yucatan minipigs for 5 and 9 weeks. Normal bone regeneration occurred in both groups. At 9 weeks, bone penetrated 1.4 mm into both scaffold designs. The percent bone ingrowth in the penetration zone was higher in the orthogonal channel design but not statistically different due to the low number of samples. However, the overall shape of the regenerated bone tissue was significantly different. In the orthogonal design, bone and HA formed an interpenetrating matrix, while in the radial design, the regenerated bone formed an intact piece at the center of the implant. These preliminary results showed that controlling the overall geometry of the regenerated bone tissue was possible through the internal architectural design of the scaffolds.

## **6.7 Clinical Practises in the Design and Manufacturing of Custom Bone Implants**

The production of medical models from CT and MRI data via rapid prototyping technologies have been reported to be beneficial to surgeons for diagnosis, planning, in the fabrication of custom implants, and the production of surgical devices. Through the use of the medical models, patients have experienced shorter surgical procedures, with more predictable results.

### ***6.7.1 Shaping Customised Implant by Using Rapid Prototype Biomodel***

Models made by rapid prototyping techniques can be used in several ways to shape customised implants. The most simple way is to use the model as a template on which a implant may be directly shaped intraoperatively. This is well illustrated in surgery to correct malar asymmetry where restorative augmentation is required. The bone graft may be harvested from the iliac crest and shaped directly on the sterilised model (Fig. 6.9(a)). Once the contouring is satisfactory the surgeon places the graft in situ and fixes it (Fig. 6.9(b)). This approach can dramatically reduce operating time whilst improving the end result. This technique also avoids the need for repeated fitting and chipping of the graft when the patient's malar is directly used as the templates, since direct shaping is restricted by soft tissue cover and limited surgical access.

Models can be also used to preoperatively shape custom craniofacial implants of relatively low complexity. Such implants are made in acrylic or titanium for a range of conditions including: craniotomy defects, tumour resections, facial trauma, and cosmetics. A case that exemplified the use of models in restorative maxillofacial surgery was that of a man who had sustained severe injuries to his lower face. The patient had already undergone several major procedures to reconstruct his mandible that had failed. Treated at Sydney's Westmead hospital, he was scanned by CT. The data was used to generate a model of his mandible. The model displayed the midline defect with both rami missing and the remains of the body deformed by previous surgery and bone grafting. The model was used firstly to preoperatively shape a titanium plate to fit the defect and restore the patient's occlusive bite. The titanium was implanted and fastened to the remaining ends of the mandible whilst a vascularised fibula graft was harvested and shaped according to the model. The graft was implanted on top of the plate and fastened with mini-screws. A free vascularised forearm graft was then used to cover the reconstructed mandible and micro-vascular anastomoses performed.

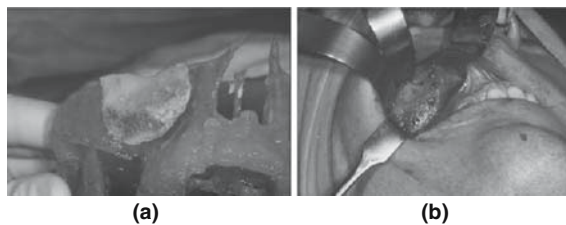


**Fig. 6.9** (a) Bone graft being shaped to augment biomodel maxilla, (b) Bone graft fitted exactly to patient with bone screws (<http://www.anatomics.com/resources/DOCUMENT/PS.BM.CS.Maxfac.Arvier.pdf>, Case courtesy of Dr. John Arvier, Brisbane, Australia)

Another approach is to use acrylic, or a similar material, to pre-operatively create a master implant to serve as a guide for the shaping of the bone graft intraoperatively. This is particularly appropriate when the graft requires a complex shape. The surgeon can minimise operating time by pre-operatively moulding the acrylic to the exact shape required, using the model as the template.

Singare [54] presented the design and manufacturing methods for medical prototyping (RP) of a custom-fabricated chin augmentation implant. Helical CT data was used to create a 3D model of the deficient mandible. Based on this data, the inner surface of the prosthesis was designed to fit the bone surface exactly. The outer geometry was generated from a dried human mandible to create anatomically correct shape prosthesis. RP was used for production of the physical models. The surgical planning was performed using the implants and skull models. The resulting SLA implant was used for the production of a mol, which is used to cast the titanium part. Patients with a congenital small chin or a small and asymmetric mandible underwent reconstruction with individual pre-fabricated implant. The result showed significant chin augmentation and excellent intra-operative fit. Postoperatively, the patients experienced the restoration of a natural chin contour. Over the mean follow-up period of 1.5 years, there were no complications and no implant had to be removed. This clinical case demonstrated the potential value of CAD/CAM and RP-based custom fitted and anatomically correct shape prosthesis fabrication and presurgical planning in craniofacial surgery.

Eppley [55] reported the effectiveness and safety of using computer-generated alloplastic hard tissue replacement (HTR) implants for the reconstruction of large defects of the cranio-orbital region when combined with simultaneous bone tumor excision. Seven patients who had large non-malignant bony lesions of the anterior cranial vault and orbit underwent simultaneous bony excision and reconstruction with preoperatively fabricated custom alloplastic implants. At the time of surgery, the implant was secured into position with either metal or resorbable plates and screws. In cases where the frontal sinus was in proximity to the implant, it was either cranialized and covered with a pericranial flap or obliterated with hydroxyapatite cement. All patients have healed uneventfully with a minimum of 1 year follow-up (average, 2.6 years). In all cases, excellent contours have been maintained and all patients have remained infection-free.

Bargar [56] reviewed the rationale and the efficacy of using a computed tomography-generated CAD/CAM custom femoral component in cementless total hip arthroplasty. One hundred and fifty-six cases (81 primary and 75 revisions) were reviewed with follow-up times of 6 weeks to 3 years (mean, 22 months). A subset of 48 hips (25 primary and 23 revisions) were followed for a minimum of 2 years. For the primary hips, the custom group was found to have statistically higher Harris pain scores (less pain) at all follow-up intervals as compared to a prior series by the same surgeon using an off-the-shelf (OTS) prosthesis. Revision customised hip implants had lower Harris pain and total

scores than primary custom hips, but 80% were in the none or slight pain category. In revision cases, the use of custom components decreased the need for structural bone grafting and achieved stability on host bone in situations in which it was not possible using OTS components. Complications included failure by aseptic loosening of one primary and one revision case. Initial subsidence of more than 3 mm of the collarless custom design occurred in 8%, the majority being in revision cases. All cases but one appear to have stabilized.

A group of researchers and doctors from the National University of Singapore, the National University Hospital and the Temasek Polytechnic have used FDM fabricated PCL bone scaffolds that fit neatly into the hole and bone defects of patients. A 23-year-old patient who met with an industrial accident 2 years ago was admitted to NUH as one of the first test subjects to receive the new FDM scaffold. The 3D PCL scaffold was fabricated to follow the curvature of the patient's skull; then some of his living bone cells were injected into the interconnected architecture of the scaffold. More than 2 years have passed and the patient is doing well, giving clinical confidence for the long-term usage of the FDM scaffold. His hair grew back and the scaffold fused smoothly with the surrounding tissue. In addition, the designed burr plug shaped like a flattened button mushroom can be directly manufactured for filling the holes when doctors have drilled one or two holes in the skull of a trauma or stroke patient to remove blood clots. After a clinical follow-up of 3 months, more than 14 patients who had been fitted with the implants showed good integration of plugs into the skull bone. For the first time new bone grew back to fill the hole which would otherwise have remained as a permanent depression [36].

### ***6.7.2 Cost Effectiveness***

Peckitt [57] stated that the cost of intra oral reconstruction utilizing stereolithographic model planning and a customized titanium implant manufacture in 1999 was £14,535 per case for purchasers, which was lower than that utilizing traditional free flap techniques which was estimated at £25,000. Also, if one considers the 2 year mortality for advanced mouth cancer to be in the region of 70%, the average cost of caring for a patient for a 2 year period is £85,000 for the free flap group assuming survival rate of three out of ten patients. Whereas, a group of seven patients with large tumours treated with customised implants, there have been no deaths in four and a half years at a cost of £14,535 per case and further investigation is warranted on much larger groups of patients. With respect to the management of trauma cases savings are higher per unit case as a function of the consequences of reduced surgical trauma. Savings of £30,000 are possible with projections of reduced operating times, less dependency on critical care facilities, earlier discharge from hospital, and enhanced rehabilitation. One case attending from the USA involved documented savings of \$150,000 for the purchasers.

## 6.8 Summary, Challenge and Future Directions

### 6.8.1 Summary

Recent investigations with RP and RM have demonstrated the potential to fabricate custom bone implants and scaffolds for individual patients. In particular, metal based implants with customised geometry have been able to be directly manufactured by RM techniques. Laser net-shape, selective laser melting and electron beam melting are able to process bio-grade metal materials such as titanium alloys and have shown the potential to fabricate custom metal implants for load bearing applications such as hip implants. Acram has sold the EBM12 system to a service bureau (Protocast S.R.L) who aims to use the EBM system predominantly for orthopaedic implants with an estimated yearly volume of 3000 parts. Another EBM system has been ordered by an Italian company in the biomedical field for volume production of orthopaedic implants. Examples of the biomedical industry beginning to use latest rapid manufacturing technologies for the volume production of customised implants illustrates the promise of rapid manufacturing technology for the customised implants production.

There have also been some successes in the research of rapid manufacturing of bioactive and biodegradable bone implants and scaffolds which may incorporate bioactive ceramics or bio-growth factors to enhance their biological performance and functions. Selective laser sintering (SLS) has been used to directly fabricate bone scaffold scaffolds and implants using bio-degradable polycarbonate (PCL) and bioactive ceramic/polymer composites (HA/PEEK, HA/PVA, HA/PLLA, etc). Recent studies have demonstrated the capability of SLS to process HAPEX<sup>TM</sup>, a clinically established bio-composite material. FDM is capable of processing PCL and several composites (PCL/HA, PCL/TCP) and has been used to fabricate PCL scaffolds for bone defect treatment such as plugs to fill the drilled holes which demonstrate good integration of the scaffolds into the skull bone in the clinical studies. Precise extrusion manufacturing (PEM) and low-temperature deposition manufacturing (LDM) were developed to fabricate PLLA and PLLA/TCP bone scaffolds. The in vivo study to repair segmental defects in canine radiuses show that bone marrow like tissues regenerated and the scaffold degraded after 24 weeks.

Novel RM techniques have shown the potential to process hybrid materials combined of artificial materials and biological materials such as cells, proteins and growth factors. The Bio-Plotter is especially noteworthy for its capability to fabricate a wide range of biomaterials and print viable cell/material constructs. Therefore, it might be possible to build bone implants and scaffolds with multiple, biocompatible materials with living cells/genes/proteins. In addition, low-temperature deposition manufacturing (LDM) [41] demonstrates the potential to process bio-degradable polymer/bioactive ceramic bone scaffolds and load protein and biogrowth factors in the scaffolds. It may also be possible

to deposit bone cells in the process due to the low temperature environment which preserve the biological performance of such materials.

### **6.8.2 Challenge**

In spite of the increasing success of using RM techniques for customised implants production, there are several challenges in terms of materials, mechanical strength, bioactivity, and resolution.

The range of biomaterials for direct RM is still limited due to the specific requirement of each RM process. Also, each RM technique requires a specific form of input material such as filament, powder, solid pellet or solution.

The matching of implants and bone tissue in respect to mechanical strength has not been achieved. Metal implants can be used for load bearing application, but the higher stiffness of these materials compared with natural bone can lead to stress shielding and consequently the loosening of the implants. Biopolymer and bioceramic composites have achieved properties similar to cancellous bone but not cortical bone.

Some RM technologies can process HA and TCP ceramic based composite materials to improve the bioactivity of the implants and tissue scaffolds. The capability of processes to incorporate biological growth factors may establish improved integration interfaces between implants and bone tissue. It is also important to investigate the strategy for controlled release of these growth factors to encourage cell response and tissue regeneration.

Morphology and internal architecture design have not been entirely optimised for the bone ingrowth and regenerations. Scaffold morphology and surface topography affect the adhesion and migration of cells. Pore size, pore morphology and interconnectivity are key parameters to encourage bone ingrowth and regeneration for implants to establish integration with existing structures or even replace natural bone when bio-degradable implants are used. Efficient CAD solutions need to be developed to provide highly complex biomimetic design.

### **6.8.3 Future**

There has, and continues to be, extensive research efforts being conducted worldwide to enhance and latterly exploit the capabilities of layer manufacturing techniques for the rapid manufacturing of customised implants. Looking towards the future, rapid manufacturing holds great potential in the fabrication of not only customised implants but also bioactive implants for bone replacement and tissue growth. The future research will focus on the investigation of bioactive process materials, emerging processes to construct hybrid biological/



artificial materials, the optimisation of mechanical properties and the control of bone growth and regeneration mechanisms.

## References

1. Salgado, A. J., Coutinho, O. P. and Reis, R. L. (2004). "Bone tissue engineering: State of the art and future trends." *Macromolecular Bioscience*, 4(8), 743–765.
2. Branemark, P. I. (1983). "Osseointegration and its experimental background." *Journal of Prosthetic Dentistry*, 50(3), 399–410.
3. Rimell, J. T. and Marquis, P. M. (2000). "Selective laser sintering of ultra high molecular weight polyethylene for clinical applications." *Journal of Biomedical Materials Research*, 53(4), 414–420.
4. Hieu, L. C., Zlatov, N., Sloten, J. V., Bohez, E., Khanh, L., Binh, P. H., Oris, P. and Toshev, Y. (2005). "Medical rapid prototyping applications and methods." *Assembly Automation*, 25(4), 284–292.
5. Moore, K. L. and Dalley, A. F. (1999). *Clinically Oriented Anatomy*, Lippincott Williams & Wilkins, Maryland.
6. Katti, K. S. (2004). "Biomaterials in total joint replacement." *Colloids and Surfaces B: Biointerfaces*, 39(3), 133–142.
7. Davis, J. R. (2003). *Handbook of Materials for Medical Devices*, ASM International.
8. Hollister, S. J., Lin, C. Y., Saito, E., Lin, C. Y., Schek, R. D., Taboas, J. M., Williams, J. M., Partee, B., Flanagan, C. L., Diggs, A., Wilke, E. N., Van Lenthe, G. H., Muller, R., Wirtz, T., Das, S., Feinberg, S. E. and Krebsbach, P. H. (2005). "Engineering craniofacial scaffolds." *Orthodontic Craniofacial Research*, 8, 162–173.
9. Leong, K. F., Cheah, C. M. and Chua, C. K. (2003). "Solid freeform fabrication of three-dimensional scaffolds for engineering replacement tissues and organs." *Biomaterials*, 24(13), 2363–2378.
10. Hutmacher, D. W., Sittinger, M. and Risbud, M. V. (2004). "Scaffold-based tissue engineering: rationale for computer-aided design and solid free-form fabrication systems." *Trends in Biotechnology*, 22(7), 354–362.
11. Hing, K. A., Best, S. M., Tanner, K. E., Bonfield, W. and Revell, P. A. (2004). "Mediation of bone ingrowth in porous hydroxyapatite bone graft substitutes." *Journal of Biomedical Materials Research Part A*, 68A(1), 187–200.
12. Rezwan, K., Chen, Q. Z., Blaker, J. J. and Boccaccini, A. R. (2006). "Biodegradable and bioactive porous polymer/inorganic composite scaffolds for bone tissue engineering." *Biomaterials*, 27(18), 3413–3431.
13. Hedges, M. (2003). "Lens™ Technology, Set to Revolutionise Medical Device Manufacture." [www.opnews.com/articles/126.sep.2003/articles.php](http://www.opnews.com/articles/126.sep.2003/articles.php).
14. "www.optomec.com."
15. Das, S., Hollister, S. J., Flanagan, C., Adewunmi, A., Bark, K., Chen, C., Ramaswamy, K., Rose, D. and Widjaja, E. "Computational design, freeform fabrication and testing of Nylon-6 tissue engineering scaffolds." *Rapid Prototyping Technologies*, Dec. 3–5 2002, Boston, MA, United States, 205–210.
16. Williams, J. M., Adewunmi, A., Schek, R. M., Flanagan, C. L., Krebsbach, P. H., Feinberg, S. E., Hollister, S. J. and Das, S. (2005). "Bone tissue engineering using polycaprolactone scaffolds fabricated via selective laser sintering." *Biomaterials*, 26(23), 4817–4827.
17. Partee, B., Hollister, S. J. and Das, S. (2006). "Selective laser sintering process optimization for layered manufacturing of CAPA (R) 6501 polycaprolactone bone tissue engineering scaffolds." *Journal of Manufacturing Science and Engineering-Transactions of the Asme*, 128(2), 531–540.

18. Lee, G., Barlow, J. W., Fox, W. C. and Aufdermorte, T. B. (1996) "Biocompatibility of SLS-formed calcium phosphate implants." *Proceedings of Solid Freeform Fabrication Symposium*, Austin, TX, 15-22. 12-14th August, 1996.
19. Vail, N. K., Swain, L. D., Fox, W. C., Aufdermorte, T. B., Lee, G. and Barlow, J. W. (1999). "Materials for biomedical applications." *Materials & Design*, 20(2-3), 123-132.
20. Tan, K. H., Chua, C. K., Leong, K. F., Cheah, C. M., Cheang, P., Abu Bakar, M. S. and Cha, S. W. (2003). "Scaffold development using selective laser sintering of polyetheretherketone-hydroxyapatite biocomposite blends." *Biomaterials*, 24(18), 3115-3123.
21. Tan, K. H., Chua, C. K., Leong, K. F., Naing, M. W. and Cheah, C. M. (2005). "Fabrication and characterization of three-dimensional poly(ether-ether-ketone)/hydroxyapatite biocomposite scaffolds using laser sintering." *Proceedings of the Institution of Mechanical Engineers Part H-Journal of Engineering in Medicine*, 219(H3), 183-194.
22. Chua, C. K., Leong, K. F., Tan, K. H., Wiria, F. E. and Cheah, C. M. (2004). "Development of tissue scaffolds using selective laser sintering of polyvinyl alcohol/hydroxyapatite biocomposite for craniofacial and joint defects." *Journal of Materials Science: Materials in Medicine*, 15(10), 1113-1121.
23. Cruz, F., Simoes, J., Coole, T. and Bucking, T. (2005) "Direct manufacturing of hydroxyapatite based bone implants by selective laser sintering." *2nd International Conference on Advanced Research in Virtual and Rapid Prototyping*, Leiria, Portugal.
24. Coole, T., Cruz, F., Simoes, J. and Bocking, C. (2005). "Customisation of bio-ceramic implants using SLS." *Virtual Modeling and Rapid Manufacturing – Advanced Research in Virtual and Rapid Prototyping*, Taylor & Francis Group, 147-151.
25. Hao, L., Savalani, M. M., Zhang, Y., Tanner, K. E. and Harris, R. A. (2006). "Selective laser sintering of hydroxyapatite reinforced polyethylene composites for bioactive implants and tissue scaffold development." *Proceedings of the Institution of Mechanical Engineers Part H-Journal of Engineering in Medicine*, 220(H4), 521-531.
26. Savalani, M. M., Hao, L. and Harris, R. A. (2006). "Evaluation of CO<sub>2</sub> and Nd : YAG lasers for the selective laser sintering of HAPEX<sup>(R)</sup>." *Proceedings of the Institution of Mechanical Engineers Part B-Journal of Engineering Manufacture*, 220(2), 171-182.
27. Hao, L., Savalani, M. M., Zhang, Y., Tanner, K. E. and Harris, R. A. (2006). "The effect of material and processing conditions on characteristics of hydroxyapatite and high density polyethylene bio-composite by selective laser sintering." *Proceedings of the IMechE Part L, Journal of Materials: Design & Application*. Accepted for publication.
28. Goodridge, R. D., Lorrison, J. C., Dalgarno, K. W. and Wood, D. J. (2004). "Comparison of direct and indirect selective laser sintering of porous apatite mullite glass ceramics." *Glass Technology*, 45(2), 94-96.
29. Goodridge, R. D., Dalgarno, K. W. and Wood, D. J. (2006). "Indirect selective laser sintering of an apatite-mullite glass-ceramic for potential use in bone replacement applications." *Proceedings of the Institution of Mechanical Engineers Part H-Journal of Engineering in Medicine*, 220(H1), 57-68.
30. Hayashi, T. (2005). "Selective laser sintering method using titanium powder sheet toward fabrication of porous bone substitutes." *JSME International Journal Series A*, 48(4), 369-375.
31. Hunt, J. A., Callaghan, J. T., Sutcliffe, C. J., Morgan, R. H., Halford, B. and Black, R. A. (2005). "The design and production of Co-Cr alloy implants with controlled surface topography by CAD-CAM method and their effects on osseointegration." *Biomaterials*, 26(29), 5890-5897.
32. Wehmoller, M., Warnke, P. H., Zilian, C. and Eufinger, H. (2005). "Implant design and production – a new approach by selective laser melting." *Computer Assisted Radiology and Surgery*, 1281, 690-695.
33. Hollander, D. A., von Walter, M., Wirtz, T., Sellei, R., Schmidt-Rohlfing, B., Paar, O. and Erli, H.-J. (2006). "Structural, mechanical and in vitro characterization of

- individually structured Ti-6Al-4V produced by direct laser forming." *Biomaterials*, 27(7), 955–963.
34. Zein, I., Hutmacher, D. W., Tan, K. C. and Teoh, S. H. (2002). "Fused deposition modeling of novel scaffold architectures for tissue engineering applications." *Biomaterials*, 23(4), 1169–1185.
  35. Endres, M., Hutmacher, D. W., Salgado, A. J., Kaps, C., Ringe, J., Reis, R. L., Sittinger, M., Brandwood, A. and Schantz, J. T. (2003). "Osteogenic induction of human bone marrow-derived mesenchymal progenitor cells in novel synthetic polymer-hydrogel matrices." *Tissue Engineering*, 9(4), 689–702.
  36. Rai, B., Teoh, S. H., Ho, K. H., Hutmacher, D. W., Cao, T., Chen, F. and Yacob, K. (2004). "The effect of rhBMP-2 on canine osteoblasts seeded onto 3D bioactive polycaprolactone scaffolds." *Biomaterials*, 25(24), 5499–5506.
  37. Shao, X. X., Hutmacher, D. W., Ho, S. T., Goh, J. C. H. and Lee, E. H. (2006). "Evaluation of a hybrid scaffold/cell construct in repair of high-load-bearing osteochondral defects in rabbits." *Biomaterials*, 27(7), 1071–1080.
  38. Yeong, W.-Y., Chua, C.-K., Leong, K.-F. and Chandrasekaran, M. (2004). "Rapid prototyping in tissue engineering: challenges and potential." *Trends in Biotechnology*, 22(12), 643–652.
  39. Wang, F., Shor, L., Darling, A., Khalil, S., Sun, W., Guceri, S. and Lau, A. (2004). "Precision extruding deposition and characterization of cellular poly-epsilon-caprolactone tissue scaffolds." *Rapid Prototyping Journal*, 10(1), 42–49.
  40. Xiong, Z., Yan, Y. N., Zhang, R. J. and Sun, L. (2001). "Fabrication of porous poly(L-lactic acid) scaffolds for bone tissue engineering via precise extrusion." *Scripta Materialia*, 45(7), 773–779.
  41. Xiong, Z., Yan, Y. N., Wang, S. G., Zhang, R. J. and Zhang, C. (2002). "Fabrication of porous scaffolds for bone tissue engineering via low-temperature deposition." *Scripta Materialia*, 46(11), 771–776.
  42. Yan, Y. N., Xiong, Z., Hu, Y. Y., Wang, S. G., Zhang, R. J. and Zhang, C. (2003). "Layered manufacturing of tissue engineering scaffolds via multi-nozzle deposition." *Materials Letters*, 57(18), 2623–2628.
  43. Landers, R., Hubner, U., Schmelzeisen, R. and Mulhaupt, R. (2002). "Rapid prototyping of scaffolds derived from thermoreversible hydrogels and tailored for applications in tissue engineering." *Biomaterials*, 23(23), 4437–4447.
  44. Landers, R., Pfister, A., Hubner, U., John, H., Schmelzeisen, R. and Mulhaupt, R. (2002). "Fabrication of soft tissue engineering scaffolds by means of rapid prototyping techniques." *Journal of Materials Science*, 37(15), 3107–3116.
  45. Carvalho, C., Landers, R., Mulhaupt, R., Hubner, U. and Schmelzeisen, R. (2005). "Fabrication of soft and hard biocompatible scaffolds using 3D-Bioplotting (TM)." *Virtual Modeling and Rapid Manufacturing – Advanced Research in Virtual and Rapid Prototyping*, 97–102.
  46. Li, J. P., de Wijn, J. R., Van Blitterswijk, C. A. and de Groot, K. (2006). "Porous Ti6Al4V scaffold directly fabricating by rapid prototyping: Preparation and in vitro experiment." *Biomaterials*, 27(8), 1223–1235.
  47. Sachs, E., Cima, M., Williams, P., Brancazio, D. and Cornie, J. (1992). "Three dimensional printing. Rapid Tooling and prototypes directly from a CAD model." *Journal of Engineering for Industry, Transactions of the ASME*, 114(4), 481–488.
  48. Sherwood, J. K., Riley, S. L., Palazzolo, R., Brown, S. C., Monkhouse, D. C., Coates, M., Griffith, L. G., Landeen, L. K. and Ratcliffe, A. (2002). "A three-dimensional osteochondral composite scaffold for articular cartilage repair." *Biomaterials*, 23(24), 4739–4751.
  49. Dutta Roy, T., Simon, J. L., Ricci, J. L., Rekow, E. D., Thompson, V. P. and Parsons, J. R. (2003). "Performance of degradable composite bone repair products made via three-dimensional fabrication techniques." *Journal of Biomedical Materials Research – Part A*, 66(2), 283–291.

50. Seitz, H., Rieder, W., Irsen, S., Leukers, B. and Tille, C. (2005). "Three-dimensional printing of porous ceramic scaffolds for bone tissue engineering." *Journal of Biomedical Materials Research – Part B Applied Biomaterials*, 74(2), 782–788.
51. Chu, G. T. M., Brady, G. A., Miao, W., Halloran, J. W., Hollister, S. J. and Brei, D. (1999) "Ceramic SFF by direct and indirect stereolithography." *Solid Freeform and Additive Fabrication: a Materials Research Society Symposium*, Boston, USA, 119–123.
52. Chu, T.-M. G., Halloran, J. W., Hollister, S. J. and Feinberg, S. E. (2001). "Hydroxyapatite implants with designed internal architecture." *Journal of Materials Science: Materials in Medicine*, 12(6), 471–478.
53. Chu, T.-M. G., Orton, D. G., Hollister, S. J., Feinberg, S. E. and Halloran, J. W. (2002). "Mechanical and in vivo performance of hydroxyapatite implants with controlled architectures." *Biomaterials*, 23(5), 1283–1293.
54. Singare, S., Dichen, L., Bingheng, L., Zhenyu, G. and Yaxiong, L. (2005). "Customized design and manufacturing of chin implant based on rapid prototyping." *Rapid Prototyping Journal*, 11(2), 113–118.
55. Eppley, B. L. (2002). "Craniofacial reconstruction with computer-generate HTR patient-matched implants: use in primary bony tumor excision." *Journal of Craniofacial Surgery*, 13(5), 650–657.
56. Bargar, W. L. (1989). "Shape the implant to the patient. A rationale for the use of custom-fit cementless total implants." *Clinical Orthopaedics Related Research*, 249, 73–78.
57. Peckitt, N. S. (2001) "Rapid prototypes and customized implants in maxillofacial reconstruction." In *Rapid Prototyping Casebook*, Professional Engineering Publications, 191–200.

# Chapter 7

## Direct Digital Manufacturing of Complex Dental Prostheses

B. Vandenbroucke and J. -P. Kruth

### 7.1 Introduction

Over the last decade Reverse Engineering, Computer-Aided Design, Computer-Aided Manufacturing and Rapid Prototyping (RE, CAD, CAM, RP) have been applied to medicine and dentistry (Gibson, 2005). Diagnostic tools have become increasingly more sophisticated and medical imaging technology can now present patient data with high precision. Virtual planning environments allow data visualization and manipulation. Many dedicated CAD/CAM systems were introduced to the medical and dental community (Rudolph et al., 2003). With RP there came a way to produce custom physical models of patient anatomy providing doctors the means for tactile interaction which facilitates preoperative planning of complex surgeries. In addition, RP-generated replicas act often as basis for customization of treatment devices such as craniofacial plates. RP-techniques are also used to create custom treatment aides such as dental drilling guides (Ref. Materialise website) that transfer the digital planning to the patient in a reliable way.

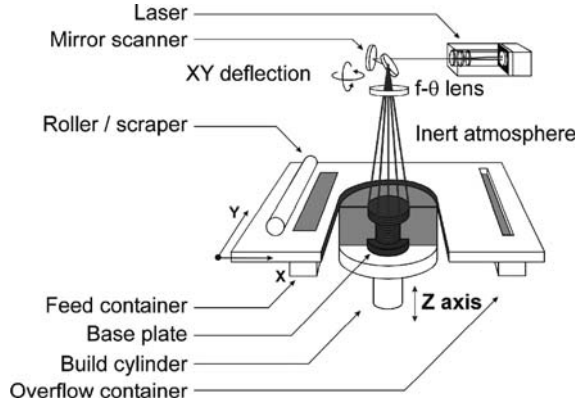
Because of cost advantages and standardizing possibilities it's clear that digitizing and automation have gained an important place in the fabrication of medical products. However, many dental metal parts are still being produced by manual and inefficient conventional methods. Offering a digital solution to the dental profession implies a real challenge because patient and dentist set high requirements on quality, material and precision. No existing CAD/CAM system can totally replace the traditional dental practices, but emerging technologies may expand the capabilities of future systems (Strub et al., 2006).

In recent years, Rapid Prototyping evolved to Rapid Manufacturing (RM) because of technical improvements of Layer Manufacturing (LM) processes and due to the possibility to process all kinds of metals (Levy et al., 2003).

---

B. Vandenbroucke  
Division PMA, Department of Mechanical Engineering, Katholieke Universiteit Leuven,  
Belgium  
ben.vandenbroucke@mech.kuleuven.be

**Fig. 7.1** Scheme of SLM process



Dental applications could take advantage of this evolution by using LM not only for plastic devices like visual anatomical models or one-time surgical guides, but also for functional implants or prostheses with long-term consistency made from a biocompatible metal (Abe et al., 2000).

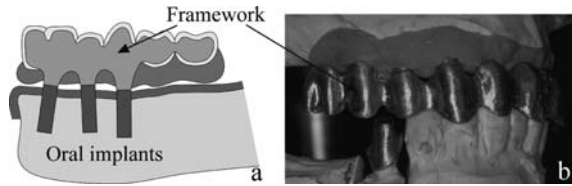
Selective Laser Melting (SLM) has taken the lead as Direct Digital Manufacturing (DDM) technique for metal parts. SLM (Fig. 7.1) is a layer-wise material addition technique that allows generating complex 3D parts by selectively melting successive layers of metal powder on top of each other, using the thermal energy of a focused and computer controlled laser beam (Over et al., 2002; Kruth, Mercelis et al., 2005). The competitive advantages of SLM are geometrical freedom and material flexibility (metals). Dental parts, like crowns, bridges and frameworks, are very suitable to be produced by SLM due to their complex geometry, low volume, strong individualization and high aggregate price. Moreover, the manufacturing of multiple unique parts in a single production run enables mass customization.

This chapter discusses the use of SLM as RM technique for metal frameworks for complex dental prostheses. Procedures are described for dental data capture, for digital design and for manufacturing by SLM. Quality control has been performed on produced frameworks and the procedures were validated by clinical cases.

## 7.2 Frameworks for Complex Dental Prostheses

This study presents a digital solution to design and produce implant-supported biometal frameworks for complex dental prostheses (Fig. 7.2) (Ortrop et al., 2000). The intended framework is the metal base structure of the prosthesis. It is supported by oral implants placed in the jawbone of the edentulous patient. Such framework is fixed to the jaw by screws retaining it on the implants. The framework supports the artificial teeth that are attached on top of the framework. The 'upper' shape of the framework (i.e. teeth side) depends on the type of tooth aesthetics. When standard polymer teeth are used, a bar shape is sufficient.

**Fig. 7.2** (a) Scheme of implant-supported prosthesis; (b) Framework fitting on upper jaw model



When a veneering porcelain layer is applied to create the individual tooth surfaces, the tooth shapes should be included in the design of the framework.

The framework can be made from ceramics, mainly alumina- or zirconia-based, from precious metal alloys, mainly gold- and platinum-based or from non-precious metal alloys, mainly cobalt-chromium or titanium alloys (Strietzel, 2004). This study will focus on the non-precious metal alloys. Cobalt-chromium and titanium alloys combine good mechanical and biocompatible properties and can be processed successfully by SLM. According to the state-of-the-art, laser-based RM processes are yet not able to process ceramics to accurate parts with good mechanical properties.

A framework is patient specific and has to meet strict requirements of accuracy to minimize the risk of mechanical or biological failures of the prosthetic system. To avoid high stresses in the jawbone causing the oral implants to loose and to diminish the risk for colonization of bacteria resulting in infection and eventually bone loss, severe fit criteria below 40  $\mu\text{m}$  are necessary at the framework-implant junctions (Jemt et al., 1998; Riedy et al., 1997).

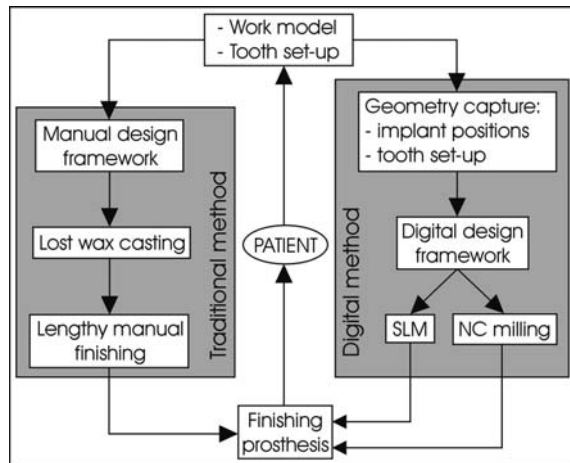
Digital procedures have been developed for designing and manufacturing of dental frameworks. They replace the traditional methods based on a manual design by ‘clay’ modeling and a production by lost wax casting. These conventional processes are still widely used, although they are time consuming and inefficient. The lost wax method is a lengthy and labor-intensive process and comprises many manual steps: creating, embedding and burning out the wax pattern, metal casting and post-processing. Moreover, its accuracy is generally lower than for digital procedures.

Figure 7.3 compares the traditional with the digital method for fabricating a dental framework. After installing the oral implants into the jawbone of the patient, a plaster work model with implant replicas is made representing the position of the implants. Upon this work model a tooth set-up is shaped from which the patient validates the aesthetics. This tooth set-up looks the same as the final prosthesis but the internal framework is still absent.

The digital procedure consists of three main steps: the digital geometry capture of implant positions and tooth set-up, the digital design of the framework and the computer-driven production of the framework by NC milling or by SLM. Fixing the artificial teeth (porcelain or polymer) on top of the framework finishes the prosthesis and the final prosthesis can be installed in the mouth of the patient.

In recent years many CAD/CAM systems based on NC milling have been developed for different dental applications. Dedicated dental milling units are

**Fig. 7.3** Traditional and digital method to manufacture a dental framework



commercially available for producing ceramic or metal crowns, small bridges and tooth-supported frames, e.g. *Cercon* (Degudent), *CEREC* (Sirona), *President DCS* (DCS), *Lava* (3M ESPE), etc. By these milling stations the dental laboratories can fabricate the dental restorations in house. The other possibility is that the dental laboratories handle only the CAD issues, while central production centers deal with the CAM issues and NC milling, e.g. implant-supported frameworks by *Procera* (Nobel Biocare).

The key advantages of NC milling are the high achievable accuracy and the possibility to process ceramics (mostly in green stage). The subtractive fabrication can create complete frameworks effectively, but at the expense of wasted material. Complex tool path calculations and spatial restrictions can limit the production of complex frameworks by NC milling.

The rest of this chapter will focus on SLM for the manufacturing of frameworks. SLM allows an efficient and customized production of the complex framework for different metal alloys. Remaining unprocessed powder can be reused. Two commercial systems use already SLM as central production process for crowns, small bridges and small tooth-supported frames from cobalt-chromium and precious alloys, *Medifabricating* (BEGO) and *infiniDent* (Sirona). K.U.Leuven developed a procedure to manufacture implant-supported frameworks by SLM from titanium and cobalt-chromium alloys (Kruth, Vandenbroucke et al., 2005).

### 7.3 Dental Data Capture

The first step of every dental CAD/CAM system is digitizing the oral environment of the patient. For the framework application, the input geometry is twofold: the implant positions and the tooth set-up. No existing system can yet acquire this dental data directly in the mouth of the patient with high



precision. However, emerging technologies and new research will put emphasis on developing accurate intra-oral scanners (Strub et al., 2006). In this way, manual interventions like taking impressions and making plaster work models could be avoided.

The position and inclination of each implant vary depending on the presence of qualitative and quantitative surrounding bone and on the anatomical location of nerves and blood vessels. The measurement of the position of the implants has to be very accurate with regard to the final fit between framework and each implant. Due to the complexity of the upper part of the implants and because implants are often installed deeply in the tissue, mechanical or optical techniques have difficulties to measure directly the position of the implants. Therefore the use of registration elements is preferred. Figure 7.4(a) shows for example cylindrical registration elements mounted upon the implant replicas of the work model.

These registration elements can be measured by contact digitizers or by optical scanners. There has also been tried to measure them by 3D Micro Computer Tomography (*Tomohawk*), but the outcome could not fulfill the required precision and this procedure is more relevant when cross-sectional images are wanted.

Contact digitizers are more accurate than optical scanners but the digitizing process is slower and less easy to automate. For a rapid and fully digital procedure, optical scanners are preferred. For one case with five framework-implant connections, the measurement results of five different optical scanning systems have been compared with the outcome of a contact digitizer. As contact measurement method a tactile probe (*Renishaw*) mounted on a Coordinates Measurement Machine (*Mitutoyo*) has been operated manually to measure the position and inclination of each registration element with high precision ( $<10\ \mu\text{m}$ ), as shown on Fig. 7.4(b).

Five different optical scanners (Table 7.1) have also measured these five registration elements. Two dedicated dental scanners and three scanners for general purpose were tested. The accuracy stated by the manufacturers varies from 20 to 40  $\mu\text{m}$  for all five types<sup>1</sup>. An optical scan of the mounted

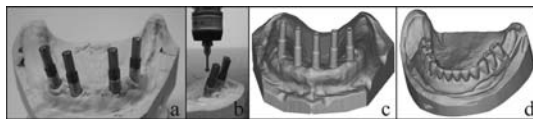


**Fig. 7.4** (a) Registration elements; (b) Tactile probe; (c) Meshed scan of registration elements; (d) Meshed scan of tooth set-up  
(Source: K.U.Leuven)

<sup>1</sup> The accuracies stated by the manufacturers are not really comparable as they are obtained under different conditions and represent quite different quantities: e.g.  $1\sigma$ ,  $2\sigma$  or  $3\sigma$  values, variation on individual measuring points or on geometrical feature size or position, etc.

**Table 7.1** The five tested optical scanners with their manufacturer and measurement principle

Optical scanner	Company	Measurement principle
Dental 3D Scanner D-250	3shape	Laser line scanning (2D triangulation)
Dental Laserscan 3D	Willytec	Laser line scanning (2D triangulation)
Atos Small Objects 3D Digitizer	GOM	White light pattern projection (3D triangulation)
Optical probe LC50 (Coupled to 3D CMM)	Metris	Laser line scanning (2D triangulation)
3D Digitizer VI-910	Minolta	Laser line scanning (2D triangulation)

registration elements typically leads to a point cloud of more than 300.000 points (Fig. 7.4(c)).

Using numerical algorithms the position and inclination of each registration element were computed. The midpoint coordinates of every implant top plane were compared with the ones obtained by tactile measurement. The maximum deviation in the direction perpendicular to the implant plane was 15  $\mu\text{m}$  and within the plane 35  $\mu\text{m}$ . Consequently, optical scanning can capture the implant positions with sufficient precision.

The measurement of position and inclination of the registration elements provide sufficient information to design the ‘lower’ part of the framework that fits on the implants. The precision of digitizing the tooth set-up is not very critical, in contrast to the position of the implants, because no major effect is stated with regard to possible biological or mechanical failures. Any optical scanner can digitize the tooth set-up (Fig. 7.4(d)). Since the data of the implant positions will have to be combined with the tooth set-up data, both measurements are mathematically matched with the work model as reference object.

## 7.4 Digital Design

The second step of any digital solution to fabricate dental parts is the virtual design based on the digitized input geometry. Many dedicated CAD software programs are commercially available to design dental restorations like crowns, bridges and small frames (Rudolph et al., 2003). However, no commercial CAD system exists today for complete design of implant-supported frameworks for complex prostheses replacing multiple teeth. K.U.Leuven has developed a design method for these frameworks based on the captured implant positions and digitized tooth set-up.

This digital design replaces the conventional manual design, requiring a lot of experience and good skill of the dental technician who builds up the framework from wax material. Based on the many manual actions of the technician, several design rules were defined and were put in a certain sequence. This design strategy was implemented in a software module by translating the design rules to computer tools. Some user interaction is still required to design the

framework since a fully automated CAD system seemed not possible for these complex parts.

An important issue during the design step is the manipulation of the complex dataflow. The different and large data files have to be filtered and combined to one geometrical model in a fast and convenient way. Because the input data files are mainly point clouds without mathematical surface representation and because the file format for SLM is the STL (Standard Triangulation Language) format, it is preferred to use STL-based CAD software instead of conventional CAD software. K.U.Leuven used the STL-based *3Matic* software from Materialise (Ref. Materialise website).

The design of the framework depends on the type of tooth aesthetics. For standard polymer teeth, a bar-shaped framework is sufficient, while for veneering porcelain teeth, the tooth shapes should be included in the design of the framework.

The framework design process for porcelain tooth aesthetics is illustrated in Fig. 7.5 (*left*). Firstly, the measured point cloud data of the tooth set-up is converted into a triangular mesh model (a), representing the desired shape of the final prosthesis (b). Each artificial tooth of the final prosthesis needs a support surface for porcelain veneering on top of the framework. The different teeth can be identified by means of a curvature analysis (c). Each separate tooth surface, obtained by cutting the tooth set-up model, is incomplete because the side surfaces are missing (d). These side surfaces are needed to compute the offset of the total tooth surfaces. Therefore, each incomplete tooth surface is matched with a full model of the corresponding standard tooth surface (e). A digital library of standard tooth surfaces is available. The support surfaces of the framework are then computed by a defined offset of the completed tooth surfaces (f). The measured position and inclination of the implants are transferred to the design environment. Conical fitting structures are designed according to these data (g) and connected to the support surfaces of the teeth (h). Detail features like screw holes and fillets are added which finishes the digital design of the framework (i).

A similar framework design process for polymer tooth aesthetics is developed. Figure 7.5 (*right*) shows the bar-shaped outcome for a framework with six

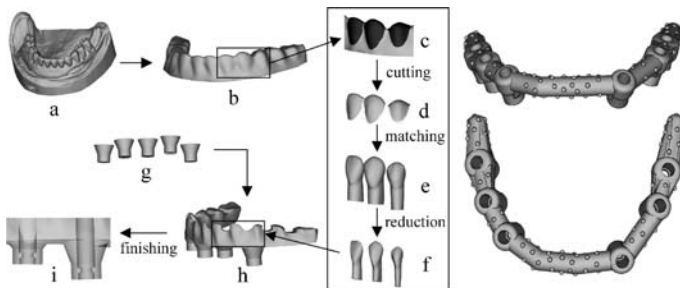


**Fig. 7.5** (*left*) Framework design strategy for veneering porcelain teeth; (*right*) Framework bar-shaped design for standard polymer teeth (Source: K.U.Leuven)

implant-junctions. Small ball-features were added to the surface to increase the mechanical retention and adhesion between teeth and framework. Dr. Leu at the University of Missouri-Rolla has developed a similar design method for dental bars (Leu et al., 2006).

State-of-the-art CAD packages allow designing complex dental parts in an efficient way. Further developments may include simpler GUI (Graphical User Interface) and integration of virtual articulators, which would lead to further automation of dental restoration design (Strub et al., 2006).

## 7.5 Production by SLM

The third step of the digital procedure is the manufacturing of the dental framework by SLM. This Rapid Manufacturing technique uses a computer controlled laser beam for scanning successive layers of powder material to create the 3D framework. Based on the slicing of the digital design, scanning patterns of each layer are computed automatically. Full part density is reached within one step by melting the metal powder completely by the laser beam. The CAM component consists only of positioning the framework virtually in the build volume of the SLM machine, slicing this positioned CAD model and setting the optimal process parameters.

Two commercial systems use already SLM as central production process for dental restorations, other than implant-supported frameworks. The German company BEGO uses *Trumaform* (Trumpf) laser-melting machines to produce crowns, bridges and small tooth-supported frames from cobalt-chromium and precious alloys (Ref. BEGO website). This CAD/CAM system is called *Medifactoring*. The German company Sirona has a central production unit, called *infiniDent*, where *EOSINT* (EOS) laser-melting machines are used to produce similar dental restorations from the same alloys (Ref. Sirona website). Figure 7.6 shows a tooth-supported frame and bridge made by *Medifactoring* and *infiniDent*, respectively.

K.U.Leuven has used an M3linear (Concept Laser) laser-melting machine to produce implant-supported frameworks from titanium and cobalt-chromium alloys (Naert et al., 2005). The titanium material used was a commercial powder and the cobalt-chromium powder was made in house by IGAP (Induction melting Gas Atomization Process), which led to spherical particles with very



**Fig. 7.6** (left) Tooth-supported frame made by BEGO *Medifactoring*; (right) Tooth-supported bridge made by Sirona *infiniDent*

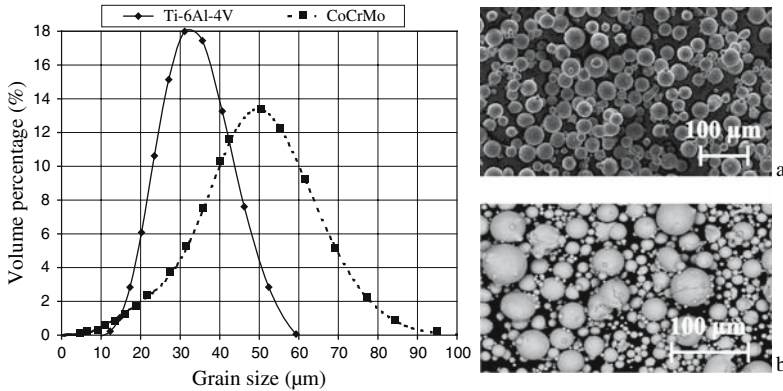


**Fig. 7.7** Grain size distribution and micrographs of titanium (a) and cobalt-chromium (b) powder used (Source: K.U.Leuven)

low amount of interstitial impurities. Figure 7.7 shows the grain size distribution of both powders, determined by laser diffraction, and SEM micrographs indicate the morphology. Because of high reactivity of titanium to interstitial elements such as oxygen, nitrogen and hydrogen, the SLM process was carried out in a closed chamber continuously flushed with argon gas to reduce the oxygen level (< 0.1%). Cobalt-chromium was processed in a nitrogen atmosphere.

SLM is a complex thermo-physical process that depends on a lot of material, laser, scan and environmental parameters (Table 7.2). For both selected materials, a parameter study has been performed to optimize the process regarding part density, since porosity has a harmful effect on the mechanical properties of the part. Four main process parameters were selected for experimentation: laser power, layer thickness, scan speed and hatch spacing. These factors determine the energy supplied by the laser beam to a volumetric unit of powder material, defined as energy density, an experimental quantity that has large influence on part density:

$$E_{density} = \frac{P_{laser}}{V_{scan} S_{hatch} t_{layer}}$$

**Table 7.2** Process parameters of SLM, divided into four categories

Material	Laser	Scan	Environmental
Composition	Mode	Scan speed	Gas type
Powder density	Wave length	Hatch spacing	Oxygen level
Morphology	Power	Layer thickness	Pressure
Grain diameter	Frequency	Scan strategy	Preheating
Distribution	Pulse width	San sectors	
Thermal properties	Offset	Pulse distance	
Flow properties	Spot size	Scaling factors	

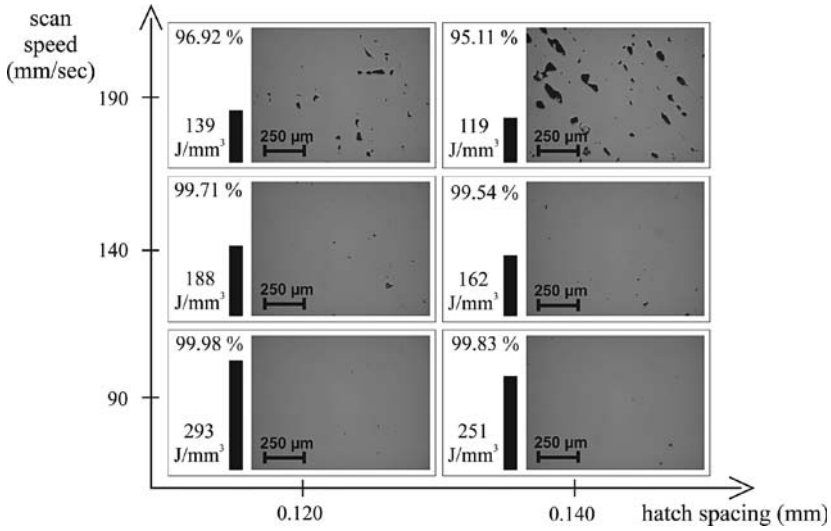


**Fig. 7.8** SLM process parameter study for Ti-6Al-4V. Used energy density, measured part density and one micrograph are shown for six parameter sets (Source: K.U.Leuven)

where  $E_{density}$  = energy density,  $P_{laser}$  = laser power,  $v_{scan}$  = scan speed,  $s_{hatch}$  = hatch spacing,  $t_{layer}$  = layer thickness.

Figure 7.8 shows some results of the parameter study for titanium material (Ti-6Al-4V). Laser power (95W) and layer thickness ( $30\ \mu\text{m}$ ) were kept constant and scan speed and hatch spacing were varied. The energy density, the measured part density and one micrograph are shown for each tested parameter set. It is clear that higher energy density leads to higher part density. For low energy input, successive scan tracks are not fully molten and large pores appear along the scan lines. For titanium as well as for cobalt-chromium alloys, part densities up to 99.9% and even higher are reached. Because of physical properties of the material the SLM process is easier to control for cobalt-chromium and high part density is reached with higher build rate ( $4\ \text{cm}^3/\text{h}$  vs  $2\ \text{cm}^3/\text{h}$  for titanium).

Before the production of the framework can be started, some geometrical decisions have to be taken with regard to the position of the framework within the build volume of the SLM machine. Firstly, the framework is positioned upside down (i.e. teeth side below) to guarantee well-finished implant fitting planes and secondly, the framework is tilted to reduce the stair effect and the volume of support structures.

Top surfaces of a part manufactured by SLM have a relatively low roughness and high accuracy. Bottom or overhanging surfaces are not finished well because of two reasons. Firstly, since the laser beam scans in loose powder instead of on solid material, heat transfer decreases and temperature increases leading to instable melt pools. Secondly, stalactite

patterns are formed because the melt sinks in the loose powder by gravity. The fitting planes of the framework that make the connection with the implants need to be very accurate. Therefore the framework is positioned upside down within the build volume to guarantee an accurate finish of the fitting planes.

Due to the layer-wise production of SLM a stair effect appears on the inclined fitting planes of the framework. This yields gaps between the framework and the implants, leading to local inaccuracies (Fig. 7.9(a)). Since the inclination angles of the implants and hence of the fitting planes differ, only one plane can be positioned horizontally and thus the stair effect cannot be avoided.

The gap size can be reduced by decreasing the layer thickness or by increasing the sloping angle. The layer thickness is difficult to change because its value depends on the powder grain size. By tilting the framework in the build volume the fitting planes become steeper and more stairs appear while the gaps become smaller (Fig. 7.9(a) right).

When choosing the tilt angle of the framework to minimize the gap size of all fitting planes, the need for support structures has to be taken into account. Support structures are used to avoid down-facing or low-angle overhanging surfaces and to connect the part to the base plate. After the part has been produced, the support structures have to be removed manually and thus their volume should be as low as possible. The support structures are shaped as a grid to make a clear difference between part and support material at the junction (Fig. 7.9(b) bottom).

As a result of the developed procedure, including dental data capture, digital design and production by SLM, Fig. 7.10 shows a dental framework from titanium (Ti-6Al-4V).

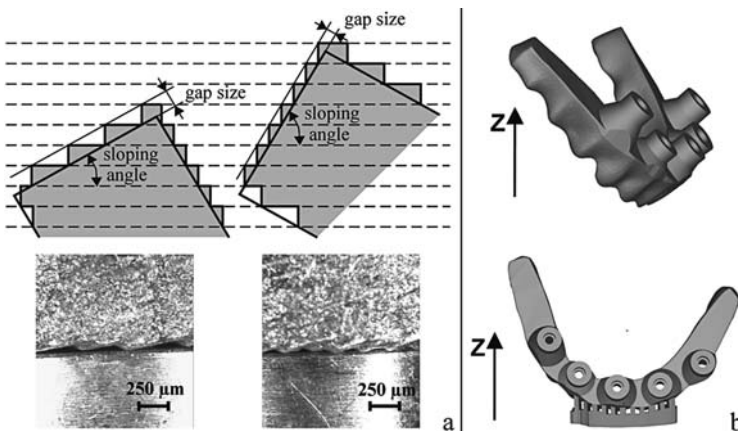


**Fig. 7.9** (a) Stair effect of layer-wise production leading to gaps between framework fitting plane and implant. Small/Large sloping angle leads to few/many stairs with large/small gap size (left/right). (b) Tilted position of framework (*up*) and design of support structures (*down*) (Source: K.U.Leuven)

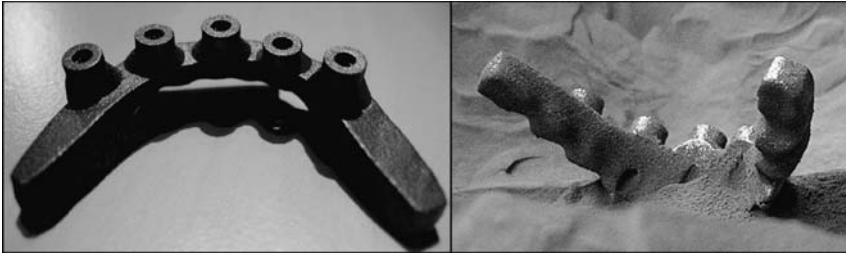


**Fig. 7.10** (left) Bottom view of dental framework made by SLM from titanium; (right) Framework emerging from the powder bed (Source: K.U.Leuven)

## 7.6 Quality Control

To turn SLM into a manufacturing technique for implants or prostheses, some important conditions have to be fulfilled. The laser-melted parts have to meet strict requirements regarding mechanical and chemical properties and the process must guarantee high accuracy. Next to these quality requirements the breakthrough of SLM as a medical Rapid Manufacturing technique will depend on reliability, performance and economical aspects like production and cost. K.U.Leuven has fully characterized the SLM process for cobalt-chromium and titanium alloys (Vandenbroucke et al., 2006).

Many mechanical tests have been performed on both materials. Figure 7.11 shows for example stress-strain curves of tensile tests on titanium SLM samples. The graphs prove high repeatability for mechanical properties. The table in Fig. 7.11 summarizes all measured mechanical properties for Ti-6Al-4V SLM samples. The obtained properties are compared with those of bulk material, STA

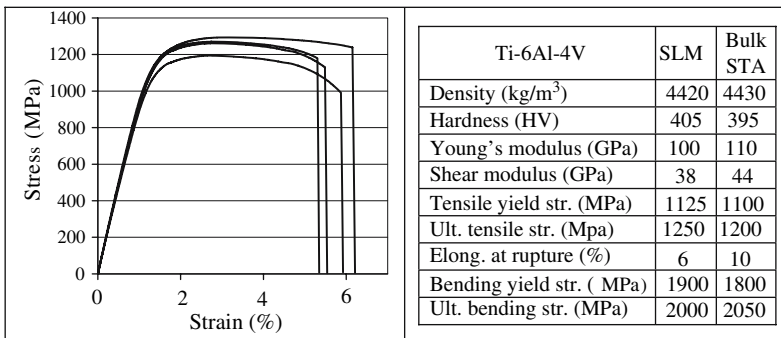


**Fig. 7.11** (left) Stress-strain graphs of tensile tests for titanium samples; (right) Mechanical properties of titanium SLM samples and of bulk material STA (= Solution Treated Aged) (Source: K.U.Leuven)



(Solution Treated Aged), from literature. The results for SLM are similar to the stated properties of the bulk material, except for elongation at rupture. The ductility is somewhat lower because during the SLM process the melt pool cools down very rapidly when the laser beam has passed, leading to slight embrittlement. The full mechanical analysis shows that the SLM material fulfills the required strength and stiffness for the dental framework applications.

Both selected materials have also been tested for their chemical properties. The corrosion behavior is of high interest to value biocompatibility. Titanium as well as cobalt-chromium alloys are considered as corrosion resistant and biocompatible materials. Nevertheless, the very complex chemistry of the oral cavity may reveal surprises concerning corrosion processes (Strietzel et al., 1998). The corrosion characteristics of SLM samples were examined by static immersion tests in a corrosion solution. The solutions were analyzed by ICP-OES (Inductively Coupled Plasma-Optic Emission Spectrometry) to determine the different ion emissions. Figure 7.12 shows for example the corrosion rate of titanium as a function of time. The emission of Ti-ions decreases rapidly within the first few days to approach a final low value, similar to corrosion rates of bulk titanium material. These chemical analyses demonstrate favorable corrosion behavior for the SLM samples.

Dimensional analyses on benchmark parts have been performed to test the SLM process accuracy. For parts smaller than a dental work model ( $60 \times 60 \times 30 \text{ mm}^3$ ) the overall point-to-point accuracy is below  $60 \text{ }\mu\text{m}$ . In dental literature there is a growing consensus that the final gap size between framework and implant should not exceed  $40 \text{ }\mu\text{m}$  to avoid failures of the prosthetic system (Renouard, 1999). Therefore, the accuracy of the fit between framework and implants has been analyzed. When the framework is screw-retained on all implants very slightly, the mean gap size between framework and implants amounts to  $25 \text{ }\mu\text{m}$ . This means that SLM guarantees the needed precision by optimal process parameters and an appropriate production strategy.

The developed procedure allows an efficient production of complex frameworks by SLM. The build time per framework declines for increasing number of frameworks produced during the same build, because powder-depositing time is spread

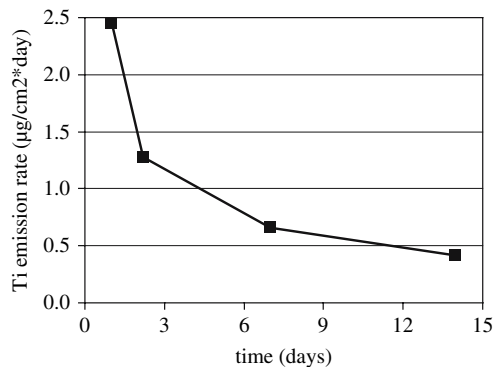
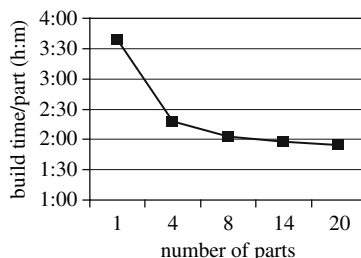


**Fig. 7.12** Titanium corrosion rate of SLM samples as a function of time (Source: K.U.Leuven)

**Fig. 7.13** Build time per framework versus number of produced frameworks (Source: K.U.Leuven)



over all frameworks (Fig. 7.13). When eight frameworks are produced during one production run, the build takes sixteen hours or two hours per framework, which is half of the build time when only one framework is produced. A lot of time and money can thus be saved by producing multiple unique frameworks in a single production run, leading to mass customization and to a lower price.

## 7.7 Clinical Cases

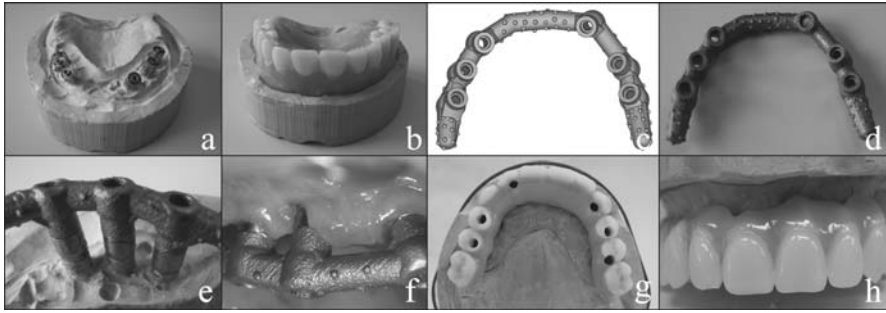
The developed procedure to digitally design and manufacture dental frameworks has been applied for five clinical cases. Table 7.3 indicates for each case the number of implants, the jaw on which the framework fits (lower jaw = mandible or upper jaw = maxilla) and the level of installation (implant or abutment level). For all cases the artificial teeth were standard polymer teeth and all frameworks were produced from titanium.

Figure 7.14 shows some pictures of the procedure for clinical case 1. The position of the implant replicas of the plaster work model (a) was measured and the tooth set-up (b) was digitized. Based on these data the digital design of the framework (c) was made. After the SLM production of the framework (d) the fit between framework and implants was checked on the work model (e) and in the mouth of the patient (f). The fit has been approved and the artificial teeth were attached on the framework (g, h). Finally, the prosthesis has been permanently installed in the mouth of the patient.

For all five cases the production of the framework by SLM was successful with a good fit between framework and implants, leading to satisfying results for the patients.

**Table 7.3** Information on five performed clinical cases

Case	Jaw	Number of implants	Installation level
1	Mandible	6	Abutment
2	Maxilla	4	Abutment/implant
3	Maxilla	4	Implant
4	Maxilla	4	Implant
5	Maxilla	4	Abutment



**Fig. 7.14** Pictures of clinical case 1  
(Source K.U.Leuven)

## 7.8 Conclusions

All dental CAD/CAM systems have three functional components: data capture of the oral environment, digital design of the dental restoration and CAM to produce the part. Several CAD/CAM systems are commercially available today to fabricate dental restorations like crowns, bridges and frames. They differ strongly for their technology, software, materials and limitations.

Selective Laser Melting (SLM) is a suitable Rapid Manufacturing technique for customized parts with high complexity at a small quantity. K.U.Leuven has developed a CAD/CAM procedure to fabricate implant-supported frameworks for dental prostheses by SLM. The patented procedure (Vandenbroucke et al., 2005) provides an efficient and fast method to digitally design and manufacture complex frameworks from titanium or cobalt-chromium.

Quality control has been performed on produced frameworks to verify their mechanical, chemical and geometrical properties. Optimal process parameters and an appropriate SLM production strategy guarantee an accurate fit between framework and implants, needed to avoid mechanical or biological failures of the prosthetic system. The procedure has been successfully applied for five clinical cases. SLM allows an efficient and customized Direct Digital Manufacturing of frameworks with high economical potential.

## References

- Abe F., Osakada K., Kitamura Y., Matsumoto M. and Shiomi M., 2000, Manufacturing of titanium parts for medical purposes by selective laser melting, Proc. 8th Int. Conf. Rapid Prototyping.
- BEGO website: <http://www.bego.com>.
- Gibson I., 2005, Advanced Manufacturing Technology for Medical Applications, Wiley ed., ISBN 0-470-01688-4.

- Jemt J. and Lekholm U., 1998, Measurements of Bone and Framework Deformations Induced by Misfit of Implant Superstructures, a Pilot Study, *Clinical Oral Implants Research* 1998, Vol. 9, Issue no. 4, p. 272–280.
- Kruth J.-P., Mercelis P., Van Vaerenbergh J., Froyen L. and Rombouts M., 2005, Binding Mechanisms in Selective Laser Sintering and Melting, *Rapid Prototyping Journal*, Vol. 11, Issue no. 1, Jan. 2005, p. 26–36, ISSN 1355-2546.
- Kruth J.-P., Vandenbroucke B., Van Vaerenbergh J. and Naert I., 2005, Rapid Manufacturing of Dental Prostheses by means of Selective Laser Sintering/Melting, *Les 11ièmes Assises Européennes du Prototypage Rapide*, Paris, 4–5 October 2005, reference S4-2.
- Leu M.C. and Gawate A., 2006, Computer Aided Dental Bar Design, U.S. Patent Application.
- Levy G., Schindel R. and Kruth J.-P., 2003, Rapid Manufacturing and Rapid Tooling with Layer Manufacturing Technologies, State of the Art and Future Perspectives, *CIRP Annals* 2003 Vol. 52/2.
- Materialise website: <http://www.materialise.com>.
- Naert I., Vandenbroucke B., Van Vaerenbergh J. and Kruth J.-P., 2005, Digital Manufacturing of Biocompatible Metal Frameworks for Complex Dental Prostheses by SLS/SLM, *Proc. of 2nd Int. Conf. on Advanced Research in Virtual and Rapid Prototyping*, Leiria, Portugal, Sept. 2005, p. 139–145.
- Ortrop A. and Jemt J., 2000, Clinical Experiences of CNC-milled Titanium Frameworks Supported by Implants in the Edentulous Jaw: a One-Year Prospective Study, *Clinical Implant Dentistry and Related Research* 2000, Vol. 2: p. 2–9.
- Over C. and Meiners W., 2002, Selective Laser Melting a New Approach for the Direct Manufacturing of Metal Parts and Tools, *Proc. of SME conf. on Rapid Prototyping and Manufacturing*, Cincinnati, May 2002.
- Renouard F. and Rangert B., 1999, Risk Factors in Implant Dentistry, Quintessence Publishing Co, Paris, ISBN 0-86715-355-5.
- Riedy S., Lang R.B. and Lang E.B., 1997, Fit of Implant Frameworks Fabricated by Different Techniques, *The Journal of Prosthetic Dentistry* 1997, Vol. 78, p. 596–604.
- Rudolph H., Quaas S. and Luthardt R.G., 2003, CAD/CAM – Neue Technologien und Entwicklungen in Zahnmedizin und Zahntechnik, *Deutsche Zahnärztliche Zeitschrift* 58, 2003, Vol. 10, p. 559–569.
- Sirona website: <http://www.sirona.com>.
- Strietzel R., 2004, Production of Metallic Frames Using the BEGO Medifabricating Process, *Dental Technology* no. 50, p. 37–44.
- Strietzel R. and Hösch A., 1998, In Vitro Corrosion of Titanium, *Biomaterials* Vol. 19, 1998, p. 1495–1499.
- Strub J.R., Rekow E.D. and Witkowski S., 2006, Computer-Aided Design and Fabrication of Dental Restorations, Current Systems and Future Possibilities, *JADA*, Vol. 137, September 2006, p. 1289–1296.
- Vandenbroucke B. and Kruth J.-P., 2006, Selective Laser Melting of Biocompatible Metals for Rapid Manufacturing of Medical Parts, *Proc. of 17<sup>th</sup> Solid Freeform Fabrication Symposium*, Austin, Texas, USA, 14<sup>th</sup>–16th August, 2006, reference #9.
- Vandenbroucke B., Kruth J.-P. and Naert I., 2005, Procedure for design and production of implant-based frameworks for complex dental prostheses, Patent number WO 2006/079188, priority date 25th of January 2005.

# Chapter 8

## Digital Design and Fabrication in Dentistry

Ming C. Leu, Parthiban Delli and Mary P. Walker

### 8.1 Introduction

In the past three decades, the fast growing technology of Computer-Aided Design and Computer-Aided Manufacturing (CAD/CAM) has been continuously developed and applied to many fields in engineering, manufacturing, entertainment, and medicine. While maturing in some of the fields, CAD/CAM is still in developing stages in the medical and dental arena.

From industry surveys, more than 240 million people are missing one or more teeth in North America, Europe and Japan. There are approximately 400,000 dentists in the United States and Europe, with 20,000 dental laboratories making over 40 million dental devices/restorations (crowns, bridges, implant restorations, dentures) each year to treat the patients (Nobel Biocare, 2005).

Traditionally, dental restorations have been manually fabricated, which is a lengthy process. Initially, an impression of the patient's mouth is made with a rubber-like material and a gypsum (plaster) model or cast, often called a "stone model," is made from this impression. A wax pattern of the restoration is then created by manually adding wax to the stone model using small instruments with magnification. The completed wax pattern is then encased in a heat-resistant investment mold with the wax pattern burned out in an oven. Melted metal alloy is then cast into the mold to make the replacement tooth or restoration. This process, also called the 'lost-wax technique' is very labor intensive.

Although the concept of CAD/CAM for dentistry was advocated in 1970s by Francois Duret (Duret, 1988; Schmitt, 2001), the actual use of this computer automated design and manufacturing technology has been slow to evolve until lately. In the past, dental automation was difficult because the software and hardware needed for the automation was not fully reliable and too expensive.

---

Ming C. Leu

Department of Mechanical and Aerospace Engineering, University of Missouri-Rolla, Rolla, Missouri 65409, USA  
mleu@umr.edu

Today, advances in imaging, digital design, and solid freeform fabrication plus their increasing cost advantages have enabled CAD/CAM technology to become increasingly attractive compared to the traditional dental restoration practices.

One of the major driving forces behind the transition to CAD/CAM technology in dentistry is the severe shortage of qualified dental laboratory technicians. There are at least ten different commercially available CAD/CAM systems for making dental restorations, and with the exception of one system all of them are laboratory-based. With this technology, many of the labor intensive steps of restoration fabrication are computer-based, allowing the technicians to focus on the more artistic aspects of the restoration process, such as adding the final layer of esthetic porcelain to the restoration framework. In the case of the office-based system, patients no longer need to make multiple visits to the clinicians, and there is no need for temporary restorations. However, the office-generated restorations are limited to simpler, one-tooth restorations, rather than more complex bridges used to replace missing teeth.

This chapter describes and discusses digital technologies for design and fabrication of dental restorations including crowns, inlays, bridges, and dental bars for implant restorations. The remainder of this chapter is structured as follows. Section 8.2 provides an overview of commercially available dental CAD/CAM systems. Section 8.3 describes digital data acquisition methods by use of contact and non-contact digitizers. Section 8.4 presents techniques for surface reconstruction from the acquired digital data. Section 8.5 describes methods of digital design for standard teeth, inlays, and dental bars. Section 8.6 discusses digital fabrication processes including computer numerical control machining, rapid prototyping followed by investment casting, and direct digital manufacturing.

## 8.2 Commercial Dental CAD/CAM Systems

There are many dental CAD/CAM systems available in the market today to aid orthodontists and prosthodontists. These systems differ in the technology principle, application area, and cost. Before getting into the principles of technology behind these systems, we will first provide an overview of commercially available dental systems.

### 8.2.1 Nobel Biocare – Procera<sup>®</sup>

The Procera<sup>®</sup> System was marketed by Nobel Biocare starting 1991. In the first few years this system was able to fabricate titanium crowns by copy-milling and spark erosion techniques followed by applying porcelain onto copings. Later versions of this system can fabricate crowns, laminates, abutments and bridges.

A versatile part of Procera<sup>®</sup> is its separation of the scanning unit from the fabrication unit. If clinicians cannot afford to buy the whole system, they can just buy the scanning unit. The scanned digital data can then be sent across the Internet to a dental laboratory where the crowns, bridges and veneers are fabricated. Figure 8.1(a) shows Procera<sup>®</sup> Piccolo, which does the scanning. The scan data is imported into the built-in software of the system, which allows the user to design restorations with desired strength and esthetics as shown in Fig. 8.1(b).

The final design model can be sent via the Internet for immediate fabrication at laboratories authorized by Nobel Biocare. The clinicians have the choices of using materials like zirconia or alumina for the restoration. The CAD model is exported to a milling machine to make a die, which is used to form the ceramic framework using alumina powder pressing technology. Excess powder can be removed by milling and then the crown or bridge framework is sintered to attain the desired hardness and density. If zirconia is used instead of alumina, a block of pre-sintered zirconia is milled and the resulting framework sintered. In either situation, the final framework is inspected and veneered with porcelain to obtain the final functional tooth-shaped restoration.

### 8.2.2 CEREC<sup>®</sup>

The CEREC<sup>®</sup> system was released to the market in 1985 by Sirona, which introduced several upgraded versions over the years. The system consists of an image acquisition unit and a milling unit. These tools combined with the system's software allow dentists to create ceramic restorations within an hour. It covers a wide range of restorations, from inlays, onlays, veneers, and crowns.

The acquisition unit includes a computer integrated with a measuring camera and a microprocessor-controlled image capture card. The card

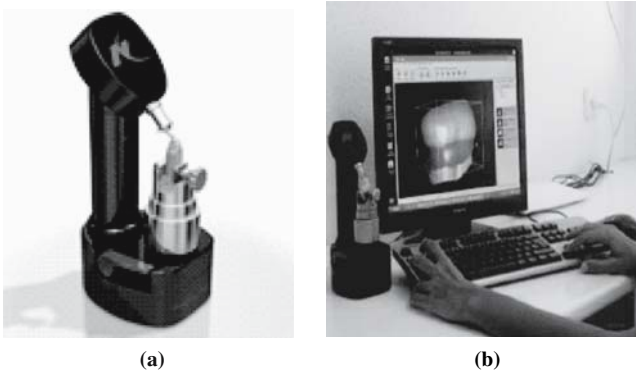


**Fig. 8.1** Procera<sup>®</sup>: (a) Procera Piccolo; (b) the full Procera system

(Source: Nobel Biocare website)

processes the images from the camera in real time and viewed through a monitor. Figure 8.2(a) shows the acquisition unit. Figure 8.2(b) shows CEREC<sup>®</sup> Chairline, which is an ergonomically designed treatment center. The system holds all the clinical tools, the measuring camera, and the computer hardware. The CEREC<sup>®</sup> milling unit, as shown in Fig. 8.2(c), is a dual-spindle machine with two diamond burs working simultaneously to make ceramic restorations rapidly (Fig. 8.2(d)). The milling unit and acquisition unit are interconnected through a cable or wirelessly.

The CEREC<sup>®</sup> software can be used to design various types of dental restorations, such as inlays, onlays, veneers, and crowns (Fig. 8.3). From the acquired image data, the software can automatically generate design solutions from its database, to achieve the desired design in a short time.

As already stated, there have been numerous upgrades to this system. This has resulted in improved restoration fit. With some of the earlier systems, the marginal gap between the tooth was quite large and beyond the clinically acceptable maximum of 100  $\mu\text{m}$  (Molin et al., 1996; Akbar et al., 2005). For example, with CEREC 1 and CEREC 2, marginal gaps were respectively reported to range in 191–308  $\mu\text{m}$  and 85–207  $\mu\text{m}$  (Mormann and Krejci, 1991; Denissen et al., 2000; Bindl and Mormann, 2003). With newer CEREC systems, marginal adaptation has improved. A recent study (Akbar et al., 2005) reported marginal gaps ranging from 26 to 130  $\mu\text{m}$  (Fig. 8.4). These improvements are the result of an enhanced intraoral optical scanner, better software imaging and design capabilities, and more true-to-detail milling (Mormann, 2000).

Because the restorations are milled from materials, such as feldspar- or leucite-based glass ceramics, the restorations are monoceramic, i.e. they do not include a zirconia ceramic framework veneered with porcelain by a laboratory technician. As a result, these restorations can be fabricated within the dental office, making this a one-appointment procedure. In addition, the materials are completely sintered prior to milling, so the restoration design does not

**Fig. 8.2** CEREC<sup>®</sup>:  
 (a) acquisition unit;  
 (b) Chairline system;  
 (c) milling unit,  
 (d) restoration being milled  
 (Source: CEREC website)

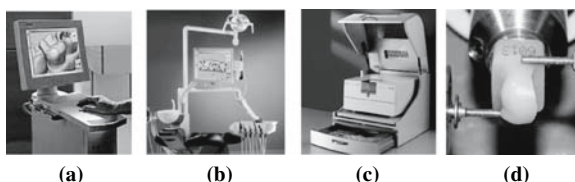
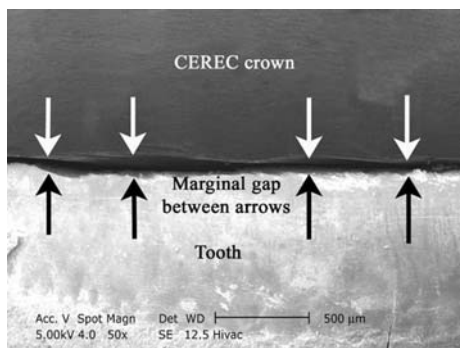


**Fig. 8.3** CEREC<sup>®</sup>  
 generated inlay, onlay,  
 veneer, and crown  
 (Source: Buddy Auten,  
 Sirona Inc.)





**Fig. 8.4** SEM image of the marginal gap between a CEREC crown and the prepared tooth



require any compensation for sintering shrinkage. For testing and analysis of the design, it also has verification modules to check the degree of contact with adjacent teeth and contact or occlusion with opposing teeth.

### 8.2.3 Cercon<sup>®</sup>

The Cercon<sup>®</sup> system (DENTSPLY Ceramco) consists of a group of individual units for design and fabrication of metal-free zirconia dental restorations. The overall system comprises a precision laser-optical scanner for laboratory stone models (Cercon Eye), combined with CAD software (Cercon Art). The digital design from these can be transmitted to an integrated scanning and milling system (Cercon Brain).

Cercon Brain unit can also scan a wax pattern prepared on a stone model, consistent with all-ceramic preparation and design guidelines, digitize this pattern and proceed to milling. The system uses standard sized blanks of zirconium oxide (12, 30, 38 and 47 mm sizes). The barcode scanned by the laser reader in the Cercon Brain ensures that the correct sized blank is picked, as well as integrating a pre-measured milling expansion factor to compensate for sintering shrinkage (~ 18% linear). A sintering furnace (Cercon Heat) enables the post-processing of zirconia substructures milled in the semi-sintered state.

Another option is for labs using the Cercon Art and Eye to electronically transmit their design to a central manufacturing service for zirconia substructures (Compartis<sup>™</sup>), and receive sintered Cercon zirconia substructures ready for veneering.

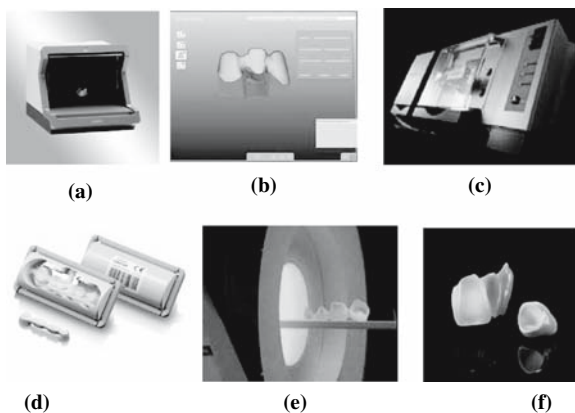
After sintering, the framework is fitted to the stone model and then manually veneered with Cercon<sup>®</sup> Ceram KISS<sup>™</sup>, Ceramco<sup>®</sup> PFZ or Sakura<sup>®</sup> Interaction<sup>™</sup> porcelains to complete the restorations. Pressable ingots are also available for these systems, that enable a lab to wax and injection mold the veneering material onto a framework. The pressing option enables the production of homogenous, shrinkage-free veneering, and the delivery of precise porcelain margins.

Figure 8.5(a) shows the Cercon Eye scanner, and the Cercon Art CAD software is demonstrated in Fig. 8.5(b). The Cercon Brain milling unit is shown in Fig. 8.5(c), along with a blank and a milled framework shown in Fig. 8.5(d). The sintering furnace is displayed in Fig. 8.5(e), and a completed Cercon restoration in Fig. 8.5(f).

### 8.2.4 Cynovad

Cynovad was founded in 1998 in Montreal, Canada. It introduced Pro 50<sup>TM</sup> and WaxPro<sup>TM</sup> for dental design and fabrication. Pro50<sup>TM</sup> consists of a 3D scanner and a CAD design package. The scanner digitizes traditional stone models and integrates the scan data into the design software. The scanning is based on chromatic coding technology and can capture undercuts in the profile. The design software imports the scan data and converts it into a solid 3D model. It can automatically generate proposed solutions such as automatic filling of undercuts by taking into account various clinical situations. A huge database of different tooth morphologies facilitates the user to choose a solution from the library for the desired restoration. The package is capable of designing a variety of prostheses including copings for single crowns, and simple and complex frameworks for various bridge configurations. The system also includes a 'virtual' articulator, which allows simulation of chewing movements facilitating improved functional restoration design. Figure 8.6 shows the Pro50<sup>TM</sup> system and example designs generated by this system. The virtual model of the designed framework from Pro50<sup>TM</sup> is exported in STL format.

Compared to other systems, Cynovad has more options. For example, the designed framework can be either sent to any manufacturing unit for ceramic framework milling, or the framework design can be imported into WaxPro<sup>TM</sup> to carry out the fabrication of wax patterns (Fig. 8.6(e)). With the capability of



**Fig. 8.5** Cercon<sup>®</sup>:  
 (a) Cercon Eye scanner;  
 (b) Cercon Art CAD  
 software; (c) Cercon Brain  
 milling unit; (d) Cercon base  
 milled blank; (e) Cercon  
 Heat sintering furnace;  
 (f) veneered restoration  
 (Courtesy of Dentsply  
 Prosthetics)

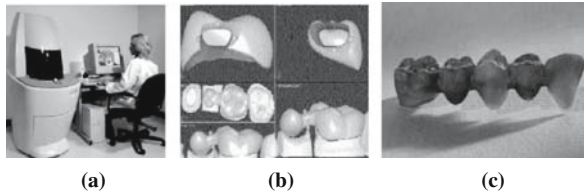


**Fig. 8.6** Cynovad: (a) Pro50™, (b) example designs generated by Pro50™, (c) bridge wax pattern (Source: Cynovad website, Maryse Milton, Cynovad Inc., Montreal, Quebec)

generating 200 wax pattern units per day, the wax patterns are used in typical investment casting procedures to make metal-based crowns or bridges.

Cynovad also offers a digital shade matching system (colorimeter) called ShadeScan™. It captures the photo image of a tooth and compares the shade of the tooth to standard shades in the database. It also measures other important aspects of teeth such as translucency and texture. The ShadeScan™ software is a high-end tool that analyzes and processes data to produce detailed shade maps.

### 8.2.5 Lava™

Lava™ is the CAD/CAM system of 3M ESPE company for fabrication of crowns and bridges (Ref: 3M ESPE website). The system’s work flow of restorations through various stations is shown in Fig. 8.7. The dental preparation is

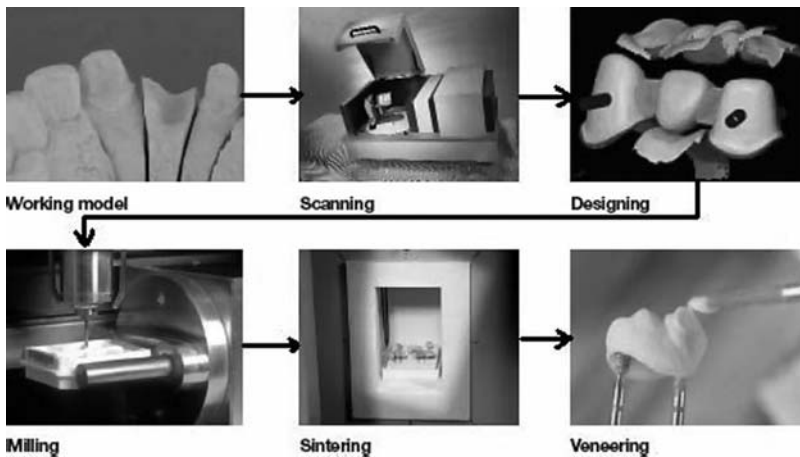


**Fig. 8.7** Lava™ process flow (Source: 3M ESPE website)

digitalized using Lava™ Scan, which is an optical scanning system. The scanned data of the stone model and occlusal/bite impression from Lava™ Scan are imported into Lava™ CAD for designing the restorations. The designed restorations are sent to Lava™ Milling to generate crown copings and bridge frameworks from pre-sintered zirconia blanks. The shrinkage allowance pertaining to sintering is automatically compensated in the restoration design used in the milling tool path. Lava™ Therm oven is used to sinter the machined coping or framework to desired density and strength.

After finishing and fitting the framework to the stone model (Fig. 8.8(a)), Lava Ceram porcelain is veneered onto the framework (Fig. 8.8(b)) to complete the functional and aesthetic restoration (Fig. 8.8(c)).

### 8.2.6 OrthoCAD™

Introduced in 1999, OrthoCAD™ is the first commercial CAD system developed for bracket bonding in orthodontics (Ref: OrthoCAD website). Unlike the other CAD/CAM systems discussed above, OrthoCAD™ is solely a CAD solution that imports a set of point cloud data (from any digitization method), processes it to design the bracket, and exports the model to be made by a rapid

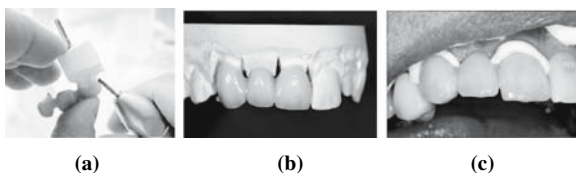


**Fig. 8.8** Lava: (a) machined, sintered framework fitted to model; (b) porcelain veneer added to framework to complete restoration; (c) restoration cemented onto teeth

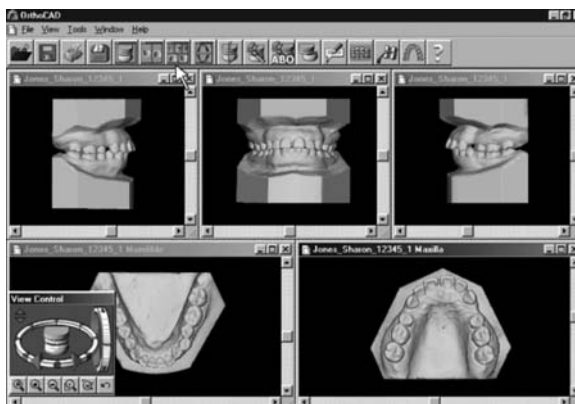


**Fig. 8.9** Five different views of the maxilla and mandible in OrthoCAD™ (Source: OrthoCAD website)

prototyping machine. From the bite impression of a patient's mandible and maxilla taken by the clinician, a cast plaster is made and scanned. The scanned data is imported into the OrthoCAD<sup>TM</sup> software to construct a virtual model, which is diagnosed with a bracket that is virtually placed at a location confirmed by the orthodontist. The final position of the bracket is transferred onto a physical model by digital fabrication. The OrthoCAD<sup>TM</sup> software package allows the orthodontist to place the bracket in a virtual environment and check for the effectiveness of bracket placement. The software interface allows different views of the model as shown in Fig. 8.9.

### 8.3 Digital Data Acquisition Methods

A dental CAD/CAM system comprises three basic components: Input Unit, Processing Unit and Output Unit. The input unit uses a data acquisition system to digitalize the physical model. The processing unit converts the digitized data into a virtual model and carries out the design process. The output unit fabricates a physical part from the CAD model. The oral information of the patient can be directly extracted from a patient's mouth or indirectly by means of a stone model generated through making an impression. The data acquisition techniques were originally developed for reverse engineering and intensively used in manufacturing industries. Gradually their strengths are recognized and these techniques are also applied in the medical field. In this section, an overview of commonly used digitizers in dentistry is given. The acquisition systems are divided into two basic categories: Contact and Non-contact Digitizers.

#### 8.3.1 Contact Digitizers

A contact digitizer is a mechanical device designed to move a measuring probe to determine coordinates of points on a workpiece surface with respect to a fixed coordinate system. It shares the same basic principle of operation as a Coordinate Measuring Machine (CMM). A contact digitizer is comprised of four components: machine body, measuring probe, computer hardware, and software. Contact digitizing machines are available in different sizes and designs.

The probe in a contact digitizer is moved manually or by a software program. When the probe's tip touches the part surface with a distinct force, it gets deflected. This deflection is sensed through a transducer in the probe head. The current probe's position is registered and the probe is lifted by a fixed increment and moved along the same axis. The shape and size of the probe tip affects the accuracy of measurement.

The software of the digitizer saves the  $(x, y, z)$  coordinates of the measured points, which can be imported into commercial CAD/CAM systems. This set of points is called a point cloud. Some contact digitizers have built-in software that

automatically regenerates surfaces and even numerical control programs directly from the measured data.

MicroScribe<sup>®</sup> digitizer uses a linkage having rotation measurement sensors (Ref: MicroScribe website). The physical model to be digitized is mounted firmly by using a fixture. The probe head is then operated manually to go over the surface to be digitized. While the probe tip is in contact with the surface, the digitizer records the sensory data. Another contact digitizer is MAXNC<sup>™</sup> (Ref: MAXNC website). It is basically a desktop 3-axis milling machine, whose spindle head can be fitted with a probe in replacement of a cutter. The probe detects change in height along *Z*-axis as the probe moves in *XY* plane. The software provided by MAXNC<sup>™</sup> facilitates setting values of process parameters. The output data is a DXF file, which is a translated file that contains the information of *x*, *y* and *z* coordinate values and the lines connecting them. From these files it is easy to extract the point cloud data. The digitized data can be imported by AutoCAD and other commercial software. Pictures of MicroScribe<sup>®</sup> and MaxNC<sup>™</sup> are shown in Fig. 8.10. The digitization of a stone model with 5 implants using a MaxNC is shown in Fig. 8.11(a). The point cloud data extracted from the measurement is show in Fig. 8.11(b).

The advantages of contact digitizers relative to non-contact digitizers are:

- The contact digitizer is relatively cheap.
- The computer hardware requirements are less.
- Good accuracy ( $\pm 0.01$  mm) can be achieved at a more affordable price.
- No special setup or work environment is required.

The drawbacks of contact digitizers are:

- The digitizing process is relatively slow.
- The digitization accuracy is limited by the diameter of the contact probe and the probe deflection.

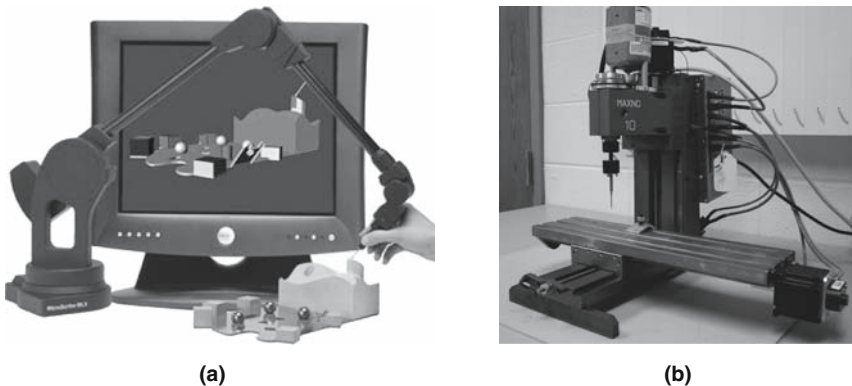


**Fig. 8.10** Contact digitizers: (a) MicroScribe<sup>®</sup> (Ref: MicroScribe website, reproduced by permission of Immersion Corp.); (b) MAXNC<sup>™</sup>

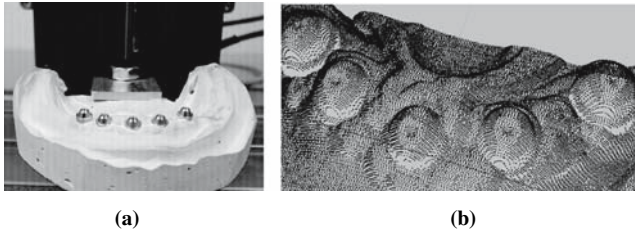


**Fig. 8.11** Contact digitizing: (a) digitizing a plaster model using MAXNC™; (b) point cloud data extracted from the measurement (Delli, 2006)

- It is difficult to obtain oral data directly from a patient's mouth because of the requirement of physical contact.

### 8.3.2 Non-Contact Digitizer

As the name implies, these types of digitizers do not touch the surface of the physical model. These digitizers use a visible light, laser, X-ray, magnetic or acoustic signals to digitize the part. The emitted waves from the source are reflected by whatever object is being imaged and the reflected waves are detected by the sensor inside the digitizer. Each scanning technology uses a different principle as discussed below.

#### 8.3.2.1 CT Scanning

Computed Tomography (CT), also known as Computed Axial Tomography (CAT), is an imaging procedure that uses a combination of X-rays to produce cross-sectional images of the 3D body. A series of 2D cross-sectional X-ray images are bound together to form the 3D model. A CT scanner from Siemens is shown in Fig. 8.12(a).

The first commercial CT system was invented in 1971 (Ref: Wikipedia). The technology is presently in its fourth generation of evolution and is widely used in the medical field. Figure 8.13 shows a cross-sectional image of the brain taken by

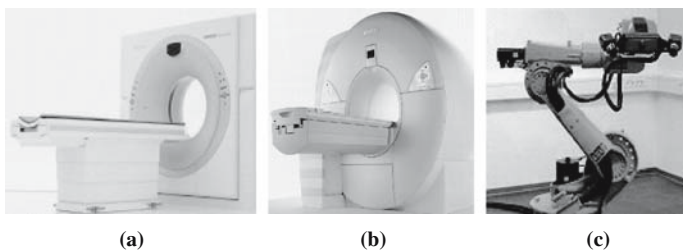
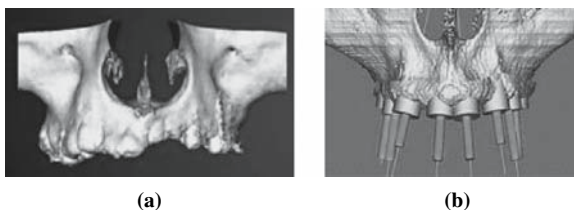


**Fig. 8.12** Some non-contact digitizers: (a) SOMATOM CT system (Ref: Siemens website); (b) MAGNETOM Avanto MIR system (Ref: Siemens website); (c) ATOS: Advanced TOPometric Sensor (Ref: GOM website)

**Fig. 8.13** A CT scan showing a cross-sectional image of the brain (Courtesy of Yousef Mohammad, M.D., M.Sc.; Neurology Division of Cerebrovascular Diseases, The Ohio State University Medical Center)



**Fig. 8.14** (a) A virtual model from CT scanned data imported in Dentascan software; (b) planning of implant location on the virtual model (Ref: Boca Radiology)



CT scanning and shows the structure of the brain. There are commercial CT scanners specifically made for dental application. For example, the CT Dentascan is a computerized reformatting program which obtains cross-sections of the mandible and maxilla from the obtained CT scans of a patient being considered for dental implant surgery. It enables the prosthodontist and dental surgeon to visualize the bony structures and plan the implant restoration and surgical procedures before actual surgery. A virtual maxilla model generated by Dentascan is displayed in Fig. 8.14(a). The dental implant planning done on the virtual model is shown in Fig. 8.14(b).

### 8.3.2.2 Magnetic Resonance Imaging (MRI)

MRI is a widely used dental data acquisition technique in recent years. The external look of an MRI unit is much like a CT scanner, though the working principle and technology is very different. The human body is subjected to a strong magnetic field. Each atom acts as a tiny magnet. Due to this magnetic field the hydrogen atoms are in their excited state. The body is then exposed to radio frequency waves. The excited state rapidly decays to a lower energy state while emitting its own unique radio frequency signal which can be detected by an external radio-frequency coil or antenna. By using mathematical calculations these signals are converted into 2D and 3D images. The relative brightness of individual points in the tomographic slice of the body provides information on the relative hydrogen content in a particular volume element (voxel). The patient is laid on a horizontal tube which runs linearly into the magnetic field.



Once the body part to be scanned is in the center or isocenter of the magnetic field, the scan can begin. MRI scanners vary in size and shape, and newer models have some degree of openness around the sides. An MRI unit (MAGNETOM Avanto) is shown in Fig. 8.12(b).

### 8.3.2.3 Optical Digitization

Depending on the techniques employed to perform data acquisition, optical digitizers can be categorized into Active and Passive Optical Digitizers. An active optical digitizer emits a ray and detects the reflection to probe an object. Typically, it uses intensified monochromatic light or LASER fringes emitted from a source. The reflected rays from the object surface are captured by the detector. A series of overlapping images can be taken by rotating the object. These images form a point cloud or edge data, which could be later converted into a surface or 3D model. Time-of-flight and optical triangulation are two methods of active digitizing.

The time-of-flight laser scanner uses laser light to probe the subject by means of the speed of light. The triangulation scanner projects a light spot (or fringe) on the object and utilizes a light detector to find the location of the spot. Based on the depth of the point on the surface the point appears at a particular location on the detector. The distance of the object from the detector is calculated by triangulation, using the triangle formed by the surface point, the detector, and the laser emitter. Fringe stripes can also be used instead of a point light. This increases the speed of data acquisition.

A passive optical digitizer captures the images of the object in ambient light. A stereoscopic digitizer uses two cameras slightly apart. The differences between the images seen by the two cameras are analyzed and used to determine the coordinates of each point on the object surface. Another example of a passive digitizer uses silhouette, which captures a sequence of photo images of the object and creates outlines from them using an image processing technique. The silhouettes are intersected to form a visual hull approximation of the object.

Fraunhofer IOF has developed several dental CAD/CAM systems and optical scanners (Ref: Fraunhofer website). One of them is Hi-Scanµ (Fig. 8.15(a)), which uses the principle of digital fringe projection in combination with a multi-view technique to generate a point cloud of the visible surface of a measuring object. The generated point cloud can be post processed with a commercial software package. An example virtual model from Hintels is shown in Fig. 8.15(b).

Another optical scanning system is ATOS (Advanced TOPometric Sensor), as shown in Fig. 8.12(c). It is a high-end 3D digitizer based on the principle of triangulation with multipoint view. It projects different fringe patterns onto the object's surface using a white light projection unit, as shown in the Fig. 8.16(a). Each projected image is viewed by two CCD cameras. From the images, a point cloud defining the surface of the measured object is obtained. Depending on the resolution of the CCD cameras in the ATOS digitizer, up to 4 million points can

**Fig. 8.15** (a) Hintels (Hi-Scanμ) optical 3D scanner; (b) a virtual model extracted from Hintels (Ref: Frounhofer IOF website)

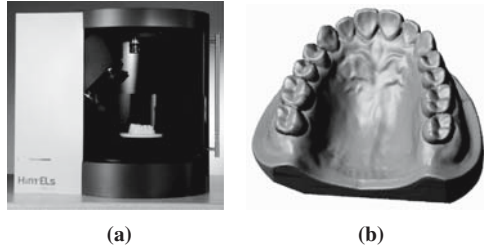


**Fig. 8.16** (a) Light fringes projected on an object; (b) a rendered virtual model from the extracted digital data (Ref: GOM website)

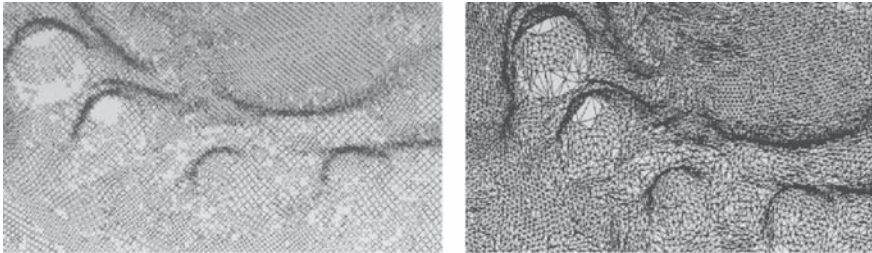
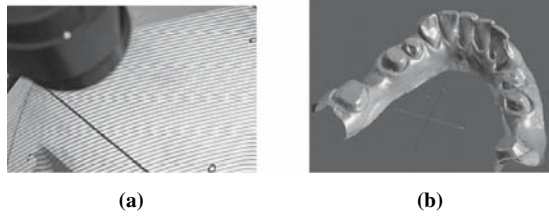


**Fig. 8.17** (a) Point cloud data from a plaster model; (b) triangular mesh constructed from the data (Delli, 2006)

be captured in less than 8 seconds. The point cloud is then converted into a surface mesh, which can be rendered as shown in Fig. 8.16(b). The point cloud data extracted from a stone model and the triangulated surface mesh are shown in Fig. 8.17.

## 8.4 Surface Reconstruction Techniques

The digital data acquired through various techniques and instruments discussed in the previous section are converted into standard format so that the data can be processed utilizing the capabilities of a CAD/CAM system. This section discusses how the extracted data is processed into useful information and format for digital design and manufacturing.

Most of data acquisition methods, no matter using contact or non-contact devices, give the  $x$ ,  $y$  and  $z$  coordinates of data points in a point cloud. Techniques like CT and MRI produce 2D cross sections of the solid, which are broken down into lines and points. A fundamental issue is how to connect these points to form the boundary surface of the 3D solid represented by a triangular mesh. If the points are taken in parallel planar slices, one way to reconstruct the surface is to first connect them into contours in planar slices and then tile these contours into triangular facets as illustrated in Fig. 8.18.

The conversion of a set of points into triangular facets is generally based on four steps (Fabio, 2003):

1. **Pre-processing:** Any data acquisition technique registers some noise or data that is not desired. In the preprocessing stage, the outliers and noise are filtered to trim the point cloud. This involves sampling of scanning data, noise filtering, outlier rejection, and filling of gaps in the point cloud data.
2. **Determination of global topology:** This derives relations between adjacent portions of a surface. It requires some global sorting techniques like fuzzy logic and curve of best fit to apply topological constraints and maintain special features.
3. **Generation of triangular mesh:** This is the main part of surface reconstruction. Based on some technique these points are connected into triangular facets representing the boundary surface.
4. **Post-processing:** The last phase of surface reconstruction typically involves refining the model created through the above three phases. The created triangular mesh may need some refinements to correct imperfections and errors in the surface.

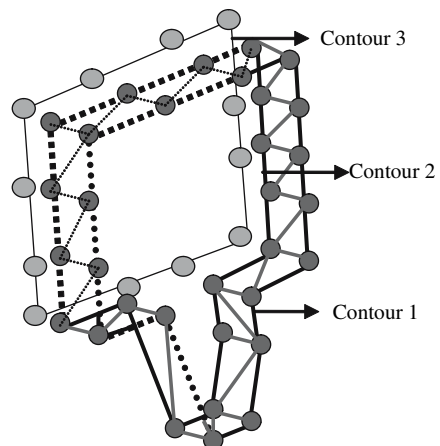


**Fig. 8.18** Parallel planar contours connected to form triangular facets (Asam, 2006)

### ***8.4.1 Surface Reconstruction from Point Cloud***

A widely used basis of many triangulation methods is Delaunay triangulation. It is a methodology of connecting the points in a point cloud to get the optimal closed surface in the form of triangles. The algorithm can be used to generate a triangular mesh of the point cloud obtained from the patient's mouth. The virtual model can then be used in CAD software to generate various dental components like inlays, onlays, bridges, implants, dental bars.

If the point cloud data are obtained by digitizing the surface along parallel scan lines as in the case of using a contact digitizer or an active optical digitizer with light stripes, the measured points are more structured and can be connected together to form a triangular mesh with a simpler, heuristics-based tiling algorithm as follows. First, two consecutive scan lines are selected. Starting from the first point of the first scan line, its distance from all the points in the second scan line is calculated. For ' $n$ ' points in the second scan line, there would be ' $n$ ' distances for the first point, and so on. The shortest of all these distances is selected and the corresponding two points are connected. This procedure is repeated for all the points in the first scan line to find out the corresponding points in the second scan line that have the shortest distances to these points. The points in the second scan line are ordered in increasing distance from each point in the first scan line. If the point in the second scan line with the shortest distance to the  $(n+1)$ th point in the first scan line is to the left of the point in the second scan line with the shortest distance to the  $n$ th point on the first scan line, then the point in the second scan line with the next shortest distance is selected till the point in the second scan line corresponding to the  $(n+1)$ th point in the first scan line is the same or to the right of the point in the second scan line corresponding to the  $n$ th point in the first scan line. The objective of this is to eliminate intersections among the connected edges. The rest points can be connected easily to form a triangular mesh as shown in Fig. 8.19.

As an example, a stone model is scanned using a contact digitizer to create a point cloud. Figure 8.20(a) shows the point cloud data in the pattern of points on scan lines and Fig. 8.20(b) shows the triangulated mesh from these points with surface rendering.

### ***8.4.2 Voxelization and the Marching Cube Algorithm***

The surface reconstruction can also be performed by evaluating the volumetric space of a 3D object in the form of Voxels. A voxel is a basic volume element on a regular grid in 3D space. This is analogous to a pixel in 2D space. Voxels are frequently used in the visualization and analysis of medical and scientific data. Some 3D displays use voxels to describe their internal resolution.

Voxelization is the process of adding depth to a set of cross-sectional images represented in pixels on planar slices. The space between any two pixels in one

**Fig. 8.19** Triangulation between two scan lines (Leu et al., 2005)

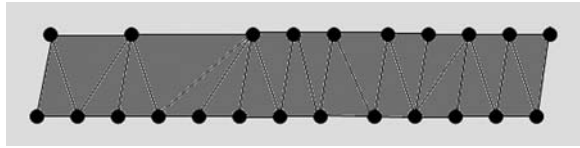


**Fig. 8.20** (a) Point cloud data; (b) triangulated mesh with surface rendering (Delli, 2006)

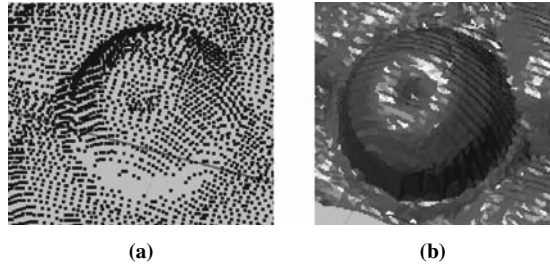
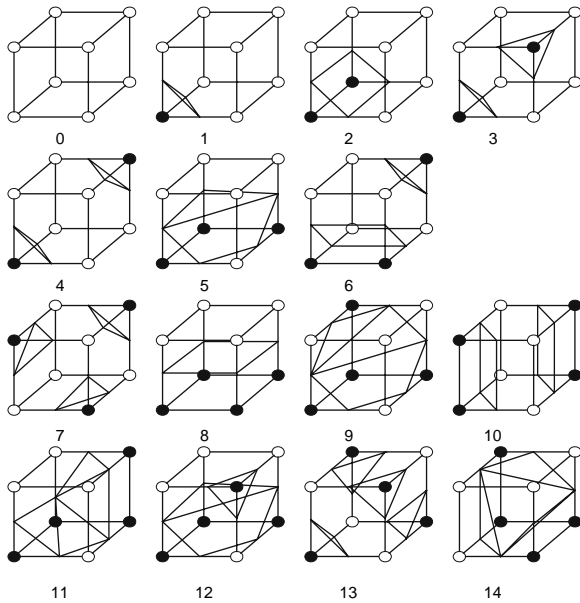


**Fig. 8.21** Fifteen cases in the marching cube algorithm for surface rendering



slice is referred to as interpixel distance, and the distance between any two slices is referred to as interslice distance.

Lorenson and Cline (1987) invented a surface construction and visualization algorithm called the Marching Cube, which is a widely used technique for real-time visualization of 3D models represented in voxels. This algorithm can be applied for visualization of voxelized data generated from CT or MRI images. The marching

cube algorithm traverses all boundary cells of an entire volume and determines the triangulation within each cell based on the values of cell vertices, each having a value of 0 or 1, to represent whether the corresponding voxel is empty or occupied by the object. This method first partitions the entire volume into cells, each consisting of eight voxels. Then it decides the surface triangulation for each cell according to 15 possible configurations shown in Fig. 8.21.

## 8.5 Digital Design

After the point cloud data are converted into some representation of a surface or solid, the next step involves a digital design process for the dental part. Designing crowns, copings, inlays, and bridges are simpler as compared with dental bars. The digital designs of some dental components are discussed below.

### 8.5.1 Modeling of Standard Teeth

There are many commercial dental CAD/CAM systems for automating the dental design process as reviewed previously. In these systems the basic models of teeth are available in their own libraries. However, general forms of teeth geometry provided by these CAD/CAM systems can only give raw shapes. There are always some manual alterations and modifications required as every patient is unique and every tooth has its own topological features.

The procedure based on the work of Song et al. (2005) can assist developing a system to form such a library with standard teeth models. It formulates a way of modeling a standard tooth based on the special topological features pertaining to that tooth. In this method, the data points are extracted from the surface of a tooth using a 3D digitizer as shown in the Fig. 8.22(a).

The digital data can be used to create a standard prosthetic crown using a B-spline surface. For an array of  $(m+1)$  by  $(n+1)$  control points, the equation of the surface is

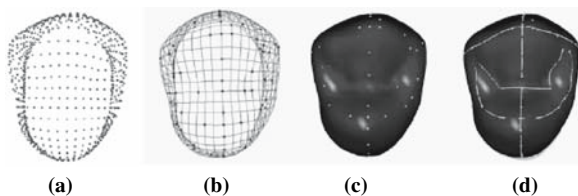


**Fig. 8.22** (a) Point cloud data; (b) B-Spline surface mesh; (c) the surface in shaded image; (d) feature-based curves (Song et al., 2005)

$$P(u, v) = \sum_{i=0}^n \sum_{j=0}^m P_{ij} N_{i,k}(u) N_{j,l}(v)$$

where  $P(u, v)$  is a point on the B-spline surface,  $P_{ij}$  are the control points, and  $N_{i,k}(u)$  and  $N_{j,l}(v)$  are polynomial functions. The values of  $m$ ,  $n$ ,  $k$  and  $l$  were selected by Song et al. (2005) as 30, 33, 4 and 4, respectively. These values imply that there are  $29 \times 32$  control points and the B-spline function is a bi-cubic surface in the form

$$P(u, v) = \sum_{i=0}^{30} \sum_{j=0}^{33} P_{ij} N_{i,4}(u) N_{j,4}(v)$$

The B-spline surface generated based on these control points is shown in Fig. 8.22(b) and (c). Adjustment of the control points affects a local area, and it may be a tedious job for the user to adjust the entire area using this adjustment. To facilitate an easier and more effective adjustment, some of the feature points can be put together to form a feature curve so that editing the curve automatically changes the feature points. The feature curve can be represented by a cubic B-spline function as follows:

$$P(u) = \sum_{i=0}^n P_i N_{i,4}(u)$$

Thus a feature curve can be modified by adjusting its feature points, and this modification results in the global modification of the tooth surface. In this way the topological features of the B-spline curves remain unchanged while the points are moved to customize the tooth design. The feature curves of the discussed tooth model are shown in Fig. 8.22(d). With the above technique a set of 28 standard teeth as shown in Fig. 8.23 were modeled by Song et al. (2005). These models can be stored in the library and retrieved later for any customized design.

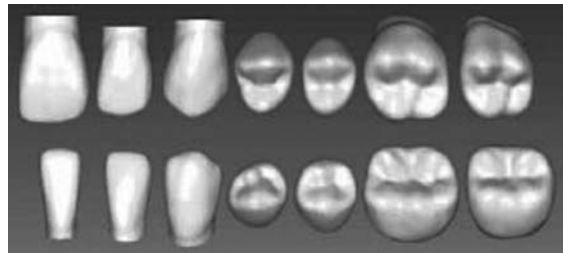


**Fig. 8.23** Feature based models of teeth (Song et al., 2005)

### 8.5.2 Modeling of Inlays

The design process of an inlay restoration involves representing the surface of the fitting inlay. This can be obtained by comparing the model of a prepared tooth with a library tooth model as illustrated in Fig. 8.24 (Adolph and Gurke, 2001). This figure provides a 2D illustration of a reference tooth model, the model of a prepared tooth, the adapting model obtained from Boolean difference between these two models, and the inlay model reconstructed from the adapting model.

The reference tooth model comes from modifying a library tooth model. It is paired with the model of the prepared tooth, whose geometry can be reconstructed from the digital scan data of the working tooth. The bottom surface of the inlay should be the same as the scanned surface of the prepared tooth, and the top surface of the inlay should be the same as that of the tooth model. These two surfaces are blended together in a meshing process to form the boundary surface of the inlay. Figure 8.25 shows the model of a prepared tooth and the inlay that fits into the tooth.

The inlay design can be sent to a milling machine for making the physical inlay. This automation will save time and effort for the dentists and lab technicians compared with the traditional process used in most dental practices and laboratories today.

**Fig. 8.24** Schematic illustration of the process of generating an inlay model (Adolph and Gurke, 2001)

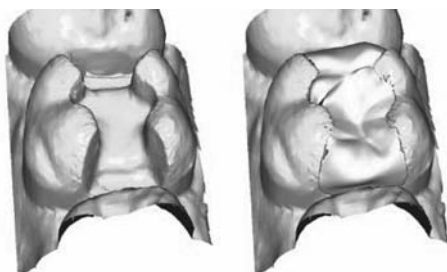
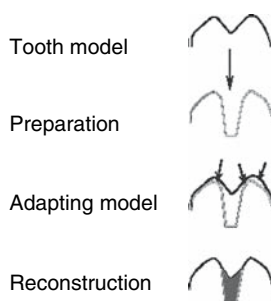


**Fig. 8.25** A virtual tooth prepared and the inlay that fits into the preparation (Adolph and Gurke, 2001)



### ***8.5.3 Modeling of Dental Bars for Implant Restorations***

The traditional methods of producing dental bars that support implant restorations, such as implant-retained overdentures, involve tedious and time-consuming operations that demand substantial human labor and good skill. There exists no commercial CAD/CAM system today for complete design and fabrication of dental restorations for multiple missing teeth requiring the use of implants in the restorations. Most of the prosthodontists still use transfer impression techniques to extract a patient's oral scenario and produce a stone model to duplicate the intra-oral configuration of implants and remaining teeth. In this process, there are multiple stages in the design and fabrication of such dental restorations.

In this kind of dental restoration, the patient undergoes a surgery to insert dental implants. The implants are made of titanium and take 3–6 months to heal and affix themselves in the patient's maxillary or mandibular jaw bone. Following the surgery, the tissue is sutured and closed over the implants. During the healing period, the bone cells grow around the dental implants; this process is called "osseointegration". After osseointegration, a tissue punch is used to make a small tissue opening to expose the implants, and healing abutments are attached to the exposed implants. Following tissue healing, an impression of the patient's mouth is made using transfer/impression copings. From the impression, a stone model is made with implant replicas attached to the transfer copings. The transfer copings are removed from the stone model and actual implant abutments (that will be used in the dental bar) are seated and fastened with screws to the implant replicas. Depending on the type of bar (Hader or Dolder), the bar is chosen and cut to size by physically marking it with the implant abutments. The bar segments and the abutments are luted together temporarily using polymerizing resins. The framework is removed from the stone model and transferred to another working index to perform soldering. The bar segments are soldered at the lute joints and then removed from the index. The bar is now ready to be attached to the implants in the patient's jaw. Figure 8.26 shows the traditional process flow of preparing a dental bar that could be used to support an implant overdenture. Figure 8.27 presents an overdenture bar attached to four implants and the tissue side of the denture with bar attachment clips.

In an attempt to digitally automate the processes of designing dental bars, a method has been developed by Dr. Ming Leu and his students at the University of Missouri-Rolla, and a software package called Dentabyte has been developed using this method. It uses the digitized point cloud data of the patient's oral scenario as the input (Leu and Gawate, 2006; Gawate, 2005; Asam, 2006; Delli, 2006). The digital data can be obtained using any of the data acquisition methods discussed previously. The software automatically generates a dental bar in STL format, which can be used to fabricate a

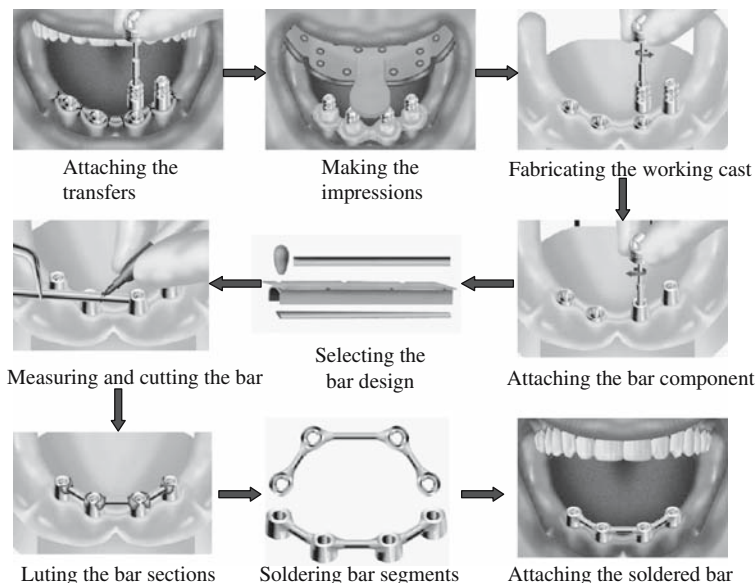
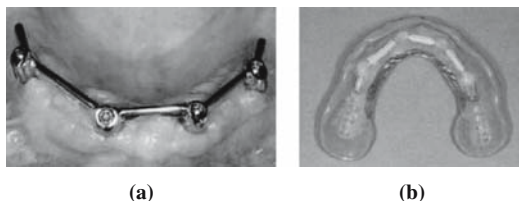


**Fig. 8.26** The traditional process of preparing dental bar (Zimmer Dental website)

**Fig. 8.27** (a) Implant overdenture bar; (b) internal surface of denture with bar attachments (*clips*)



physical bar by computer numerical control of machining or solid freeform fabrication.

The automated dental bar design process is illustrated in Fig. 8.28. The acquired point cloud data is first converted into a triangular mesh model representing the surface of the gingiva. The digital data are also used to compute the positions and orientations of the healing abutments, which are aligned with the axes of the inserted implants. From these position and orientation data the models of the bar cylinders and the connecting bar are generated in the form of triangular meshes for their boundary surfaces. The dental bar model is then created through Boolean operations among the gingiva model, the connector model, and the cylinder model as shown in the figure. The Boolean operations can be done using the dixel data extracted from these models. The resultant dixel data after Boolean operations can then be used to reconstruct the surface of the dental bar, which is represented by triangular facets and can be easily coded into an STL file.

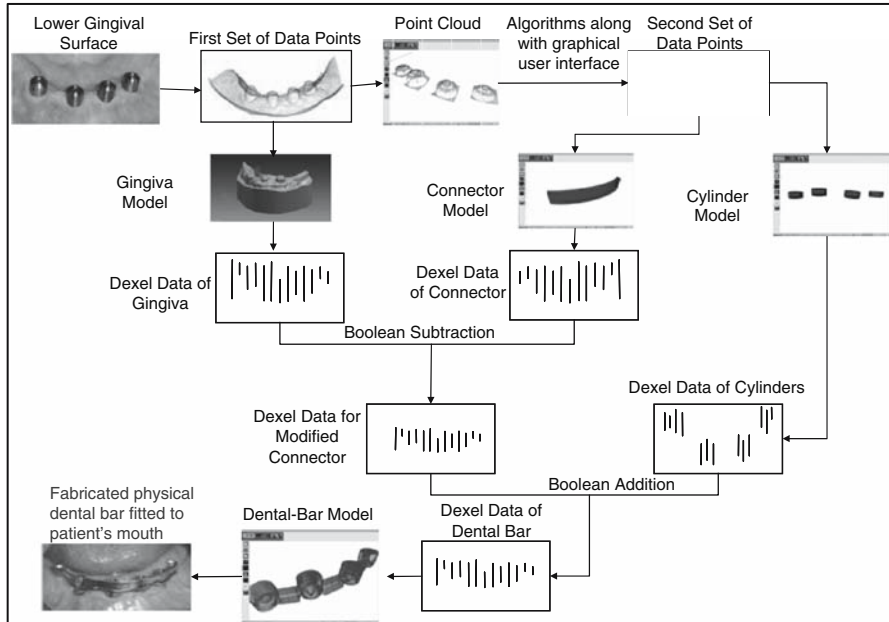


**Fig. 8.28** Automating the design process of implant-retained dental restorations (Leu and Gawate, 2006)

### 8.6 Digital Fabrication Processes

This is the last phase of the dental CAD/CAM process. It involves transforming a CAD model into a physical part that is later post-processed and polished before being inserted into a patient’s mouth. Examples of parts fabricated for dental applications are crowns, bridge frameworks, and implant retained dental bars. The designed model can be transferred to a CAM system directly or through translator files in a neutral format such as STL, IGES, or STEP.

Several methods can be employed to fabricate the physical parts. These methods can be Additive or Subtractive. Additive methods add material to fill in the cross sections of a CAD model layer-by-layer. This process is called Solid Freeform Fabrication, also known as Rapid Prototyping. The primary advantage of additive construction is its ability to create parts of almost any geometry. Subtractive techniques remove material from a block of raw piece to form a desired shape and size same as the digital model. The removal of material can be done by conventional machining (e.g. milling) and unconventional machining (e.g. EDM, laser machining). The main advantage of the subtractive process is that it can perform on a wide range of materials and at a higher accuracy.

### 8.6.1 Computer Numerical Control (CNC) Machining

Machining generally includes conventional processes such as milling, turning, grinding, and unconventional processes such as Electric Discharge Machining (EDM), wire-EDM, laser cutting, and abrasive jet machining. With the aid of computers and digital technology, CNC machining is one of the most efficient and reliable fabrication processes.

With the introduction of newer and tougher materials in the dental prostheses market, any fabrication process needs to provide crowns, bridges, and implant restorations economically with no compromise on quality. The evolution of CAM has enabled generating the NC tool path with less operator intervention. It also provides higher quality output at a faster rate. Most commercial CAM packages provide different options of tool path generation and a facility to simulate the tool path before actually cutting the physical part. In this way, the NC programs are ensured to be safe from gouging, material left out, heavy cut, or idle run.

Commercial systems like CEREC<sup>®</sup>, Cercon<sup>®</sup>, and Lava<sup>™</sup> use a milling station to fabricate the dental restorations. In these systems, the NC codes are automatically generated by the built-in software. As examples, Fig. 8.29(a) shows a single crown machined with a CNC milling machine, and Fig. 8.29(b) illustrates four views for milling a 3-unit bridge with two abutment retainers (crowns) at the two ends supporting the replaced missing tooth (pontic).

Besides these dedicated dental milling units, general-purpose CAM packages and selections of machineries are also available. Software packages like Uni-graphics, PRO/E, Surf-CAM, DelCAM, and MasterCAM offer high-level NC programming modules. DelCAM offers separate modules, DentMILL and PowerMILL, to mill dental restorations. PowerMILL is a CAM system that produces NC toolpaths from CAD models for machining with 2, 3, 4 and 5-axis milling machines. It can import data from any CAD system, through standard transfer files in IGES, STEP, VDA, STL or a variety of direct interfaces. PowerMILL generating NC paths and simulation of NC machining for a single crown is shown in Fig. 8.30.

Machining crowns, onlays, and bridges is simpler, as their basic features are very similar although the size and scale vary. Though these variations are critical in design, they are insignificant in generating NC programs. There are other dental components like dental bars for implant-supported restorations, which are more difficult to design and plan the machining process because they are functions of several variables (e.g. the number of implants, positions and orientations of the implant abutments). Nevertheless, they can still be fabricated by CNC machining with cutter paths generated by CAM packages like Uni-graphics, PRO/E, DelCAM. As an example, a 3-implant dental bar machined from a titanium block from its digital design model is shown in Fig. 8.31.

A key advantage of CNC machining is the tight tolerance and high accuracy achieved by this process. Further, CNC machined parts require little or no secondary finishing work. A main limitation of CNC milling is the geometric

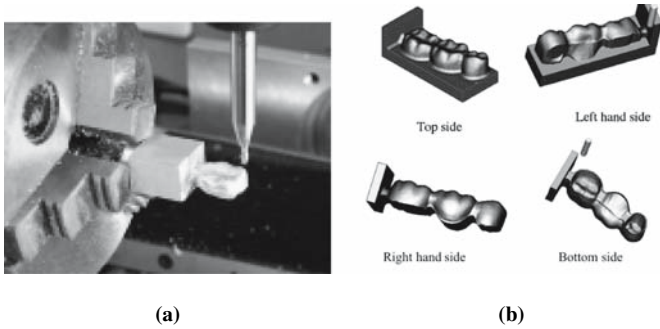


**Fig. 8.29** CNC milling: (a) single crown machined with a milling unit; (b) four views for machining a bridge (Chang et al., 2003)

**Fig. 8.30** PowerMILL: (a) tool path generated; (b) simulation of NC machining (Ref: DelCAM website)

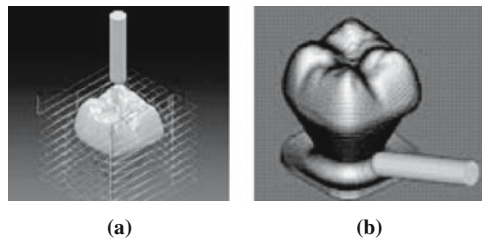
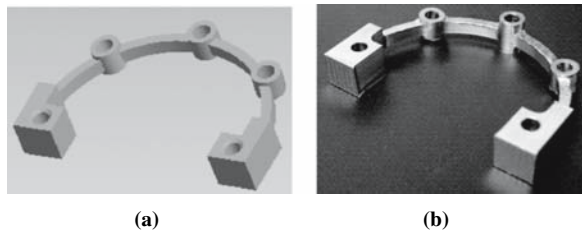


**Fig. 8.31** The 3-implant dental bar: (a) digital design model; (b) machined physical part in titanium (Delli, 2006)



complexity of machined part that can be achieved. Narrow or deep cavity preparations or features like undercuts or sharp corners cannot be easily replicated by milling operations. In these situations, special techniques like EDM and ultrasonic machining may be of assistance.

### 8.6.2 Rapid Prototyping

Rapid prototyping (RP) refers to the fabrication of 3D physical models by slicing a CAD model and building it physically layer by layer. In recent years, rapid

prototyping techniques have been extensively used to produce complex 3D parts and are becoming more attractive in dental automation. RP alone cannot produce the final metal parts. The polymer patterns formed by rapid prototyping are used in investment casting to produce dental parts from desired materials.

As a standard, all the commercial RP machines import 3D models in STL format. The file typically consists of information of individual triangles that define the surface of the solid model. Each individual triangle defines a normal vector directed away from the triangular facet followed by the xyz coordinates of the three vertices. The reason for converting a 3D model into this particular format is its ease of generating 2D contours by finding the intersections of the slice plane and the triangle edges. All the commercial CAD systems have the provision of converting a 3D model into an STL file.

Some of the commonly used RP processes are Stereolithography (SLA) and Selective Laser Sintering (SLS), Fused Deposition Modeling (FDM), 3D Printing (3DP), and Laminated Object Manufacturing (LOM). In Stereolithography (SLA), a pool of liquid resin (photopolymer) exposed to a moving laser beam instantly cures along the beam path and forms a thin layer of polymer. Once a layer is built, the platform is lowered by one layer thickness to build the next layer. The process repeats until the part building has been completed. An SLA pattern of a 4-implant dental bar and the generated metal bar by investment casting with nickel-chromium alloy are shown in Fig. 8.32 (Delli, 2006). Another example of a dental bar cast from a wax pattern made by Thermojet printing is illustrated in Fig. 8.33 (Liu et al., 2006). Figure 8.34 shows a third example of a dental bar pattern created by the Rapid Freeze Prototyping (RFP) process (Zhang et al., 1999; Leu et al., 2000; Sui and Leu, 2003; Liu et al., 2004; Liu and Leu, 2006; Liu et al., 2006) and the investment cast metal bar from this pattern (Huang et al., 2007).

### 8.6.3 Direct Digital Manufacturing

Direct Digital Manufacturing (DDM) is an additive layered manufacturing process which generates the final functional part with desired material directly from a CAD model. This fabrication process is highly suitable for making customized parts at a small quantity. Like rapid prototyping processes, DDM

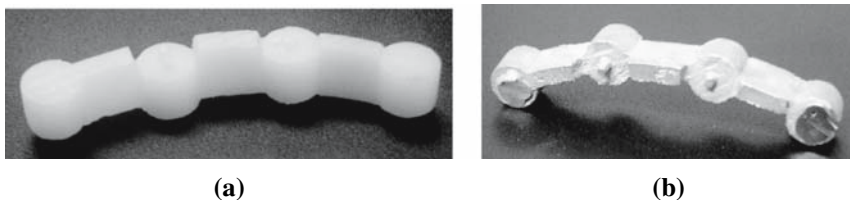


**Fig. 8.32** The 4-implant dental bar: (a) SLA pattern; (b) metal bar cast from Ni-Cr alloy (Delli, 2006)



**Fig. 8.33** The 4-implant dental bar: (a) wax pattern; (b) metal bar cast from Ni-Cr alloy (Liu et al., 2006)

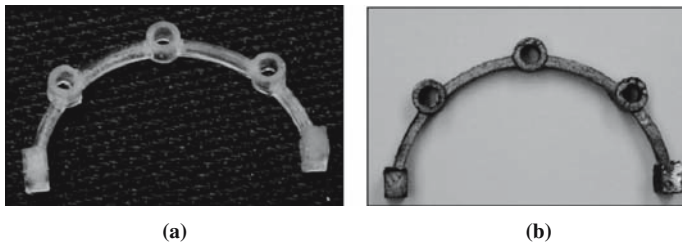


**Fig. 8.34** The 3-implant dental bar: (a) Ice pattern by rapid freeze prototype; (b) metal bar cast with ice pattern (Huang et al., 2007)

is advantageous over traditional processes on fabricating parts with internal features and complex geometries.

Selective Laser Melting (SLM) is a process of fabricating 3D metal parts using a technology similar to Selective Laser Sintering (SLS) but with higher laser power. SLM generates metal parts in layers by selectively melting the metal powder with a focused laser beam (Vanderbroucke et al., 2006). Metallic powder is fully fused in slices to produce a part of full density. Standard metals like stainless steel and hot worked steel are commonly used materials in this process. Other materials like cobalt-chromium alloys and titanium alloys can also be used to fabricate 3D parts with this process. A 3-implant dental bar fabricated by SLM from a titanium alloy is shown in Fig. 8.35(a).

Another DDM process for producing fully functional metal parts directly from CAD models is 3D metal printing, which prints the part layer-by-layer from metal powder. After a layer of metal powder is spread on the platform, the binder material is selectively dispensed over the layer of metal powder using inkjet printing technology. The zone filled with binder holds together while the other area is left with loose metal powder. After building one layer, the platform is lowered by one layer thickness and a new layer of powder is spread. The process is repeated until the complete green metal part has been built. The unbound powder is removed and the green metal part is sintered

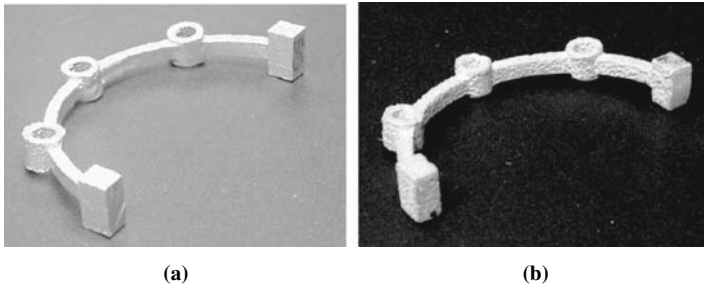


**Fig. 8.35** (a) The 3-implant dental bar fabricated by SLM with Ti-6Al-4V; (b) physical part of same geometry fabricated by 3D printing with stainless steel (Delli, 2006)

to obtain the final metal part. A stainless steel dental bar fabricated by this process is shown in Fig. 8.35(b).

## 8.7 Conclusion

Automating the design and fabrication of dental restorations involves acquiring the patient's oral digital data, surface reconstruction from the digital data, use of the surface information to design dental restorations, and fabrication of physical parts from the digital designs. Acquiring the patient's oral data can be done with a contact or non-contact digitizer. A contact digitizer is relatively inexpensive and fairly accurate. However, it is slower and can be used only on a stone model. A non-contact digitizer can acquire data faster and a miniature optical device can be placed inside the patient's mouth for direct data acquisition. The acquired digital data in either case needs to be converted into a surface representation such as a triangular mesh in STL format for purposes of visualization rendering and further data processing for digital design and fabrication. This requires surface reconstruction from the digital data when the data represents a set of points on the object surface.

When the digital data is from CT or MRI images, the data can be converted into a voxel model, with its surface evaluated and rendered using a marching cube algorithm. After the acquired digital data has been converted into a surface or solid representation, the digital design process can begin. This may involve, e.g., using a B-spline function to represent the surface of a tooth and to edit it by adjusting feature points and curves. Design of a dental bar for a restoration involving implants can also be automated by using the measured data to determine the positions and orientation of the healing abutments, with which to construct the cylinders and connecting bar of the dental bar model. Finally, the design model representing an inlay/onlay, crown, bridge, or implant dental bar can be transferred into a physical dental part of the same



geometry through a digital fabrication process such as CNC machining, rapid prototyping plus investment casting, or direct digital manufacturing.

Dental automation available from commercial CAD/CAM systems today has made the creation of some restorations, such as veneers, inlays, onlays, or crowns, possible in a single visit to a dentist. However, in-office technology cannot be used for more complex restorations such as bridges to replace missing teeth. In these situations, stone models must be sent to the dental lab where a laboratory automation system could be used to generate a high-strength zirconia framework that is manually veneered with porcelain to complete the restoration. Interestingly, twenty years after the introduction of in-office CAD/CAM technology, there is still only one in-office system while more than ten laboratory-based CAD/CAM systems are available today. This probably reflects the fact that although one-appointment, in-office milled restorations are convenient, the more important current issue may be the dental technician manpower shortage, which is addressed with laboratory automation systems.

In spite of the progress with dental laboratory technology, present systems for automating the design and fabrication of dental restorations involving implants have very limited capabilities and are largely under development. Automating this design and fabrication process will greatly reduce the cost and time of treatment and also improve the quality and consistency of implant-based restoration design and fabrication. Development of advanced CAD/CAM systems for such restorations is a critical area of future research in dental automation.

## References

- Adolph S, Gurke S (2001) Modeling of a fitting inlay from various information. 2001. Proc Vision, Modeling and Visualization Conference, Stuttgart, Germany, pp 309–316
- Akbar JP, Petrie CS, Walker MP, Williams K, Eick JD (2005) Marginal adaptation of Cerec 3 CAD/CAM crowns using two different finish line preparation designs. *J Prosthodontics* 15:155–163.
- Asam SG (2006) Computer automated dental bar design for removable implant-based dentures. MS thesis, University of Missouri-Rolla.
- Bindl A, Mormann WH (2003) Clinical and SEM evaluation of all-ceramic chair-side CAD/CAM-generated partial crowns. *Eur J Oral Science* 111:163–169.
- Boca Radiology: CT Dentascan, <http://www.bocaradiology.com/Procedures/dentascan/index.html>, visited in Aug 2006.
- CEREC: Product Information, <http://www.cereconline.com/>, visited in Sep 2006.
- Cercon Smart Ceramics, <http://www.cercon-smart-ceramics.com/>, visited in Sep 2006.
- Chang CC, Lee MY, Ku YC (2003) Biomedical engineering application basis and communications: digital custom denture design with new abrasive computer tomography and rapid prototyping technologies. Center for Biomedical Engineering, Taiwan.
- Cynovad: Product information, <http://www.cortexmachina.com/index.htm>, visited in Sep 2006.
- DELCAM: Dental Machining with PowerMill, <http://www.dental-cadcam.com/general/powermill.asp>, visited in Sep 2006.
- Delli P (2006) Automated design and fabrication of dental bars. MS thesis, University of Missouri-Rolla.

- Denissen H, Dozic A, van der Zel J, van Waas, M (2000) Marginal fit and short-term clinical performance of porcelain-veneered CICERO, CEREC, and Procera onlays. *J Prosthet Dent* 84:244–248.
- Duret F (1998) CAD/CAM in Dentistry. *J Am Dent Assoc* 117:715–720.
- Fabio R (2003) From point cloud to surface: the modeling and visualization problem. Int workshop on Visualization and Animation of Reality-based 3D Models XXXIV–5/W10.
- Fraunhofer IOF: Optical Systems, [http://www.iof.fraunhofer.de/index\\_e.html](http://www.iof.fraunhofer.de/index_e.html), visited in Aug 2006.
- Gawate AA (2005) Computer aided software tool for design of dental bar. MS thesis, University of Missouri-Rolla.
- GOM Optical Measuring Techniques: ATOS Product information, <http://www.gom.com/EN/index.html>, visited in Sep 2006.
- Huang C, Leu MC, Richards VL (2007) Investment casting with ice patterns and comparison with other types of rapid prototyping patterns. Proc 2nd Int Symposium on Shape Casting, Orlando, Florida.
- Lava: Technical Product Profile, [http://solutions.3m.com/en\\_US/](http://solutions.3m.com/en_US/), visited in Sep 2006.
- Leu MC, Peng X, Zhang W (2005) Surface reconstruction for interactive modeling of free-form solids by virtual sculpting. *Annals of CIRP* 54(1):131–134.
- Leu MC, Zhang W, Sui G (2005) An Experimental and Analytical Study of Ice Part Fabrication with Rapid Freeze Prototyping. *Annals of the CIRP* 49(1):147–150.
- Leu MC, Gawate A (2006) Computer aided dental bar design. U.S. Patent Pending.
- Liu Q, Leu MC (2006) Investigation of interface agent for investment casting with ice patterns. *ASME J Manuf Science and Eng* 128(2):554–562.
- Liu Q, Leu MC, Schmitt SM (2006) Rapid prototyping in dentistry: technology and application. *Int J Adv Manuf Technology* 29:317–335.
- Liu Q, Leu MC, Richards V, Schmitt SM (2004) Dimensional accuracy and surface roughness+ of rapid freeze prototyping ice patterns and investment casting metal parts. *Int J Adv Manuf Technology* 24:485–495.
- Liu Q, Richards VL, Daut KP, Leu MC (2006) Curing kinetics of ceramic slurries used in investment casting with ice patterns. *Int J Cast Metals Research* 19(3):195–200.
- Lorenson WE, Cline HE (1987) Marching cube: a high resolution 3D surface construction algorithm. *Computer Graphics* 21:163–169.
- MAXNC: Product Catalog, <http://www.maxnc.com/>, visited in Aug 2006.
- MicroScribe: Microscribe Digitizers, <http://www.microscribe-digitisers.co.uk/>, visited in Aug 2006.
- Molin MK, Karlsson, SL, Kristiansen MS (1996) Influence of film thickness on joint bend strength of a ceramic/resin composite joint. *Dent Material* 12:245–249.
- Mormann WH (2000) The right step to Cerec 3. *Int J Comput Dent* 3:3–4.
- Mormann WH, Krejci I (1992) Computer-designed inlays after 5 years in-situ: clinical performance and scanning electron microscopic evaluation. *Quintessence Int* 23:109–115.
- Nobel Biocare Annual Report (2005) Market Analysis 2005.
- Nobel Biocare Procera, <http://www.nobelbiocare.com/global/en/default.asp>, visited on Sep 2006.
- OrthoCAD: Product information of OrthoCAD iQ, <http://www.orthocad.com/>, visited in Sep 2006.
- Schmitt SM (2001) Dental lab technology in the digital age. *J Dental Technology* 18(1):18–21.
- Song YL, Li J, Huang T, Gao P (2005) The feature-based modeling of standard tooth in a dental prosthetic database. IEEE, Eng. in Medicine and Biology 27th annual conference, pp 6930–6933.
- Sui G, Leu MC (2003, August) Investigation of layer thickness and surface roughness in rapid freeze prototyping. *ASME J Manuf Science and Eng* 125(3):556–563.
- Vanderbroucke B, Kruth JP (2006) Selective laser melting of biocompatible metals for rapid manufacturing of medical parts. Proc SFF Conference.

Wikipedia: Computed Tomography, [http://en.wikipedia.org/wiki/CT\\_scan](http://en.wikipedia.org/wiki/CT_scan), visited in Aug 2006.

Zhang W, Leu MC, Ji Z, Yan Y (1999) Rapid freezing prototyping with water. *J Mat and Design* 20:139–145.

Zimmerdental: Restorative manual for immediate bar fabrication, [www.zimmerdental.com/pdf/lib\\_guidTsvAdvRestMan9of11.pdf](http://www.zimmerdental.com/pdf/lib_guidTsvAdvRestMan9of11.pdf), visited in Sep 2006.

# Chapter 9

## The Development of an Artificial Finger Joint

I. Gibson, S. P. Chow, K. W. Lam, W. W. Lu, A. H. W. Ngan,  
W. Y. Yip and K. Y. Chiu

### 9.1 Introduction

Joint replacement surgery is a challenging procedure in orthopaedic surgery that deals with pathological changes and degenerations of human joints. From the 1950s it has gained success in relieving pain and recovering motion of diseased joints where normal medication and physiotherapy has had little effect. Almost all mobile joints can be replaced by artificial ones. However, complications such as the lack of functional motion, recurrent joint deformity, implant loosening, wear and component fracture are still common and revision surgery is often required. An ideal solution for any implant system is still awaited with eager anticipation.

The greatest achievements in joint replacement are probably in the area of total hip arthroplasty (THA) stimulated by Charnley's [1] low-friction arthroplasty based on the articulating couple of metallic femoral head and polymeric acetabular cup, circa 1969. Gunston [2] employed this metal-on-plastic concept to develop a polycentric knee joint design, which is still widely accepted as the gold standard in total knee arthroplasty (TKA). Charnley's implants reported long-term survival of about 90% at 10 years and 80% at 20 years in follow-up studies [3, 4]. Similar encouraging survival rates up to 83% at 16 years and 88% at 14 years were noted in new TKA systems [5, 6].

Joint replacement in the upper extremities has not shown the same level of accomplishment. Implant loosening is a major problem with a failure rate from 25% to 50% for condylar replacements of the elbow joint [7]. Neviassen [8] even pointed out that a constrained design of shoulder arthroplasty was so unsuccessful that over 90% of reviewed cases exhibited implant loosening, deformation or breakage.

Swanson, in 1972 [9], introduced an arthroplasty replacing arthritic finger joints with a joint spacer made of silicon rubber. Swanson's silastic implant has

---

I. Gibson  
Department of Mechanical Engineering, National University of Singapore  
mpegi@nus.edu.sg

dominated finger joint replacement despite high fracture rate of 14% in a large series of studies with average follow-up of 8 years [10]. It is necessary to reconsider the working principles for design of implant systems for the upper extremity.

## 9.2 Finger Joint Arthroplasty

Arthritis, in particular rheumatoid arthritis, affects over two million patients in the US. Consequences of rheumatoid arthritis start with inflammation of synovitis and joint swelling, leading to joint destruction and deformity causing pain, joint instability and tendon rupture. Rheumatoid arthritis is somehow related to the disturbance of the immune system although the exact details are not clear. Artificial joint replacement has found to be effective in removing pain and recovering most joint functions.

Pathological disturbance by osteoarthritis, posttraumatic arthritis and rheumatoid arthritis can lead to loss of joint function. Affected joints usually end up with erosions in the articular cartilage and bone resulting in unstable bony support, synovitis and inflammatory responses, which can destroy the surrounding soft tissues. Secondary joint problems include joint deformity and dislocation arising from imbalanced tendon load and loosened ligamentous supports from a destroyed articulating structure. Consequences are pain, joint instability, loss of mobility, excessive deformity and unrecoverable disability of hand function from soft tissue rupture. Indications of the need for finger joint reconstruction include persistent pain prior to destruction by arthritic diseases, signs of joint deformity, and joint contracture with limited flexion arc.

Flatt [11] first introduced a metallic hinge-type prosthesis, based on the work of Brannon [12], in metacarpophalangeal (MCP) and proximal interphalangeal (PIP) joints affected by rheumatoid disease. Postoperative results showed that it could restore some function, remove joint destruction and deformity, and most importantly relieve pain. Follow-up by Zachariae [13] revealed that the fixed center of rotation of this prosthesis did not accommodate the normal rotation of a real finger joint. Excessive stresses due to muscular imbalance promoted progressive bone resorption, penetration to cortex with consequent prosthetic loosening and joint deformity.

Swanson invented another hinge-type finger joint prosthesis made of silicone material [9]. He claimed this implant could deform with respect to biomechanical variances and distribute the load to the bone shaft. The simplicity in operation allows this implant to be the most commonly adopted implant for finger joint arthroplasty. Although satisfactory feedback was received from patients, there are doubts over its long-term performance. Jackson [14] reported cases of erosion at the bone-silicone interface and silicone breakages are frequent. Henk et al. describe long-term findings [15] with limited range of motion

(30°–40°) and signs of silicone-induced synovitis from wear particles in patients with the Swanson implant.

Another major problem in joint prostheses is aseptic loosening with failure at the anchoring between the bone and the implant. Revell et al. [16] described severe wear particles from articulating surfaces inducing adverse biological reactions in the host tissue, causing localized resorption at the bone implant interface and loosening of the artificial joint. Fisher [17] reported on studies by Green [18] that too high a concentration of these particles with sizes ranging from 0.1 to 7  $\mu\text{m}$  could stimulate macrophages to act upon osteoblasts and osteoclasts resulting in bone resorption and wear-debris-induced osteolysis. Fisher et al. [19] also suggested that polyethylene prosthetics were more susceptible to wear-debris-induced osteolysis due to the wear rate and the size of the wear particles.

Metal-on-metal (MOM) and ceramic-on-ceramic (COC) articulations have recently become popular as metallic corrosion and brittle fracture of ceramic have diminished by advancement of materials processing and proper design. Large joint replacements have shown great success with reduced wear rate [20–22]. Greenwald et al. [23] indicates that the wear rates of MOM and COC couples, compared with polyethylene, can be reduced by 50 and 1000 times respectively.

Problems arising from constrained implants have been overcome using semi-constrained articulating surfaces, termed ‘surface replacement’. The RMS design uses an articulating surface matching the anatomical shape of a real joint. Joint stability relies on the integrity of the surrounding soft tissues. Clinical trials undertaken by Johnston [24] revealed excellent performance of the RMS prosthesis (later known as AVANTA) with range of motion (ROM) to an average of 70°, pain relief and sufficient joint stability. However, aseptic loosening is still a potential problem from the polyethylene component of the prosthesis. An adapted model from Lundborg uses titanium dental screw fixation to introduce osseointegration across the bone-implant interface. A study [25] by Moller et al. suggested good osseointegration without apparent loosening but fractures of the silicone components were observed in high incidences (25%).

Some problems arising from finger joint arthroplasty have been overcome but an ideal design providing stability, functionality and durability is not yet available. It is believed that with recent advancements in technology, a design which adopts anatomical structure, improved corrosion and wear resistance and osseointegration fixation can yield a new generation of finger joint prosthesis.

### 9.3 Design Objectives for a New Artificial Finger Joint

The objectives are to develop a new finger joint prosthesis that provides:

1. an anatomical structure with intrinsic joint stability to reproduce joint balance and a near normal range of motion,

2. stable anchoring at the bone-implant interface by press-fit mechanical interlocking and long-term fixation to bone by osseointegration, and
3. high wear resistance through the use of advanced materials.

To integrate these novel ideas, the following issues had to be solved:

1. The linkage between the modular connection of joint components and the fixation to bone was considered.
2. A critical design of the articulating surface which can reproduce the normal range of motion and joint stability with sufficient thickness to withstand wear and tear long-term was developed.
3. The right materials and the manufacturing process were determined to produce a reliable and durable end product.
4. A testing protocol for the preclinical evaluation of artificial finger joint was developed for the examination of the performance of the new joint design in accordance with specifications.

All implant systems should restore original function with minimal side effect to the implanted body. Synthetic biomaterials face problems of fatigue failure and degradation which doesn't match the healing and regeneration processes of living tissue. Implantation triggers responses from the immune system attacking both healthy tissues and implant. Furthermore, pathological disturbance by surgical intervention compounds the difficulty of functional restoration. Operative techniques are still inadequate in providing fully recovered function. This strongly governs the effectiveness particularly in the case of orthopaedic implants where joint stability, mobility and deformity correction are of prior concern.

Early finger joint designs focused on functional features such as resembled ROM and joint stability. Newer designs emphasize restoration of functional anatomy and bone implant adaptation. Any new design must follow 3 main requirements: (1) Anatomical compatibility, (2) Functional compatibility and (3) Materials compatibility. Mechanical hinge joints maximize the stability of a finger joint without collateral ligament support but loosen due to poor bone-implant adaptation. Silastic implants have minimal constraint on bone but face problems of materials fracture. Unconstrained prostheses provide the best functional ROM but joint stability is insufficient and high recurrent deformities persist. It is suggested that there be a good compromise among all design criteria since all issues on implant design cannot be fully achieved as illustrated in Fig. 9.1.

Criteria for the new design of artificial PIP joint should conform to:  
Anatomical compatibility including:

- minimal resection to bone thereby maintaining the joint integrity with the supportive soft-tissue structure;
- minimal invasive surgery thereby inducing fewer traumas to the tendon network essential for joint mobility;

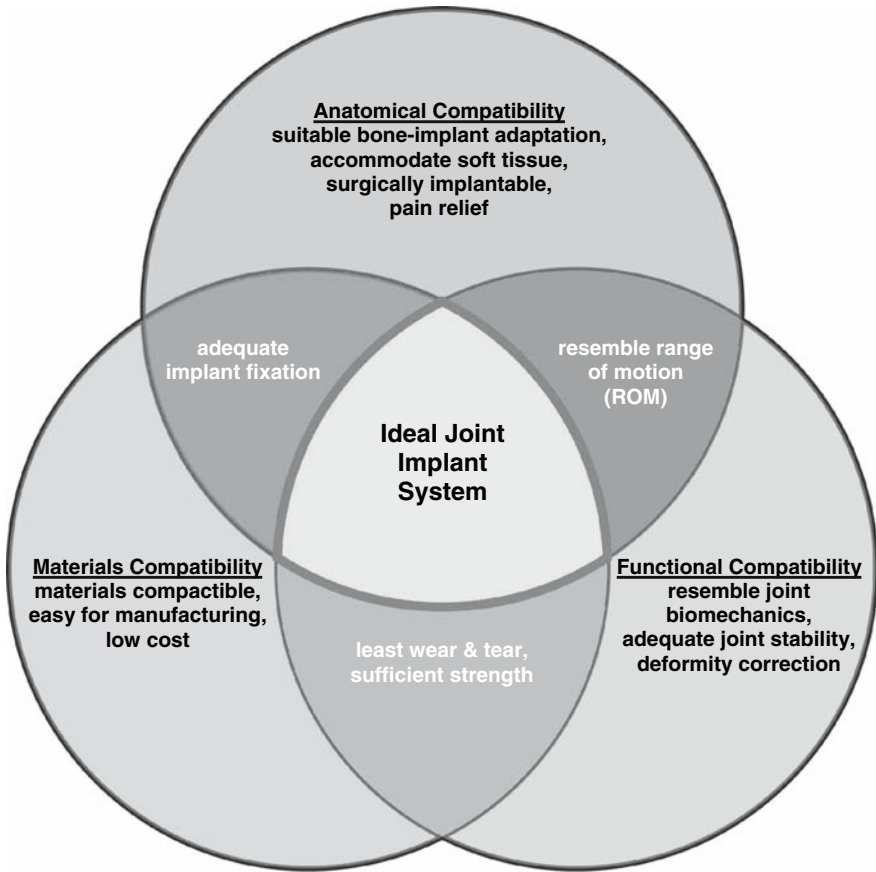


Fig. 9.1 Compromised design considerations for ideal joint implant system

- resemble the diameter of the natural joint in lateral direction maintaining a proper moment arm and mechanical advantage;
- maintain joint space and the original bone length of the replaced joint;
- fit into the internal medullary canal of phalangeal bones thereby achieving press-fit macro-interlocking fixation;
- a large variety of implant size and stem size thereby providing a coherent bone-implant adaptation;

Functional compatibility including:

- withstand loading under physiological conditions and effectively transmit joint load to the bony bed underneath;
- unconstrained articulation thereby promoting recovered ROM;
- intrinsic stability from the unconstrained articulation thereby enriching the support from attenuated collateral ligaments;



- proper alignment to the respective phalangeal bones;
- resist dislocation force thereby correcting deformity to improve cosmetic appearance;

Material compatibility including:

- biocompatibility;
- sufficient strength to bear loading without permanent failure;
- superior wear and tear properties thereby improving the service life;
- ability to be manufactured into a delicate shape.

## 9.4 Study of Finger Joint Morphology for Implant Design

A series of implant designs were generated during development of this new artificial PIP joint with progressive modifications and improvements over previous models [26]. Anatomical compatibility was given priority since it is to be used with the natural bony and ligamentous structures. Most recent artificial knee joints focus on anatomical restoration in contrast with older designs using a fixed hinge. Recent finger prostheses follow the trend by employing substantial consideration of the functional anatomy of both the IP and MCP joints, with minimal bone excision, the modeling of true anatomical articular surface as well as corresponding soft-tissue balance incorporated into the design [27, 28].

Morphometrical data directly from real phalangeal bones were measured to provide a basis for an anatomical implant design. Similar to total condylar knee prostheses [29], geometric parameters were established for the design of different functional parts of the artificial PIP joint with reference to previous works on Caucasian finger joints [30–31]. These functional parts for the joint design are illustrated in Fig. 9.2 and include (1) major sizes of proximal and distal implant components, (2) sizes of fixation stems on proximal and distal components, (3) coverage of joint curvatures at head of proximal phalanx and base of middle phalanx for the design of implant ROM, (4) contour of articulating surfaces for the design of implant bearing surface and (5) backing surfaces of proximal and distal components which will be supported by resected bony bed.

The radial and ulnar condyles on the head of the proximal phalanxes exhibit asymmetry on different digits [31] favoring convergence of the digits towards the palm. Inter-digital variation of skeletal structure among population compounds the difficulty to unify a design suitable for all fingers. 8 different PIP joint designs are required for the index, long, ring and small fingers on both the left and right hands. If 5 sizes of each joint implant to accommodate variations in population, then there are at least 40 implants and associated surgical instrumentation needed for a complete implant system for the PIP joint. All current artificial finger joint systems do not consider condylar asymmetry and a

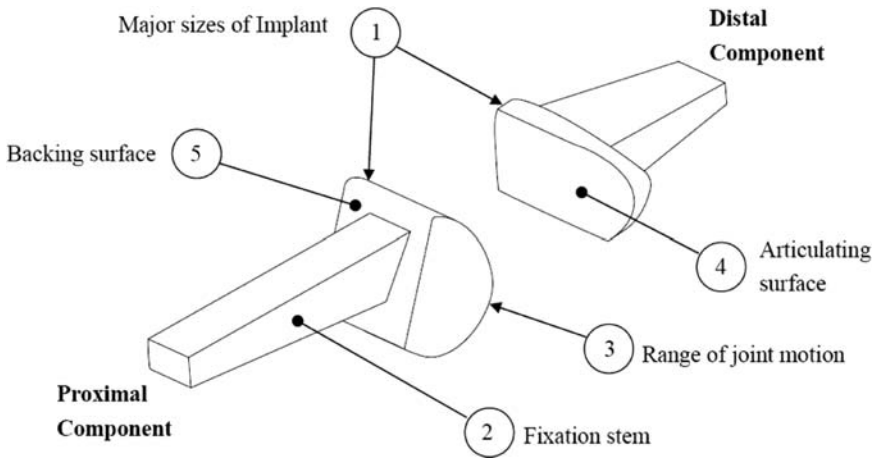


**Fig. 9.2** Functional elements of artificial finger joint design

common joint design compromise for PIP joints on all digits is applied in clinical practice.

Ten embalmed Asian hand specimens with a mixed gender were used to study the morphological characteristics on phalangeal bones. The proximal and middle phalanges from index, long, ring and small fingers were cleared of soft-tissue attachments. 80 phalangeal bones were then mounted in angle holders for x-ray imaging. Basic bone dimensions denoting the bone length 'Lpp', the head diameter 'Dh', the head width 'Wh' of the proximal phalanges and the bone length 'Lmp', the base height 'Hb', the base width 'Wb' of the middle phalanges as indicated in Fig. 9.3, were measured by an engineering CAD system.

Preferably, one physical quantity of the phalangeal bone should be chosen as a common denominator for the best fitting implant for all digits. All other dimensions can then be defined by scaling to this denominator, which should be easily obtained through direct or x-ray examination to facilitate preoperative planning.

Size matching for some finger joint implants is based on best fitting of the stem to the space of the medullary cavity of the bone shaft. Mismatched implant size is suggested to have inferior effects on the active ROM due to an erratic joint rotational centre and a changed flexor moment arm [32, 33]. Recent studies recommend the selection of implant type to enable the restoration of the original joint rotational centre and a best-fit head diameter of the proximal phalanx in the sagittal plane [31]. Examination of the head diameter 'Dh' was undertaken as the possible denominator for the implant design. Although variations exist among different digits, the mean head diameter from the mixed group showed no significant difference for all individual digits. A single implant design generated from Dh as denominator can be applied to all digits excluding the thumb with 99% level of confidence. Dh from the mixed group

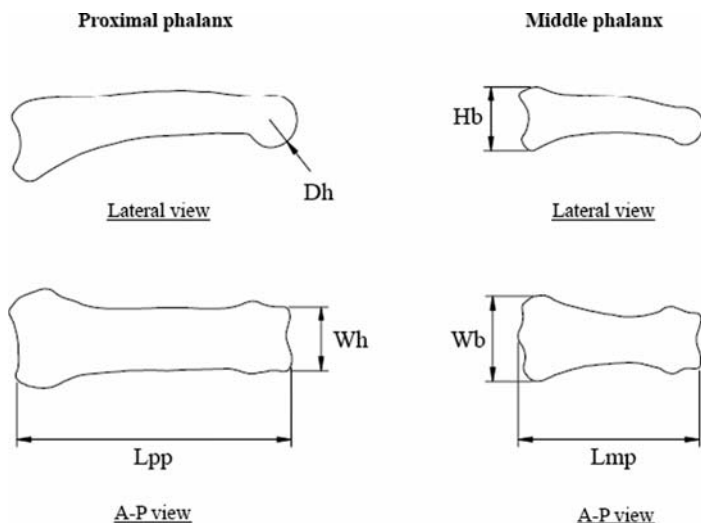


**Fig. 9.3** Major dimensions of phalangeal bones

ranged from 5.14 to 9.12 mm and followed a normal distribution with prominent sizes of 7 and 7.5 mm representing 40% of the sample population.

Measurements of the head width 'Wh' of the proximal phalanx, the base height 'Hb' and the base width 'Wb' revealed a pattern comparable to the bone lengths. The basic joint dimensions have a strong dependency on joint size which in turn correlates with the head diameter. Statistical analyses revealed good consistency and no significant difference of the Wh/Dh, Hb/Dh or Wb/Dh ratios amongst the mixed group. This essentially provides Dh as a single parametric quantity that enables a common design suitable for all digits to be established.

## 9.5 Intramedullary Dimensions for Fixation Stem Design

Implant fixation governs the success and survival of implant surgery and loosening is still a prime concern. An ideal fixation must provide firm anchoring of the implant with sufficient stability and to allow proper load transfer across the bone-implant interface. Fixation by mechanical or biological means has been the subject of rigorous research.

Bone cement fixation involves setting a viscous polymer in the space between the bone and the implant. A fixation stem with less conforming geometry to the containing bone can still be rigidly anchored in place. This concept was initiated by Charnley who employed poly-methylmethacrylate (PMMA) as bone cement to fix hip joint endoprostheses in bone in the 1950s [34]. Since then it has become routine for THR and TKA with excellent survival of over 90% in long-term

studies [35]. However, necrosis of the contact bone may result from the high setting temperature during polymerisation [36] and with the release of toxic monomer (MMA) [37]. Revision surgery is difficult, especially in small joints when cured bone cement is to be removed due to infection or implant loosening. Cement fixation has been reported in some finger joint replacements [38, 39] but there is general agreement that use in small joint arthroplasty should be avoided [33, 40, 41].

Cementless, biological fixation later emerged as an alternative for the hip and knee prostheses in the 1980s, using methods such as porous coating, ion-implantation or grit blasting, coating with titanium or hydroxyapatite, etc. Results are controversial with some successes [42–44], including reported histological evidence up to 50% bone ingrowth [45]. Similar success was achieved by Lundborg who used titanium screws in MCP joints [46]. Based on the concept of osseointegration, Beckenbaugh developed a series of artificial finger joints using pyrolytic carbon [28] showing evidence of retarded implant dislocation and/or loosening.

However, results are poor compared to current hip and knee replacements. Surface modification of implant stems may not be applicable to small finger joints since porous coating, with pore sizes ranging from 20–500 $\mu\text{m}$ , may limit the core cross-section of the fixation stem bounded by rigid materials whereas the outermost pores may initiate cracks which then propagate towards the core to lead to fracture, as in the case of hip implants. One should consider biological fixation as supplementary since it can only be promoted when the implant surfaces are in good contact with the bone stock. Micromotion of less than 0.6mm across the bone-implant interface has positive effects on introducing osseointegration whereas high incidence of radiolucent lines could be observed when such micromotion exceeds 1.9 mm [47].

Although many finger joint prostheses have been attempted [33], little has been documented about geometry of medullary canals of phalangeal bones [30, 48]. The internal cross-sections of medullary canals of the proximal and middle phalanges are generally elliptical in shape, transforming smoothly to a semi-circular form towards the proximal end with the flat edge located at the palmar aspect. A straight uniform section for the fixation stem of the proximal component and a double convergence section for the distal component should provide good conforming geometries for fixations to the respective intramedullary canals.

Morphologic data from medullary canals were measured from radiographs of the 80 phalangeal specimens. Correlations of the canal dimensions to Dh were examined. This did not reproduce a relationship to joint size as strong as the external bone morphology, which is also noted in other studies [30] and thought to be due to cortical wall thinning with age. Linear canal dimensions were divided by Dh to provide a geometric ratio independent of joint size to provide basis for a common design of fixation stem. After normalization, statistical analyses showed that the effects due to variations in joint size among different digits were diminished.

Four basic geometries; round, elliptical, rectangular and octagonal sections for design of the fixation stem were examined. The round section cannot resist rotation, whilst the others have translational and rotational stability within the medullary cavity. With best fit and minimal reaming to the wall thickness of the medullary canals, a fixation stem with elliptical shape fits best inside the space of the canal. An octagonal section also fits well. However rectangular or round sections do not match the cavity well and provide the least anchorage to the internal wall. Intramedullary reaming of the phalangeal bone shaft can improve fitting of the fixation stem, but this is traumatic to the bony structure and may induce cracking if overdone. The chosen shape should therefore correspond to both a minimum allowable reaming of bone to achieve stability and a maximum possible tolerance to size when reaming is necessary. When the size margin from full contact up to full cortical thickness is considered, the elliptical and octagonal sections have possible stem enlargement of 50% and 68% respectively from the minimum contact size. This is in sharp contrast to the round and rectangular sections which show only 0% and 24% possible enlargement. An octagonal section of the fixation stem is most suitable to be fitted into the medullary canals of phalangeal bone based on flexibility to allow best stability, tolerance on stem size and maximum reaming before penetrating full cortical thickness of bone shaft.

To enhance stability of the implant in resisting multi-directional joint loads and to minimize piston effect or subsidence along the bone shaft, multiple flanges were designed along the stem. The basic dimensions of these flanges were similar to a standard cortical bone screw. One flange surface is perpendicular to the direction of the stem axis to achieve maximum resistance to pullout force. Supplementary fixation by bone ingrowth between flanges could be introduced during a healing process by surface treatment to promote osseointegration.

## 9.6 Relationship of Sagittal Curvature of Condyles to ROM

Abduction-adduction at the PIP joint is constrained by a bi-condylar configuration on the articulating surface and the collateral ligament support. Only flexion extension, similar to a mechanical hinge joint, is possible in general as the joint motion. The hand digits exhibit convergent arcs during flexion towards the palm. Their axes of rotation vary and are not perpendicular to the longitudinal axes of phalangeal bones, except in the long finger [49, 50], due to asymmetry at the radial and ulnar condyles. The PIP joint is at neutral position ( $0^\circ$ ) when the middle phalanx is straightly aligned with the longitudinal axis of the proximal phalanx. The active ROM of the PIP joint ranges from  $108^\circ$  to  $113^\circ$  with an average of  $110^\circ$  [51]. Hyperextension of a joint is possible but limited to  $-5^\circ$ , constrained by the volar plate and its

check-reins ligament at the palmar aspect. The functional ROM was found to be  $36^{\circ}$ – $86^{\circ}$  for a selection of most common prehensile activities from daily living [52]. Passive joint motion is larger in extension but about the same in flexion to the active range.

To achieve a joint flexion over  $90^{\circ}$ , the head of the proximal phalanx is slightly offset from the longitudinal axis of the bone shaft. Figure 9.4 shows the motion from a PIP joint where the middle phalanx is indicated at its relative positions from full extension to flexion forming a maximum ROM of  $110^{\circ}$ . The arcs of coverage of the articulating surfaces on the head of proximal phalanx and the base of middle phalanx are denoted ' $\alpha_h$ ' and ' $\alpha_b$ ' respectively. Based on this arrangement, the dimension of  $\alpha_h$  can be determined as not smaller than the sum of ( $\alpha_b$  plus ROM of  $110^{\circ}$ ). These two dimensions were measured from the appearance of the layer of underlying calcified cartilage right above the subchondral bone. Measurements show mean values of  $201.5^{\circ}$  and  $76.3^{\circ}$  of the mixed group of the angle arc of coverage on the head of proximal phalanx and base of middle phalanx respectively. The measurements agree with the assumed condition of  $\alpha_h \geq \alpha_b + \text{ROM}$  ( $201.5^{\circ} \geq 76.3^{\circ} + 110^{\circ}$ ) under full joint contact. The dimensions ' $\alpha_h$ ' and ' $\alpha_b$ ' of the arc of coverage of the articulating surfaces are applied to the design of the artificial joint surfaces on the proximal and distal components respectively. Increasing the arc of coverage on the distal component denoted by dimension ' $\alpha_b$ ' could enhance the implant stability in resisting joint subluxation on both the dorsal and palmar directions accordingly, but possible ROM would be lessened as a consequence.

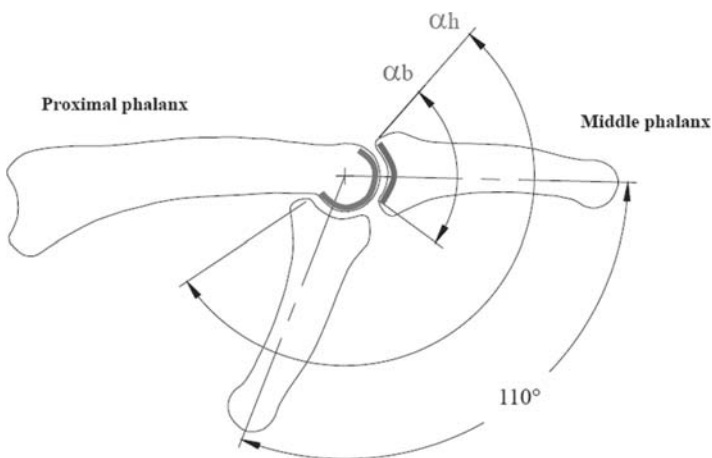


**Fig. 9.4** Major arc dimensions on articulating surfaces for ROM

## 9.7 Generation of Implant Articulating Surface

The feature geometry of an articulation provides stability of the skeletal support favoring joint motion in the desired directions whilst resisting abnormal joint movement. Contribution to joint stability relies not only on the feature geometry of the articulation, but also on the integrity of the ligament and tendon arrangement, the joint load from muscle contraction, as well as the magnitude and direction of the externally imposed distraction. A more constrained design may be necessary to compensate partially for the effects from soft-tissue attenuation.

The bi-condylar configuration of a PIP joint is naturally more stable than the ball and socket configuration of an MCP joint. With the MCP joint, the load from the line of action coincides with the joint rotational center in the coronal plane where any laterally imposed loading would alter the system balance. The stability of MCP joint is highly reliant on the soft-tissue balance of the interossei. Ulnar drift is the most prominent deformity being unsolved for patients suffering from degenerative disease where the balance of soft-tissue is progressively attenuated. Good results from surface replacement techniques are more indicative for cases with osteoarthritis or traumatic arthritis based on their less affected soft-tissue integrity than rheumatoid arthritis [28, 39]. Surface replacement with stabilized features was thereafter proposed [53]. It is therefore suggested that a joint feature geometry that incorporates the contribution of joint load could enhance joint stability by maximizing the effect from muscle action. A flattened condylar articulation is proposed to cope with this inadequate condition from an unconstrained design. Before accounting for the effect of joint stability from such a semi-constrained design, numerical analysis has shown that the maximum Hertzian contact stresses [54] in a flattened joint design could be substantially reduced by 73% from that in a total condylar design. Lower contact stresses could reduce wear and tear damage and improve the long-term performance of an artificial joint.

With a profile similar to a natural joint, the surface area of the design can be maximized to achieve a more uniform stress distribution. The joint load can also be properly transferred to the rigid cortical support of the resected bone end. The head of the proximal phalanx is trapezoidal in shape in the transverse view. This shape produces a cam effect to tighten up the collateral ligaments during flexion such that joint stability can be enhanced in a gripping motion [55]. The base of the middle phalanx is generally elliptical with the dorsal tubercle smaller in radius. These geometries at the bone ends of the PIP joint were studied and featured dimensions denoting the angle of condylar divergence, ' $\theta d$ ', on the head of proximal phalanx, and the dorsal radius, ' $Rd$ ' and palmar radius, ' $Rv$ ' on the base of middle phalanx, were measured from photographic imaging as shown in Fig. 9.5.  $\theta d$  has a mean value of  $28.54^\circ$ .  $Rd$  and  $Rv$  have mean values of 6.84 mm and 11.35 mm respectively.

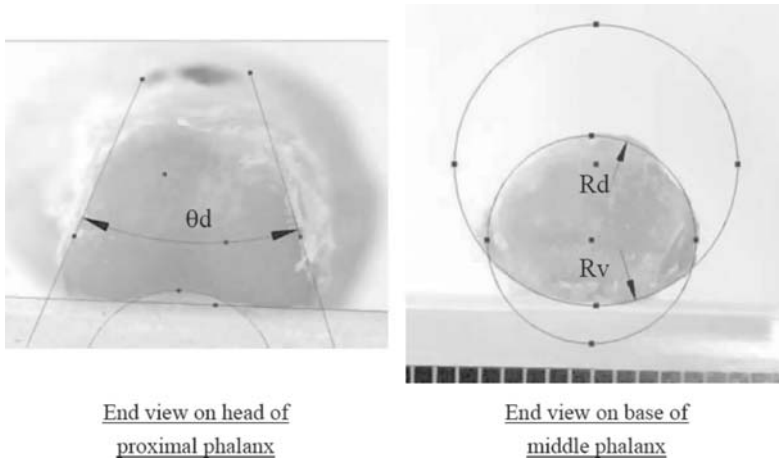


**Fig. 9.5** Major dimensions for articulating surface design

These radii were normalized using  $D_h$ . Statistical analysis of the results showed a consistent trend with no significant differences among digits. These consistent factors help in designing a common joint contour for all digits.

## 9.8 Implant Design Related to Surgical Procedure

A good implant design cannot perform well without proper positioning of the prosthesis, size comparable to the original articulation, and a balanced soft-tissue management. A detailed study on instrumentation, bone bed preservation, corresponding soft-tissue release and reconstruction are necessary to maximize the functionality of any implant system. Planning of surgical procedure should provide practicality as well as reproducibility. Instrumentation should be user friendly, simple, and eliminate incorrect surgical steps and sizing problems. Consideration of surgical procedures should be incorporated into the joint design where possible to simplify all corresponding procedures downstream. Surgical techniques for finger joint arthroplasty have not been well developed compared to hip and knee replacement. Various surgical techniques have been extensively studied, but most literature focuses on soft-tissue management and ligamentous reconstructions, rather than effectiveness of instrumentation, the bone bed preparation, the implant selection, the effect from implant sizing, as well as implant alignment and positioning [56, 57].

Due to the complicated chain mechanisms from the extensor and flexor tendons running across the PIP joint structure [49], restoration of normal



ROM is unpredictable. The surrounding soft-tissue structures require extensive release from their attachments to enable proper joint exposure for bone resection and implant insertion. Some systems require excision of the articulation beyond the collateral ligaments [11, 28, 40], as this is crucial in maintaining the stability of the finger [59, 60]. The present design aims to preserve as much original soft-tissue attachments as possible, for effective reconstruction of major tendon and ligamentous structures.

The feasibility to perform the proposed osteotomy was examined using computer simulation and rapid prototyping (RP) techniques, Fig. 9.6. Removal of joint surfaces were performed and matings to the implant backing system were verified using 3D modeling in a virtual environment. The new design of artificial PIP joint in conjunction with the phalangeal bones after precise osteotomy was produced by RP model, showing good bone-implant adaptation while preserving most of the original soft-tissue structures. Based on the satisfactory result from the RP model, a set of copper prostheses was produced for trial cadaveric implantation. By properly displacing the extensor mechanism, the head of the proximal phalanx and the base of the middle phalanx were removed by a powered sagittal saw without disruption of the collateral ligaments. With mild intramedullary reaming, the trial prosthesis could be accurately anchored into the phalangeal bone showing firm stability without side displacement relative to the bony bed. Figure 9.7 shows the accurate implantation of the new joint.

Under x-ray examination, the fixation stems generated from the normalized data showed congruent fit to both medullary cavities, suggesting good fixation. The active ROM was also examined based on passive excursion to the extensor and flexor tendons. This indicated a good resembled ROM with postoperative ROM comparable to preoperative. Full evaluation of this instrumentation was outside the scope of this work, and further study of this issue will be performed together with clinical trials.

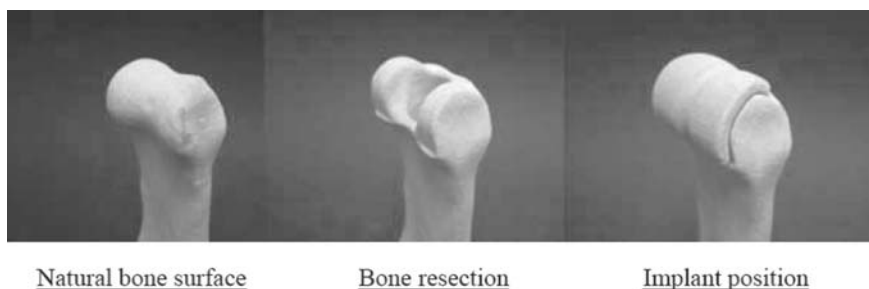


**Fig. 9.6** Trial implantation using RP models

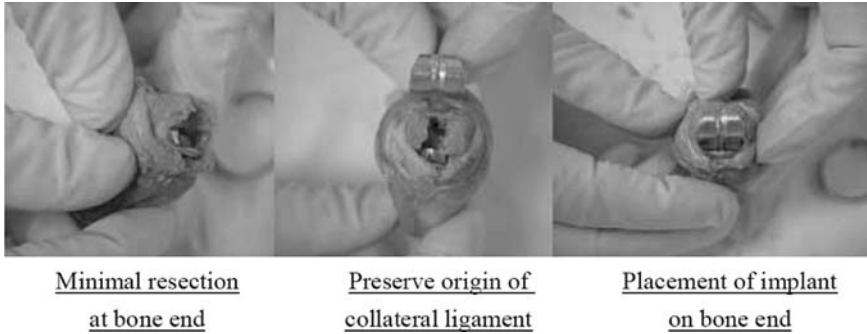


**Fig. 9.7** Verification of bone implant adaptation by cadaveric implantation

### 9.9 Implant Sizing Relating to Finger Joint Biomechanics

The size of the head diameter of the proximal phalanx ranged from 5.14 to 9.52 mm, based on measurements from an Asian sample. To accommodate variations in size, a range of implant sizes should be made available. Ash suggested 4 integral sizes (7 mm, 8 mm, 9 mm and 10 mm) of a PIP joint model to cover 97.6% of Caucasian population [31], but the reason behind a step change of 1mm between the implant sizes was not mentioned. The lack of recovered joint motion in finger joint arthroplasty is reported to be dependant on the severity of affection, preoperative condition, implant selection, success in surgical operation related implantation and corresponding soft-tissue management as well as the rehabilitation program post-surgery. However, no attempt has been made to correlate clinical results to the contributing factor of a mismatched implant size.

The effect from a change in implant size was based on Landsmeer's model [60] which suggests that finger joint motion is directly proportional to the amount of tendon excursion passing the joint surface. Finger tendons are composed mostly of fibrocollagenous tissue without the presence of elastic fibers as could be seen in most soft-tissue architectures [61] so the tendon length connecting the muscle and the corresponding phalangeal bone could be considered finite. Changing either the moment arm or the tendon length would have direct effect on ROM. This partly contributes to lack of joint motion from diseased joint or from trauma injuries where muscle contracture and damage to the tendon mechanisms frequently occurs.

Incorrect selection of implant size would have detrimental effects on the overall ROM. Too large an implant would result in flexion insufficiency while too small an implant would introduce extensor lag. To quantify this relationship between the mismatched implant size and the ROM, two mathematical models were developed from Landsmeer's articulation model [60] and Linscheid's mathematical expression [33]. These two models predict that the change

in joint flexion is  $\theta' = 1.92 R/R'$  for an oversize implant, and the extensor lag is  $\theta_{\text{lag}} = (1.92 - 1.92R')/R'$  for an undersized implant, where  $R$  and  $R'$  denote the original and the changed radii of the joint curvature respectively.

Implant size has significant effects on the recoverable joint motion from finger joint implant surgery. A perfectly matching implant size could eliminate unfavorable conditions but is not easily achieved, unless the implant is custom-made. Custom-making of implants is not impossible as a result of current developments in RP and manufacturing technologies, but is highly unlikely from an economic point of view. The normal practice is to produce an implant design in different sizes.

Employing the methodology of implant sizing by Ash [31], two smaller implant sizes (5.5 and 6.5 mm) and two larger sizes (8.5 and 9.5 mm) were added to the 7.5 mm reference size. The range of finger joint matching each implant size was fixed to be  $\pm 0.5$  mm and the percentage coverage of each size follows a normal distribution with the reference implant size covering 40% of the overall population.

An alternative set was also selected based on a percentage change of 10%. Based on this, two smaller implant sizes (5 and 6.1 mm) and one larger implant size (9.2 mm) were added. The percentage coverage of each integral size follows a normal distribution with the reference implant size covering 55% of the overall population.

Sizing based on a constant change of 5% was also studied. In this case, four smaller sizes (5.1, 5.6, 6.2 and 6.8 mm) and two larger sizes (8.3 and 9.2 mm) were added to the 7.5 mm reference joint. The coverage of each integral size again follows a normal distribution with the reference implant size covering 32.5% of the overall population.

For the series of implants with a step change of 1 mm, the possible loss of flexion or extension varies amongst the range and is found to increase with the reduction of size. This is probably due to a varied percentage deviation of each implant size. This results in less predictable joint motion although implants with a constant size change would be simpler to implant and manufacture. Implant sizing differing by a constant percentage provides a consistent possible loss of joint motion where the maximum possible loss of flexion and extensor lag at 10% size deviation are  $10^\circ$  and  $8.4^\circ$  respectively. Reducing the size deviation to 5%, although requiring seven different sizes, reduces the maximum possible loss of flexion and extensor lag to  $5.2^\circ$  and  $4.5^\circ$  respectively. For the new design, the sizing scheme with 5% step change is therefore recommended.

## 9.10 Generation of Prototype Model

The new PIP joint consisting of two components was designed to be implanted onto the proximal and middle phalanx respectively, as shown in Fig. 9.8. The proximal component was fashioned similar to the proximal phalanx head with

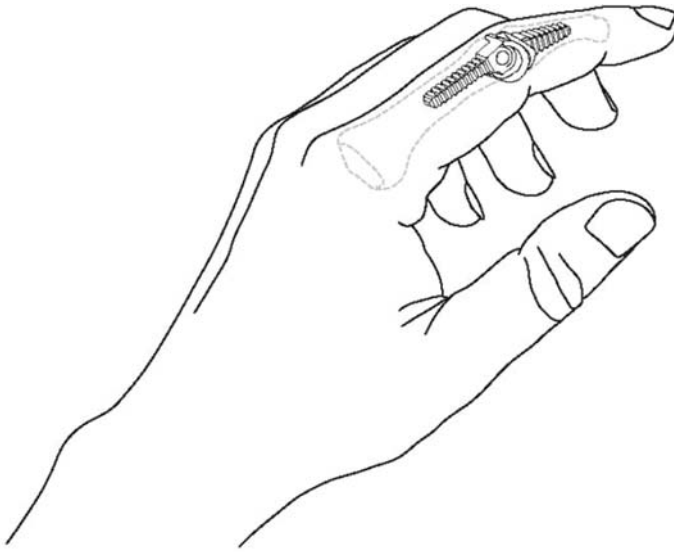


**Fig. 9.8** Illustration of implantation of the the new PIP joint in the hand

an articulating surface covering an arc of curvature of about  $200^\circ$ . The distal component is similar to the base of the middle phalanx having an elliptical external profile. The surface of the distal component follows the anatomical articulation of the base of the middle phalanx with a  $76^\circ$  curvature to provide a range of motion of about  $110^\circ$  when coupled with the proximal component. The articulating surface mimics a bicondylar structure but both convex condyles were modified to symmetrical flat condyles to enhance joint stability.

Fixation of the implant used specially designed backing surfaces and an intramedullary stem. The backing surface of the proximal component has a cup and cone configuration where joint load from any joint flexion angle can be resolved into a force component perpendicular to the bony bed support. The backing surface of the distal component has a bevel shape which resists rotation under normal compressive joint load. The fixation stems follow the medullary canals in both the proximal and middle phalanx, with a straight fixation stem shape for the proximal component and a double tapered shape for the distal stem. Flanges were created along the stem axis for enhancing bone anchorage by mechanical interlocking to the endosteal interface and allowing supplementary fixation by possible bone ingrowth to the inter-space between the flanges. Osseointegration across the bone-implant interfaces could be introduced based on material and surface modification of the fixation stems.

## 9.11 Materials Strength Requirement for Artificial Finger Joint

The stress fields on phalangeal bones under various physiological loading conditions are not very well-understood since most empirical stress data on bone loading interactions are limited to large joints such as the hip and knee. Although the finite element method (FEM) can estimate the stress field in a real situation, complicated tendon kinematic chains induce uncertainties which prohibit application in small joint simulation. At present, the loading capacity of finger joints is mostly predicted from simplified 2D theoretical models [62, 63] or more recently by 3D modelling [64, 65]. In An's model [62], the joint loadings in an index finger can be estimated from the unit applied force normal to the distal phalanx. Using this mathematical model with tip pinch strength of 66N estimated from clinical data [66], the maximum internal joint forces of an index finger can be calculated as 179N, 331N and 299N for the DIP, PIP and MCP joints respectively. The joint force from a power grip can also be estimated from this model. According to empirical data, the mean contributions of individual finger from the total grip strength were found to be 30% at index finger, 30% at long finger, 22% at ring finger and 18% at small finger [63]. In particular, forces exerted normal to the distal, middle and proximal phalanx of a single digit were evaluated in the ratios of 1:0.34:0.66 from a grip function [62]. The force component on the distal phalanx of an index finger from a power grip was thereby determined as 81N based on average maximum grip strength of 55.2 kg from a clinical study [67]. Substituting this force component into An's model, the maximum internal joint forces of an index finger from a gripping function were estimated at 281N, 442N and 391N for the DIP, PIP and MCP joints respectively. The joint force at the MCP joint is slightly lower than that in the PIP joint, contradictory to common claims that MCP joints experience the highest joint load [68].

Examination of the required strength of materials for the new design was conducted based on loads and positions that produce the maximum detrimental effect. The effect is considered most critical when maximum load from the middle phalanx is applied in a direction perpendicular to the long bone axis of the proximal phalanx. This perpendicular joint load essentially produces a turning moment at the proximal component.

The maximum bending stress for the new design can be determined from a bending moment of 1.66 Nm due to a maximum joint load of 442 N. With a neutral axis distance of 0.8 mm and a moment of inertia of  $1.81e^{-12} \text{ m}^4$  taken from the previously determined geometry of the best-fit fixation stem, this bending stress was calculated to be 734 MPa. To prevent failure from occurring, the strength of the candidate material for the fixation stem has to be higher than this maximum bending stress.

With a bending stress of 734 MPa at the fixation stem region, polymeric biomaterials were excluded due to their insufficient mechanical strength. Three groups of metallic biomaterials, stainless steels, cobalt chromium and titanium

alloys, can satisfy such a strength requirement. The biocompatibility of these three metallic materials has been proven at the acceptable level which allows them to be extensively applied in orthopaedic applications. To accommodate the additional requirement as a bearing material, the superior wear resistance of CoCr was considered to be more suitable for the new design. Apart from metals, bioceramics are also good candidate materials for wear-resistant applications.

Thus, in the new joint design, CoCr alloy and  $Al_2O_3$  ceramic were employed for the following reasons:

1. Simulator studies of hip joints with MOM and COC articulations have shown good wear resistance of at least 50 to 100 times better than polyethylene [69].
2. Retrieval of hip joint components and respective periprosthetic tissues indicated that the wear and wear debris from MOM and COC articulations were substantially less than polyethylene on CoCr.
3. Accumulated debris may mediate cascade osteoclastic bone resorption at periprosthetic tissues resulting in progressive osteolysis and ultimately aseptic loosening to the implant [70–72].

Standard medical-grade CoCr rods were purchased for the fabrication of the new joint design. F90 CoCr alloy was chosen in preference to other variants due to superior mechanical properties and being more biologically compatible with less nickel than some others. Cold rolling resulted in a 99% increase in hardness from the original annealed state. The corresponding tensile strength at this hardness value was estimated to be around 1.6 GPa.

Fabrication of the new design (Fig. 9.9) was performed by electrical discharge machining (EDM) which can machine extremely hard metals when conventional tool-cutting machining becomes infeasible. The EDM process

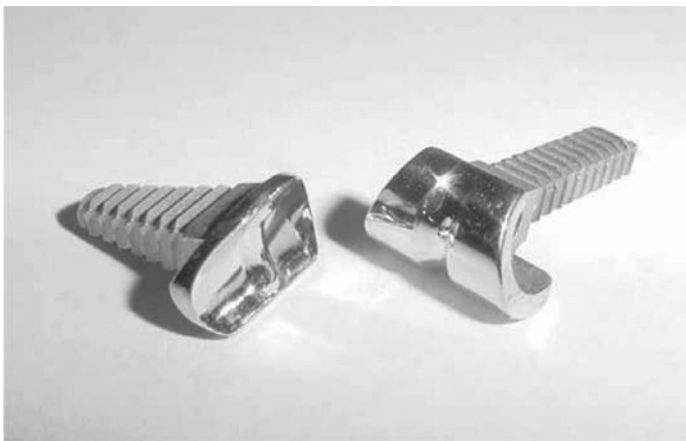


**Fig. 9.9** Prototype of the new design manufactured in CoCr

also offers good dimensional accuracy and complicated geometries can be produced by proper design of tooling.

Production of ceramic components requires geometry shaping and sintering. The properties rely on the purity of the ceramic powder, the grain size and the density free from entrapped porosity. Due to its brittleness, the physical characteristics of alumina ceramics for implant application are subject to stringent demands as outlined in ASTM F603. Additional processes such as hot isostatic pressing at high pressure (200 MPa) and high temperature (2500°C) are normally used to make alumina components with the desired density and strength. These complicated manufacturing processes and the demanding physical properties have limited the application of alumina to simple geometries for hip prosthetic components.

In this work, trial alumina articulating components of proximal and distal joints were produced as shown in Fig. 9.10 by a manufacturing process known as ceramic injection molding (CIM). CIM is a near-net-shape production process for complex geometries with high dimensional accuracies [73]. CIM is still a relatively new production process and much fine tuning of the processing parameters is required to produce high-quality products. From the several trial runs attempted, manufacturing flaws such as cracks and porosity commonly observed in CIM-produced parts [74] were also found in the components produced. Assessment of the mechanical properties of the ceramic components by micro-indentation revealed an average hardness value of 13.4 GPa which is below the minimum limit of 18GPa required in ASTM F603. The trial runs reported here show the possibility of using CIM to make ceramic parts of artificial finger joints. Further fine-tuning of the process is necessary to make parts of sufficient strength. This is left as a potential topic for future investigation.

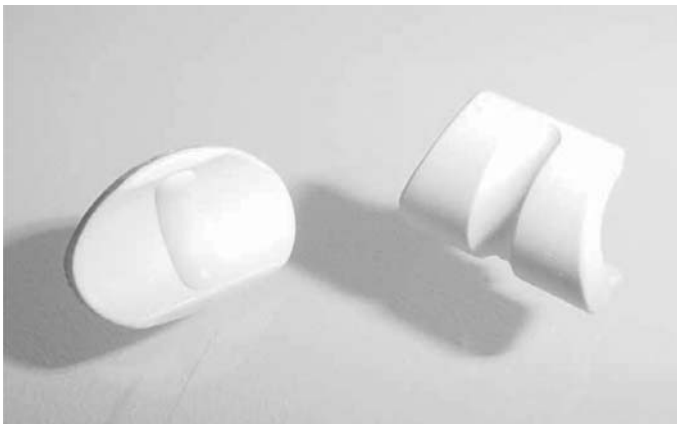


**Fig. 9.10** Prototype of the new design manufactured in  $\text{Al}_2\text{O}_3$  ceramic

## 9.12 Design Optimization by Finite Elements Model

To diminish wear damage due to the potentially high contact stresses in the articulating components in the new design, FEM was employed to optimize the surface geometry of these components. Finite element models of the artificial joint were created using Algor ver12.04. Linear stress analyses were performed based on load acting across the joint components from the middle phalange towards the head of the proximal phalanx. Depending on the angular position of the middle phalanx with respect to the proximal phalanx, the joint load acting on the latter could be from  $0^\circ$  at full extension to  $90^\circ$  at full flexion. To examine the static behavior of joint components to changes in the loading direction, analysis was performed using a two dimensional model across the sagittal section.

Three different shapes of the proximal component were examined to evaluate the optimum geometry favorable for load transfer with minimal contact stresses and distortion to the articulating surfaces. The modal joint size of 7.5 mm was employed and a value of 10 mm was assigned to the joint thickness in the plane stress condition. Model 1 has a proximal component with a thin profile on the articulating surface based on the requirement of minimal excision to the bone joint. Model 3 has a proximal component with complete solid support underneath the articulating surface. Model 2 has a proximal component with a geometry intermediate between models 1 and 3, with the articulating surface partially supported by solid materials. The articulating surface of the distal component was assumed to be in congruence fit to the proximal component and only a short region of the fixation stem was included in the 2-D model to reduce computational time. Appropriate boundary conditions were applied at the bottom edge of the proximal component to restrain both translational and rotational movements in x, y and z directions. A maximum joint load of 442 N was applied perpendicular to the top edge of the distal component. Isotropic 2-D elasticity element was assigned to the distal and proximal components with Young modulus of 210 GPa and Poisson ratio of 0.3 for CoCr. The two components were meshed in quadrilateral elements with a mesh density of 8000, angular step of  $15^\circ$  and geometry ratio not greater than 1.25.

From the computed displacement fields, deformation happens mainly on the joint surface of model 1 which results in the highest bending stresses at the joint surface. With the aid of solid support underneath the joint surface in model 3, deformation shifts to the junction of the stem region and the induced internal stresses in the proximal component are lower than model 1. Since deformation is shared by both the joint surface and the stem region in model 2, the maximum stress induced in the proximal component in model 2 is the smallest among the three models.

The model with the lowest contact stress on the joint surface of the distal component and the lowest bending stress in the stem junction of the proximal



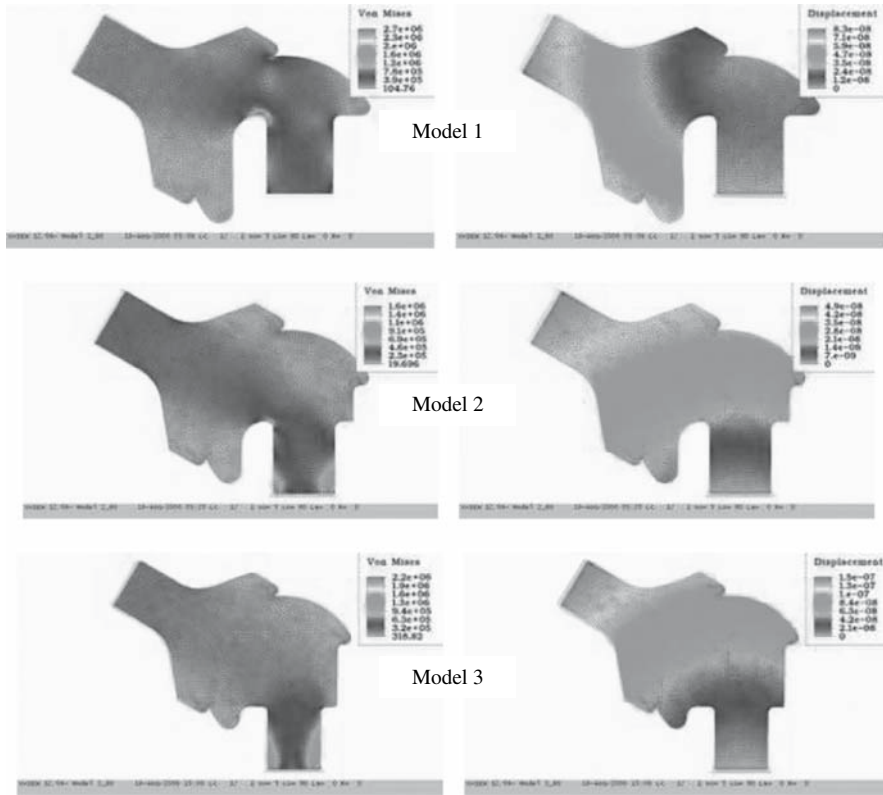


**Fig. 9.11** Stress (*left*) and displacement patterns for the 3 models taken at  $60^\circ$ . Please note that these are b/w images taken from colour originals and therefore some detail is lost

component, as shown in the examples in Fig. 9.11, was chosen for the new design of the artificial PIP joint. Model 3 was found to be the optimum geometry with the smallest contact and bending stresses in the joint components in all the loading directions.

### 9.13 Long-Term Performance Testing

To ensure prolonged service, pre-clinical evaluation of an artificial joint is required to assess for wear damage. The present design involves a new concept of a bearing couple replacing the diseased joint and no joint simulator for testing and no suitable industrial standard for conducting such a test is available, so a new simulation machine had to be devised.

A finger joint motion simulator was fabricated for conducting wear and fatigue studies of the new artificial joint. The simulator can perform wear and fatigue tests on 3 artificial finger joints simultaneously under the same testing conditions. The motion generator simulates a planar motion from flexion-extension of a finger joint with one rotational degree of freedom. It is actuated by an electric motor with controllable speed to provide motion from  $0^\circ$  to  $110^\circ$  flexion. The proximal component of the finger joint is mounted on the upper rotating jaw for motion from flexion and extension while the lower jaw containing the distal component is connected to a pneumatic piston applying a physiologic joint load up to 500 N during each cycle. A load cell is installed in between the pneumatic piston and the artificial joint to monitor loading throughout the test. The complete setup is controlled by a programmable logic controller. Various conditions can be written to the system such as constant loading for a wear test and cyclic loading for fatigue. The position of the joint flexion and extension is monitored by means of a digital encoder to provide real time recording of the joint load with respect to the corresponding angular joint position.

The motion simulator (Fig. 9.12) enables cyclic loading and varied motion frequency to be applied to the test specimen, so that wear and fatigue characteristics can be assessed in a single run. Motion was set between  $0^\circ$  and  $90^\circ$  to simulate a normal range of flexion-extension in a PIP joint. The simulator employs a free movement cycle of the finger joint at a light loading between 10 and 15 N, running at 3 Hz. Following this a heavy pinch function cycle runs at 1 Hz applying a loading up to 110 N. The ratio between free movement and heavy pinch was set to 50:1, estimated from Joyce's study [75]. The simulator



**Fig. 9.12** Joint motion simulator for wear testing

runs for 500 free movements then 10 heavy pinches and stops after half million cycles for component examination.

Six sets of the new design were subjected to simulator study. They were formed by precision EDM machining and grit blasted to produce a rough surface on the fixation stem. The bearing surface was polished by metallurgical means to a surface finish below  $0.05 \mu\text{m Ra}$ , which is comparable to standards for commercial hip and knee implants. Using a coordinate measuring machine, the average clearances between all proximal and distal bearing couples after polishing were measured to be 0.56 mm. One pair of specimens was used as a control without being subjected to mechanical loading to study possible weight change from reacting with the simulated chemical environment alone. The other five pairs were mounted onto the fixture by clamping.

Each testing chamber was topped up with diluted bovine serum solution with 75% deionised water according to known standards for hip (ASTM F1714) and knee joints (ASTM F1715). The solution was supplemented by 0.2% sodium azide to retard bacterial growth and EDTA to prevent precipitated calcium phosphate on the articulating surface of the test specimen. The solution was filtered to remove particulates which could potentially result in third body wear. A quartz lighting system was used to warm the serum to about  $37^\circ\text{C}$ , which was then monitored and controlled using a thermocouple. New serum was added periodically to bring the level back to the original value, and to maintain the concentration as constant as possible. All tests were performed at a dual cycle mode to a total of 5 million cycles. The simulator was stopped every 0.5 million cycles to enable gravimetric measurement of the specimens using a micro-balance with a resolution of 0.01 mg. The surface topography of the specimens was assessed quantitatively by non-contact 3-D interference microscopy for roughness (Ra) data, and qualitatively using scanning electron microscopy. The serum solution with suspended wear debris from each lubricating chamber was collected and stored at  $-18^\circ\text{C}$  to allow isolation and characterization of the wear particles later on.

The serum lubricant was centrifuged at 2000 g for 60 min to produce a pellet of metal wear particles. The pellet was then suspended in 4 mL filtered distilled water with 3 mL 12 M potassium hydroxide (BDH) at  $60^\circ\text{C}$  for 48 h by shaking and sonicating frequently. Lipids and proteins were removed by extraction with 2:1 chloroform/methanol and repeated washes with 50% acetone. The metal wear particles were separated by sonication and filtered onto  $0.1 \mu\text{m}$  polyester membranes. A section of each filter was analysed using a field-emission SEM at high magnification.

Energy dispersive X-ray analyses were performed to determine the elemental compositions of the wear particles. Captured images were analyzed using software to characterize the particle size distribution according to ASTM F1877.

The evaluation of the new PIP joint by the simulator study was stopped after 5 million flexion extension cycles. Wear damage of the distal component was most prominent with visible depressions due to material loss. Damage also extended to the central guiding track and the ridges of the distal and proximal

components respectively but the overall profile was maintained. Magnification at 200x revealed fine linear scratches parallel to the joint motion but no crack or contact fatigue damage was observed.

The wear damage indicates average material loss of 14.57 mg and 10.99 mg of the proximal and distal components per half million cycles. The proximal component has a larger articulating surface area and longer sliding distance so wear loss was slightly higher than the distal component. Based on a density of  $9.13 \text{ g/cm}^3$  for CoCr and areas of the contact surfaces of  $112.06 \text{ mm}^2$  and  $57.35 \text{ mm}^2$  for the proximal and distal components, the cumulative wear volume and respective thickness loss can be calculated. The total volumetric wear and thickness loss after 5 million cycles were  $15.95 \text{ mm}^3$  and  $142.37 \text{ }\mu\text{m}$  for the proximal component, and  $12.04 \text{ mm}^3$  and  $209.95 \text{ }\mu\text{m}$  for the distal component. This corresponds to volumetric wear of  $3.19 \text{ mm}^3$  and  $2.41 \text{ mm}^3$ , and thickness loss of  $28.47 \text{ }\mu\text{m}$  and  $41.99 \text{ }\mu\text{m}$  per million cycles, for the proximal and distal components respectively. Volumetric wear was found to be similar to MOM articulation in the hip joint ( $0.12\text{--}11.2 \text{ mm}^3/\text{year}$ ). However, thickness loss of the finger joint model was relatively high, since standard hip joints observe thickness loss no greater than  $10 \text{ }\mu\text{m}/\text{year}$  [76]. This might be due to the small chamfers on the component edges of the finger joint design. The chamfer radius should therefore be enlarged in future designs to reduce material wear.

The surface topography was assessed using interference microscopy. Scanning was oriented perpendicular to the linear sliding scratches so that the maximum numbers of peaks and valleys could be taken into account. The (arithmetic) average roughness (Ra) was measured after each intermediate stop of half a million cycles. The specimen after fine polishing produced a mean Ra value below  $0.03 \text{ }\mu\text{m}$ . The surface roughness increased to a peak value of  $1 \text{ }\mu\text{m}$  at the first half million cycles, as is typically observed in most simulator studies as a “bedding-in” phenomenon. A self-polishing action was observed subsequently, corresponding to a decrease of the surface roughness until reaching a plateau from 1.5 to 3 million cycles to  $0.7 \text{ }\mu\text{m}$ . There was then increase in surface roughness after 3 million cycles, showing accelerated wear and loss of the edge chamfer.

EDX measurements on the wear debris showed the same composition as the F90 CoCr alloy. The wear particles have an average value of  $0.178 \text{ }\mu\text{m}$ , and range from sub-micron to a few microns. These results are in good agreement with MOM articulations of the hip joint.

## 9.14 PIP Joint Stability

A well functioning finger joint comprises good range of motion and adequate stability to interact with demanding activities of the hand. Clinical instability of finger joints presents a major complication which significantly alters the hand function of those suffering from arthritic diseases. Contributions to a stable PIP

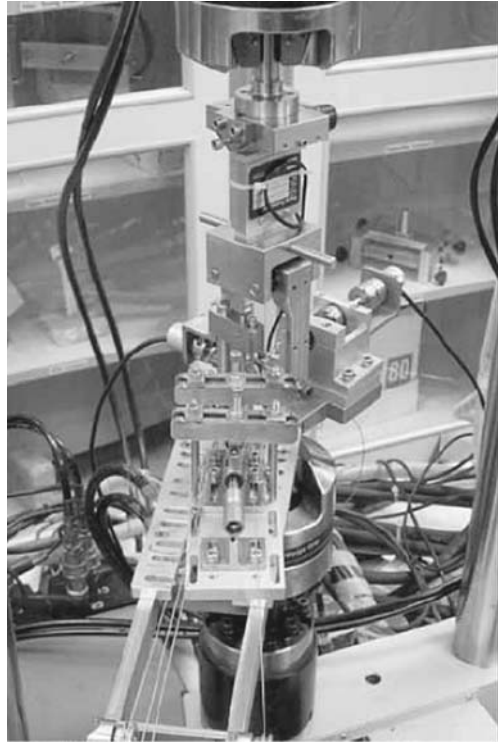
joint rely on integrity of three major elements of the bony geometric constraint, the musculotendinous pull and the ligamentous support. Ligamentous support is a primary stabilizer against external distraction forces and instantaneous joint loads from dynamic motion [77]. Under pathologic disturbances, which are predominantly rheumatoid arthritis and the corresponding inflammation processes, attenuation of the capsuloligamentous support commonly results in functional impairment of the hand from imbalanced kinematic chains and gross digital deformity [78]. This design was based on the rationale of a semi-constrained articulation, with supplementary stability to counterbalance the attenuated ligamentous support. Biomechanical evaluation of the lateral stability of the new design was performed to compare with the natural human joint and other commercial implant systems.

A kinematics test rig was built to assess the degree of lateral constraint in response to a radial distraction force. Different joint loads were applied to simulate an in-vivo condition by musculotendinous pull. The degree of lateral constraint was then assessed in terms of the magnitude of the resisting constraint force measured by a force sensor with a continuously applied angular lateral displacement to the articulation. A rotating table was constructed between the mounting fixtures of the proximal and middle phalanxes to allow the effects of a varying joint flexion angle to be studied. Mounting fixtures were specially designed to permit examination of the new design and other commercial implant systems, as well as natural phalangeal bones using the same testing conditions.

To minimize the effects of the large variations in mechanical properties of the soft-tissue structure, the setup adopted a simplified kinematic chain model from Stokoe's simulator [79]. This has been demonstrated to be compatible to the loading pattern of an intact joint and employs multiple mechanical pulleys and tension wires to mimic the configuration of a natural finger joint. Deadweight was added to tension wires to maintain a constant joint load across the articulation independent of the joint displacement. The test specimen was actuated by the loading axis of a testing machine, which provided continuous dislocation forces at quasi-static conditions (Fig. 9.13). The holder for the distal joint component was mounted on the moving axis of the machine to provide a dislocation motion against the proximal component. The holder for the proximal joint component was mounted onto the rotating table at a specific flexion angle and kept in stationary position on each test run. Since the angular displacement to dislocate the articulation from varied joint designs may not be linearly related to the motion of the machine axis, a magnetic resonance angular encoder with negligible frictional was added to the rotating axis of the middle phalanx so real-time angular displacement of the articulation could be accurately monitored.

Comparative studies of the lateral stabilities of the new PIP joint design and three commercial PIP joint implants from Ascension (Pyrocarbon PIP), Wright (Swanson PIP), and Depuy (Neuflex PIP) were made. The 7.5 mm proximal and distal joint components of the new joint design and the respective size of other

**Fig. 9.13** Finger joint kinematic testing rig



implants were mounted horizontally onto phalangeal implant holders. For the new design and the Pyrocarbon PIP implant, both using an unconstrained surface design, silicon oil was added between the joint surfaces to diminish frictional effects.

Testing was also conducted on 6 cadaveric middle-finger bone joints of similar sizes. The joint capsule and collateral ligament were released to isolate the effects from soft-tissue constraint to examine solely the geometric constraint from a bony articulation. Normal saline was added on the articular cartilage to keep the bone joint moist and serve as a lubricant. Examination of a cadaveric intact joint was also performed to reveal the compound effect from ligamentous and bony geometric constraints. This test, however, was only done in the full extension position.

All tests applied lateral displacements to the distal joint component up to  $10^\circ$  angulation from the neutral position, in accordance with the measured normal physiologic laxity of a PIP joint [80]. A constant load of 250 g was applied to the flexor tension wire, 200g to the extensor tension wire and 50g to each intrinsic tension wire producing a summation of joint load of 5.4 N across the articulation, based on the methodology of Uchiyama [81]. A series of constant joint loads of 16.2, 26.9, 37.8 and 48.6 N were applied on each test to account for an

increasing musculotendinous pull across the articulation. This covers the normal range from isometric hand function [82]. Based on mean bone length of 26.21 mm, radially imposed loading applied by the cross-head was set perpendicular to the bone axis and kept constant at 25 mm distal from the PIP joint center, similar to the approach of Kieffhaber [80]. A 4N imposed loading would therefore represent a 0.1 Nm bending moment to the joint center according to this moment arm. The load was applied by displacement control at a rate of 0.5 mm/s [83] for 6 complete cycles to eliminate reading errors and dynamic effects of the joint components. Tests on five different constant joint loads and four varied flexion angles ( $0^\circ$ ,  $30^\circ$ ,  $60^\circ$ ,  $90^\circ$ ) were performed to cover the physiologic range on each implant type and the bony joints. The reaction forces from resisting the angular displacement were monitored and recorded according to the degree of joint angulation.

Dynamic responses were observed to have restraining forces from the new PIP joint design consistently higher than the natural bony joint and all other commercial implant types. The constraining forces, obtained by increasing the joint load across the articulation, was highest for the new PIP joint design, followed by the natural bony joint, the pyrocarbon implant and lowest for the Swanson and Neuflex implants. Increasing the joint flexion angle generally has little effect on the constraining forces in the Swanson and Neuflex implants. The constraining forces produced in the Pyrocarbon implant were continuously raised by increasing the joint flexion angle from  $0^\circ$  to  $90^\circ$ . The constraining forces in the new PIP joint design were similar to the natural bony joint and found to be maximum at a flexion angle of  $60^\circ$  in agreement with the findings of Minamikawa [59].

The dynamic behavior falls into two types according to the mechanism of the implant design. The silastic type implants by Swanson and Neuflex showed a gentle increase in the constraining force without an apparent peak value with increasing lateral angular displacement up to the set point of  $10^\circ$ . In contrast, the unconstrained designs in the new PIP joint and the Pyrocarbon implant showed a bi-linear behavior with an initial step increase in the constraining force, followed by a slight reduction from the peak value. This bi-linear characteristic is comparable to a real bony joint presumably because of the anatomic compatibility of the surface design in these implants with the natural articulation. The stabilized surface geometry of the new design leads to an overall 30% increase in the maximum constraining force compared to natural bony joints, and a 68% increase compared to the Pyrocarbon implant. These results contrast with the joint stability from the silastic-type implants, which only exhibited 34% and 22% respectively of the constraining force of a natural bony joint.

The average values of the maximum constraining forces produced from each kind of articulation are compared with the intact human joint in Table 9.1. Without a joint load the intact joint maintains a stable position presumably because of the effective ligamentous constraint. Geometric constraints from the natural bony joint and all implant types without an effective joint load show a lack of joint stability. With increasing joint load up to the maximum physiologic

**Table 9.1** Comparison of results to the constraint forces at different articulations at full extension joint position

Test Specimen	Average constrain forces at different joint load conditions (N)				
	5.4 N	16.2 N	26.9 N	37.8 N	48.6 N
Intact PIP joint	11.21 ± 5.39	11.80 ± 4.10	12.44 ± 3.41	12.80 ± 2.80	13.91 ± 2.56
Bony joint	1.47 ± 0.74	2.93 ± 1.47	4.75 ± 1.73	7.43 ± 1.63	10.87 ± 2.18
New PIP joint	1.94	4.25	6.43	9.01	11.85
Pyrocarbon PIP	1.52	2.94	4.38	5.76	7.52
Swanson	0.87	0.89	1.28	2.77	–
Neuflex	0.68	1.07	1.67	2.12	–

± indicates values of standard deviation

range, joint stability of the natural bony joint and the new joint approach the stability of an intact joint. Geometric constraints from the Pyrocarbon implant show some insufficiency when compared to the natural bone joint. Both the Swanson and the Neuflex implants indicated a lack of joint stability compared to the intact joint.

### 9.15 Summary of Functional Evaluation

As the magnitude of the restraining force indicates the capacity to resist an externally imposed load to laterally dislocate the articulation, the result from the semi-constrained surface design of the new PIP joint has shown an enhanced joint stability over the natural bony joint and all the commercial implant systems studied.

Although a deflation is present after the peak value in the dynamic response of the new PIP joint, this corresponds to substantial joint stability over the natural bony joint within the range of normal laxity. This proves the intrinsic joint stability provided by the semi-constrained surface design in the new PIP joint. One inadequacy from the fully anatomical surface design of the Pyrocarbon implant is the loss of complete stability beyond 7° in angular displacement. The distal joint component was observed to have subluxated from the mating position. This is contrary to the result of a natural bony joint having a comparable joint geometry.

New unconstrained articulations such as the AVANTA PIP [84] and the Ascension Pyrocarbon PIP [28], although following the anatomical concept, suffer from recurrent deformity for patients with insufficient ligamentous support by rheumatic affection. These designs are more suitable for patients suffering from osteoarthritis or traumatic arthritis with minimal attenuation of the soft-tissue structure. This correlates with the present experimental



observations that fully anatomical articulation can reproduce only partial joint stability even with similar geometric forms. Lateral subluxation of the implant articulation was observed with angular displacements to the Pyrocarbon implant beyond a magnitude of  $7^\circ$ .

Examination of the Swanson and Neuflex implants indicated that such silastic implants reproduce minimal joint stability to a replaced finger joint. This functional inadequacy signals a lack of materials compatibility to the joint design due to the flexible properties of the implant materials.

The present biomechanical evaluation of the functional compatibility of the new design has shown superior lateral joint stability over the natural bony joint and common implant systems. This enhanced joint stability is mainly due to a semi-constrained design with improved intrinsic stability which may help in restoring the normal joint stability by counterbalancing the weakened soft-tissue constraints from diseases. Therefore, the current new PIP joint design, according to the present bio-mechanical evaluation, should be more suitable for patients suffering from RA.

## References

1. Charnley J, Kamangar A, and Longfield MD. The optimum size of prosthetic heads in relation to the wear of plastic sockets in total replacement of the hip. *Med Biol Eng* (1969) 7(1): 31–39.
2. Gunston FH. Polycentric knee arthroplasty. Prosthetic simulation of normal knee movement. *J Bone Joint Surg* (1971) 53: 272–277.
3. Brady LP, McCutchen JW. A ten-year follow-up study of 170 Charnley total hip arthroplasties. *Clin Orthop* (1986) 211: 51–54.
4. Kavanagh BF, Wallrichs S, Dewitz M, Berry D, Currier B, Ilstrup D, Coventry MB. Charnley low-friction arthroplasty of the hip. Twenty-years results with cement. *J Arthroplasty* (1994) 9: 229–234.
5. Buechel FF, Sr. Long-term follow-up after mobile-bearing total knee replacement. *Clin Orthop* (2002) 404: 40–50.
6. Sorrells RB. The clinical history and development of the low contact stress total knee arthroplasty. *Orthopedics* (2002) 25 (suppl 2): s207–s212.
7. Rydholm U, Tjornstand B, Pettersson K and Lidgren L. Surface replacement of the elbow in rheumatoid arthritis. *J Bone Jt Surg* (1984) 66B: 737–741.
8. Neviasen RJ. Management of shoulder problems. *Orthop Clin North Am* (1987) 18(3) 445–462.
9. Swanson AB. Flexible implant arthroplasty for arthritic finger joints. *J Bone Jt Surg* (1972) 54A: 435–455.
10. Gellman H, Stetson W, Brumfield RH, Costigan W and Kuschner SH. Silastic metacarpophalangeal joint arthroplasty in patients with rheumatoid arthritis. *Clin Orthop Rel Res* (1997) 342: 16–21.
11. Flatt AE. Restoration of rheumatoid finger-joint function. *J Bone Jt Surg* (1961) 43A, no.5: 753–774.
12. Brannon CEW, Klein G. Experiences with a finger-joint prosthesis. *The Journal of Bone and Joint Surgery* (1959) 41A, January, 87–102.
13. Zachariae L. Experience of Flatt finger joint prostheses. *Acta Orthop Scandinav* (1967) 38: 329–340.

14. Jackson IT. Total finger joint replacement. In *An Introduction to the Bio-mechanics of Joints and Joint Replacement* (Ed. D. Dowson and V. Wright), Mechanical engineering publication, British (1981), 234–243.
15. Henk GJ, Deutman R, Jim R. Use of the Swanson silicone trapezium implant for treatment of primary osteoarthritis. *The Journal of Bone and Joint Surgery*, 2001, 83A, 7, 999–1004.
16. Revell PA, Saffar NAL, Kobayashi A. Biological reaction to debris in relation in joint prostheses. *Proc Instn Mech Engrs*. (1997) 211H, 187–197.
17. Fisher J. Biomedical Application, in *Modern Tribology Handbook Vol. 2* (Ed. B. Bhushan), CRC Press, New York (2001), 1593–1609.
18. Green TR, Fisher J, Stone MH, Worblewski BM and Ingham E. Polyethylene particles of a critical size are necessary for the induction of cytokines by macrophages in vitro. *Biomaterials* (1998) 19: 2297–2302.
19. Fisher J, Bell J, Barbour PSM, Tipper JL, Matthews JB, Besong AA, Stone MH, Ingham E. A novel method for the prediction of functional biological activity of polyethylene wear debris. *Proc Instn Mech Engrs*. (2001) 215H: 127–132.
20. Jazrawi LM, Kummer F, DiCesare PE. Alternative bearing surfaces for total joint arthroplasty. *J Am Acad Orthop Surg* (1998) 6: 198–203.
21. Varano R, Yue S, Boby JD, Medley JB. Co-Cr-Mo alloys used in metal-metal bearing surfaces. *An Alternative Bearing Surfaces in Total Joint Replacement* (Ed. JJ Jacobs and TL Craig) (1998) ASTM STP 1346.
22. Dearnley PA. A review of metallic, ceramic and surface-treated metals used for bearing surfaces in human joint replacements. *Proc Instn Mech Engrs*. (1999) 213H: 107–135.
23. Greenwald AS, Garino JP. Alternative bearing surfaces: the good, the bad, and the ugly. *The Journal of Bone and Joint Surgery* (2001) 83A (Supp2): 68–72.
24. Johnston BR. Proximal Interphalangeal Joint surface replacement arthroplasty. *The Journal of Hand Surgery* (2001) 6 (July): 1–11.
25. Moller K, Sollerman C, Geijer M, Branemark P-I. Osseointegrated silicone implants. *Acta Orthop Scandinav* (1999) 70(2): 109–115.
26. Chow SP, Lam KW, Gibson I, Ngan AHW, Lu W, Ip WY, Chiu KY. A novel artificial prosthetic replacement for the proximal interphalangeal joint of the hand – from concept to prototype. *Hand Surgery* (2005) 10: 159–168.
27. Condamine JL, Marcucci L, Bisson P, Lebreton L. DJOA arthroplasty ten years of experience, and introducing the DJOA 3. In: Schuind F, An KN, *Recent Advances in upper extremity arthroplasty, Proceedings of the Brussels International Upper Extremity Symposium*. World Scientific (1997): 77–89.
28. Linscheid R, Murray PM, Vidal MA, Beckenbaugh RD. Development of a surface replacement arthroplasty for proximal interphalangeal joints. *J Hand Surg* (1997) 22A: 286–298.
29. Low FH, Khoo LP, Chua CK, Lo NN. Determination of the major dimensions of femoral implants using morphometrical data and principal component analysis. *Proc Instn Mech Engrs* (2000) 214H: 301–309.
30. Schulter-Ellis FP, Lazar GT. Internal morphology of human phalanges. *J Hand Surg* (1984) 9A: 490–495.
31. Ash HE, Unsworth A. Design of a surface replacement prosthesis for the proximal interphalangeal joint. *Proc Instn Mech Engrs* (2000) 214H: 151–163.
32. Gillespie TE, Flatt AE, Youm Y, Sprague BL. Biomechanical evaluation of metacarpophalangeal joint prosthesis designs. *J Hand Surg* (1979) 4A: 508–521
33. Linscheid R. Implant arthroplasty of the hand: retrospective and prospective consideration. *J Hand Surg* (2000) 25A: 796–816.
34. Charnley J. The bonding of prostheses to bone by cement. *J Bone Joint Surg* (1964) 46B: 518–529.

35. Nafei A, Kristensen O, Knudsen AM, Hvid I, Jensen J. Survivorship analysis of cemented total condylar knee arthroplasty: a long-term follow-up report on 348 cases. *J Arthroplasty* (1996) 11: 7–10.
36. Wang JS, Franzen H, Toksvig-Larsen S, Lidgren L. Does vacuum mixing of bone cement affect heat generation? Analysis of four cement brands. *Journal of Applied Biomaterials* (1995) 6: 105–108.
37. Kindt-Larsen T, Smith DB, Jensen JS. Innovations in acrylic bone cement and application equipment. *Journal of Applied Biomaterials* (1995) 6: 75–83.
38. Walker PS, Erkman MJ. Laboratory evaluation of a metal-plastic type of metacarpophalangeal joint prosthesis. *Clin Orthop* (1975) 112: 349–356.
39. Steffee AD, Beckenbaugh RD, Linscheid RL, Dobyns JH. The development, technique, and early clinical results of total joint replacement for the metacarpophalangeal joint of the fingers. *Orthopaedics* (1981) 4 (2): 175–180.
40. Sibly TF, Unsworth A. Fixation of a surface replacement endoprosthesis of the metacarpophalangeal joint. *Proc Instn Mech Engrs* (1991) 205H: 227–232.
41. Beevers DJ, Seedhom BB. Metacarpophalangeal joint prostheses: a review of past and current designs. *Proc Instn Mech Engrs* (1993); 207H: 195–206.
42. Chockalingam S, Scott G. The outcome of cemented vs cementless fixation of a femoral component in total knee replacement (TKR) with the identification of radiological signs for the prediction of failure. *Knee* (2000) 7: 233–238.
43. Aaron G. Fixation for the millennium: The Hip. *J Arthroplasty* (2002) 17(4S): 3–5.
44. Lawrence D. Fixation of the millennium: The Knee. *J Arthroplasty* (2002) 17(4S): 6–8.
45. Cook SD, Barrack RL, Thomas KS, Haddad RJ. Quantitative histological analysis of tissue growth into porous total knee components. *J Arthroplasty* (1989) 4S: S33–S43.
46. Lundborg G, Branemark P, Carlsson I. Metacarpophalangeal joint arthroplasty based on the osseointegration concept. *J Hand Surg* (1993) 18B: 693–703.
47. Farron A, Rakotomannana RL, Zambelli PY, Leyvraz PF. Total knee prosthesis. Clinical and numerical study of micromovements of the tibial implant. *Rev Chir Orthop Reparatr Appar Mot* (1995) 80: 28–35.
48. Ash HE, Unsworth A. Further studies into proximal interphalangeal joint dimensions for the design of a surface replacement prosthesis: medullary cavities and transverse plane shapes. *Proc Instn Mech Engrs* (1997) 211H: 377–390.
49. Landsmeer JMF. Anatomical and functional investigation on the articulations of the human dinger. *Acta Anatomica* (1955) 25(Suppl 24): 1–69.
50. Kuczynski K. Less-known aspects of the proximal interphalangeal joints of the human hand. *The Hand* (1975) 7(1): 31–33.
51. Mallon WJ, Brown HR, Nunley JA. Digital range of motion: normal values in young adults. *J Hand Surg* (1991) 16A: 882–887.
52. Hume Mary, Gellman Harris, McKellop H, Brumfield R. Functional range of motion of the joints of the hand. *J Hand Surg* (1990) 15A: 240–243.
53. Condamine JL, Nenoit JY, Comtet JJ, Aubriot JH. Proposed digital arthroplasty critical study of the preliminary results. *Ann Chir Main* (1988) 7(4): 282–297.
54. Stachowiak GW, Batchelor AW. In: *Engineering tribology*, 2nd edition. Butterworth-Heinemann (2001), 281–356.
55. Harris C, Rutledge F. The functional anatomy of the extensor mechanism of the finger. *J Bone Joint Surg* (1972) 54A: 713–726.
56. Fehring TK. Rotational malalignment of the femoral component in total knee arthroplasty. *Clin Orthop* (2000) 380: 72–79.
57. Poilvache PL, Insall JN, Scuderi GR, Font-Rodriguez DE. Rotational landmarks and sizing of the distal femur in total knee arthroplasty. *Clin Orthop* (1996) 331: 35–46.
58. Rhee RY, Reading G, Christie-Wray R. A biomechanical study of the collateral ligaments of the proximal interphalangeal joint. *J Hand Surg* (1992) 17A: 157–163.

59. Minamikawa Y, Imaeda T, Amadio PC, Linscheid RL, Cooney WP, An KN. Lateral stability of proximal interphalangeal joint replacement. *J Hand Surg* (1994) 19A: 1050–1054.
60. Landsmeer JMF. Study in anatomy of articulation: The equilibrium of the intercalated bone. *Acta Morph Neerl Scand* (1960) 3:287–303.
61. Wehbe M, Hunter JM. Flexor tendon gliding in the hand, Part I, in vivo excursions. *J Hand Surg* (1985) 10A: 570–574.
62. An KN, Chao EY, Cooney WP, Linscheid RL. Forces in the normal and abnormal hand. *J Orthop Res* (1985) 3(2): 202–211.
63. Amis AA. Variation of finger forces in maximal isometric grasp tests on a range of cylinder diameters. *J Biomed Eng* (1987) 9: 313–320.
64. Sancho-Bru JL, Perez-Gonzalez A, Vergara-Monedero M, Giurintano D. A 3-D dynamic model of human finger for studying free movements. *J Biomech* (2001) 34: 1491–1500.
65. Fowler NK, Nicol AC. Interphalangeal joint and tendon forces: normal model and biomechanical consequences of surgical reconstruction. *J Biomech* (2000) 33: 1055–1062.
66. Ash HE, Joyce TJ, Unsworth A. Biomechanics of the distal upper limb. *Current Orthopaedics* (1996) 10: 25–36.
67. Harkonen R, Piirtomaa M, Alaranta H. Grip strength and hand position of the dynamometer in 204 finnish adults. *J Hand Surg* (1993) 18B: 129–132.
68. Brand PW, Hollister AM, Agee JM. Transmission. In: *Clinical Mechanics of the Hand*, 3rd ed., Brand & Hollister eds, Mosby (1999), 61–99.
69. Semlitsch M, Willert HG. Clinical wear behaviour of ultra-high molecular weight polyethylene cups paired with metal and ceramic ball heads in comparison to metal-on-metal pairings of hip joint replacements. *Proc Instn Mech Engrs* (1997) 211H: 73–88.
70. Willwer HG, Bertram H, Buchhorn GH. Osteolysis in alloarthroplasty of the hip. The role of ultra-high molecular weight polyethylene wear particles. *Clin Orthop* (1990) 258: 95–107.
71. Peters PC, Engh GA, Dwyer Ka, Vinh TN. Osteolysis after total knee arthroplasty without cement. *J Bone Joint Surg* (1992) 74: 864–866.
72. Harris WH. Wear and periprosthetic osteolysis: the problem. *Clin Orthop Relat Res* (2001) 15(3): 263–273.
73. Edirisinghe MJ, Evans JRG. Review: fabrication of engineering ceramics by injection molding. II. Techniques. *Int J High Tech Ceram* (1986) 2: 249–278.
74. Tseng WJ, Hsu CK. Cracking defect and porosity evolution during thermal debinding in ceramic injection moldings. *Ceramics International* (1999) 25: 461–466.
75. Joyce TJ, Unsworth A. The design of a finger wear simulator and preliminary results. *Proc Instn Mech Engrs* (2000) 214H: 519–526.
76. Medley JB, Chan FW, Krygier JJ, Bobyn JD. Comparison of alloys and designs in a hip simulator study of metal on metal implants. *Clin Orthop* (1996) 329S: 148–159.
77. Minami Akio, An KN, Cooney WP, Linscheid RL, Chao WYS. Ligament stability of the metacarpophalangeal joint: A biomechanical study. *J Hand Surg* (1985) 10A: 255–260.
78. Faull H, Kelly P, Mullet H, Synnott K. Outcome measures following metacarpophalangeal joint replacement. *J Hand Surg* (2000) 25B: 601–603.
79. Stokoe SM, Unsworth A. A finger function simulator and the laboratory testing of joint replacements. *Proc Instn Mech Engrs* (1990) 204H: 233–240.
80. Kiefhaber TR, Stern PJ, Grood ES. Lateral stability of the proximal interphalangeal joint. *J Hand Surg* (1986) 11A: 661–669.
81. Uchiyama S, Cooney WP, Linscheid RL, Niebur G, An KN. Kinematics of the proximal interphalangeal joint of the finger after surface replacement. *J Hand Surg* (2000) 25A: 305–312.
82. Purves WK, Berme N. Resultant finger joint loads in selected activities. *J Biomed Engng* (1980) 2: 285–289.

83. Kung PL, Chou P, Linscheid RL, Berglund LJ, Cooney WP, An KN. Intrinsic stability of an unconstrained metacarpophalangeal joint implant. *Clinical Biomechanics* (2003) 18: 119–125.
84. Beckenbaugh RD. Preliminary experience with a noncemented nonconstrained total joint arthroplasty for the metacarpophalangeal joints. *Orthop* (1983) 6(8): 962–965.

# Chapter 10

## Computer-aided Development of Mega Endo-Prostheses

**B. Ravi and Manish Agarwal**

### 10.1 Introduction

Prosthesis refers to an artificial implant that can replace or substitute for a natural joint, and maintain the desired functionality, including cosmetic appearance. They are needed when joints are lost by injury (traumatic), missing from birth (congenital), or damaged by disease (such as cancer), and thereby save the remaining limbs. While a prosthesis can also be external (as in an artificial limb for amputees), the focus of this chapter is on internally placed artificial joints (or endo-prosthesis), especially those that fully replace a joint along with part of the bone (mega endo-prostheses), and provide the required functionality (see Fig. 10.1). They can be classified in different ways, depending on the articulation or site of joint, freedom of movement, material combination, extent of customization, indication for the replacement, and the fixation method. The development of such prostheses is highly challenging, requiring inter-disciplinary inputs from orthopedic surgeons, mechanical engineers, and material scientists, supported by information technology.

The development of any new prosthesis begins with the study of the patient requirements. Bio-mechanical studies are needed to determine the loads, movements, and other functional requirements of the joint. The configuration and design have to be evolved depending on the functional requirements, but compatible with the selected implant materials and manufacturing processes. Bio-compatible materials with the desired properties need to be selected for various components of a prosthesis. Manufacturing processes must be planned to achieve the desired functionality, reliability and cost. Surgical instrumentation (called armamentarium) to implant the prosthesis must also be designed, considering efficiency and quality of surgical protocol. Software tools may be used to extract the geometry of customized prostheses from the medical images of the patient; carry out design, analysis, prototyping and manufacture of the

---

B. Ravi  
Indian Institute of Technology, Bombay  
bravi@me.iitb.ac.in

**Fig. 10.1** A total knee prosthesis shown in a bone model



prosthesis; study prosthesis implantation protocols; train the surgeons; and educate the patients.

### ***10.1.1 Anatomy of Major Joints***

Prosthesis development requires an understanding of the human joint that will be replaced. There are several types of articulated joints with free movement between the bones in human body. The three major joints – knee, hip, and shoulder, are briefly described here.

#### **10.1.1.1 Knee Joint**

The knee is made up of four bones: femur (thigh bone), tibia, fibula and patella (knee cap). The femur attaches to the tibia bone by ligaments. The fibula runs parallel to the tibia. The patella rides on the knee joint as the knee bends.

The joint surfaces of the femur and tibia bones are called femoral and tibial condyles. The femoral condyle (which is round) articulates with the tibial condyle (which is flat, dish like), in a non-congruent manner. Two menisci (cartilages) between the two condyles increase the joint contact area. A smooth, resilient joint cartilage covers the condyles, giving very low friction and wear, better than any human-made joint.

The knee joint is stabilized by a system of ligaments, strong muscles, and a strong but elastic joint capsule. Two collateral ligaments on the two sides of the knee provide side stability. Two cruciate ligaments (which cross each other) in the space formed between the two femoral condyles provide stability when the knee joint moves backwards and forwards; restraining excessive glide of the round femoral condyle on the flat tibial condyle. The strong quadriceps muscle lies in the front of the knee joint next to the knee cap (patella).

The inner and outer halves of the knee joint make quite distinct joint spaces called compartments. The medial or inner compartment lies between the inner femoral condyle and the inner tibial condyle. The lateral or outer compartment lies between the outer femoral and the outer tibial condyle. The third compartment is formed by the articulation of patella with the front surface of the femoral bone. As the knee joint bends and stretches, the patella glides in a track groove on the front side of the femoral bone. This symmetric position of the patella in the groove during the whole knee movement is important for the healthy function of the knee.

The knee joint takes over 3 times body weight while walking and climbing stairs, and over 17 times body weight in running and active sports.

#### **10.1.1.2 Hip-Joint**

The hip joint is a ball-and-socket joint, formed by the reception of the round head of the femur bone into the cup-shaped cavity of the pelvic bone (called acetabulum). The ball head of the femur closely fits the acetabulum over an area extending nearly half a sphere. They are held in place by very powerful ligaments that form a complete sleeve around the joint (referred to as the joint capsule). The capsule has a delicate lining (called the synovium). The head of the femur as well as the inner wall of the socket are covered with a layer (about 3 mm thick) of smooth cartilage, which cushions the joint, and allows the bones to move on each other with very little friction.

The movements of the hip are very extensive, and consist of flexion, extension, adduction, abduction, circumduction, and rotation. When the thigh is flexed or extended, the head of the femur, on account of the medial inclination of the neck, rotates within the acetabulum with a slight amount of gliding to and fro. The forward slope of the neck similarly affects the movements of adduction and abduction. Conversely rotation of the thigh, which is permitted by the upward inclination of the neck, is not a simple rotation of the head of the femur in the acetabulum, but is accompanied by a certain amount of gliding. The hip ligaments are the strongest of all the ligaments in the body, and enable maintaining the erect position without muscular fatigue.

#### **10.1.1.3 Shoulder Joint**

The two main bones of the shoulder are the humerus and the scapula (shoulder blade). The joint cavity is cushioned by articular cartilage covering the head of



the humerus and face of the glenoid (end of the scapula). The scapula extends up and around the shoulder joint at the rear to form a roof called the acromion, and around the shoulder joint at the front to form the coracoid. Ligaments connect the bones of the shoulder, and tendons join the bones to surrounding muscles. The biceps tendon attaches the biceps muscle to the shoulder and helps to stabilize the joint. The glenoid meets the head of the humerus to form a glenohumeral cavity that acts as a flexible ball-and-socket joint. The joint is stabilized by a ring of fibrous cartilage (called the labrum) surrounding the glenoid. Unlike in the hip, there is very poor congruity between the humeral head and glenoid and they are kept apposed by ligaments and muscles.

### ***10.1.2 Bio-Mechanical Studies***

As mentioned before, bio-mechanical studies involve determination of the loads, movements, and other functional requirements of the joint. Among various joints, the biomechanics of the knee is the most complex, and is briefly described here.

Knee joint motion is a complex interaction between the four bones: femur, tibia, patella and the fibula. Besides flexion and extension, knee also moves in abduction and adduction, and in rotation about the long axis of the limb. This enables the excellent range of movement coupled with the absorption of very high loads encountered during intense activities such as jumping. Indeed, many earlier prostheses (especially simple hinged joints) failed even in normal activities because they did not consider the kinematics of the natural knee joint.

The kinematics varies depending on the geometry of the knee (which itself is a function of region, age, gender, occupation and other factors), and the gait (sitting-standing transition, slow or fast walking, climbing stairs, etc.). This is studied by researchers using special instrumentation in gait laboratories, necessary for successful design, and later evaluation, of knee prostheses.

The action of muscles during normal activities produces bone loading and joint contact forces far in excess of body weight, depending on the factors mentioned earlier. Determining the in-vivo loads in the human knee is very difficult due to the combination of complex structural anatomy, multi-degree-of-freedom movements and dynamic (often indeterminate) muscle function. Using various mathematical models, researchers have estimated various forces during walking: tibio-femoral contact force of approximately 2.8 times body weight (BW), and shear forces of 0.9 BW during extension, and 0.6–0.7 BW during deep flexion. The largest component of the joint contact force is in the direction of the long axis of the tibia, which reaches values of up to 3.1 BW. These models are being verified by sophisticated techniques like telemetry. The major limitation of existing models is that they do not consider the role of muscles, which play a substantial role in balancing the loads within the femur.

### ***10.1.3 Brief History of Prostheses***

Modern prostheses can be traced to the mid-nineteenth century when various substances were placed between resected joint surfaces to prevent the recurrence of bony or fibrous ankylosis. Initially, these interpositional substances were autogenous tissue (belonging to the same body) taken from adjacent or remote sites, including joint, muscle, fat, and skin. Later, surgeons tried various man-made substances including bakelite, glass, and celluloid as interpositional material.

In 1940, Smith-Petersen developed the Vitallium (cast cobalt-chrome-molybdenum alloy) interpositional arthroplasty of the hip, which gave better results for arthritic joints. Several surgeons also started developing prostheses in various materials to replace one side of the joint as an alternative to interpositional arthroplasty. Metal prostheses were found to have longer life and better bio-compatibility. This included the hip prosthesis by Moore and Thompson, and knee prosthesis (tibial plateau) by MacIntosh and McKeever.

The unreplaced joint surface however, remained a source of pain, especially for patients with arthritic joints. To solve this problem, total metal-on-metal prosthesis for the hip and knee joints were developed. The initial designs could not provide the normal joint function, and suffered from high failure rate caused by loosening, excessive wear, and infection.

In 1960s, Sir John Charnley developed total hip replacement consisting of a stemmed stainless steel replacement for the femoral head articulating with a high density polyethylene acetabular implant, both components being securely fixed to the supporting bone by polymethylmethacrylate cement. A similar metal-on-polyethylene cemented total knee design was developed by Gunston, which was followed by total joint designs for most of the other major joints including the ankle, shoulder, elbow, and wrist.

In 1970, the American Academy of Orthotists and Prosthetists, as well as the International Society for Prosthetics and Orthotics (with headquarters in Copenhagen, Denmark) were formed to bring together the steadily increasing number of professionals engaged in research, development, testing and implantation of orthopedic devices, implants and prostheses.

The 1980s witnessed the growth of biomaterials such as hydroxyapatite coatings to improve the integration of metallic implants in the human body, and bone graft substitutes.

Computer-assisted orthopedic surgery systems started appearing in the late 1990s. This enabled better alignment of the prostheses in the body of the patient, even by less-skilled surgeons.

At present, a large number of hip and knee replacements are being performed each year, as well as a smaller number of shoulder and elbow replacements. They are able to relieve pain, provide motion with stability, and correct deformity, as seen in both short-term and medium-term follow-up studies.

Standards and certification for the development and testing of the implants and prostheses have been evolved by ISO, European Union and the US FDA.

These include guidelines and controls related to: design of the implant and clinical use; raw material procurement, storage, issue and use; manufacturing processes and equipment to ensure fault-free products; testing standards; and maintenance and calibration of equipment for quality control.

## 10.2 Mega Endo-Prosthesis Development

The various steps in computer-aided development of mega endo-prostheses are described here. A case study of a saddle prosthesis development for a patient with a malignant tumor in pelvic bone is provided in the next section to illustrate the technologies and methodologies involved.

The first step is to reconstruct a 3D medical model of the affected region for visualizing the defect, designing patient specific prosthesis, pre-operative planning, virtual implantation, and reference data generation for actual surgery. The prosthesis configuration and materials are decided next, followed by detailed design and analysis. Finally, the prosthesis is manufactured, tested, and implanted in the patient. These steps are described here.

### 10.2.1 Medical Imaging and 3D Reconstruction

The 3D medical model of the relevant region is reconstructed from a contiguous set of 2D images usually acquired from computerized tomography (CT), or Magnetic Resonance Imaging (MRI) techniques. While CT provides information of dense structures such as bone, MRI is used to generate structural images of relatively soft human body tissues.

Reconstruction of 3D models from a series of axial CT/ MRI slices comprises several stages as shown in Fig. 10.2. The acquired CT image data is stacked and interpolated to convert a stack of images into volumetric data. The interpolated data are pre-processed to reduce the noise. Then 3D segmentation is performed to segregate the objects of interest by thresholding of volumetric data. The objects are visualized using a special rendering algorithm. Popular software programs that provide these functions include MIMICS

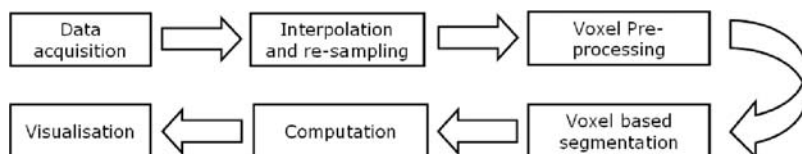


Fig. 10.2 Steps in virtual 3D reconstruction of medical models

(Materialise, Belgium), and 3D-Doctor (Able Software, USA). The stages are briefly described here.

The 2D images are usually stored in standard DICOM (Digital Imaging and Communications in Medicine) format, which also includes details about the patient, system manufacturer, scanning institute, and the scanning portion of patient. Each image comprises typically  $512 \times 512$  pixels. Each pixel  $[f(x, y)]$  is assigned a numerical value on a normalized scale of Hounsfield units (HU) in the scale  $[-1024, +3071]$ . Water has HU value of zero, and bones have typically HU values between 400 and 2000.

The CT/MRI slices are stacked in the direction as they are acquired to create a volumetric (or voxel) model. The voxel size can be set as equal to pixel size. If the inter-slice thickness is more than pixel size, then linear interpolation between adjacent slices is carried out to generate the missing slices. The acquired images may contain noise, which is generally measured using contrast to noise ratio. The images are pre-processed to remove the noise using a filtering algorithm.

The next step in 3D reconstruction is segmentation. This refers to extraction of the object or region of interest using intensity thresholds. The acquired data may consist of several objects representing distinct tissues: tumor, invasion, marrow, bone, fat, muscle and others. Each of these objects is characterized by a range of intensity values, or threshold range ( $I_{\min}$  and  $I_{\max}$ ). The object flags are set in a single pass, by checking whether the intensity value of a particular voxel  $v$  lies within the threshold range for a specific type of object.

$$v(x, y, z) = \begin{cases} 1 & \text{if } f(x, y, z) > I_{\min} \\ 1 & \text{if } f(x, y, z) < I_{\max} \\ 0 & \text{otherwise} \end{cases} \quad (10.1)$$

A realistic display of volumetric data requires information about surfaces and their normals. This can be generated by surface fitting (which is computationally expensive), or by estimating the surface normal of the boundary voxels depending configuration of neighboring voxels. Voxels of each object of interest (for example, bone, muscle, fat, and cartilage) are assigned a shading coefficient (from 0 to 1) according to their true intensity values. Each of these shading coefficients is then given a color and a transparency coefficient. This transparency coefficient can be modulated by the operator, allowing viewing options such as muscles without bones, or bony structures without soft tissues.

The volumetric model also lends itself to geometric analysis such as thickness mapping, which is very useful for custom implant design, and correct implantation. For example, the stem of a total knee prosthesis must be accurately positioned in femur or tibia bones to reduce the possibility of misalignment leading to failure by breakage of bone. Object thickness distribution also helps in predicting diseases at earlier stages: for example, erosion in articular cartilage between distal femur and proximal tibia caused by knee arthritis.

### ***10.2.2 Configuration and Design***

The configuration and design of prostheses depend on the functional requirements (FRs) of the joint that they have to replace. The FRs may include the range of motion (for example, a knee joint must provide a flexion-extension angle of 135 degrees), load bearing capacity, geometric constraints (for example, the condyle portion of a knee joint must allow the patella to glide over it), life (typically several million cycles of operations), and other requirements as follows.

#### **A. Type of movement in the joint:**

- **Ball-and-socket joint (shoulder and hip):** This involves a wide range of motion, including rotation.
- **Hinge joint (elbow and knee):** This involves only constrained flexion and extension movement.
- **Other types of joints:** saddle motion (thumb), condyloid motion (palm and foot), pivot motion (neck), and gliding motion (wrist).

#### **B. Indication for the replacement:**

- **Resurfacing prosthesis:** This is used to replace only worn-out or minimally damaged tissue, where the natural joint is still functioning.
- **Mega prosthesis:** This is used for replacing the natural joints damaged by tumor or trauma, and thus saving the remaining limbs.
- **Expandable mega prosthesis:** This is used to replace the growing ends of bones in children (generally for tumors).

#### **C. Freedom of movement:**

- **Unconstrained prosthesis:** This includes standard replacements for osteoarthritic joints, where the components are articulated with each other and kept in place by natural muscles and ligaments.
- **Fully constrained, as in a hinged prosthesis:** This is used in situations where there is extensive tissue loss, including tumors.
- **Semi-constrained prosthesis:** This can offer constraint in one or more directions, depending on the situations.

#### **D. Extent of customization:**

- **Customized prosthesis:** Each prosthesis is unique, since it is developed to match the anatomy and situations for a specific patient.
- **Standardized prosthesis:** The prosthesis is designed considering a larger population and caters to a wide range of patients.
- **Modular prosthesis:** A range of standard components are available to match different anatomical sizes and situations, allowing a surgeon to intra-operatively decide the best size and fit for the patient.

#### E. Fixation method:

- Cemented prosthesis: Here the prosthesis is fixed in the natural bone using an acrylic bone cement.
- Uncemented prosthesis: This prosthesis has special surfaces for promoting bone in-growth and osteo-integration.

### ***10.2.3 Prosthesis Materials***

The materials used for medical applications, including implants, prostheses, bone cements, scaffolds and tissues, are referred to as biomaterials. Biomaterials for prostheses require demanding properties for adequate function, safety and life, as follows.

- High bio-compatibility, for tolerance and acceptance by the native tissue, without evoking allergic immune response.
- High strength, to prevent bending or breaking, and fatigue resistance to prevent failure in the case of implants with periodic loading patterns.
- Low density, to minimize the weight of the prosthesis, and thereby fatigue to the patient.
- Comparable stiffness (modulus), to prevent ‘stress-shielding’, atrophy and eventual failure of the shielded bone; the implant must have the same stiffness as the tissue that it replaces.
- Low coefficient of friction, when relative motion is required between adjacent components of a prosthesis.
- High wear resistance, important when relative movement between different components of prosthesis is involved, to avoid release of wear particles in surrounding tissues, which leads to osteolysis.
- High corrosion resistance, in the presence of body fluids, so that harmful metallic ions are not released into the patient’s body.
- Other properties, such as bio-absorbability for special applications.

Biomaterials can be largely classified as metals, polymers and ceramics. They are used in combinations, depending on application:

- Metal-plastic articulation: Polymer parts are used to prevent metal-to-metal contact in joints, which otherwise leads to metallosis and infection. The coefficient of friction in polymer-metal contact surfaces is also lower than traditionally manufactured metal-to-metal contact surfaces.
- Metal-ceramic and ceramic-ceramic articulation: This has lower wear compared to metal-metal and metal-polymer combinations, but the ceramic components are brittle and expensive to manufacture.

Major metallic alloys used for orthopedic implants and prostheses include titanium alloys, cobalt-chromium-molybdenum alloys and stainless steels.

- Titanium-aluminum-vanadium (Ti-Al-V) alloys: These are characterized by high bio-compatibility, high strength coupled with low density, low stiffness (preventing undesirable stress-shielding), and excellent corrosion resistance in body fluids, but poor wear resistance and high cost of manufacture. They are suitable for stem components that must promote bone ingrowth.
- Cobalt-chrome-molybdenum (Co-Cr-Mo) alloys: These have high strength and wear resistance, and are suitable for weight-bearing articular surfaces. The material and manufacturing costs are in between those for titanium alloys and stainless steel.
- Stainless steel: Austenitic (non-magnetic) stainless steels have good strength and corrosion resistance, coupled with lower cost of manufacture (compared to Ti and Co-Cr-Mo alloys). They were the first choice of materials for prostheses, and still very popular, especially in total hip replacements. They have however, lower bio-compatibility and fatigue life compared to Ti and Co-Cr-Mo alloys.

Major non-metallic implant materials include polymers, ceramics and other organic and inorganic materials.

- Ultra high molecular weight poly ethylene (UHMWPE): it is an extremely inert material with excellent frictional and wear characteristics with both metals and ceramics, and is extensively used to separate adjacent metallic or ceramic components.
- Ceramics (aluminum oxide and zirconium oxide) have excellent frictional and wear characteristics in conjunction with polymers, but poor impact resistance. They are suitable for femoral heads.
- Polymethylmethacrylate (PMMA) or acrylic bone cements: These polymers are used for positioning and securing the stems of prostheses in bone, by acting as space fillers and load-transferring materials.
- Hydroxyapatite (HA) coatings: They are used to promote bone ingrowth on to the surface of the implant or prosthesis.
- Bio-absorbable polymers, such as LPLA (L-actide) and LPLA-HA: orthopedic pins, screws, plates, rods, tacks and suture anchors made with these materials degrade and transfer the load to the growing new tissue, avoiding 'stress-shielding' and atrophy. They however, have lower strengths, and cannot normally be used for high load-bearing applications.

#### ***10.2.4 Prosthesis Manufacture and Testing***

A modular prosthesis comprises several components, some of which may be standardized and others modular. For example, a total knee prosthesis includes the main joint (condyle portion, tibial platform, pin, bush, etc.), and several modular parts (femoral stem, tibial stem, modular links, etc.) that provide intra-operative flexibility. The main joint itself may have several versions: left and right joint, and large, medium and small joint, depending on the patients. The

different components are usually in different materials, and the manufacturing process must be planned to achieve the desired geometric fidelity, internal properties, tolerances, and surface finish.

The prosthesis prototype can be fabricated using a suitable Rapid Prototyping (RP) system. These are very useful for visualizing the articulation and checking the dimensions. The anatomical structure of the patient can also be fabricated using a RP system, and is useful for checking for fitting with the prosthesis, surgery protocol planning and patient education. Some RP systems use translucent materials, enabling visualization of internal features. The prototypes can also be used for manufacturing custom implants in metal or any other material, through a series of conversion processes such as plaster or silicon rubber molding and investment casting.

Simple metallic components of prostheses can be machined from bar stock. Titanium and Co-Cr-Mo alloys are more difficult to machine than stainless steel, in terms of cutting tool wear. The stock is usually obtained from forging, to achieve good internal properties, including strength, toughness and fatigue resistance. Intricate shapes such as the condyle of knee joint can be more economically produced by investment casting process, though internal porosity may reduce their reliability owing to lower strength and fatigue resistance. This may be improved by Hot Isostatic Pressing, which may however, take the cost to the same levels as that involved in machining.

The most important polymer used in medical applications is UHMWPE (ultra high molecular weight poly ethylene). These components for the knee are manufactured in one of two ways: machining from bar stock, or direct compression molding. The machining process can result in areas of high stress, which may eventually lead to breakdown of the polymer component. Direct compression molding provides a more uniform and harder surface, and gives a more durable component, but is economical only when the requirement is significant.

Surgical instrumentation, called armamentarium is required for correct resection of the malignant bone to match the available (modular) shapes and sizes of the prosthesis parts, and for proper alignment and implantation of the prosthesis in the bone after resection. The instrumentation for total knee prosthesis includes length and angle measurement devices, rotational alignment marking devices, resection guide and saw, bone reamer, reamer driver and stabilizer, tibial alignment device, tibial stem punch, hammer, and various adapters. These are usually manufactured in medical grade stainless steel using machining processes.

Prosthesis testing involves mechanical as well as bio-compatibility testing. Mechanical testing mainly includes strength and wear testing. The prosthesis is loaded in a joint simulator, and subjected to cyclic tensile, compressive and torsion loads as per the available standards. Failures such as joint loosening and breakage due to fatigue are easily observed. Long term wear of various components requires finer instrumentation. More advanced tests require a tribo-corrosion rig with simulated body fluids.



Medical and bio-compatibility testing includes: (i) toxicity and bio-compatibility studies of various parts and the prosthesis as a whole, and (ii) osteo-integration studies of various bone cements that anchor the prosthesis in bone. This is necessary to ensure that the proposed prosthesis is not rejected by the body, and gradually integrates with the natural bone.

### 10.3 Case Study: Pelvic Saddle Prosthesis

The steps in mega endo-prosthesis development are illustrated here using a case study carried out at Tata Memorial Hospital, Mumbai. It involved a patient (female, 46) diagnosed as having a malignant tumor in the left pelvic bone just above the hip joint (see Fig. 10.3). The pelvic bone has an intricate shape that is difficult to visualize by radiography images alone. The main challenge was to gauge the extent of bone tumor and determine the optimum resection length for removing the tumor while leaving sufficient gap for saddling the hip prosthesis. The prosthesis has a cemented fit at the femoral end and a close but uncemented fit with the resected portion of the pelvic bone. Excessive gap between the prosthesis and pelvic bone could lessen the prosthesis stability whereas a very tight fit could lead to intraoperative fractures. Medical modeling and rapid prototyping played an important role in developing the custom prosthesis by aiding the surgeon and prosthesis manufacturer. The steps are briefly described here.

#### 10.3.1 Medical Modeling and Virtual Surgery

The radiography images were used for identifying the location, shape and extent of the tumor, plan the resection line, and design the pelvic prosthesis. The saddle portion of the prosthesis has to fit the (yet to be) resected line of the pelvic bone. This was achieved by 3D reconstruction of the affected portion of

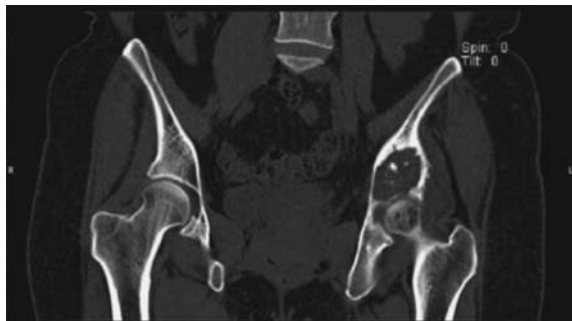


**Fig. 10.3** Preoperative radiograph showing bone tumor above left hip joint

the pelvic bone, and haptic-based virtual surgery to determine the position of the resection line as well as the shape of the bone left after resection.

The main input included 105 CT scans in DICOM format with the following parameters: pixel width = 0.8 mm, slice thickness = 2.1 mm, and inter slice distance = 3.0 mm. For 3D reconstruction, the voxel size was set to pixel size, increasing the total number of effective slices to 394 with a resolution of 0.8 mm. The bone segmentation was performed using the intensity threshold values [400, 2000]. The final volume model is displayed along with sagittal, coronal, and axial images on sectional planes passing through the middle of model (Fig. 10.4). The tumor region was found to be inside the pelvic bone, just above the hip joint in the left leg of the patient.

Internal thickness was computed and displayed for the affected half of the pelvic model to aid the surgeon and prosthesis manufacturer (Fig. 10.5): black denotes minimum thickness (4.1 mm) and white denotes maximum thickness (11.3 mm). This was very useful for surgery planning and designing the matching portion of the prosthesis.

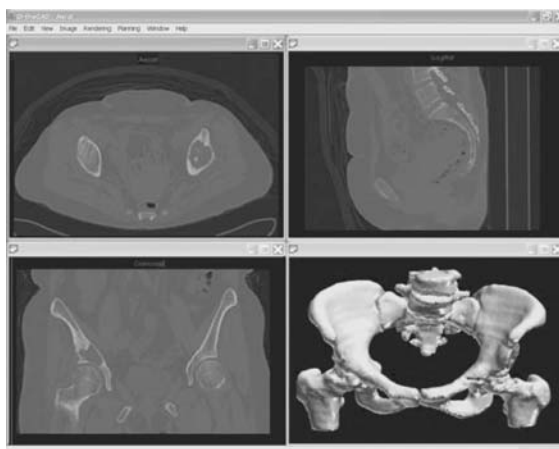


**Fig. 10.4** Reconstruction of 3D medical model from CT images



**Fig. 10.5** Internal thickness mapping in a cross-section of pelvic bone

For planning the resection, the location of tumor with respect to the external surface of the pelvic bone has to be visualized and demarcated to plan the line of resection. Since this is difficult to achieve through a conventional solid modeling program, which can handle only regular (engineering) solids, a haptic solid modeling system (FreeForm, from Sensable Technologies, USA) was employed. The 3D model reconstructed in the medical imaging software was converted into a faceted surface model, exported in standard STL format, and imported in the haptic software. Then a smoothening function was used to remove miniature irregularities on the surface. Small holes created by missing facets were filled up. These two operations were carried out carefully to avoid loss of vital features and introduction of excessive error. Then the model was shown to the surgeon, who demarcated the boundary of the tumor on the surface of the pelvic bone model, and planned the line of resection (Fig. 10.6). Based on the location of the resection line, the model was clipped away to retain only the region of immediate interest. The other components of the prosthesis were designed based on the position of the saddle, and morphology of the other bones as seen in the radiograph (Fig. 10.7).

### 10.3.2 Prosthesis Manufacture and Actual Surgery

A rapid prototype of the medical model used for virtual resection was fabricated using Objet RP system (Objet Geometries Ltd., Israel), and provided to the prosthesis manufacturer (Fig. 10.8(a)). The manufacturer used the physical model to take the dimensional measurements required for accurate manufacture of the saddle component, as well as fit-check the component (Fig. 10.8(b)).

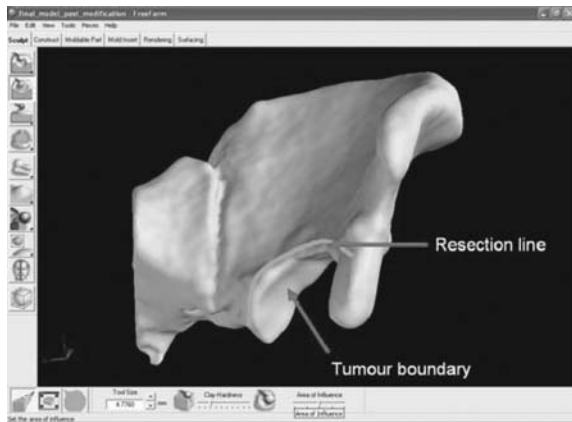
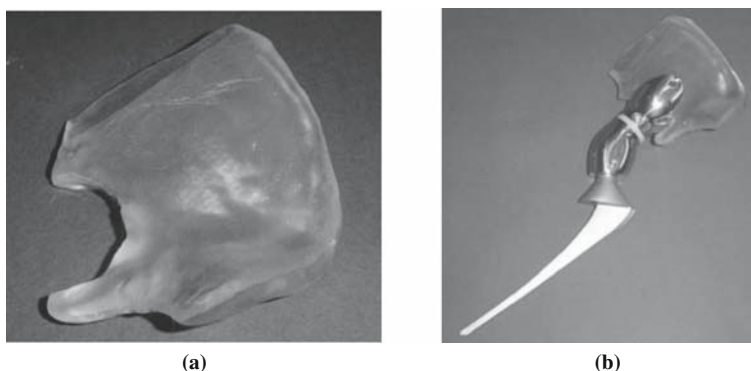


Fig. 10.6 Virtual resection of pelvic bone using a haptic-CAD system

**Fig. 10.7** Design and positioning of pelvic saddle prosthesis



**Fig. 10.8** (a) Rapid prototype of resected pelvic bone; (b) fit-check of prosthesis

An additional saddle component with a larger depression was also manufactured to ensure a good fit even in the event of additional resection during actual surgery.

The surgical procedure was carried out as planned. The pelvic bone was resected along the line as indicated earlier, the tumour was removed, and replaced by the pelvic prosthesis. The femoral stem of the prosthesis was inserted into the femur bone, the saddle was placed around the resected portion of the pelvic bone, and the two portions were connected at the ball-and-socket hip joint (Fig. 10.9(a)). The fit between the saddle component and resected pelvic bone was found to be about 1.5 mm, as planned. This was confirmed by post-operative radiographs (Fig. 10.9(b)). The patient was able to walk and navigate stairs aided by a walker within three months of the surgical intervention.



**Fig. 10.9** (a) Implantation of prosthesis; (b) post-operative radiograph

## 10.4 Conclusion

The development of customized mega endo-prostheses is made possible due to recent developments in medical imaging and 3D reconstruction, coupled with the use of computer-aided design, prototyping, and manufacturing technologies. Many problems however, remain to be solved: prosthesis weight reduction, better wear resistance and bone compatibility, faster and more accurate fixation techniques, and ease of revision. This requires continuous improvements of prostheses in terms of design, materials, manufacturing, instrumentation and computer-assisted surgery protocols. Another major problem relates to implant-cell interaction: allowing body cells to infiltrate, grow and replace the original missing parts (fully or partially, supported by a prosthesis). Newer technologies are being explored for this purpose: tissue engineering to create absorbable scaffolds for missing or resected portions of original tissue, nanotechnology to produce nano-tubes of carbon fibre or titanium on the implant surface, increasing its area of contact with the cells and thereby improving osteo-integration, and gene therapy to modify the genes, enabling prevention of damage to tissues, and repair of damaged tissue or providing proteins and growth factors for bone or other tissue formation.

**Acknowledgment** The authors wish to acknowledge the support of the Office of the Principal Scientific Advisor to the Government of India, New Delhi, in conducting a study of the status of orthopedic implants and prostheses, which provided useful material for this chapter. Two graduate students: Anip Sharma and Sandeep Patil, assisted the authors in developing the pelvic saddle case study. The medical modeling was carried out by research scholar K. Subburaj. The prosthesis was manufactured by Sushrut Surgicals, Mumbai.

## References

1. B. Ravi, M. Agarwal and K. Balasubramanian, *Orthopaedic Implants and Prostheses*, Position Paper, Office of the Principal Scientific Advisor to the Government of India, New Delhi, 2006.
2. K. Subburaj, S. Patil and B. Ravi, "Voxel-based Thickness Analysis of Intricate Objects," *International Journal of CAD/CAM*, 6(1), 105–115, 2006.
3. B. Ravi, Anip Sharma and Manish Agarwal, "Haptic Solid Modeling for Pelvic Bone Tumor Resection Planning and Prosthesis Development," *International CAD Conference*, Bangkok, June 20–24, 2005.
4. K. Subburaj and B. Ravi, "High Resolution Medical Models and Geometric Reasoning starting from CT/MR Images." *International Conference on CAD and Graphics*, Beijing, China, Oct. 15–18, 2007.

# Index

- Acetabular shell implants, titanium, 3, *3f*  
Acetabulum, 193  
Acrylates, in hydrogels, 50–51  
Acrylic bone cements, 90, 199, 200  
Alginate, 17, *18f*  
Allografts, bone, 79  
Armamentarium, 201  
Arthritis, 157  
Articular cartilage, 68  
ATOS (Advanced TOpometric Sensor),  
*135f*; 137–138, *138f*  
Austenitic steel, 5  
Autografts, bone, 79
- Ball-and-socket joint, 193, 198  
Biceps tendon, 194  
Bio-absorbable polymers, 200  
Biocompatibility, 1–2  
  of bone implants, 83–84  
  of ceramics, 10  
  of endoprostheses, 191  
  of finger joint prosthesis, 162  
  of hydrogels, 49, 51, *52t*  
  of mega endo-prostheses, 202  
  of metals, 2  
    *See also* specific metals  
  of polymer composite systems, 22, 23  
  of polymers, 15  
  of polyurethanes, 27, 28, 37, 40–41, *41f*  
  of prosthesis materials, 199  
  of zirconia, 11  
    *See also* specific materials  
Biodegradation  
  of bone implants, 81, 82  
  of polyurethane-based materials, 36,  
    41–44, *43f*  
  of scaffold architecture, 69  
  of synthetic polymers, 15  
Bioglass, 22
- Biomaterials  
  applications of, 2  
  definition of, 1  
  history of, 195  
    *See also* specific materials  
Biomer™, 30  
Biomimetic composites, for bone implants,  
  82, 84, 87  
Bio-Plotter, 96–97  
Biospan® , 30  
Bone, 79  
  cortical, 81  
  matrix of, 81  
  modeling and design of, 84  
  structure and properties of, 80–81  
  trabecular, 80–81  
Bone grafts, 79  
Bone implants  
  materials for, 81–82  
  requirements for, 82–83  
Bone implants, customized replacement and  
  growth, 79–104  
  bone modeling and design in, 84  
  bone structure and properties in,  
    80–81  
  challenges in, 103  
  clinical practices in design/ manufacturing  
    of, 98–102, *99f*  
  future of, 103–104  
  implant materials for, 81–82  
  implant requirements for, 82–83  
  novel techniques in, 102–103  
  overview of, 79–80  
  rapid manufacturing of, 85–98  
    *See also* Rapid manufacturing of  
    customized bone implants  
Bone remodeling, Wolff's law of stress  
  induced, 21  
Breast implants, polyurethane, 41–42

- CAD/CAM systems in dentistry, 125–152  
*See also* Dentistry, CAD/CAM systems in
- Calcium alginate microcapsules, 17, 18*f*
- Cancellous bone, 81
- Carbon fiber reinforced epoxy plates, 22, 22*f*
- Carbon nanotubes, 23–25, 24*f*
- Cardiothane<sup>®</sup>, 30
- Cartilage regeneration, scaffold architecture on, 68–71, 70*f*, 71*f*
- Cement fixation, 165
- Cementless, biological fixation, 165
- Central nervous system regeneration, engineered scaffold architecture on, 71–76  
 guidance tubes in, 71  
 oriented channels in, 71  
 in rat brain/spinal cord defect model, 72–73, 72*f*–74*f*  
 in rat spinal cord transection model, 73–75, 74*f*, 75*f*, 76*t*  
 reinforcing for stiffness in, 72  
 syringomyelia from, 72
- Ceramic-on-ceramic (COC) articulations, 159, 199
- Ceramics, 9–12, 200  
 applications of, 10  
 for artificial finger joint, 176, 176*f*  
 for bone implants, 81–82  
 definition and properties of, 9–10  
 hydroxyapatite, 10, 11*f*  
 for orthopedic implants and prostheses, 200  
 zirconia, 11–12, 12*f*
- Cercon<sup>®</sup> system, 129–130, 130*f*
- CEREC<sup>®</sup> system, 127–129, 128*f*, 129*f*
- Chain extender, 33, 33*f*
- Chondroconductive materials, 67
- Collateral ligaments, of knee, 193
- Colloidal-crystal templating, 53, 54*f*
- Compact bone, 81
- Compartments, of knee joint, 193
- Computed tomography (CT) scanning, as dental digitizer, 135–136, 135*f*, 136*f*
- Computer-aided design and computer-aided manufacturing (CAD/CAM), 125  
 in dentistry, 125–152  
*See also* Dentistry, CAD/CAM systems in
- Computer-aided design (CAD), of mega endo-prostheses, 191–206  
*See also* Mega endo-prostheses, computer-aided development of
- Computer numerical control (CNC) machining, 148–149, 149*f*
- Condyle, 166–167, 167*f*, 192
- Confocal laser scanning lithography, 56, 57*f*
- Contact digitizers, 133–135, 134*f*, 135*f*  
 advantages of, 134  
 for dental data capture, 113, 113*f*  
 drawbacks of, 134–135  
 MAXNC<sup>™</sup>, 134, 134*f*, 135*f*  
 MicroScribe<sup>®</sup>, 134, 134*f*  
 probe in, 133  
 software of, 133–134
- Cortical bone, 81
- Cruciate ligaments, of knee, 193
- Customization  
 of bone implants, 79–104  
*See also* Bone implants, customized replacement and growth of prostheses, 198  
*See also* specific types
- Cynovad Pro 50<sup>™</sup>, 130–131, 131*f*
- Cynovad ShadeScan<sup>™</sup> system, 131
- DeLaunay triangulation, 140, 140*f*
- Dental bar design modeling, 145–146, 146*f*, 147*f*
- Dental data capture, 112–114, 113*f*, 114*t*
- Dental prostheses  
 driving forces in digital design/  
 fabrication of, 126  
 frameworks for, 110–112, 111*f*, 112*f*  
 history of digital design and fabrication of, 125–126  
 surface reconstruction techniques for, 138–142  
*See also* Surface reconstruction techniques, in dentistry
- Dental prostheses, direct digital manufacturing of, 109–123, 150–152, 152*f*  
 clinical cases of, 122, 122*t*, 123*f*  
 dental data capture in, 112–114, 113*f*, 114*t*  
 digital design in, 114–116, 115*f*  
 frameworks in, 110–112, 111*f*, 112*f*  
 history and overview of, 109–110  
 quality control in, 120–122, 120*f*–122*f*  
 selective laser melting in, 110, 110*f*, 116–119, 116*f*–120*f*, 117*t*
- Dentistry, CAD/CAM systems in, 125–152  
 commercial, 126–133  
*See also* Dentistry, commercial dental CAD/CAM systems in



- digital data acquisition methods in, 133–138
  - See also* Dentistry, digital data acquisition methods in
- digital design in, 142–147
  - See also* Dentistry, digital design in
- digital fabrication in, 147–152
  - See also* Dentistry, digital fabrication in
- driving forces in, 126
- history of, 125–126
- surface reconstruction techniques for, 138–142
  - See also* Surface reconstruction techniques, in dentistry
- Dentistry, commercial dental CAD/CAM systems in, 126–133
  - Cercon<sup>®</sup>, 129–130, 130f
  - CEREC<sup>®</sup>, 127–129, 128f, 129f
  - Cynovad Pro 50<sup>™</sup> and WaxPro<sup>™</sup>, 130–131, 131f
  - Cynovad ShadeScan<sup>™</sup>, 131
  - Lava<sup>™</sup>, 131–132, 131f, 132f
  - Nobel Biocare Procera<sup>®</sup>, 126–127, 127f
  - OrthoCAD<sup>™</sup>, 132–133, 132f
- Dentistry, digital data acquisition methods in, 133–138
  - contact digitizers, 133–135, 135f, 136f
    - See also* Contact digitizers
  - for design and fabrication, 133–138
    - See also* specific methods
  - for direct digital manufacturing, 112–114, 113f, 114t
  - non-contact digitizers, 135–138, 135f, 136f
    - See also* Non-contact digitizers
- Dentistry, digital design in, 142–147
  - driving forces in, 126
  - modeling of dental bars for implant restorations in, 145–146, 146f, 147f
  - modeling of inlays in, 144, 144f
  - modeling of standard teeth in, 142–143, 142f, 143f
- Dentistry, digital fabrication in, 147–152
  - computer numerical control (CNC) machining in, 148–149, 149f
  - direct digital manufacturing in, 109–123, 150–152, 152f
    - See also* Dental prostheses, direct digital manufacturing of
  - driving forces in, 126
  - overview of, 147
  - rapid prototyping in, 149–150, 150f, 151f
- Digital design
  - of dental prostheses, 114–116, 115f
  - in dentistry, 142–147
    - See also* Dentistry, digital design in
- Digital fabrication, in dentistry, 147–152
  - See also* Dentistry, digital fabrication in
- Digitizers
  - contact, 133–135, 134f, 135f
    - See also* Contact digitizers
  - non-contact, 135–138
    - See also* Non-contact digitizers
  - passive optical, 137
- Dip moulding/coating, of polyurethanes, 38, 38f
- Direct digital manufacturing (DDM), 110
  - of dental prostheses, 109–123, 150–152, 152f
    - See also* Dental prostheses, direct digital manufacturing of
- Direct laser form (DLF), for bone implants, 91–92, 92f
- Elasthane<sup>®</sup>, 29
- Elastomers
  - polyurethane, 29, 32–33, 33f
  - segmented behavior of, 34–35, 34f, 35f
    - See also* specific types
- Electrical discharge machining (EDM), 175–176
- Electron beam melting (EBM), 92–93, 93f, 94f
- Electrospinning, of polyurethanes, 38–39, 39f
- Endo-prosthesis, 191, 192f
  - See also* Mega endo-prostheses, computer-aided development of; Prostheses; specific types and materials
- Engineered scaffold architecture, 67–76
  - for bone formation, 67
  - on cartilage regeneration, 68–71, 70f, 71f
  - on CNS regeneration, 71–76
    - See also* Central nervous system regeneration, engineered scaffold architecture on
  - mechanical and mass transport properties and, 69
  - for soft tissue regeneration, 67–68
- Expandable mega-prosthesis, 198
- Extrusion based techniques, 93–97
  - Bio-Plotter, 96–97
  - fused deposition modelling (FDM), 93–95
  - precision extruding deposition (PED), 95
  - precision extruding manufacturing (PEM), 95–96

- Femoral condyle, 192
- Femoral stem implants  
 hydroxyapatite, 10, *11f*  
 titanium, 3–4, *3f*, *4f*
- Femur  
 in hip joint, 193  
 in knee joint, 192
- Fiber reinforced polymers, 22, *22f*
- Finger joint, artificial, 157–186  
 design objectives for, 159–162, *161f*  
 design objectives for, anatomical  
 compatibility in, 160–161, *161f*  
 design objectives for, basics of, 159–160  
 design objectives for, functional  
 compatibility in, 161–162, *161f*  
 design objectives for, issues to be solved  
 in, 160  
 design objectives for, materials  
 compatibility in, *161f*, 162  
 design optimization by finite element  
 method for, 177–178, *178f*  
 finger joint arthroplasty in, 157–158  
 functional evaluation summary for,  
 185–186  
 history of, 157–159  
 implant articulating surface for,  
 168–169, *169f*  
 implant design and surgical procedure  
 for, 169–170, *170f*, *171f*  
 implant sizing and finger joint  
 biomechanics in, 171–172  
 intramedullary dimensions for fixation  
 stem design in, 164–166  
 long-term performance testing of,  
 178–181, *179f*  
 materials strength requirement for,  
 174–176, *175f*, *176f*  
 morphology study for implant design in,  
 162–164, *163f*, *164f*  
 PIP joint stability in, 181–185, *183f*, *185t*  
 prototype model generation in,  
 172–173, *173f*  
 sagittal curvature of condyles and ROM  
 in, 166–167, *167f*
- Finger joint arthroplasty, 157–158
- Finger joint kinematic testing rig, 182, *183f*
- Finger joint morphology, for implant  
 design, 162–164, *163f*, *164f*
- Finite element method (FEM), 174,  
 177–178, *178f*
- Fixation, of prosthesis, 199  
 See also specific types
- Freedom of movement, of prosthesis, 198
- Functional gradient materials, for bone  
 implants, 82
- Fused deposition modelling (FDM), 93–95
- Glenoid, 194
- Gold, 9
- GORE-TEX<sup>®</sup>, 15–17, *16f*, *17f*
- Heparin, on polyurethane elastomer,  
 40–41, *41f*
- Hinge joint, 198
- Hintels Hi-Scanm, 137, *138f*
- HIPing, 7, *7f*
- Hip joint anatomy, 193
- Hip movements, 193
- Hi-Scanm, 137, *138f*
- History  
 of artificial finger joint, 157–159  
 of biomaterials, 195  
 of CAD/CAM systems in dentistry,  
 125–126  
 of CAD in mega endo-prosthesis  
 development, 195  
 of digital design and fabrication of dental  
 prostheses, 125–126  
 of direct digital manufacturing of dental  
 prostheses, 109–110  
 of polyurethane-based materials for  
 medical devices, 30  
 of prostheses, 195
- Hot isostatic pressing (HIPing), 7, *7f*
- Humerus, 193–194
- Hydrogels, 16–17, *17f*, *18f*, 49–59  
 acrylate-based, 50–51  
 applications of, 49  
 bioactive, design of, 51–53, *53f*  
 chemistry of, 49, *50f*  
 laser scanning lithography of, 56, *57f*  
 photolithographic patterning of, 54–55,  
*55f*, *56f*  
 photopolymerization in, 51, *52t*  
 polyethylene glycol-based, 49–50, *50f*,  
 53, *53f*  
 polymers in, 49, *50f*  
 porous, templating techniques for, 53, *54f*  
 three-dimensional rapid prototyping of,  
 57–59, *58f*, *59f*
- Hydroxyapatite, 10, *11f*, 200
- Implants, bone, *see* Bone implants
- Inlay modeling, 144, *144f*
- Isocyanates, polyurethane from, 30–33,  
*30f–33f*

- Joint  
 ball-and-socket, 193, 198  
 hinge, 198  
 See also specific joints
- Joint capsule, hip, 193
- Joint replacement surgery, 157–158  
 See also Finger joint, artificial; specific joints
- Kinematics, 194
- Knee implants, zirconia, 11–12, 12*f*
- Knee joint  
 anatomy of, 192–193  
 loads on, 193, 194  
 motion of, 194
- Labrum, 194
- Landsmeer's model, 171
- Laser-based layer-by-layer polymerization, 57–58, 58*f*
- Laser engineered net shaping (LENS), 76*f*, 85–87
- Laser scanning lithography, of hydrogels, 56, 57*f*
- Lava™ system, 131–132, 131*f*, 132*f*
- Layer-by-layer polymerization, laser-based, 57–58, 58*f*
- Layer manufacturing, 85, 109–110
- Ligaments  
 of knee joint, 193  
 of shoulder joint, 194
- Liquid crystal display (LCD) projection  
 photolithography, 55, 56*f*
- Lithography  
 confocal laser scanning, 56, 57*f*  
 stereolithography, 98
- Low carbon steel, 5
- Low-shrinkage polymer systems, for dental applications, 20–21
- LPLA, 200
- LPLA-HA, 200
- Lycra®, 29
- Magnetic resonance imaging (MRI), as  
 dental digitizer, 135*f*, 136–137
- Marching cube algorithm, 141–142, 141*f*
- Martensitic stainless steel, 5
- MAXNC™, 134, 134*f*, 135*f*
- Mega endo-prostheses, computer-aided  
 development of, 191–206  
 background on, 191–192  
 biocompatibility in, 202  
 biomechanical studies in, 194  
 configuration and design in, 198–199  
 hip joint anatomy in, 193  
 history of, 195  
 knee joint anatomy in, 192–193  
 in manufacture and testing, 200–202  
 materials for, 199–200  
 medical imaging and 3D reconstruction  
 in, 196–197, 196*f*  
 newer technologies for, 206  
 patient requirements in, 191–192  
 pelvic saddle prosthesis case study in,  
 202–206  
 See also Pelvic saddle prosthesis case  
 study  
 problems to solve in, 206  
 shoulder joint anatomy in, 193–194
- Mega prosthesis, 198
- Menisci, 192
- Metacarpophalangeal (MCP) joint,  
 artificial, see Finger joint, artificial
- Metal alloys and metallic biomaterials, 2–9  
 advantages of, 2  
 for artificial finger joint, 175, 175*f*  
 gold, 9  
 noble metals, 8–9  
 for orthopedic implants and prostheses,  
 199–200  
 platinum, 9  
 shape memory alloys, 6–8, 7*f*, 8*f*  
 silver, 9  
 stainless steel, 4–5, 5*f*, 6*f*  
 for structural applications, 21  
 titanium, 2–4, 3*f*, 4*f*  
 See also specific metals
- Metal-ceramic articulation, 199
- Metal-on-metal (MOM) articulations, 159
- Metal-plastic articulation, 199
- Metals, 2
- Methacrylate-based photopolymerizable  
 resins in, 18
- Micro-filled polymers, for dental  
 applications, 19
- MicroScribe®, 134, 134*f*
- Motion simulator, finger joint, 179–180, 179*f*
- Multiphoton excitation, in 3D rapid  
 prototyping of hydrogels, 58–59, 59*f*
- Nano-filled polymers, for dental  
 applications, 19–20, 20*f*
- Nanomaterials, 23–25, 24*f*
- NC milling, 111–112
- Neuroconductive materials, 67
- Nitinol, 6–8, 7*f*, 8*f*

- Nobel Biocare Procera<sup>®</sup> system,  
126–127, 127*f*
- Noble metal, 8–9
- Non-contact digitizers, 135–138  
CT scanning, 135–136, 135*f*, 136*f*  
MRI, 135*f*, 136–137  
optical digitization, 135*f*, 137–138, 138*f*
- Object thickness distribution, 197
- Optical digitization, 135*f*, 137–138, 138*f*
- Optical scanners, for dental data capture,  
113–114, 114*t*
- OrthoCAD<sup>™</sup> system, 132–133, 132*f*
- Osteoarthritis, 157
- Osteoconductive materials, 67
- Passive optical digitizer, 137
- Patella, 193
- Pellathane<sup>®</sup>, 29–30
- Pelvic bone, 193
- Pelvic saddle prosthesis case study, 202–206  
medical modeling and virtual surgery in,  
202–204, 203*f*–205*f*  
patient preoperation in, 202, 202*f*  
prosthesis manufacture and actual  
surgery in, 204–205, 205*f*, 206*f*
- Performance testing, of artificial finger  
joints, 178–181, 179*f*
- Phalangeal bones  
major dimensions of, 163, 164*f*  
stress fields on, 174
- Photoinitiators, for hydrogels, 51, 52*t*
- Photolithographic patterning, of hydrogels,  
54–55, 55*f*, 56*f*
- Photolithography, liquid crystal display  
(LCD) projection, 55, 56*f*
- Photopolymerization  
of 3D structures, 59, 59*f*  
in hydrogels, 51, 52*t*
- Platinum, 9
- Point cloud, 133, 139, 140
- Polyethylene glycol, in hydrogels, 49–50,  
50*f*, 53, 53*f*
- Polymer biomaterials, synthetic, 15–23  
for bone implants, 82  
for dental restorative applications, 17–21  
*See also* Polymers for dental  
restorative applications  
nanomaterials, 23–25, 24*f*  
polytetrafluoroethylene (PTFE), 15–17,  
16*f*, 17*f*  
properties and uses of, 15  
for structural applications, 21–23, 22*f*
- Polymer-ceramics, for bone implants, 82
- Polymers for dental restorative applications,  
17–21  
characteristics and performance of,  
17–18  
low-shrinkage systems in, 20–21  
methacrylate-based photopolymerizable  
resins in, 18  
problems with, 18–19  
reinforced polymers in, 19–20, 20*f*
- Polymethylmethacrylate (PMMA) bone  
cements  
in bioactive ceramics, 88  
hydrogels from, 53  
for orthopedic implants and  
prostheses, 200
- Polytetrafluoroethylene (PTFE), 15–17, 16*f*,  
17*f*, 82
- Polyurethane-based materials for medical  
devices, 27–45  
advantages of, 28, 39–40  
applications of, 28–30, 29*f*  
biocompatibility of, 27, 28, 37, 40–41, 41*f*  
biodegradation of, 41–44, 43*f*  
biodegradation of, application of, 44  
biodegradation of, approaches to, 42–43  
biodegradation of, hydrolytic enzymes  
in, 43–44  
biodegradation of, in breast implants,  
41–42  
biodegradation of, in catheter leads for  
pacemakers, 42  
biodegradation of, oxidation in,  
43–44, 43*f*  
biodegradation of, reactive oxygen  
radicals in, 43, 43*f*  
biological systems on, 29  
chemistry of, 30–33, 30*f*–33*f*  
as coatings, 32  
elastomers in, 29, 32–33, 33*f*  
as fibers, 31–32  
as foams, 32  
history of, 30  
physical properties of, 32*f*, 34–36,  
34*f*–36*f*  
problems with, 29  
processing of, 37–39, 37*f*–39*f*  
synthesis of, 30–31, 30*f*–32*f*  
toxicity of, 31, 32*f*
- Polyurethanes, 27
- Porous hydrogels, templating techniques  
for, 53, 54*f*
- Precision extruding deposition (PED), 95

- Precision extruding manufacturing (PEM), 95–96
- Precision turning screw, 95
- Procera<sup>®</sup> system, 126–127, 127*f*
- Prostheses, 191, 192*f*
- CAD configuration and design of, 198–199
  - customization of, 198
    - See also specific types
  - fixation of, 199
  - freedom of movement of, 198
  - history of, 195
  - manufacture and testing of, 200–202
  - materials for, 199–200
  - mega, *see* Mega endo-prostheses,
    - computer-aided development of
    - replacement of, indications for, 198
    - standards and certifications for, 195–196
    - See also specific types and materials
- Pro 50<sup>™</sup> system, 130–131, 131*f*
- Proximal interphalangeal (PIP) joint, artificial
- stability of, 181–185, 183*f*, 185*t*
  - See also Finger joint, artificial
- Rapid manufacturing, 109
- Rapid manufacturing of customized bone implants, 85–98
- electron based, 92–93, 93*f*, 94*f*
  - extrusion based, 93–97
    - See also Extrusion based techniques
  - laser based, 85–92
  - laser based, laser engineered net shaping (LENS), 76*f*, 85–87
  - laser based, selective laser melting (SLM), 91–92, 92*f*
  - laser based, selective laser sintering (SLS), 87–91, 88*f*, 90*f*, 91*f*
  - printing based, 97
  - stereolithography, 98
- Rapid prototype biomodel shaping, 99–101, 99*f*
- Rapid prototyping, 109
- in bone modeling and design, 84
  - in digital fabrication in dentistry, 149–150, 150*f*, 151*f*
  - of hydrogels, 3D, 57–59, 58*f*, 59*f*
  - of mega endo-prosthesis, 201
- Registration elements, for dental data capture, 113–114, 113*f*
- Reinforced polymers, for dental applications, 19–20, 20*f*
- Replacement, of prosthesis, 198
- Resurfacing prosthesis, 198
- Reverse engineering, in bone modeling and design, 84
- Rheumatoid arthritis, 157
- Rutile, 2
  - See also Titanium
- Scaffold, bone
- materials for, 81–82
  - requirements for, 83
- Scaffold architecture, engineered, 67–76
- for bone formation, 67
  - on cartilage regeneration, 68–71, 70*f*, 71*f*
  - on CNS regeneration, 71–76
    - See also Central nervous system regeneration, engineered scaffold architecture on
  - mechanical and mass transport properties in, 69
  - for soft tissue regeneration, 67–68
- Scapula, 193–194
- Screws
- bio-absorbable polymer, 200
  - in bone grafts, 99, 99*f*
  - precision turning, 95
  - stainless steel, 4, 5, 5*f*
  - titanium, 3, 91, 159, 165
- Segmentation, 196–197
- Selective laser melting (SLM), 110
- for bone implants, 91–92, 92*f*
  - for dental prostheses, 116–119, 116*f*–120*f*, 117*t*, 151, 152*f*
  - See also Dental prostheses, direct digital manufacturing of
  - for dental prostheses, quality control in, 120–122, 120*f*–122*f*
- Selective laser sintering (SLS), 87–91, 88*f*, 90*f*, 91*f*, 151
- Shape memory alloys, 6–8
- applications of, 7–8, 8*f*
  - description of, 6–7, 7*f*
- Shoulder blade, 193–194
- Shoulder joint anatomy, 193–194
- Silicon hydrogels, 17
- Silver, 9
- Single photo excitation, in 3D rapid prototyping of hydrogels, 57–58, 58*f*
- Soft tissue
- engineered scaffold architecture on regeneration of, 67–75
  - See also Engineered scaffold architecture
  - mechanical properties of, 68, 68*t*

- Spandex, 32
- Sphere-templating, 53, 54*f*
- Spongy bone, 81
- Stainless steel, 4–5, 5*f*  
 applications of, 4–5, 5*f*, 6*f*  
 description of, 4  
 for orthopedic implants and prostheses, 200
- Staple fixation system, stainless steel, 5, 5*f*
- Stereolithography, 98
- Stress shielding, 83
- Surface reconstruction techniques, in  
 dentistry, 138–142  
 marching cube algorithm in, 141–142, 141*f*  
 from point cloud, 139, 140, 141*f*  
 from point cloud, data conversion to  
 triangular facets in, 139–140,  
 139*f*, 140*f*  
 voxelization in, 140–141
- Surface replacement, 159
- Synovium, 193
- Synthetic polymers, 15–23  
*See also* Polymer biomaterials, synthetic
- Teeth  
 modeling of, 142–143, 142*f*, 143*f*  
*See also* Dentistry
- Teflon<sup>®</sup>, 15–17, 16*f*, 17*f*
- Tegaderm<sup>®</sup>, 28
- Templating techniques, for porous  
 hydrogels, 53, 54*f*
- Theriform 3D printing, 97
- Thermoplastic elastomers, 32–33, 33*f*  
 segmented behavior of, 34–35, 34*f*, 35*f*
- Thickness mapping, 197
- Three-dimensional rapid prototyping of  
 hydrogels, 57–59, 58*f*, 59*f*  
 multiphoton excitation in, 58–59, 59*f*  
 single photo excitation in, 57–58, 58*f*
- 3D printing (3DP), 97  
 of dental prostheses, 151–152, 152*f*
- Tibia, 192
- Tibial condyle, 192
- Time-of-flight laser scanner, 137
- Titanium, 2–4  
 applications of, 3–4, 3*f*, 4*f*  
 description of, 2–3  
 for orthopedic implants and prostheses, 200
- Titanium alloys, 2
- Total knee prosthesis, 191, 192*f*
- Trabecular bone, 80–81
- Triangulation scanner, 137
- Two-photon effect, 58–59, 59*f*
- Ultra high molecular weight polyethylene  
 (UHMWPE), 82, 200, 201
- Volumetric model, 197
- Voxelization, 140–141, 197
- Washer, stainless steel, 5, 5*f*
- WaxPro<sup>™</sup>, 130–131, 131*f*
- Wolf's law of stress induced bone  
 remodeling, 21
- Zirconia, 11–12, 12*f*